

## University of Groningen

### Laser cooling and trapping of barium

De, Subhadeep

**IMPORTANT NOTE: You are advised to consult the publisher's version (publisher's PDF) if you wish to cite from it. Please check the document version below.**

*Document Version*

Publisher's PDF, also known as Version of record

*Publication date:*

2008

[Link to publication in University of Groningen/UMCG research database](#)

*Citation for published version (APA):*

De, S. (2008). *Laser cooling and trapping of barium*. s.n.

**Copyright**

Other than for strictly personal use, it is not permitted to download or to forward/distribute the text or part of it without the consent of the author(s) and/or copyright holder(s), unless the work is under an open content license (like Creative Commons).

The publication may also be distributed here under the terms of Article 25fa of the Dutch Copyright Act, indicated by the "Taverne" license. More information can be found on the University of Groningen website: <https://www.rug.nl/library/open-access/self-archiving-pure/taverne-amendment>.

**Take-down policy**

If you believe that this document breaches copyright please contact us providing details, and we will remove access to the work immediately and investigate your claim.

*Downloaded from the University of Groningen/UMCG research database (Pure): <http://www.rug.nl/research/portal>. For technical reasons the number of authors shown on this cover page is limited to 10 maximum.*

# Laser Cooling and Trapping of Barium

To Ma, Baba

COVER: Photograph of trapped barium atoms. The bright spot visible through the center of the optical port is fluorescence from a cloud of trapped barium atoms.

This work has been performed as part of the research program of the “Stichting voor Fundamenteel Onderzoek der Materie” (FOM) through programme 48 (TRI $\mu$ P), which is financially supported by the “Nederlandse Organisatie voor Wetenschappelijk Onderzoek” (NWO) under VIDI grant 639.052.205. Additional funding was provided by the European Commission under contract HPRI-CT-2001-50034 (NIPNET) and HPRI-CT-2001-50022 (Ion Catcher).

Druk: Facilitair Bedrijf, University of Groningen, Groningen, September 2008

RIJKSUNIVERSITEIT GRONINGEN

# Laser Cooling and Trapping of Barium

## Proefschrift

ter verkrijging van het doctoraat in de  
Wiskunde en Natuurwetenschappen  
aan de Rijksuniversiteit Groningen  
op gezag van de  
Rector Magnificus, dr. F. Zwarts,  
in het openbaar te verdedigen op  
vrijdag 12 september 2008  
om 16.15 uur

door

**Subhadeep De**

geboren op 17 oktober 1979  
te Chuchura, Hooghly, West Bengal, India

Promotor: Prof. dr. Klaus Jungmann

Copromotor: Dr. Lorenz Willmann

Beoordelingscommissie: Prof. dr. Reinhard Morgenstern

Prof. dr. Erling Riis

Prof. dr. Peter van der Straten

**ISBN:** 978-90-367-3515-5 (printed version)

**ISBN:** 978-90-367-3516-2 (digital version)

# Contents

<b>1</b>	<b>Introduction</b>	<b>1</b>
<b>2</b>	<b>Searching for Electric Dipole Moments with Trapped Atoms</b>	<b>5</b>
2.1	Permanent Electric Dipole Moments . . . . .	6
2.2	EDM's and the Standard Model . . . . .	7
2.2.1	Worldwide EDM Experiments . . . . .	7
2.2.2	Principle of an EDM Measurement . . . . .	10
2.3	Radium Isotopes . . . . .	12
2.3.1	Schiff Moments . . . . .	12
2.3.2	Magnetic Quadrupole Moments . . . . .	13
2.3.3	Degenerate States of Opposite Parity . . . . .	13
2.4	Uncertainties of EDM Measurements . . . . .	14
2.5	EDM Measurement with Trapped Sample . . . . .	17
<b>3</b>	<b>Heavy Alkaline-earth Elements: Barium and Radium</b>	<b>19</b>
3.1	Radium . . . . .	19
3.2	Barium . . . . .	22
3.3	Laser Cooled Atoms . . . . .	23
3.3.1	Laser Cooling of Leaky Systems, Barium and Radium . . .	26
3.3.2	Discussion of Atomic Beam Slowing . . . . .	31
<b>4</b>	<b>Experimental Tools</b>	<b>37</b>
4.1	Barium Atomic Beam . . . . .	37
4.2	Lasers . . . . .	39
4.2.1	Multiple Frequency Generation . . . . .	43
4.2.2	Stabilization of the Lasers . . . . .	45
4.2.3	Optics Layout . . . . .	47
4.3	Fluorescence Detection . . . . .	49

4.4	Data Acquisition . . . . .	51
4.5	Magnetic Field . . . . .	51
<b>5</b>	<b>Laser Cooling of Barium</b>	<b>57</b>
5.1	Decay Branching of the $5d6p\ ^3D_1^o$ State . . . . .	58
5.1.1	Decay Branching Ratios . . . . .	59
5.1.2	Measurements . . . . .	61
5.2	Deceleration of the Barium Atomic Beam . . . . .	66
5.2.1	Cooling Transition . . . . .	69
5.2.2	Repumping Transitions . . . . .	69
5.3	Velocity Distribution in the $6s5d\ ^3D$ -States . . . . .	71
5.3.1	Measurements . . . . .	76
5.3.2	Analysis . . . . .	78
<b>6</b>	<b>Barium in a Magneto Optical Trap</b>	<b>83</b>
6.1	MOT Setup . . . . .	84
6.2	Characterization of the Barium MOT . . . . .	88
6.2.1	Capture Velocity of MOT . . . . .	92
6.2.2	Trap Loss . . . . .	93
6.2.3	Frequency Detunings of Repump Lasers . . . . .	100
6.2.4	Trapping Laser Intensity . . . . .	103
6.2.5	Temperature of the Trapped Cloud . . . . .	104
6.2.6	Loading Efficiency of the MOT . . . . .	107
6.3	Lifetime of the $5d^2\ ^3F_2$ State . . . . .	108
<b>7</b>	<b>Outlook</b>	<b>117</b>
<b>A</b>	<b>Numerical Calculation: Magnetic Field</b>	<b>121</b>
<b>B</b>	<b>Calibration Quantum Efficiency of the PMT</b>	<b>123</b>
<b>C</b>	<b>Atom-Photon Interactions</b>	<b>127</b>
	References	129
	Summary	143
	Samenvatting	145

# Chapter 1

## Introduction

Fundamental symmetries play a central role in modern physics. Symmetries have significantly contributed to the development of the presently accepted physical theories. To date the Standard Model (SM) [1–4] is the best theory to describe the electromagnetic, the weak and significant parts of the strong interactions. Gravity is not included yet in this framework. The SM does not fully explain the underlying structure in nature. Many aspects, e.g., the number of particle generations, the fundamental fermion masses, the origin of parity violation or the dominance of matter over antimatter in the universe can not be derived from this theory. The recent observations in connection with searches for neutrino oscillations can however be accommodated by small modifications in the SM [5]. Speculative theoretical models such as Super SYmmetry (SUSY) [6], LeftRight symmetry [7] and many others have been developed to expand the SM in order to gain deeper insights into its not well understood features. Experimental tests of the SM are attempts to identify new physical processes that would shed light on not well understood physical facts observed in nature and to gain hints into which theoretical direction the SM needs to be expanded.

Of particular interest are the discrete symmetries Charge conjugation (C), Parity (P) and Time reversal (T). In 1956 was first a suggestion to search for P violation by T. D. Lee and C. N. Yang [8]. The experimental observation of P violation in the  $\beta$ -decay of  $^{60}\text{Co}$  by C. S. Wu and her collaborators came soon after [9]. Since then many experiments have confirmed the result with increasing precision in a number of systems. Furthermore, the combined symmetry CP is violated as it has been observed in the  $K^0$  and  $B^0$  meson decays [10, 11]. Such CP violation could lead to matter-antimatter asymmetry in the baryogenesis, but

the experimentally observed mechanism, which fully lies within the SM, is not sufficient to explain the matter-antimatter asymmetry in the universe [12]. Other sources of CP-violation could manifest themselves in nonzero permanent Electric Dipole Moments (EDM's) of fundamental particles [13]. The existence of an EDM of an elementary particle require P and T violation. Under the assumption of an invariance of physics under the combined C, P, and T transformations, which is the CPT theorem [14], a permanent EDM also violates CP.

Recently radium (Ra) has been identified as a new candidate for sensitive EDM searches in neutral atoms [15]. Radium isotopes exhibit a high sensitivity to parity and time reversal violating effects which arise from their nuclear and atomic structure. The sensitivity to a possible EDM of nucleons can be orders of magnitude larger than the original particle EDM. This stems from shape deformations of the nucleus. Octupole deformations in nuclei of radium isotopes near the valley of nuclear stability are associated with near degeneracy of states of opposite parity. The enhancement is due to mixing of these states in the external field created by nucleon EDM. The isotope  $^{225}\text{Ra}$ , for example, has such a large octupole deformation in the nuclear ground state. Theoretical estimates yield an enhancement of 50-500 for a nucleon EDM [16, 17]. Radium in an excited state also offers a higher sensitivity to nuclear and electron EDM's due to its atomic level structure [18, 19]. According to the available atomic level data one finds almost degenerate states of opposite parity, i.e., the  $7s7p\ ^3P_1$  and the  $7s6d\ ^3D_2$  states [20]. The energy difference is reported to be as small as only  $\sim 10^{-3}$  eV, a feature not found in any other atomic system. The enhancement of a nuclear or electron EDM can be as large as several  $10^4$  [18, 19]. This is significantly larger than the enhancement in the mercury atom ( $^{199}\text{Hg}$ ) from which the most stringent limit for a nuclear EDM was obtained [21]. Because of these properties radium offers great potentials for searches for permanent EDM's.

An efficient method to collect a large number of particles is required in order to exploit the high sensitivity of rare and radioactive radium isotopes. Modern atomic physics methods offer tools for neutral atom trapping, which promise to be ideal for such experiments. In this thesis laser cooling and trapping strategies for heavy alkaline-earth elements, i.e., barium (Ba)<sup>1</sup> and radium are discussed (see Figs. 1.1 and 1.2). These elements require an expansion of known laser cooling schemes. Laser cooling requires reiterative excitation of a single strong transition and subsequent spontaneous decay of the excited state. For any possi-

---

<sup>1</sup>For convenience the relevant part of the barium atomic level scheme is available as a fold-up next to the last page of this book (see Fig. F.1)

ble cycling transition in barium and in radium that could provide strong cooling forces the excited state has a very large branching probability to metastable states. Laser cooling can be achieved only by adding several lasers which bring the atoms back into the cycling transition. In this work barium atoms were efficiently collected in a magneto-optical trap (MOT) by large optical forces from the  $6s^2\ ^1S_0 \rightarrow 6s6p\ ^1P_1$  transition. Six lasers were employed for repumping. Barium has the leakiest cooling cycle of all atomic species trapped so far.

In this work permanent electric dipole moments will be introduced and possible ways to measure them will be described for radium (Chapter 2). Laser cooling and trapping was identified among the main obstacles on the way to searches for EDM's in radium (Chapter 3). The experimental tools which were developed and used throughout are described (Chapter 4). The development of an efficient slowing scheme for barium is described (Chapter 5). In particular the relevant branching ratios from excited states were determined, which take part in optical repumping schemes for efficient laser cooling and trapping. The performance of a magneto-optical trap is characterized in terms of loss rates and temperatures (Chapter 6). Finally, the consequences from the results of this work towards trapping of radium are discussed (Chapter 7).

This work is the first to describe optical cooling and trapping of the heavy alkaline-earth element barium. The developed scheme is very efficient. The results can be transferred to radium due to the similarities in its atomic level structure with the barium atom. For radium trapping the frequencies of the seven necessary lasers need to be adapted. The next steps towards efficient trapping of radium and searches for EDM's in its isotopes are thereby enabled.

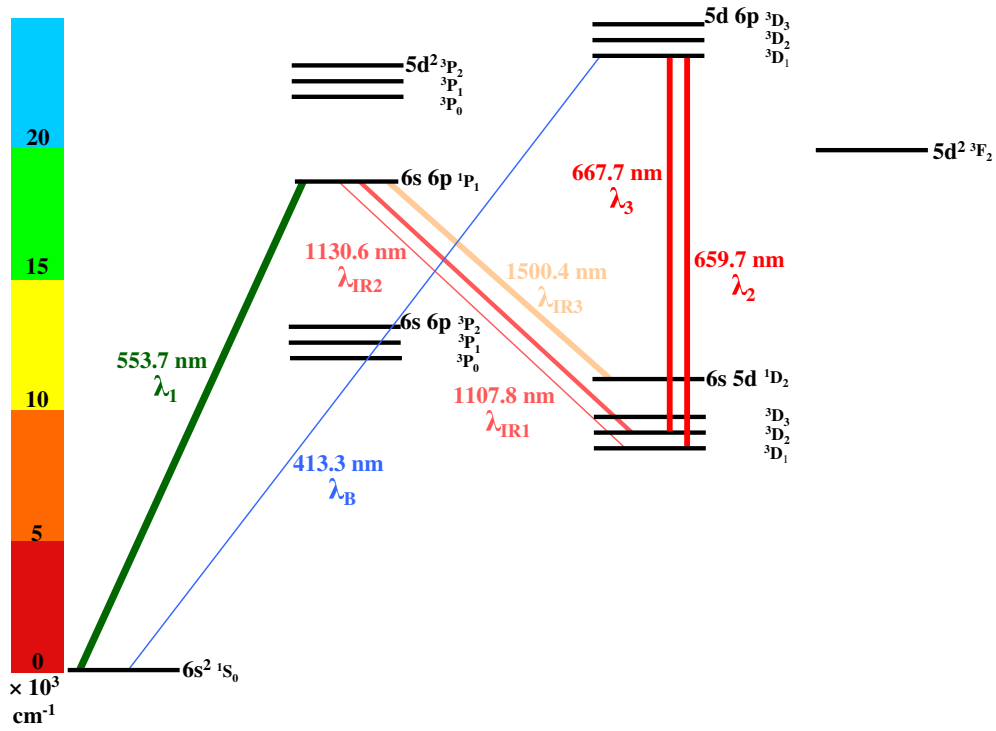


**Fig. 1.1:** Level scheme of atomic barium. The low lying states, which are relevant to the experiments in this work, are shown.

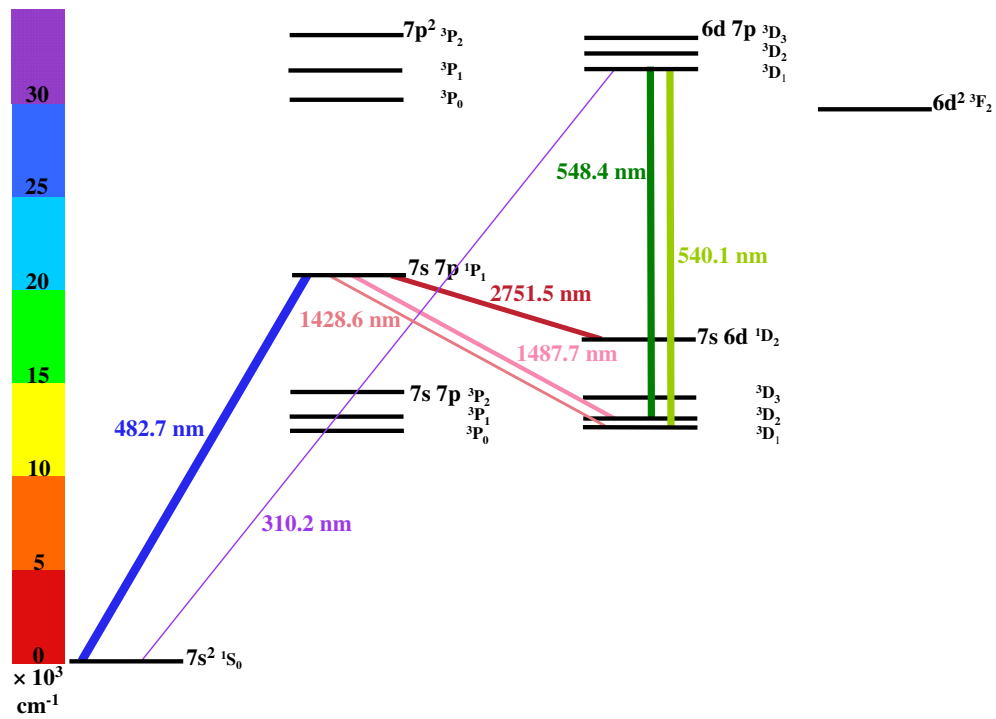


**Fig. 1.2:** The lowest lying states in atomic radium. Only those states are shown, which are relevant to the laser cooling scheme.

## Chapter 2

# Searching for Electric Dipole Moments with Trapped Atoms

The observation of any permanent electric dipole moment (EDM) of a fundamental particle at the presently possible limits of sensitivity would be a sign of physics beyond the Standard Model (SM). Consequently many different experimental searches for EDM's are currently underway. EDM's violate parity and time reversal symmetries (see Fig. 2.1). The assumption that the combination of all three discrete symmetries CPT is conserved in nature together with the observed breaking of the combined CP-symmetry yields values for EDM's within the Standard Model for all fundamental particles. They are not zero, however several orders of magnitude below the sensitivity of any presently possible experimental search.

The search for EDM's in radium isotopes is one of the major goals of the TRI $\mu$ P programme at the Kernfysisch Versneller Instituut (KVI) of the University of Groningen. The TRI $\mu$ P facility is operational and can produce short-lived radioactive isotopes [22–35]. In particular,  $^{213}\text{Ra}$  has been made in a precursor experiment [36] to determine production cross sections. In subsequent experiments also a number of neighboring isotopes to  $^{213}\text{Ra}$  have been produced at the TRI $\mu$ P facility [37]. Due to the high sensitivity of radium isotopes to EDM's it is important to survey the possible experimental methods, which could be used to find such an EDM. In particular the uncertainties of the techniques, which are currently employed in searches for nuclear EDM's in  $^{199}\text{Hg}$ , can provide guidance in the design of new experiments, e.g., in radium. Some of the main systematic uncertainties are expected to be reduced by changing to a new measurement technique which uses ultracold trapped atoms. Trapped samples can have much

longer interaction times as compared to atoms in, e.g., atomic beams. This can be exploited to decrease the statistical and systematic uncertainties of precision experiments. The approach within the TRI $\mu$ P programme has two major intermediate goals (i) selecting a system with a high intrinsic sensitivity and (ii) developing better experimental methods with reduced measurement uncertainties.

## 2.1 Permanent Electric Dipole Moments

Two charges of opposite sign and the same absolute value,  $q$ , which are separated by a distance,  $\vec{r}$ , from each other, have an electric dipole moment

$$\vec{d} = q \cdot \vec{r}. \quad (2.1)$$

Its direction points from the negative to the positive charge (see Fig. 2.1). A more general definition of an electric dipole moment is the first moment of a charge distribution,  $\rho(\vec{r})$ , i.e.,

$$\vec{d} = \int \rho(\vec{r}) \cdot \vec{r} \, d^3r, \quad (2.2)$$

where  $\vec{r}$  is the position vector relative to the center of mass of the system. The dipole moment  $\vec{d}$  of a fundamental particle has to be proportional to its spin,  $\vec{I}$ , since any contribution orthogonal to the spin direction will be averaged out to zero. Further, in a quantum mechanical system there can be only one vectorial quantity to which all other vectors describing the system such as the magnetic moment and an EDM have to be proportional. Therefore any potential EDM

$$\vec{d} \propto \vec{I}. \quad (2.3)$$

Only particles with spin can have an EDM.

Already in 1950 Purcell and Ramsey discovered that the existence of a permanent electric dipole moment for a fundamental quantum mechanical object implies that parity is violated [38]. Later it was realized that EDM's also violate T and CP [39,40]. Composed systems may have larger EDM's compared to their individual constituents due to features of the internal structure or CP violating forces in the composed system. Large enhancements have been predicted in particular for atoms, e.g., radium (Ra) [15], plutonium (Pu) [19], mercury (Hg) [21], xenon (Xe) [41], radon (Rn) [42], cesium (Cs) [43], ytterbium (Yb) [44], francium (Fr) [45], gold (Au) [45], actinium (Ac) [46] and protactinium (Pa) [46].

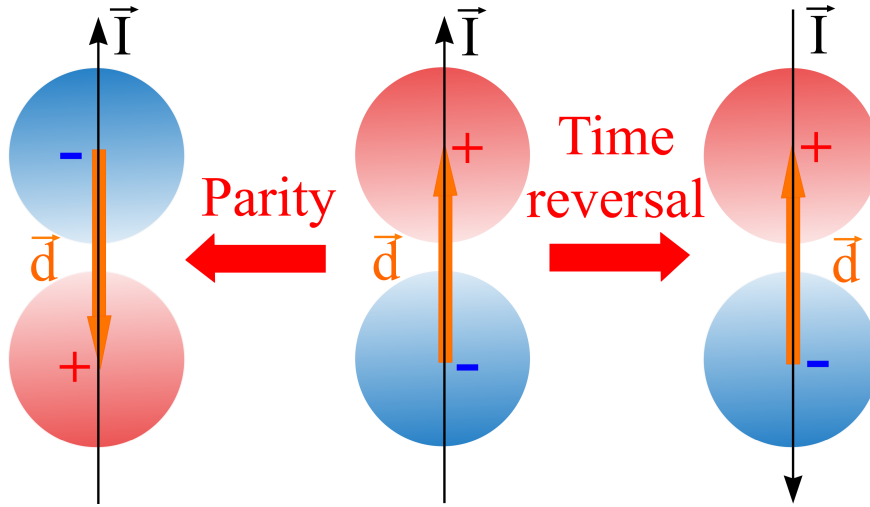


**Fig. 2.1:** Parity (P) and time reversal (T) transformations for a particle with an EDM. The parity operator exchanges the charges and hence changes the direction of the electric dipole moment, but leaves the spin  $\vec{I}$  unchanged. The time reversal operator changes the sign of the spin and leaves the charges in place. In both cases the resulting particles would have an electric dipole moment opposite in its direction with respect to the spin as compared to the original particle.

## 2.2 EDM's and the Standard Model

The values for EDM's, which can be derived within the SM, arise from known CP-violation and are very small. They are below the scale of any present experimental sensitivities. In contrast, some extensions to the SM, which try to address various not understood features in particle physics, provide for rather large EDM's. Theoretically predicted EDM values in models such as SUSY [6] or LeftRight symmetry [7] are just below the current bounds on EDM's (see Table 2.1). There is no preferred system to search for an EDM. In fact, one needs to investigate different systems to identify any underlying mechanism for an EDM (see Fig. 2.2).

### 2.2.1 Worldwide EDM Experiments

Searches for possible EDM's have been and are being performed on a wide variety of systems. These are atoms (Hg [21], Xe [41], Rn [42], Tl [47], Cs [48], Ra [49,50]), fundamental particles (electron [51], muon [52], tauon [53]), nucleons (neutron [54], proton [55]), molecules (TlF [55], YbF [56], PbO [57]), molecular ion (HfF<sup>+</sup> [58]) and condensed matter systems (Gadolinium Gallium Garnet [59],

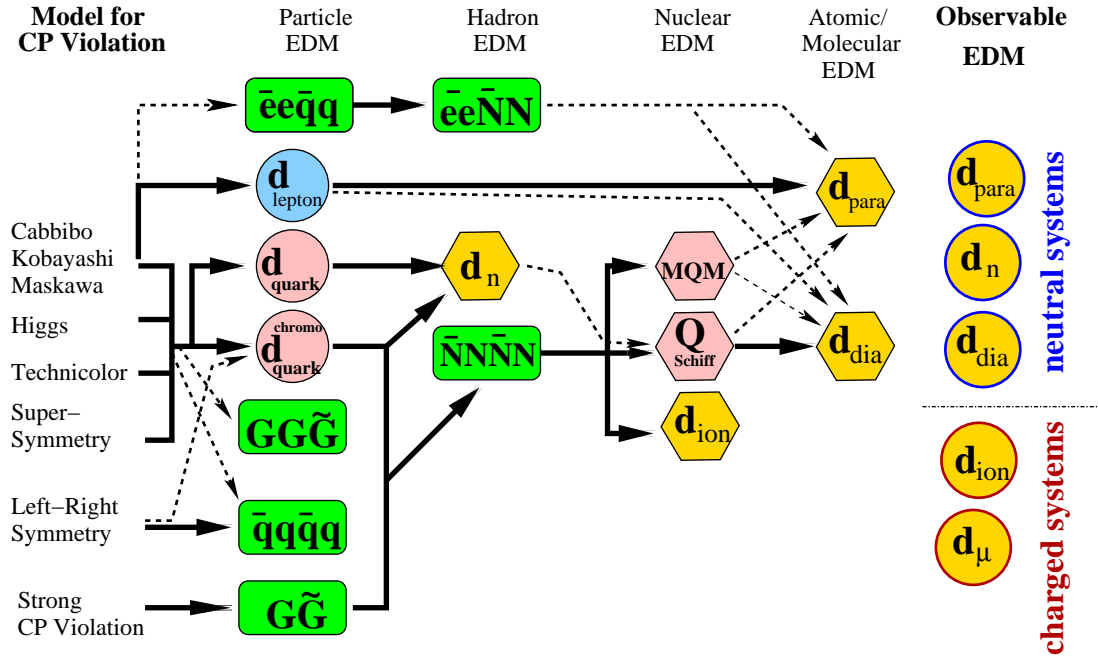


**Fig. 2.2:** A variety of theoretical speculative models exist in which an EDM could be induced in fundamental particles and composite systems through different mechanisms. A combination of measurements can provide access to the underlying sources of an observed EDM (from [64, 65]).

Gadolinium Iron Garnet [60]). To date there is no experimental evidence for a finite EDM in any system and experiments gave only upper bounds (see Table 2.1). An overview of the current activities to search for EDM's can be found in Ref. [64, 65]. An EDM in non-elementary systems can arise from EDM's of different fundamental particles and from CP odd or T odd parts in the interactions between them. The origin of an EDM in a composed system is not obvious from a single measurement of this quantity (see Fig. 2.2). The results from measurements in different systems are complementary to each other and in general a set of measurements will eventually enable the identification of the underlying sources of an EDM.

The most sensitive experiments yielding EDM limits were performed in composite systems, e.g., atoms and molecules. Theory will be needed to connect any future observed finite EDM with the underlying source of symmetry violation (see Fig. 2.2). The theories are layered in terms of the energy scales of the interactions. In some cases there are attenuations of the dipole moments, which are expressed in the values of, e.g., Schiff moments. In other cases large enhancement factors can be expected, e.g., in some atoms and polar molecules.

Particle	Experimental Method	Limits [e cm]	SM factors to go	New Physics factors to go
e [51]	Thallium beam	$< 1.6 \times 10^{-27}$	$10^{11}$	$\leq 1$
$\mu$ [52]	Tilt of precession plane in anomalous magnetic moment measurement	$< 2.8 \cdot 10^{-19}$	$10^8$	$\leq 200$
$\tau$ [53]	Electric form factor in $e^+e^- \rightarrow \tau\tau$ events	$< 4.5 \cdot 10^{-17}$	$10^7$	$\leq 1700$
n [54]	Ultra cold neutrons	$< 2.9 \cdot 10^{-26}$	$10^4$	$\leq 30$
p [55]	120kHz thallium spin resonance	$< 3.7 \cdot 10^{-23}$	$10^7$	$\leq 10^5$
$\lambda^o$ [61]	Spin precession in motional electric field	$< 3.0 \cdot 10^{-17}$	$10^{11}$	$10^9$
$\nu_{e,\mu}$ [62]	Inferred from magnetic moment limits	$< 2 \cdot 10^{-21}$	-	-
$\nu_\tau$ [63]	Z decay width	$< 5.2 \cdot 10^{-17}$	-	-
$^{199}\text{Hg}$ [21]	Spin precession in external E and B field	$< 2.1 \cdot 10^{-28}$	$\leq 10^5$	various

**Table 2.1:** Limits on the EDM's of different fundamental particles and the systems in which they have been determined. The factors between the established limits and the SM predictions as well as the predicted values from extensions to the SM are included. This table has been adapted from [64, 65].

The largest known atomic enhancement factor for a nuclear or electron EDM was predicted for radium. For polar molecules enhancement factors of up to  $10^6$  can be expected. However the experimental exploitation of that appears to be very difficult and could not be demonstrated sufficiently well yet. The most sensitive measurements for molecules in terms of statistical uncertainty have been reported for YbF molecules [56]. However, no stringent limit for an EDM has been published yet, because the ongoing analysis of systematic uncertainties which could mimic an EDM signal.

At present the best experimental limit on a nuclear EDM was determined with  $^{199}\text{Hg}$ . The upper bound of a possible EDM is  $2.1 \cdot 10^{-28}$  e cm (95% c.l.) [21]. The value for a nucleon EDM in the SM is  $10^{-33}$  e cm, which is 5 orders of magnitude below the experimental limit. Nevertheless, some SM extensions are compatible with a nucleon EDM within a factor of 30 of the present experimental limit. The  $^{199}\text{Hg}$  experiment is still in progress and the reduction of systematic uncertainties due to the measurement process is at the center of the attention.

## 2.2.2 Principle of an EDM Measurement

A possible principle for an EDM measurement was first described by E.M. Purcell and N.F. Ramsey [38] and most experiments are based on that idea. A particle with magnetic moment  $\vec{\mu} = \mu \cdot \vec{I}$  precesses in a magnetic field<sup>1</sup>,  $\vec{B}$ , if the spin  $\vec{I}$  is orthogonal to the field, i.e.,  $\vec{I} \perp \vec{B}$ . In an additional electric field,  $\vec{E}$ , parallel or antiparallel to  $\vec{B}$ , i.e.,  $\vec{E} \uparrow\uparrow \vec{B}$  or  $\vec{E} \uparrow\downarrow \vec{B}$ , an extra torque acts on a particle with an EDM  $\vec{d}$  [21]. The interaction Hamiltonian,  $H_{\text{em}}$ , in the electromagnetic field is

$$H_{\text{em}} = \hbar \omega = -\vec{\mu} \cdot \vec{B} - \vec{d} \cdot \vec{E} = -(\mu \vec{B} + d \vec{E}) \cdot \frac{\vec{I}}{|\vec{I}|}, \quad (2.4)$$

where  $\omega$  is the precession frequency of the spin  $\vec{I}$ . An EDM  $d$  of a spin  $I = 1/2$  system, such as  $^{213}\text{Ra}$  in the atomic ground state, can be determined by measuring the difference of the two precession frequencies,  $\omega_1$  and  $\omega_2$ , for the two different relative orientations of the electric  $\vec{E}$  and magnetic  $\vec{B}$  fields (see Fig. 2.3).

$$\omega_1 = \frac{(2\mu |\vec{B}| + 2d |\vec{E}|)}{\hbar}, \quad (2.5)$$

$$\omega_2 = \frac{(2\mu |\vec{B}| - 2d |\vec{E}|)}{\hbar}, \quad (2.6)$$

---

<sup>1</sup>Because in this work only vacuum environment is of importance, the magnetic induction  $\vec{B}$  is used synonymously for the magnetic field.

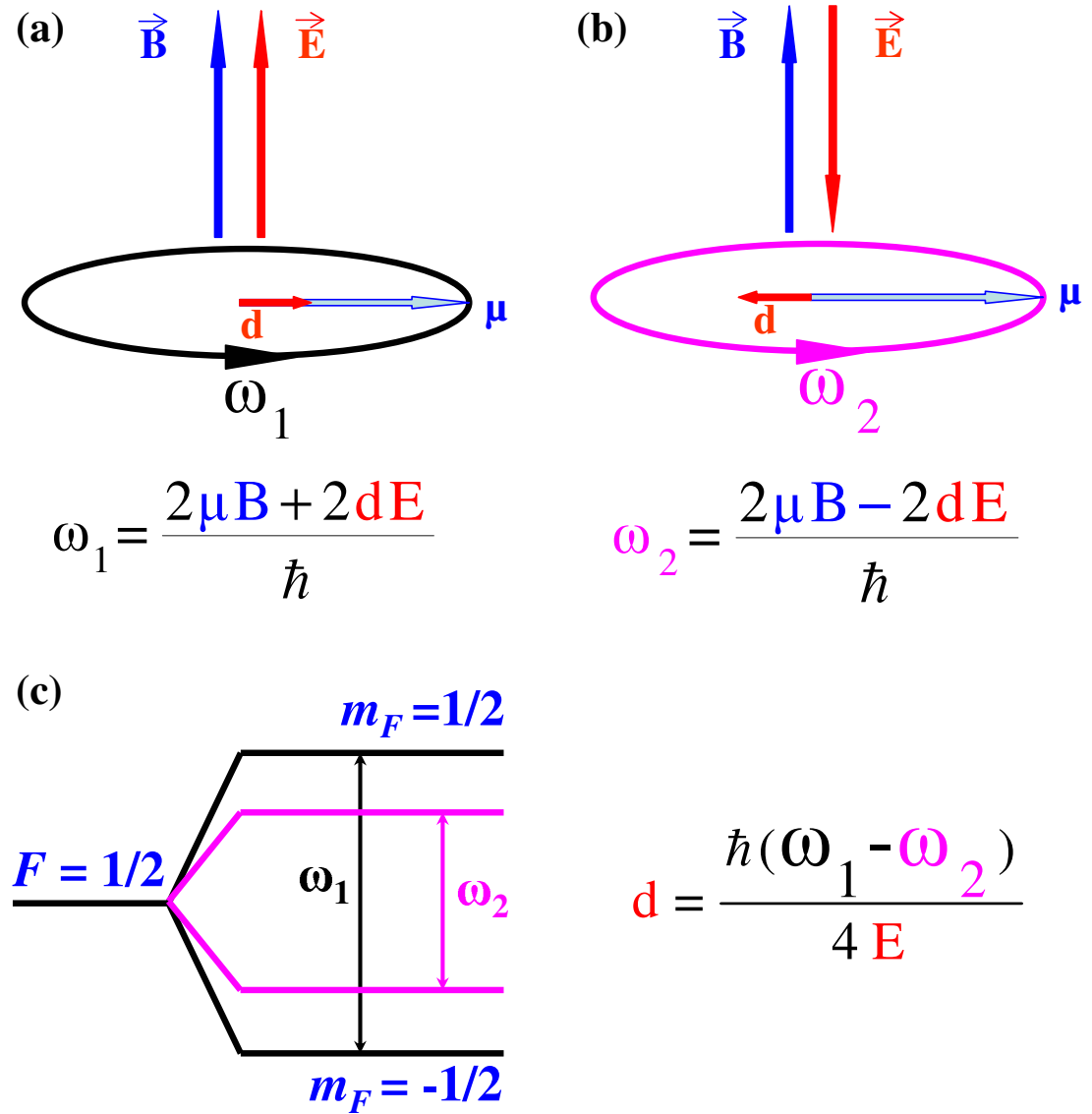


**Fig. 2.3:** Principle of an EDM measurement, where a spin 1/2 particle is alternatively subjected to parallel and antiparallel external magnetic and electric fields orthogonal to its spin, respectively magnetic field. EDM manifests itself as a difference in the spin precession frequencies  $\omega_1$  and  $\omega_2$  for both cases.

$$\Delta\omega = (\omega_1 - \omega_2) = \frac{4d |\vec{E}|}{\hbar}. \quad (2.7)$$

The difference frequency,  $\Delta\omega$ , is proportional to the EDM  $d$  and the absolute strength of external electric field  $|\vec{E}|$

$$d = \frac{\hbar \Delta\omega}{4 |\vec{E}|}. \quad (2.8)$$

The signature of the permanent electric dipole moment is a linear dependence of the energy splitting  $\omega_1$  and  $\omega_2$  of the levels corresponding to the two electric field  $\vec{E}$  orientations and hence of  $\Delta\omega$  on the electric field strength  $|\vec{E}|$ . It can be distinguished from induced dipole moments, which show a quadratic dependence on the electric field [66]. The challenge of a precise experiment is an accurate measurement of the precession frequencies  $\omega_1$  and  $\omega_2$ .

## 2.3 Radium Isotopes

Atomic radium has intrigued theorists in recent years in connection with its sensitivity to symmetry violations. It appears to be the most sensitive system in a survey of atomic parity and time reversal symmetry violations in heavy elements [67]. Different symmetry violating effects have been calculated with high precision. The discussion here is restricted to EDM's, although radium isotopes could also be candidates to measure parity non-conservation in atoms, i.e., the weak charge or anapole moments [18]. A number of theoretical calculations have been performed by several groups to calculate the enhancement of a nuclear EDM and an atomic EDM induced by the nucleus or the electrons in different radium isotopes [15–19, 68–70].

### 2.3.1 Schiff Moments

The EDM of a nucleus might have two contributions: one is due to EDM's of individual nucleons and the other arises from the charge distribution in the nucleus. In a classical picture the Schiff moment,  $\vec{S}$ , is defined as a radially weighted dipole moment due to nuclear charge distribution [71]. For nuclei with spin  $I = 1/2$  the Schiff moment is [16]

$$\vec{S} = \frac{1}{10} \int \rho_{\text{ch}}(\vec{r}) \left( r^2 - \frac{5}{3} r_{\text{ch}}^2 \right) \vec{r} \cdot d^3r, \quad (2.9)$$

where  $\rho_{\text{ch}}(\vec{r})$  is the nuclear charge density,  $\overline{r_{\text{ch}}^2}$  is the mean square charge radius. An atomic EDM arises from the interaction of electrons with the Schiff moment  $\vec{S}$ . The interaction with electron can weaken or enhance a nuclear EDM depending on details of the atomic level structure. Sanders has separated the Schiff moment in three different parts [72]

1. EDM's originating from the difference of the r.m.s. distribution of nucleon EDM's and nuclear charge,
2. a nucleon EDM due to the charge distribution which vanishes for a spherical distribution,
3. contributions arising from the relative separation between the center of the neutron and proton distributions inside a nucleus.

For heavy atoms the spin dependent electron-nucleon interactions as well as the neutron-neutron and neutron-proton interactions are enhanced due to the large number of nucleons. This effect deforms the nucleus and the second part of the Schiff moment becomes the largest contribution in atomic radium. The Hamiltonian,  $H_{\text{edm}}^{\text{Schiff}}$ , due to the Schiff moment  $S$  is [18]

$$H_{\text{edm}}^{\text{Schiff}} = 4\pi S \frac{\vec{I}}{|\vec{I}|} \cdot \nabla \rho(\mathbf{r}), \quad (2.10)$$

where  $4\pi \nabla \rho(\mathbf{r})$  is the electron part of the operator  $H_{\text{edm}}^{\text{Schiff}}$ .

### 2.3.2 Magnetic Quadrupole Moments

The nuclear interaction with the nuclear magnetic quadrupole moment (MQM) also induces an atomic EDM in the  $7s6d \ ^3D_2$  state of radium. For isotopes with nuclear spin  $I \leq 1$  the MQM is zero. The MQM can be as large as the Schiff moment [18].

### 2.3.3 Degenerate States of Opposite Parity

States of opposite parity are mixed in an external electric field. The electric field due to a fundamental EDM can polarize the composed system and the resultant EDM will be modified. The polarizability of a systems is inversely proportional to the energy difference between the states of opposite parity. The EDM,  $d_{3D_2}$ ,

of the  $7s6d\ ^3D_2$  state is [18]

$$d_{3D_2} = \frac{\langle 7s6d\ ^3D_2 | -e r | 7s7p\ ^3P_1 \rangle \langle 7s7p\ ^3P_1 | H_{\text{edm}}^{\text{Schiff}} | 7s6d\ ^3D_2 \rangle}{E(7s6d\ ^3D_2) - E(7s7p\ ^3P_1)}, \quad (2.11)$$

where  $-e r$  is the electric dipole operator and  $H_{\text{edm}}^{\text{Schiff}}$  is the EDM operator due to the Schiff moment (see Eqn. 2.10). This yields an EDM in radium which is about  $10^5$  times larger than the one for  $^{199}\text{Hg}$  [18].

The interaction of an electron EDM,  $d_e$ , with the electric field produced by the nucleus induces also an atomic EDM. The relativistic nature of the nucleons produces an instantaneous electric field effective to the electrons although the classical shielding theorem is still true. In radium the two close lying opposite parity states with identical angular momentum  $7s6d\ ^3D_1$  and  $7s7p\ ^3P_1$  mix stronger due to this interaction compared to the  $7s6d\ ^3D_2$  and the  $7s7p\ ^3P_2$  states. In the  $7s6d\ ^3D_1$  state the EDM is [18]

$$d_{3D_1} = \frac{\langle 7s6d\ ^3D_1 | -e r | 7s7p\ ^3P_1 \rangle \langle 7s7p\ ^3P_1 | \tilde{H}_{\text{edm}} | 7s6d\ ^3D_1 \rangle}{E(7s6d\ ^3D_1) - E(7s7p\ ^3P_1)}, \quad (2.12)$$

with the Hamiltonian,  $\tilde{H}_{\text{edm}}$ , due to the interaction of the electron EDM,  $d_e$ , with the atomic electric field  $\vec{E}$ . The Hamiltonian has a form [18]

$$\tilde{H}_{\text{edm}} = -d_e \beta (\vec{\Sigma} \cdot \vec{E}), \quad (2.13)$$

where  $\beta$  is the Dirac matrix and  $\vec{\Sigma}$  is the relativistic spin operator. Detailed calculations show that the EDM in the  $7s6d\ ^3D_1$  state of radium is enhanced by a factor 5370 [18] compared to the electron intrinsic EDM  $d_e$ . Similar enhancement factors for francium and gold isotopes are 910 and 260, respectively [45].

Furthermore, in some isotopes near the valley of stability, e.g.,  $^{223}\text{Ra}$  and  $^{225}\text{Ra}$ , the interference between known octupole and quadrupole deformations leads to states of opposite parity in the nucleus. This causes enhancement factors, which have been estimated to be between 50 and 500 [16, 17, 19].

## 2.4 Uncertainties of EDM Measurements

The present limits on EDM's are not only due to experimental statistical uncertainties of the measurements but also to systematic uncertainties due to limited control over experimental parameters. In an experiment of the Ramsey and Purcell type any tiny unnoticed fluctuation of the electric field  $\vec{E}$  or the magnetic

field  $\vec{B}$  adds to the uncertainties of the difference frequency  $\Delta\omega$  measurement (see Eqn. 2.7). The  $^{199}\text{Hg}$  EDM experiment at the University of Washington, Seattle, USA has reached the best sensitivity so far on a  $\Delta\omega$  measurement, which is less than 1 nHz [73]. The reported EDM limit of  $^{199}\text{Hg}$  is  $2.1(0.49)(0.40)\cdot 10^{-28}$  e cm, where the first uncertainty is the statistical error and the second is due to systematic uncertainties. The statistical and systematic uncertainties are of the same size. Any improvement of this result requires a better understanding of the contributions to the systematic uncertainties. The main sources of uncertainties are [74]

- Statistical uncertainty

The statistical uncertainty,  $\delta\omega$ , of the measurement of  $\Delta\omega$  is the ratio of the mean deviation of the measured precession frequency to the signal to noise ratio, (S/N). The mean deviation of the precession frequency depends on the inverse of the spin coherence time,  $\tau$ , i.e.,  $\partial\omega = \frac{2\pi}{\tau}$ . The observable quantity is measured from an ensemble where a particle flux, F, is observed over a period, T, which leads to a particle number uncertainty of  $\sqrt{FT}$  and (S/N) =  $\sqrt{FT}$ . Hence the statistical uncertainty of a precession frequency measurement is

$$\delta\omega = \frac{\partial\omega}{(S/N)} = \frac{2\pi}{\tau \cdot \sqrt{FT}}. \quad (2.14)$$

Thus, the statistical uncertainty for an EDM is

$$\Delta d = \frac{h\delta\omega}{2\pi 4E} = \frac{h}{4E\tau\sqrt{FT}}. \quad (2.15)$$

EDM measurements use an ensemble of atoms and extend over longer time periods for a better statistics. Any inhomogeneity of the electric field over the sample region and over the period of the measurement introduces a finite distribution of spin precession frequencies.

- Motional magnetic fields

In measurements in atomic beams or in gas cells the particles are distributed over a range of velocities. Due to the motion of atoms in the external electric field  $\vec{E}$  they experience a different magnetic field  $\vec{B}'$  than the external magnetic field  $\vec{B}$ . For an atom of velocity  $\vec{v}$  the total magnetic field is [75]

$$\vec{B}' = \vec{B} + \frac{\vec{E} \times \vec{v}}{c}, \quad (2.16)$$

where  $c$  is the speed of light. Neglecting the term quadratic in  $c$  gives the strength of the magnetic field [75]

$$|\vec{B}'| = |\vec{B}| + \frac{\vec{E} \times \vec{v}}{c} \cdot \frac{\vec{B}}{|\vec{B}|}. \quad (2.17)$$

The motional magnetic field vanishes for parallel or antiparallel electric and magnetic fields, i.e.,  $\vec{E} \uparrow\uparrow \vec{B}$  or  $\vec{E} \uparrow\downarrow \vec{B}$ . However, the contribution is odd under reversal of both  $\vec{E}$  and  $\vec{B}$  fields. Any small angle  $\vartheta$  between the  $\vec{E}$  and the  $\vec{B}$  fields leads to a nonzero contribution to the frequency difference  $\Delta\omega$ , which scales with  $\sin \vartheta$  [74]. In order to suppress this systematic effect two counter-propagating atomic beams in the very same  $\vec{E}$  and  $\vec{B}$  fields can be used [75]. The problem is then shifted to the difference in the velocity distributions of the atoms in the two beams.

- Ripples in the magnetic field

A fluctuation in the driving current of the coils produces ripples in the magnetic field  $\vec{B}$ . The typical magnetic field strength in an EDM experiment is of order 50 mG. A current fluctuation at the ppm/s level would dominate all other systematic uncertainties. Also magnetic shielding of the experimental region from the surrounding magnetic fields may not be ideal. All this adds uncertainties to the measurement of the Larmor precession frequencies  $\omega_1$  and  $\omega_2$  and hence it influences into the precision of EDM searches. A continuous magnetic field monitoring is therefore indispensable. Typically atoms which are known to have negligible EDM's but magnetic moments are used as co-magnetometers in the same volume.

- Leakage current

The leakage current from the electric field plates can produce an additional magnetic field. This current contributes to the systematic uncertainties of the magnetic field. For the EDM measurement of  $^{199}\text{Hg}$  the reported leakage current is 0.6 pA. The systematic error contribution was estimated to  $0.14 \cdot 10^{-28}$  e cm, which is about 1/3 of the total systematic error [21].

- Quadratic Stark shift

An applied dc electric field  $\vec{E}$  introduces a shift in the atomic energy levels [66], which is known as the Stark shift. The corresponding frequency shift

$$\Delta\nu_{\text{Stark}} = -\frac{1}{2} \frac{|\vec{E}|^2}{h} \alpha, \quad (2.18)$$

depends on the polarizability,  $\alpha$ , of the atom and the square of the magnitude of the electric field strength. The polarizability of an atom  $\alpha$  is unique for a particular energy state. For the ground state of  $^{199}\text{Hg}$  the frequency shift due to an electric field of  $|\vec{E}| = 10 \text{ kV/cm}$  is  $\Delta\nu_{\text{stark}} < 2 \text{ nHz}$  [21].

- ac stark shift

The levels of atoms experience an ac Stark shift,  $\Delta\nu_{\text{ac}}$ , in an electromagnetic field. The shift is linearly proportional to the intensity of the laser light and the precise system dependent expressions are available elsewhere for many systems of interest, e.g., mercury [74].

The individual contributions to the overall uncertainty are all of the same order of magnitude. A further reduction of uncertainties requires improvements of the EDM measurement technique.

## 2.5 EDM Measurement with Trapped Sample - Trapping of Barium as a Precursor

Improvements on the uncertainties may be possible with trapped samples of atoms. In an experiment where atoms under investigation are supplied in a beam of flux  $F$  the number of incoming particles,  $N$ , over a duration  $T$  is

$$N = \int_0^T F dt. \quad (2.19)$$

In a trapping experiment the observation time is given by the trap lifetime of the sample, i.e.,  $T = \tau_{\text{trap}}$ . In an atomic beam the characteristic time is the time of flight through the experimental region,  $T = \tau_{\text{TOF}}$ , and in a gas cell the time scale can be long compared to  $\tau_{\text{trap}}$  and  $\tau_{\text{TOF}}$ . In a trap or in a beam the observation time is larger than the spin coherence time  $\tau$ , but in a gas cell typically the observation time is smaller than  $\tau$ .

The average velocity of trapped atoms is about three orders of magnitude lower than the velocity of atoms in an atomic beam. The strength of the motional magnetic field will thus be negligible for trapped samples. In a gas cell the average velocity of atoms is zero, but asymmetric collisions with the cell walls introduce a motional magnetic field [21].

The volume of a trapped sample is about three orders of magnitude smaller than the volume of the experimental region in a gas cell or in an atomic beam.

The strengths of an external electric field  $\vec{E}$  and a magnetic field  $\vec{B}$  can be expected to be more homogenous over a small volume. The orientation of the spin  $\vec{I}$  of individual particles relative to the electric field  $\vec{E}$  would be isotropic in a trapped sample which reduces the mean deviation  $\partial\omega$  of the spin coherence time  $\tau$ .

Leakage currents can be expected to be suppressed in the vicinity of a trapped sample in an ultra high vacuum environment. Electric fields up to  $|\vec{E}| \simeq 100$  kV/cm can be applied, which is beyond the technical possibilities of most other experimental principles. The signal of an EDM would be proportional to  $|\vec{E}|$  and therefore bigger.

In particular for rare isotopes an efficient collection trap is advantageous for exploiting a large fraction of the atomic flux. An advanced setup with a trapped sample of a radium isotope will be indispensable for a competitive EDM search. Radium atom trapping has been reported [76] recently. However, in this experiment a trapping efficiency of only  $7 \cdot 10^{-7}$  for the rare isotopes could be achieved so far, due to peculiarities in the atomic level scheme of radium. The efficiency needs to be improved significantly for a future precision experiment.

The development of the necessary techniques for cooling and trapping can better be performed with an atomic species of similar atomic level scheme which is sufficiently abundant and not radioactive. The similarities in the level schemes of radium and barium (see Figs. 1.2 and 1.1) provide the opportunity to use barium as a precursor for developing an EDM experiment. In particular the methods for efficient laser cooling and trapping can be worked out as the first step in an EDM search project. A new EDM measurement scheme with trapped atoms can then be developed with the stable barium isotopes as well. Although barium isotopes exhibit no strong enhancement factors for possible EDM's, a trapped barium sample will be a powerful tool to study systematic uncertainties and limitations of such new experimental searches for EDM's.

# Chapter 3

## Heavy Alkaline-earth Elements: Barium and Radium

Barium and radium are heavy alkaline-earth elements, i.e., they fall into the the 2<sup>nd</sup> group of the periodic table of elements. Barium has 7 stable isotopes:  $^{130}\text{Ba}$  (0.1%),  $^{132}\text{Ba}$  (0.1%),  $^{134}\text{Ba}$  (2.4%),  $^{135}\text{Ba}$  (6.6%),  $^{136}\text{Ba}$  (7.8%),  $^{137}\text{Ba}$  (11.3%) and  $^{138}\text{Ba}$  (71.7%). None of the the radium isotopes is stable. The atomic energy levels of both chemical homologous elements have a similar structure (see Figs. 1.1 and 1.2). The electronic configuration except for the principal quantum number of the outermost shell is identical for most relevant purposes.

This chapter gives an overview of the spectroscopic information available for barium and radium. A compilation of data is made, which are relevant for the development of laser cooling and trapping of these two heavy alkaline-earth elements. The scientific issues related to laser cooling and trapping of a many level leaky system are also addressed.

### 3.1 Radium

Radium was discovered by M. Curie in 1898. Important physical properties of the element are listed in Table 3.1. The activity of 1 g  $^{226}\text{Ra}$  was defined as the unit of radioactivity, i.e., 1 Ci. Four decades later in 1933 optical spectroscopy was performed for the first time by E. Rasmussen on the atom [77] and on the singly charged ion [78]. A total of 56 transitions were identified in the radium atom with a grating spectrometer [77]. The lines were recorded on a photographic film and the precision was estimated to  $10^{-3} \text{ cm}^{-1}$ , a relative accuracy of about  $10^{-6}$ , and the level structure was extracted. These measurements confirmed

	Barium (Ba)	Radium (Ra)
atomic number (Z)	56	88
atomic mass (m)	137.334 gm/mol	226.03 gm/mol
melting point	1000 K	1196 K
most abundant isotope	$^{138}\text{Ba}$ (71.7%) stable	$^{226}\text{Ra}$ (> 90%) $\tau_{1/2} = 1600$ y)
electron config.	[Xe] $6s^2$	[Rn] $7s^2$
ground state	$6s^2 \ ^1S_0$	$7s^2 \ ^1S_0$
nuclear spin (I)	even - 0 odd - $\frac{3}{2}$	even - 0 odd - many

**Table 3.1:** Atomic properties of the heavy alkaline-earth elements barium and radium.

the identification of radium as an alkaline-earth element. The term energies in the triplet system were corrected in 1934 by H. N. Russel [79]. Some levels were shifted by more than  $600 \text{ cm}^{-1}$  with respect to the original classification by Rasmussen. This reanalysis yielded also a value for the ionization potential of 5.252 eV [79]. Later, F. S. Tomkins and B. Ercoli in 1967 [80] and J. A. Armstrong, J. J. Wynnet and F. S. Tomkins in 1980 [81] could measure the Rydberg series by absorption spectroscopy in a radium cell.

Laser spectroscopy of radium isotopes started in 1983. At the ISOLDE facility of CERN in Geneva, Switzerland, radioactive isotopes with a half-life time between  $\tau_{1/2} = 23$  ms and 1600 y were produced. Collinear laser spectroscopy of the strong  $7s^2 \ ^1S_0 \rightarrow 7s7p \ ^1P_1$  transition was used to measure the hyperfine structures and isotope shifts for 18 radium isotopes [82, 83]. Later the isotope shift measurements were continued for the  $7s^2 \ ^1S_0 \rightarrow 7s7p \ ^3P_1$  and the  $7s7p \ ^3P_2 \rightarrow 7s7d \ ^3D_3$  transitions [84]. The nuclear magnetic moments of the radium isotopes  $^{213}\text{Ra}$  and  $^{225}\text{Ra}$  were determined experimentally at the same facility to  $0.7338(15)\mu_N$  and  $0.6133(18)\mu_N$ , where  $\mu_N$  is the nuclear magneton [85]. There is good agreement of the latter value with a theoretical calculation, which yields  $0.607(12)\mu_N$  [86]. Recently the  $7s6d \ ^3D_1 \rightarrow 7s7p \ ^1P_1$  transition was measured in connection with laser cooling of radium on the weak intercombination  $7s^2 \ ^1S_0 \rightarrow 7s7p \ ^3P_1$  transition [76, 87]. The frequency was found to be within 1 GHz from the value given in the reanalysis of the original grating spectrometer data [79].

The unique atomic and nuclear properties of radium isotopes make them

Radium Excitation energies [ $\text{cm}^{-1}$ ]				
State	Ref. [20]	Ref. [90] <sup>a</sup>	Ref. [90] <sup>b</sup>	Ref. [91]
7s7p $^1\text{P}_1$	20716	21156	21148	20450
7s7p $^3\text{P}_1$	13999	14072	14096	14027
7s7p $^3\text{P}_2$	16689	16855	16855	16711
7s6d $^1\text{D}_2$	17081	17806	17737	17333
7s6d $^3\text{D}_2$	13994	13974	13907	13980
7s6d $^3\text{D}_1$	13716	13672	13609	13727

Lifetimes of the excited states in radium				
State	Ref. [18]	Ref. [91]	Ref. [93]	Ref. [87]
7s7p $^1\text{P}_1$	5.5 ns	5.53 ns	5.56 ns	
7s7p $^3\text{P}_1$	505 ns	362 ns	421 ns	422(20) ns
7s6d $^1\text{D}_2$	38 ms	0.129 ms	1.37 ms	
7s6d $^3\text{D}_1$	617 $\mu\text{s}$	654 $\mu\text{s}$	719 $\mu\text{s}$	
7s6d $^3\text{D}_2$	15 s	3.3 s	3.95 s	

**Table 3.2:** Excitation energies and lifetimes of some states in radium. References [20, 87] provide the experimental values. Ref. [90]<sup>a</sup> refers to the Dirac-Coulomb (DC) and Ref. [90]<sup>b</sup> corresponds to the Dirac-Coulomb-Breit (DCB) excitation energies calculated with relativistic coupled cluster (RCC) method. Ref. [91] uses a configuration interaction method and many-body perturbation theory.

promising candidates for several scientific experiments. This provides a strong motivation to perform high precision calculations of the necessary atomic wavefunctions. The relativistic nature of the system provides a challenge for calculating the wavefunctions. High accuracy calculations of the hyperfine structures, transition rates, excited state lifetimes and their polarizabilities depend strongly on the knowledge of the wavefunctions for these heavy multi electron systems. Whereas the hyperfine structure is particularly sensitive to the part of the wavefunction near the nucleus, transition probabilities depend more on the far off the nucleus part of the wavefunctions. Not only the final analysis of the experiments, but also an evaluation of the sensitivity to symmetry breaking effects are based on such calculations. In reverse, precision measurements of these quantities give reliable input for atomic structure calculations.

The energy levels, the decay rates and the lifetimes of several states have been calculated by several groups [88–95]. They have used different theoretical

Upper level	Lower level	Wavelength (nm)	Ref. [93] $[A_{ik}]$ ( $s^{-1}$ )	Ref. [91] $[A_{ik}]$ ( $s^{-1}$ )
7s7p $^3P_1$	7s $^2$ $^1S_0$	714.3	$2.4 \cdot 10^6$	$2.8 \cdot 10^6$
	7s6d $^3D_2$		$1.8 \cdot 10^{-3}$	$1.6 \cdot 10^{-3}$
	7s6d $^3D_1$		$8.8 \cdot 10^1$	$9.8 \cdot 10^1$
7s7p $^1P_1$	7s $^2$ $^1S_0$	482.7	$1.8 \cdot 10^8$	$1.8 \cdot 10^8$
	7s6d $^1D_2$	2751.5	$3.2 \cdot 10^5$	$3.2 \cdot 10^5$
	7s6d $^3D_2$	1487.7	$3.2 \cdot 10^4$	$4.2 \cdot 10^4$
	7s6d $^3D_1$	1428.6	$1 \cdot 10^5$	$0.3 \cdot 10^4$
7s6d $^3D_1$	7s7p $^3P_1$		$7 \cdot 10^3$	$7.7 \cdot 10^3$
	7s7p $^3P_2$		$5.9 \cdot 10^1$	$7.9 \cdot 10^0$
6d7p $^3D_1$	7s6d $^3D_1$	540.1		
	7s6d $^3D_2$	548.4		
	7s6d $^1S_0$	310.2		

**Table 3.3:** Wavelengths and calculated decay rates of optical transitions relevant for laser cooling and trapping of radium. The theoretical values were obtained in two independent calculations [91, 93].

approaches such as Dirac-Coulomb and Dirac-Coulomb-Breit interactions in their high precision calculations [90]. The calculated term energies and lifetimes show a large discrepancy for some of the states (see Table 3.2). These calculations require an experimental verification and clarification of the existing discrepancies. A compilation of the decay rates and the lifetimes from the literature is given in Table 3.3.

## 3.2 Barium

Barium was discovered by H. Davy in 1808. Its main physical properties are listed in Table 3.1. Since then it has been studied extensively. There is a large body of experimental data available on many different transitions in barium atoms [96–105]. Here an overview of available data on energy levels, decay rates, lifetimes, hyperfine structure splitting and isotope shifts is given. The large amount of experimental data makes barium an excellent system to check the quality of theoretical understanding of heavy alkaline-earth elements.

Most of the decay rates were measured by Fourier transform spectroscopy using a hollow cathode discharge lamp [97–100] and laser spectroscopy using atomic

beams [101, 102]. The hyperfine structure of metastable D-states was observed with magnetic resonance technique in an atomic beam, where metastable atoms were produced by electron bombardment [106–108]. The magnetic dipole and the electric quadrupole coupling constants of the metastable states are reported in Ref. [106, 107] and the measured Lande g-factors of the respective states are given in Ref. [108]. For the chain of radioactive barium isotopes  $^{122}\text{Ba}$  to  $^{146}\text{Ba}$  the nuclear spins, the nuclear magnetic moments, the mean square charge radii, the hyperfine constants and the isotope shifts of the  $6s^2\ ^1\text{S}_0 \rightarrow 6s6p\ ^1\text{P}_1$  transition were measured at the ISOLDE facility of CERN [109]. Hyperfine structure measurements and isotope shift measurements of the  $6s^2\ ^1\text{S}_0 \rightarrow 6s6p\ ^1\text{P}_1$  transition were particularly performed for stable barium isotopes [110]. The isotope shifts of the relevant infrared transitions<sup>1</sup> are available from the work of Ref. [111]. At the TRIUMF facility of KVI the isotope shifts of the  $6s5d\ ^3\text{D}_1 \rightarrow 6s6p\ ^1\text{P}_1$  and the  $6s5d\ ^3\text{D}_2 \rightarrow 6s6p\ ^1\text{P}_1$  transitions were measured recently [112, 113]. The isotope shift of the odd isotopes is larger than predicted. This may show the importance of the contribution from core polarization to the isotope shifts [113].

Decay rates for a number of crucial transitions in barium have been calculated [88, 114–116]. The calculations present similar difficulties as for radium concerning relativistic effects [117]. Such calculations for barium can be compared with the large amount of experimental high precision data to verify the quality of the theoretical approaches. Further estimate of the uncertainties in the calculations for radium become possible [91, 95]. The lifetimes of the very long lived metastable  $6s5d\ ^1\text{D}_2$  and the  $6s5d\ ^3\text{D}_2$  states in barium have been calculated to 0.25 s and 60 s respectively [118]. The current status of knowledge about the transition wavelengths and the decay rates of states for barium below a term energy of  $25000\ \text{cm}^{-1}$  are compiled in Tables 3.4 and 3.5.

### 3.3 Laser Cooled Atoms

Cooling of ions in ion traps has been achieved already in the 1970s by H. Dehmelt, P. Toschek and their co-workers [120, 121]. A single laser with its frequency red detuned from a resonance is in principle sufficient, because the ions are trapped by forces acting on their electric charge. Imperfections in the mechanical setup

---

<sup>1</sup>In this context the transitions  $6s^2\ ^1\text{S}_0 \rightarrow 6s6p\ ^3\text{P}_1$ ,  $6s5d\ ^1\text{D}_2 \rightarrow 6p5d\ ^3\text{D}_1$ ,  $6s5d\ ^1\text{D}_2 \rightarrow 6p5d\ ^3\text{D}_3$ ,  $6s5d\ ^3\text{D}_3 \rightarrow 6p5d\ ^1\text{D}_2$ ,  $6s5d\ ^3\text{D}_2 \rightarrow 6p5d\ ^1\text{D}_2$ ,  $6s5d\ ^3\text{D}_1 \rightarrow 6p5d\ ^1\text{D}_2$ ,  $6s5d\ ^3\text{D}_3 \rightarrow 6p5d\ ^3\text{F}_2$ ,  $6s5d\ ^3\text{D}_2 \rightarrow 6p5d\ ^3\text{F}_2$ ,  $6s5d\ ^3\text{D}_1 \rightarrow 6p5d\ ^3\text{F}_2$ ,  $6s5d\ ^3\text{D}_3 \rightarrow 6p5d\ ^3\text{F}_3$ ,  $6s5d\ ^3\text{D}_2 \rightarrow 6p5d\ ^3\text{F}_3$ ,  $6s5d\ ^3\text{D}_3 \rightarrow 6p5d\ ^3\text{F}_4$ ,  $6s5d\ ^3\text{D}_1 \rightarrow 6p5d\ ^3\text{D}_1$  need to be considered.

Upper level and lifetime	Lower level	Wavelength (nm)	Decay rate [ $A_{ik}$ ] ( $s^{-1}$ )	Ref.
6s6p $^3P_1$  1345(14) ns [87]	6s $^2$ $^1S_0$	791.32	$2.99(38)\cdot 10^5$	[104]
	6s5d $^3D_2$	2923.0	$3.18(32)\cdot 10^5$	
	6s5d $^3D_1$	2775.7	$1.23(12)\cdot 10^5$	
	6s5d $^1D_2$	8056.5	$0.006\cdot 10^5$ ‡	‡ [115]
6s6p $^3P_2$  1.4 $\mu s$ [95]	6s5d $^3D_3$	2552.2	$4.8\cdot 10^5$	[115]
	6s5d $^3D_2$	2326.0	$1.0\cdot 10^5$	
	6s5d $^3D_1$	2231.8	$0.09\cdot 10^5$	
	6s5d $^1D_2$	4718.4	$0.01\cdot 10^5$	
6s6p $^3P_0$ 2.6 $\mu s$ [95]	6s5d $^3D_1$	3094	$2.6\cdot 10^5$	[115]
<b>6s6p <math>^1P_1</math></b>  8.0(5) ns [112]	<b>6s<math>^2</math> <math>^1S_0</math></b>	<b>553.74</b>	<b><math>1.19(1)\cdot 10^8</math></b>	[103]
	<b>6s5d <math>^1D_2</math></b>	<b>1500.39</b>	<b><math>0.0025(2)\cdot 10^8</math></b>	
	<b>6s5d <math>^3D_2</math></b>	<b>1130.36</b>	<b><math>0.0011(2)\cdot 10^8</math></b>	
	<b>6s5d <math>^3D_1</math></b>	<b>1107.87</b>	<b><math>0.000031(5)\cdot 10^8</math></b>	
5d $^2$ $^3F_2$  190 $\mu s$ [95]	6s6p $^3P_1$	1205.2	<b><math>0.36\cdot 10^5</math></b>	[115]
	6s6p $^3P_2$	1347.8	<b><math>0.33\cdot 10^5</math></b>	
	6s6p $^1P_1$	3479.7	<b><math>0.16\cdot 10^5</math></b>	
5d $^2$ $^3F_3$ 2.9 ms [95]	6s6p $^3P_2$	1292.7	$2.8\cdot 10^2$	[115]
5d $^2$ $^1D_2$  470 ns [95]	6s6p $^3P_2$	1047.4	$2.8\cdot 10^6$	[115]
	6s6p $^3P_1$	959.2	$0.85\cdot 10^6$	
	6s6p $^1P_1$	1999.3	$0.49\cdot 10^6$	
5d6p $^3F_2$  34(6) ns [98]	6s5d $^3D_1$	767.42	$1.50(28)\cdot 10^7$	[98]
	6s5d $^3D_2$	778.05	$0.74(15)\cdot 10^7$	
	6s5d $^1D_2$	937.26	$0.74(15)\cdot 10^7$	
	6s5d $^3D_3$	802.02	$< 0.0009\cdot 10^7$	
	5d $^2$ $^3F_2$	8842.3		
	5d $^2$ $^3F_3$	12275		
5d6p $^3F_3$  30(5) ns [98]	6s5d $^3D_2$	728.23	$2.7(5)\cdot 10^7$	[98]
	6s5d $^3D_3$	749.01	$0.60(12)\cdot 10^7$	
	6s5d $^1D_2$	865.65	$0.030(8)\cdot 10^7$	
	5d $^2$ $^3F_2$	4966		
	5d $^2$ $^3F_3$	5890		
	5d $^2$ $^3F_4$	7552.3		

**Table 3.4:** The table is continued on the next page.

Upper level and lifetime	Lower level	Wavelength (nm)	Decay rate [A <sub>ik</sub> ] (s <sup>-1</sup> )	Ref.
5d6p <sup>3</sup> F <sub>4</sub> 27 ns [95]	6s5d <sup>3</sup> D <sub>3</sub>	706.18	5·10 <sup>7</sup>	[100]
5d <sup>2</sup> <sup>3</sup> P <sub>0</sub> 160 ns [95]	6s6p <sup>3</sup> P <sub>1</sub>	945.9	1.4·10 <sup>7</sup>	[115]
	6s6p <sup>1</sup> P <sub>1</sub>	1942.2	0.0042·10 <sup>7</sup>	
5d <sup>2</sup> <sup>3</sup> P <sub>1</sub> 170 ns [95]	6s6p <sup>3</sup> P <sub>0</sub>	891.7	5.7·10 <sup>6</sup>	[115]
	6s6p <sup>3</sup> P <sub>2</sub>	1003.5	5.0·10 <sup>6</sup>	
	6s6p <sup>3</sup> P <sub>1</sub>	922.2	4.0·10 <sup>6</sup>	
	6s6p <sup>1</sup> P <sub>1</sub>	1845.1	0.0012·10 <sup>6</sup>	
5d <sup>2</sup> <sup>3</sup> P <sub>2</sub> 270 ns [95]	6s6p <sup>3</sup> P <sub>2</sub>	961.2	6.4·10 <sup>6</sup>	[115]
	6s6p <sup>3</sup> P <sub>1</sub>	886.3	3.2·10 <sup>6</sup>	
	6s6p <sup>1</sup> P <sub>1</sub>	1706.9	0.41·10 <sup>6</sup>	
<b>5d6p <sup>3</sup>D<sub>1</sub><sup>o</sup></b>  <b>17.4(5) ns [98]</b>	<b>6s5d <sup>3</sup>D<sub>1</sub></b>	<b>659.71</b>	<b>3.7(2)·10<sup>7</sup></b>	[98]
	<b>6s5d <sup>3</sup>D<sub>2</sub></b>	<b>667.71</b>	<b>1.8(2)·10<sup>7</sup></b>	
	<b>6s<sup>2</sup> <sup>1</sup>S<sub>0</sub></b>	<b>413.36</b>	<b>0.15(2)·10<sup>7</sup></b>	
	<b>5d<sup>2</sup> <sup>3</sup>F<sub>2</sub></b>	<b>3068.20</b>	<b>0.063(38)·10<sup>7</sup></b>	
	6s5d <sup>1</sup> D <sub>2</sub>	781.51	< 0.0058(17)·10 <sup>7</sup>	
	5d <sup>2</sup> <sup>3</sup> P <sub>0</sub>	10170		
	5d <sup>2</sup> <sup>3</sup> P <sub>1</sub>	14040		
	5d <sup>2</sup> <sup>3</sup> P <sub>2</sub>	36604		
	5d <sup>2</sup> <sup>1</sup> D <sub>2</sub>	8847.2		
5d6p <sup>3</sup> D <sub>2</sub>  18(3) ns [98]	6s5d <sup>3</sup> D <sub>1</sub>	645.26	1.1(2)·10 <sup>7</sup>	[98]
	6s5d <sup>3</sup> D <sub>2</sub>	652.91	3.1(6)·10 <sup>7</sup>	
	6s5d <sup>3</sup> D <sub>3</sub>	669.56	1.3(3)·10 <sup>7</sup>	
	6s5d <sup>1</sup> D <sub>2</sub>	761.26	0.11(3)·10 <sup>7</sup>	
	5d <sup>2</sup> <sup>3</sup> F <sub>2</sub>	2779.0		
	5d <sup>2</sup> <sup>3</sup> F <sub>3</sub>	3046.8		
	5d <sup>2</sup> <sup>3</sup> P <sub>1</sub>	9507.4		
	5d <sup>2</sup> <sup>3</sup> P <sub>2</sub>	16319		
5d <sup>2</sup> <sup>1</sup> D <sub>2</sub>	8303.3			
5d6p <sup>3</sup> D <sub>3</sub>  18 ns [95]	6s5d <sup>3</sup> D <sub>3</sub>	650.05	5.4(4)·10 <sup>7</sup>	[100]
	6s5d <sup>3</sup> D <sub>2</sub>	634.34	1.16(8)·10 <sup>7</sup>	
	6s5d <sup>1</sup> D <sub>2</sub>	736.13	< 0.005·10 <sup>7</sup>	

**Table 3.5:** Continuation of Table 3.4. Compilation of the optical transitions in barium among the energy levels up to 25000 cm<sup>-1</sup>. The wavelengths are in vacuum. The errors quoted for the decay rates and the lifetimes are experimental. Transitions and decay rates relevant to this work are highlighted.

of the trap are sufficient to couple the motional degrees of freedom. For atoms the situation is significantly different, because the trapping forces and the cooling act on the same atomic transition. For atom trapping, sufficiently balanced laser beams are needed to cool and confine them in all independent spatial directions.

The alkaline atoms lithium [122], sodium [123], potassium [124, 125], rubidium [126, 127], cesium [128, 129] and francium [130] have been all laser cooled and trapped. The single valence electron in the outer shell of these atoms provides an ideal level scheme for the laser cooling techniques. Alkaline atoms such as sodium and rubidium have been particularly used for the development and refinement of various cooling and trapping techniques due to the easy accessibility of the wavelengths with commercial lasers. Other effective one electron systems are metastable noble gases. Helium [131], neon [132], argon [133], krypton [133, 134] and xenon [135] but not radon have been trapped for different physics motivations. In addition, optical trapping was reported for chromium [136, 137], silver [138], ytterbium [139], erbium [140], cadmium [141] and most recently mercury [142]. The alkaline-earth atoms magnesium [143], calcium [144], strontium [144] and radium [76] have been trapped as well. Barium however had not been trapped due to its complicated atomic level scheme. No simple transition that could be exploited as a cooling transition exists and a substantially more complex laser setup is required compared to all other trapped atoms.

There are a few more elements where laser cooling experiments have been reported but which could not be trapped so far. This includes iron [145], gallium [146], aluminum [147] and indium [148]. The limiting factor for laser cooling of these atoms is also leaking from the cooling transition similar to barium. This work reports on trapping of barium, with the leakiest cooling transition among all systems that ever have been trapped.

### 3.3.1 Laser Cooling of Leaky Systems, Barium and Radium

Alkaline-earth atoms have two electrons in their outer s-shell, with a ground state configuration  $ns^2 \ ^1S_0$ , where  $n$  is the principal quantum number 2,  $\dots$ , 7. The low lying excited states are of the configurations  $ns(n-1)d \ ^3D_1$ ,  $ns(n-1)d \ ^3D_2$ ,  $ns(n-1)d \ ^3D_3$ ,  $ns(n-1)d \ ^1D_2$ ,  $nsnp \ ^3P_0$ ,  $nsnp \ ^3P_1$ ,  $nsnp \ ^3P_2$  and  $nsnp \ ^1P_1$ . The relative positions of the excited states are different in lighter and in massive elements. The level schemes barium and radium are shown in Figs. 1.1 and 1.2 as examples.

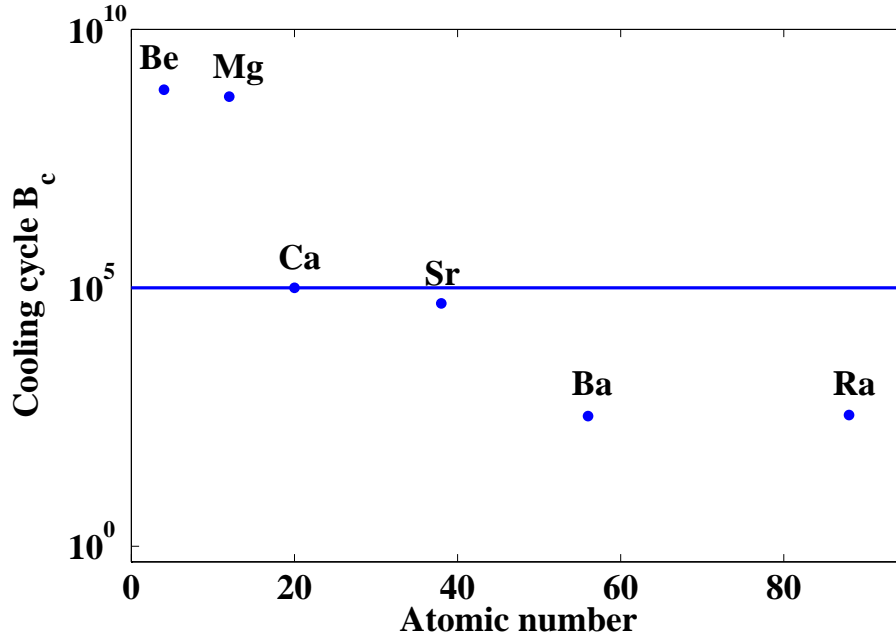


**Fig. 3.1:** Decay branching ratio  $B_c$  for the  $ns^2\ ^1S_0 \rightarrow nsnp\ ^1P_1$  transition  $n = 2, \dots, 7$ . Typically  $10^5$  scattered photons required for full deceleration of a thermal atomic beam indicated by horizontal straight line.

Two quantities, which characterize laser cooling of alkaline-earth elements with the strong  $ns^2\ ^1S_0 \rightarrow nsnp\ ^1P_1$  transition can be defined :

(1) The decay branching,  $B_c$ , is the ratio of the decay rate of the  $nsnp\ ^1P_1$  state to the ground state  $ns^2\ ^1S_0$  to the decay rates into the low lying D-states. It is given by the ratio of the spontaneous transition rates  $A_{1P_1-1S_0}$  of the cooling transition to the sum of the transition rates  $\sum_{D=^1D_2, ^3D_2, ^3D_1} A_{1P_1-D}$  into the low lying D-states

$$B_c = \frac{A_{1P_1-1S_0}}{\sum_{D=^1D_2, ^3D_2, ^3D_1} A_{1P_1-D}}. \quad (3.1)$$

(2) The change in velocity,  $\Delta v$ , corresponding to scattering  $B_c$  photons on the cooling transition is

$$\Delta v = B_c \cdot v_r = B_c \cdot \frac{\hbar k}{m}, \quad (3.2)$$

where  $v_r$  is the recoil velocity due to scattering of a single photon,  $m$  is the mass of the atom,  $\vec{k}$  is the wavevector of the transition and  $\hbar$  is Planck's constant.

The branching ratio  $B_c$  varies significantly with the atomic masses when the electron coupling scheme in the atoms changes from Russell-Saunders (L-S) cou-

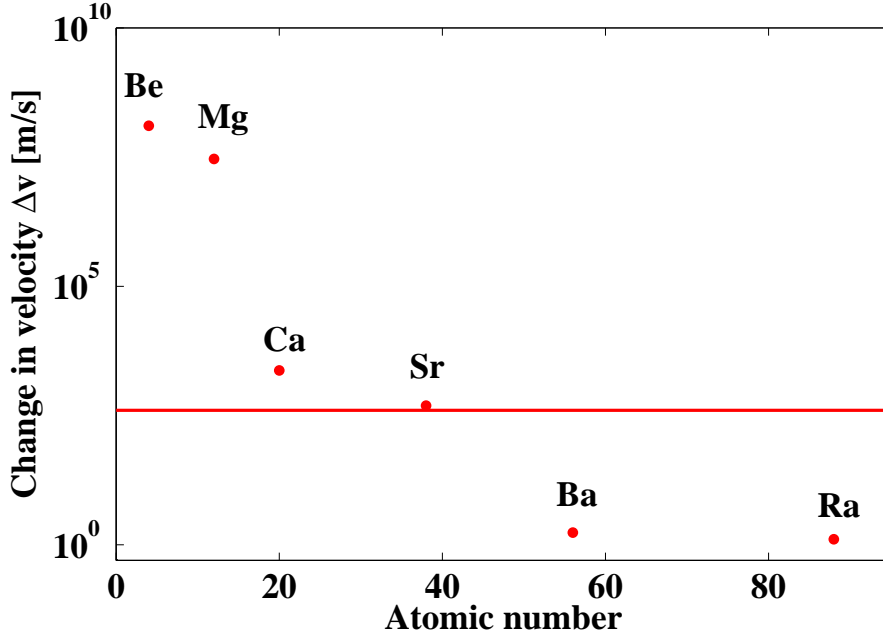


**Fig. 3.2:** Average velocity change  $\Delta v$  for alkaline-earth elements by laser light at the  $ns^2 \ ^1S_0 \rightarrow nsnp \ ^1P_1$  transition  $n = 2, \dots, 7$ . Further velocity change are not possible with only this light, because the atoms are optically pumped into the metastable D-states. The horizontal line corresponds to the  $\Delta v = 400$  m/s, which is a typical value for the most probable velocity of atoms in an atomic beam.

Alkaline-earth elements	$B_c$	$v_r$ (m/s)
Beryllium (Be)	$6.8 \cdot 10^8$	0.19
Magnesium (Mg)	$5.0 \cdot 10^8$	0.058
Calcium (Ca)	$1.0 \cdot 10^5$	0.024
Strontium (Sr)	$0.5 \cdot 10^5$	0.0099
Barium (Ba)	$3.3 \cdot 10^2$	0.0052
Radium (Ra)	$3.5 \cdot 10^2$	0.0037

**Table 3.6:** Decay branching ratio  $B_c$  for the alkaline-earth atoms for the decay into metastable D-states. The recoil velocities  $v_r = \hbar k/m$  for single photon scattering on the  $ns^2 \ ^1S_0 \rightarrow nsnp \ ^1P_1$  strong resonance transition for the most abundant isotopes, where  $n = 2, \dots, 7$ .

Symbols	Wavelength (nm)	Transition	Functionality in this work
$\lambda_1$	553.7	$6s^2 \ ^1S_0 \rightarrow 6s6p \ ^1P_1$	cooling transition and detection
$\lambda_2$	659.7	$6s5d \ ^3D_1 \rightarrow 5d6p \ ^3D_1^o$	repumping transition
$\lambda_3$	667.7	$6s5d \ ^3D_2 \rightarrow 5d6p \ ^3D_1^o$	repumping transition
$\lambda_{\text{IR1}}$	1107.8	$6s5d \ ^3D_1 \rightarrow 6s6p \ ^1P_1$	repumping transition
$\lambda_{\text{IR2}}$	1130.6	$6s5d \ ^3D_2 \rightarrow 6s6p \ ^1P_1$	repumping transition
$\lambda_{\text{IR3}}$	1500.4	$6s5d \ ^1D_2 \rightarrow 6s6p \ ^1P_1$	repumping transition
$\lambda_{\text{B}}$	413.3	$5d6p \ ^3D_1^o \rightarrow 6s^2 \ ^1S_0$	detection

**Table 3.7:** Nomenclature of the transition wavelengths and their functionality in the experiments. The transitions are shown in Fig. 3.3.

pling towards j-j coupling and the states despite a clean L-S coupling labelling have in fact admixtures from different spin states. The branching ratio  $B_c$  varies by many orders of magnitude over the alkaline-earth group of elements (see Fig. 3.1). A figure of merit is the average velocity change  $\Delta v$  before the atom is lost from the cooling cycle (see Fig. 3.2). For a velocity change of about 400 m/s, an atom needs to scatter some  $10^4 - 10^5$  photons. Laser light on the strong  $ns^2 \ ^1S_0 \rightarrow nsnp \ ^1P_1$  transition is sufficient for laser cooling of the light alkaline-earth elements Be, Mg, Ca and Sr, where  $n = 2, \dots, 5$ . For barium and radium an average velocity change of order  $\Delta v < 2$  m/s can only be achieved. This can not be considered significant deceleration with laser cooling.

For barium and radium, the leaking from the cooling cycle,  $B_c^{-1}$ , is at least three orders of magnitude larger than for the lighter alkaline-earth elements (see Table 3.6). To change the velocity nevertheless significantly by laser cooling techniques, one has to repump the atoms from the metastable states back into the cooling transition. A complete cooling cycle involves the transitions between the five states  $ns^2 \ ^1S_0$ ,  $nsnp \ ^1P_1$ ,  $ns(n-1)d \ ^1D_2$ ,  $ns(n-1)d \ ^3D_1$  and  $ns(n-1)d \ ^3D_2$  rather than just the two states  $ns^2 \ ^1S_0$  and  $nsnp \ ^1P_1$  with  $n = 6$  for barium and  $n = 7$  for radium. This requires a complex laser system for decelerating and eventually trapping of these atoms.

Several strategies are possible to achieve effective repumping of barium and radium atoms from the D-states into the cooling transition. The main goal is to provide efficient repumping from the dark states and to avoid simultaneous losses to even further states. One solution is based on three infrared transitions

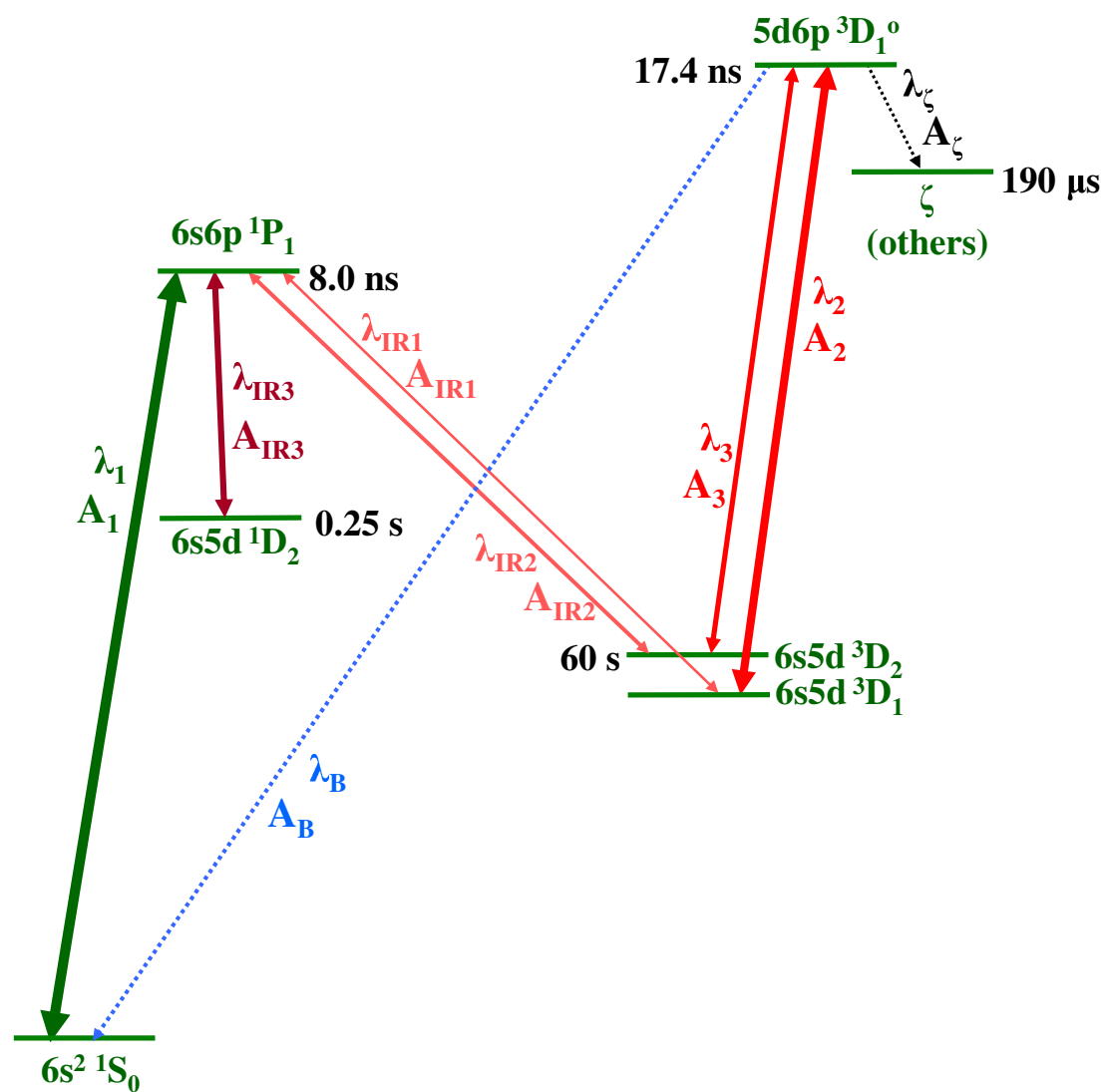


**Fig. 3.3:** Energy levels of atomic barium relevant for laser cooling. The solid lines indicate the laser light at the wavelengths  $\lambda_i$  used in the experiment and the dotted line together with the solid lines indicate the allowed electric dipole transitions. The decay rates  $A_i$  of the excited states are listed in Tables 3.4 and 3.5.

(see Table 3.7) at the wavelengths  $\lambda_{\text{IR1}}$ ,  $\lambda_{\text{IR2}}$  and  $\lambda_{\text{IR3}}$  for barium, which couple the  $6s5d\ ^1D_2$ ,  $6s5d\ ^3D_2$  and  $6s5d\ ^3D_1$  states to the excited state  $6s6p\ ^1P_1$  of the cooling transition. Repumping of the  $6s5d\ ^3D_1$  and the  $6s5d\ ^3D_2$  states via the higher lying  $5d6p\ ^3D_1^o$  state with laser light at the wavelengths  $\lambda_2$  and  $\lambda_3$  is an alternative in barium. Similarly in radium the  $7s6d\ ^3D_1$  and the  $7s6d\ ^3D_2$  states can be repumped via the  $6d7p\ ^3D_1^o$  state.

For barium the observed decay branching of the  $6s6p\ ^1P_1$  state to the  $6s5d\ ^1D_2$  state is 1 : 485(15), to the  $6s5d\ ^3D_2$  state it is 1 : 1085(35) and to the  $6s5d\ ^3D_1$  state it is 1 : 24000(3000). Without repumping from the  $6s5d\ ^3D_1$  state one can expect an average velocity change of  $\Delta v = 120(15)$  m/s. A significant part of the velocity spectrum from a thermal source can still be accessed with repumping the  $6s5d\ ^1D_2$  and the  $6s5d\ ^3D_2$  states only. The velocity range can be extended by adding a repumping laser light at the wavelengths  $\lambda_{\text{IR1}}$  or  $\lambda_2$ .

For radium the calculated decay branching of the  $7s7p\ ^1P_1$  state to the  $7s6d\ ^1D_2$  state is 1 : 550, to the  $7s6d\ ^3D_2$  state it is 1 : 1800 and to the  $7s6d\ ^3D_1$  state it is 1 : 5600 [93]. Without repumping from the  $7s6d\ ^3D_1$  state one can expect an average velocity change of  $\Delta v = 20$  m/s. In that case repumping from the  $7s6d\ ^3D_1$  state has to be implemented for the deceleration of an atomic beam. It appears that with repumping atoms from metastable D-states one can achieve significant deceleration of the heavy alkaline-earth elements.

### 3.3.2 Discussion of Atomic Beam Slowing

The velocity,  $v_c$ , up to which a magneto-optical trap (MOT) can capture atoms is typically a few ten m/s. It is not high enough for efficient loading of the trap from a thermal source because of the small number of atoms in the Maxwell-Boltzmann velocity distribution below  $v_c$ . This is of crucial importance for a trapping scheme for rare and radioactive isotopes.

During the deceleration of an atomic beam by optical forces the changing Doppler shift causes the cooling transition to shift out of resonance. A Doppler shift by one natural linewidth,  $\Gamma = \gamma/2\pi$ , corresponds to a velocity change of  $\Delta v = 10$  m/s for barium. With a fixed laser detuning the velocity range of the optical forces would be limited. Among the possible solutions to this problem are (i) frequency chirping of the slowing laser [149, 150], (ii) the use of a Zeeman slower [151] or (iii) laser cooling with frequency broadened lasers [152]. All these techniques have been implemented in several systems to compensate the changing Doppler shift during deceleration and thus keep the slowing force present at all

time. The feasibility of these techniques for decelerating a barium atomic beam have been explored.

### (i) Frequency Chirping

The changing Doppler shift can be compensated by changing the frequency of the laser according to the Doppler shift while decelerating the atoms [153]. It was first implemented in slowing of a sodium atomic beam [149]. The time span of the frequency sweep needs to be synchronized to the deceleration time of the atoms in the deceleration region. Stopping barium atoms of  $v_0 = 600$  m/s initial velocity with an acceleration  $a_{\max} = 3 \cdot 10^5$  m/s<sup>2</sup> will take  $t = 2$  ms. The frequency sweep rate must be then about 500 Hz and the sweep range is about 1.1 GHz to cover the velocity range up to  $v_0$ . The duty cycle of this process will be 0.5 %. In order to achieve the same overall efficiency as for a fixed laser frequency detuning one would have to access about a 200 times larger fraction of the velocity distribution. The repumping lasers have a similar requirement for the frequency sweeping.

### (ii) Zeeman Slower

A widely used technique is a spatially varying magnetic field along the direction of motion of the atomic beam. The Zeeman shift can be adjusted along the device to compensate the Doppler shift [151]. For achieving a continuous deceleration over the interaction length the spatial variation of the magnetic field has to match the gradient of Doppler shift.

Bringing atoms of an initial velocity  $v_0$  to rest requires an interaction length

$$x_0 = \frac{v_0^2}{2 \cdot a}, \quad (3.3)$$

where  $a$  is the deceleration. During the deceleration the velocity,  $v(x)$ , of the atom at position,  $x$ , along the propagation direction of the atomic beam will be

$$v(x) = \sqrt{2a(x_0 - x)}. \quad (3.4)$$

The Doppler shift,  $f_D(x)$ , at the position  $x$  will be

$$f_D(x) = -\frac{v(x)}{\lambda} = -\frac{\sqrt{2a \cdot (x_0 - x)}}{\lambda}, \quad (3.5)$$

where  $\lambda$  is the transition wavelength. The gradient of Doppler shift is

$$\frac{df_D(x)}{dx} = \frac{1}{\lambda} \sqrt{\frac{a}{2(x_0 - x)}}. \quad (3.6)$$

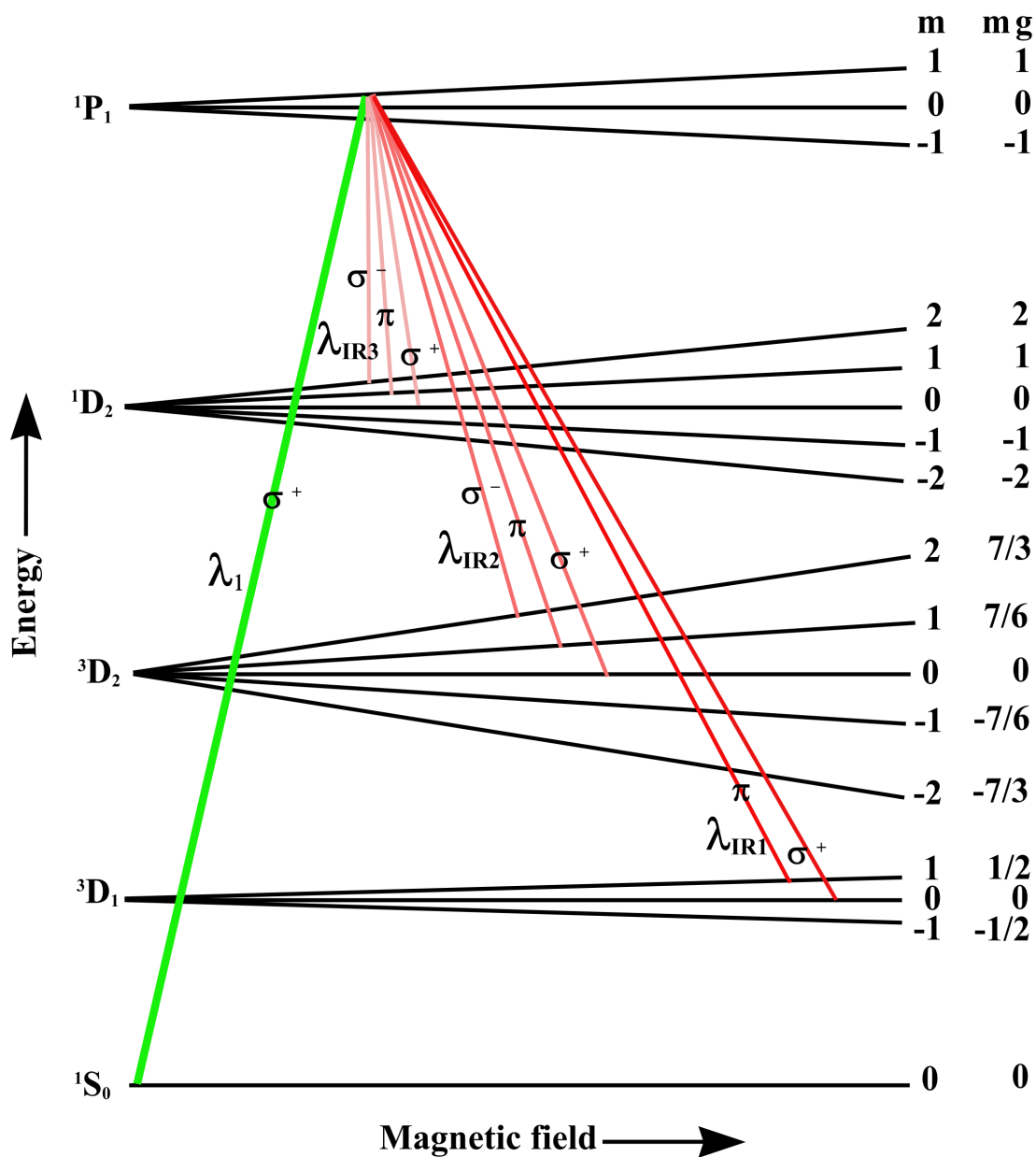


**Fig. 3.4:** Zeeman splitting of the states in the laser cooling scheme of barium. The transitions are drawn to show the possible decay to the sub-levels. The splitting of the transitions with increasing magnetic field are not drawn to the scale.

States	m	g
$ns^2 \ ^1S_0$	0	1
$ns(n-1)d \ ^3D_1$	+1, 0, -1	$\frac{1}{2}$
$ns(n-1)d \ ^3D_2$	+2, +1, 0, -1, -2	$\frac{7}{6}$
$ns(n-1)d \ ^1D_2$	+2, +1, 0, -1, -2	1
$nsnp \ ^1P_1$	+1, 0, -1	1

**Table 3.8:** Magnetic quantum numbers m and Lande g-factors g of the particular states involved in the laser cooling scheme of heavy alkaline-earth atoms.

In a spatially varying magnetic field,  $B(x)$ , the frequency shift,  $\nu_B(x)$ , of a transition due to Zeeman splitting is

$$\nu_B(x) = (m_i g_i - m_k g_k) \frac{\mu_B \cdot B(x)}{h}, \quad (3.7)$$

where  $m_i$ ,  $m_k$  and  $g_i$ ,  $g_k$  are the magnetic quantum numbers and the Lande g-factors for the i-th and k-th magnetic sublevels (see Table 3.8). In the Zeeman slower the Zeeman shift and the Doppler frequency shift cancel each other

$$\frac{d\nu_B(x)}{dx} = -\frac{df_D(x)}{dx}. \quad (3.8)$$

The spatial variation required for the magnetic field is

$$B(x) = \Theta_\lambda^p \cdot \left[ \frac{h}{\mu_B} \sqrt{\frac{a}{2} (x_0 - x)} \right], \quad (3.9)$$

where  $p = \sigma^+$ ,  $\sigma^-$  or  $\pi$  refers to the transition type (see Fig. 3.4) and  $\Theta_\lambda^p$  is a scaling factor

$$\Theta_\lambda^p = [\lambda \cdot (m_i g_i - m_k g_k)]^{-1}, \quad (3.10)$$

which determines the required gradient of the magnetic field in the Zeeman slower (see Table 3.9).

For laser cooling of  $^{138}\text{Ba}$ , which has nuclear spin  $I = 0$ , the fine structure splitting needs to be considered only. The scaling factor  $\Theta_\lambda^p$  has in general a different value for every transition (see Table 3.9). That would require a different Zeeman slowing magnetic field for every transition at the same location. This is not possible as it would violate Maxwell's equations.

Wavelength (nm)	Polarization (p)	$(m_i g_i - m_k g_k)$	$\Theta_\lambda^p$ (nm <sup>-1</sup> )
$\lambda_1$	$\sigma^+$	+1	$+\frac{1}{\lambda_1}$
$\lambda_{\text{IR1}}$	$\sigma^+$	+1	$+\frac{1}{\lambda_{\text{IR1}}}$
	$\pi$	$+\frac{1}{2}$	$+\frac{1}{2}\frac{1}{\lambda_{\text{IR1}}}$
$\lambda_{\text{IR2}}$	$\sigma^+$	$-\frac{1}{6}$	$-\frac{1}{6}\frac{1}{\lambda_{\text{IR2}}}$
	$\sigma^-$	$-\frac{8}{6}$	$-\frac{8}{6}\frac{1}{\lambda_{\text{IR2}}}$
	$\pi$	+1	$+\frac{1}{\lambda_{\text{IR2}}}$
$\lambda_{\text{IR3}}$	$\sigma^+$	+1	$+\frac{1}{\lambda_{\text{IR3}}}$
	$\sigma^-$	-1	$-\frac{1}{\lambda_{\text{IR3}}}$
	$\pi$	0	0

**Table 3.9:** The Zeeman slower scaling factor  $\Theta_\lambda^p$  for the transitions within the magnetic sub-levels involved in the laser cooling of barium, which determines the required slope of the magnetic field in a Zeeman slower.

### (iii) Frequency Broadening

Frequency broadening of the lasers or power broadening of the transition offer a further opportunity to compensate the Doppler shift change. In a moving atomic reference frame the effective frequency detuning,  $\delta$ , of a laser frequency from the atomic transition frequency is given by Doppler shift,  $\delta_D$ , and the frequency detuning of the laser,  $\delta_l$ , from resonance, i.e.,  $\delta = (\delta_l + \delta_D)$ . The photon scattering rate,  $\gamma_p$ , depends on the frequency detuning  $\delta$ . For an intense light source the power broadening increases the width of the transition to

$$\gamma' = \gamma \sqrt{(1 + S_0)}, \quad (3.11)$$

where  $S_0$  is the saturation parameter. This widens the velocity acceptance range for the slowing lasers, and the velocity change  $\Delta v$  can be many times larger than the velocity change which corresponds to a change of the detuning of the natural linewidth  $\Gamma$  of the cooling transition.

## Conclusion

In this work a barium atomic beam is slowed down with intense laser beams to power broaden all the transitions. This is sufficient to slow an atomic beam for loading into a MOT (see Chapter 6). The better option of using frequency broadened light sources for the relevant transitions has not been installed yet, as it requires a large number of, e.g., electro-optic modulators. With this further feature a larger fraction of the velocity distribution could be decelerated.

Laser cooling of the heavy alkaline-earth elements requires an extended cooling cycle with five or six states. For barium all relevant branching ratios and transition wavelengths are known from available experimental data. The situation for radium is different since only few transitions have been observed by laser spectroscopy. The main source for the transition wavelengths and the decay branching ratios are theoretical calculations.

# Chapter 4

## Experimental Tools

The main experimental topic of this work is the optical trapping of the heavy alkaline-earth element barium as a precursor for radium experiments. Trapping of atoms in a magneto-optical trap (MOT) requires an atomic source inside a vacuum chamber, coherent light sources for driving suitable atomic transitions, a quadrupole magnetic field, a detector for observing the signal from trapped atoms and a data acquisition system. The experiments require the control of up to eight different lasers at the same time.

### 4.1 Barium Atomic Beam

A barium atomic beam is produced by a resistively heated effusive oven [112]. The same basic oven design is used for several experiments at KVI: as an atom source in the Alcatraz experiment aiming for trapping of the rare isotope  $^{41}\text{Ca}$  [154] and as a source for Na trapping for recoil ion momentum spectroscopy [155, 156]. The oven is mounted on a standard CF35 flange. It is inserted into a CF35 tube of 128 mm length. An electric power of some 20 W heats the oven to a temperature of 820 K. The temperature can be measured with a K-type thermocouple, which is a model K24-1-505 (from KURVAL BV., Nieuw-Vennep, Netherlands). The oven crucible has an orifice of 1 mm diameter and 10 mm length. The divergence of the atomic beam is about 100 mrad. Far away from the oven, near the beam axis where the transverse velocity component can be neglected, the velocity distribution of the atoms in the atomic beam can be approximated with a Maxwell-Boltzmann distribution

$$dF_{\text{beam}}(v) = \frac{v^3}{2 \widetilde{v}^4} \exp\left(-\frac{v^2}{2 \widetilde{v}^2}\right) dv, \quad (4.1)$$

where  $v$  is the atomic velocity,  $m$  is the mass of a barium atom,  $k_B$  is Boltzmann's constant,  $T$  is the operating temperature of the oven and  $\tilde{v}$  is the characteristic velocity given by

$$\tilde{v} = \sqrt{\frac{k_B \cdot T}{m}}. \quad (4.2)$$

In an atomic beam the average velocity is  $\langle v \rangle = \sqrt{\frac{9\pi}{8}} \cdot \tilde{v}$ , the most probable velocity is  $v_{\text{mp}} = \sqrt{3} \cdot \tilde{v}$  and the root-mean-square velocity is  $v_{\text{rms}} = 2 \cdot \tilde{v}$ . In this distribution, a fraction of only  $4 \cdot 10^{-5}$  is below a velocity of 30 m/s, a typical capture velocity of a MOT.

The oven is loaded with 200 mg of barium carbonate  $\text{BaCO}_3$  and 500 mg zirconium Zr powder. The  $\text{BaCO}_3$  is mixed with the Zr powder. The oven is heated initially to a temperature of 1000 K, to break the carbonate bond and to produce barium oxide  $\text{BaO}$  and carbon-di-oxide  $\text{CO}_2$  in a calcination process. Zirconium works as a reducing agent for  $\text{BaO}$  to produce atomic Ba. Aluminum and silicon could be used as an alternative reducing agent in a thermite process. The flux is about  $10^{12} - 10^{14}$  barium atoms per second emerging from the oven at a temperature range of 750 – 900 K. Two identical ovens are operated in the experiment, one is filled with  $\text{BaCO}_3$  (from ACROS Organics, NJ, USA), with the seven stable natural barium isotopes. The second oven contains isotopically enriched  $^{138}\text{BaCO}_3$  of 99.7% purity (from Campro Scientific BV, Veenendaal, Netherlands).

The beam with all natural barium isotopes is used for Doppler free laser spectroscopy with the transition at wavelength  $\lambda_1$ . The obtained signal serves as a reference for stabilizing the laser frequency [112]. The isotopically pure  $^{138}\text{Ba}$  atomic beam is used in the magneto-optical trapping setup.

The vacuum chambers for both atomic beams are made of standard conflat (CF) UHV stainless steel parts. The vacuum system for the Ba atomic beam consists of the oven in a CF63 chamber and CF38 triplecross piece. To this housing two windows are mounted on opposite sides for a laser beam entry and exit, which crosses the atomic beam at right angle  $\theta = 90^\circ$  downstream of the oven. The interaction region can be viewed through a third window, which is orthogonal to the laser and atomic beams. The vacuum is maintained in this chamber by a 2 l/s ion pump (from Gamma Vacuum, MN, USA) to several times  $10^{-9}$  mbar. The isotopically pure  $^{138}\text{Ba}$  beam is connected to a vacuum system (see Fig. 4.1), which is pumped by a 10 l/s ion pump (from Gamma Vacuum, MN, USA). The vacuum is typically around  $10^{-9}$  mbar. An octagon (from Kimball Physics Inc., NH, USA) is used as the central trapping chamber. It has ports

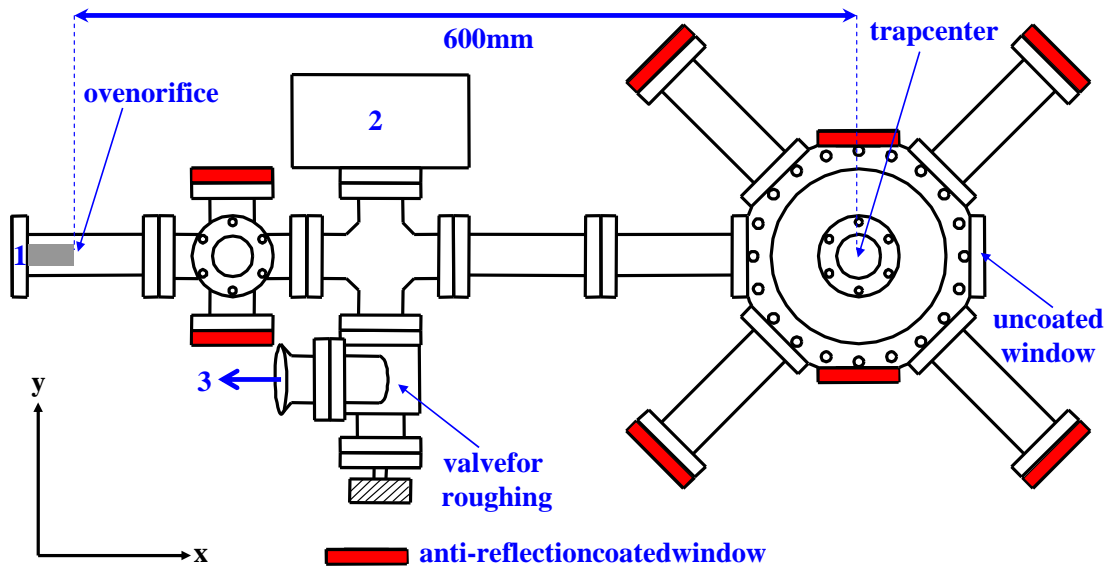


**Fig. 4.1:** Top view of the vacuum chamber for magneto-optical trapping of barium. 1 - the barium oven is mounted on a CF35 flange. 2 - a 10 l/s ion pump to maintain the vacuum. 3 - a KF port for mounting a roughing pump to the chamber. The optical windows indicated in bold are anti-reflection coated. The center of the octagon shaped part of the chamber is about 600 mm down stream of the oven orifice. Figure is drawn to scale.

for nine optical windows. Eight of the windows are made from fused silica and have a broad band anti-reflection coating to reduce the reflectivity at wavelength  $\lambda_1$  to less than 0.5%. Some of the windows are mounted on extension tubes to reduce the amount of reflected stray light coming from six trapping laser beams. The window in the direction of the atomic beam has no optical coating, since it is used for several significantly different wavelengths.

## 4.2 Lasers

Lasers at visible and infrared wavelengths are needed for driving transitions in the laser cooling cycle (see Fig. 4.1). Different types of lasers are employed, i.e., a dye laser, three fiber lasers and several diode lasers. The laser systems, the generation of multiple frequencies at one wavelength, locking schemes and the layout of the optics arrangement are described in this section.

Wavelength (nm)	Transition	Intensity	Detuning	Laser system
$\lambda_1 = 553.7$	$6s^2 \ ^1S_0 \rightarrow 6s6p \ ^1P_1$	$I_1^p$	$\Delta\nu_1^p$	Dye laser
$\lambda_2 = 659.7$	$6s5d \ ^3D_1 \rightarrow 5d6p \ ^3D_1^o$	$I_2$	$\Delta\nu_2$	Diode laser
$\lambda_3 = 667.7$	$6s5d \ ^3D_2 \rightarrow 5d6p \ ^3D_1^o$	$I_3$	$\Delta\nu_3$	Diode laser
$\lambda_{IR1} = 1107.8$	$6s5d \ ^3D_1 \rightarrow 6s6p \ ^1P_1$	$I_{IR1}$	$\Delta\nu_{IR1}$	Fiber laser
$\lambda_{IR2} = 1130.6$	$6s5d \ ^3D_2 \rightarrow 6s6p \ ^1P_1$	$I_{IR2}^p$	$\Delta\nu_{IR2}^p$	Fiber and diode lasers
$\lambda_{IR3} = 1500.4$	$6s5d \ ^1D_2 \rightarrow 6s6p \ ^1P_1$	$I_{IR3}^p$	$\Delta\nu_{IR3}^p$	Fiber and diode lasers

**Table 4.1:** Nomenclature for the intensities and frequency detunings of all laser beams in this work. Laser beams at the wavelengths  $\lambda_1$ ,  $\lambda_{IR2}$  and  $\lambda_{IR3}$  are used for two different purposes in the experiments. For those lasers the superscript p (i.e. s or t) in the detunings and intensities refers to their purpose. Where s means slowing and t means trapping.

## Dye Laser

A CR-699-21 ring dye laser (from Coherent Inc., Palo Alto, USA) is operated with Pyrromethene-567 (PM567) dye to produce light at wavelength  $\lambda_1$ . The concentration of the dye solution is 1 g in 1.5  $\ell$  of 2-phenoxyethanol (CAS No. 122-99-6). A dye circulator RD-2000 and a nozzle RD-07 (from Radiant Dyes Laser & Accessories GmbH, Wermelskirchen, Germany) are installed to the dye laser. The laser is pumped by a Verdi-V10 single frequency Nd:YAG laser (from Coherent Inc., Palo Alto, USA). The wavelength of this laser is 532 nm and it has a maximum output power of 10 W. Typically an ample amount of 420 – 440 mW output power is generated by the dye laser at wavelength  $\lambda_1$  with 5 W of pump power and 7.5 bar pressure in the dye circulator. The lasing threshold of the dye laser is reached for 2.8 W of pump power. The linewidth of the light is about 1 MHz. The dye laser frequency can be scanned over a range of 20 GHz, either internally or by an external control voltage.

## Fiber Lasers

Three custom made fiber lasers (from Koheras Adjustik and Boostik Systems, Birkerød, Denmark) are used for generating light at the infrared wavelengths  $\lambda_{IR1}$ ,  $\lambda_{IR2}$  and  $\lambda_{IR3}$ . The maximum output powers are 5 mW, 40 mW and 77 mW

Diode lasers				
Part No.	QLD-660 -80S	DL3149- 057	LD-1120 -0300-1	QFBLD -1550-20
Supplier	QPhotonics USA	Thorlabs USA	TOPTICA Germany	QPhotonics USA
Wavelength	$\lambda_2$	$\lambda_3$	$\lambda_{\text{IR}2}$	$\lambda_{\text{IR}3}$
Power (mW)	8	5	300	17
Typical frequency tuning coefficients				
Current (MHz/A)	1200	1000	175	$10^6$
Tuning Actuator	560 MHz/V (PZT)	500 MHz/V (PZT)	70 MHz/V (PZT)	21 MHz/ $\Omega$ (thermistor)

**Table 4.2:** Characteristics of the diode lasers used in the experiments.

respectively. These lasers are tunable in frequency by temperature and by piezo transducers. The frequency scanning rate by temperature tuning is limited in speed and in accuracy by the temperature controlling unit of the laser. The scanning by PZT is reproducible and scan rates of 1 GHz/ms could be achieved. The typical PZT tuning in this work is in steps of a few MHz in 100 ms to 1 s. The passive frequency stability of these lasers is very good if they are operated in a temperature stabilized environment. The frequency drift is less than 50 MHz/h and the day to day variation in the reproducibility is better than 500 MHz. They show a large hysteresis for PZT scanning in particular for large frequency scan rates. For a frequency step of 10 GHz this can amount up to about 100 MHz. Each of the laser systems has a second output, which can be used to monitor the wavelength on a wavelength meter WS6 (from High Finesse GmbH, Tübingen, Germany) and to perform further diagnostics. The power level of this monitor output is a few % of the main output power.

### Diode Lasers

Visible laser light is generated with the laser diodes QLD-660-80S (from QPhotonics, VA, USA) and DL3149-057 (from Thorlabs. Inc., NJ, USA) at the wavelengths  $\lambda_2$  and  $\lambda_3$ . For infra-red light at wavelength  $\lambda_{\text{IR}2}$  a laser diode LD-1120-0300-1 (from TOPTICA Photonics AG, Gräfelfing, Germany) is used. The

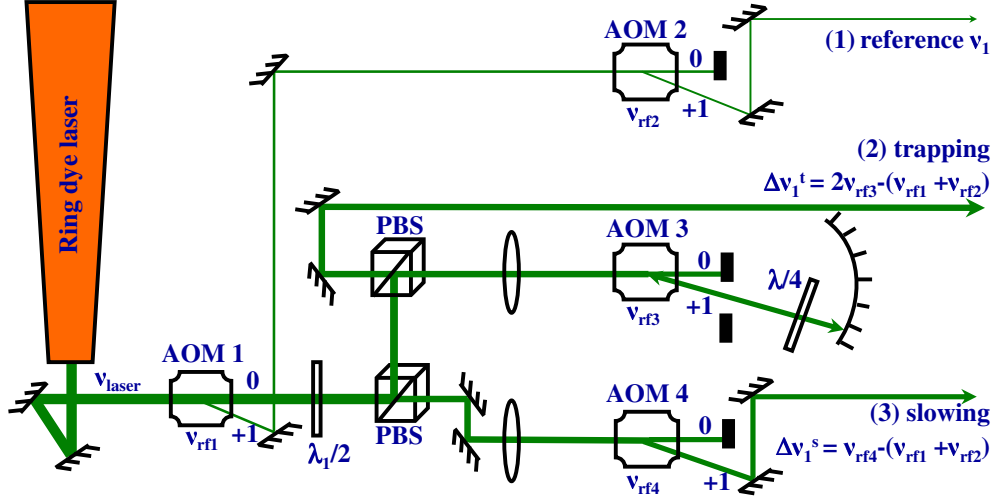


**Fig. 4.2:** Schematics for generating individual frequencies at wavelength  $\lambda_1$ . The frequencies can be tuned independently via the modulation frequencies of the acousto optic modulators AOM1, AOM2, AOM3 and AOM4. The reference beam at frequency  $\nu_1$  is for Doppler free spectroscopy of the  $6s^2 \ ^1S_0 \rightarrow 6s6p \ ^1P_1$  transition, the deceleration beam at frequency detuning  $\Delta\nu_1^s$  is for slowing the atomic beam and the trapping beam at frequency detuning  $\Delta\nu_1^t$  provides the light necessary for a MOT.

output powers are 8 mW, 5 mW and 250 mW respectively. The laser diodes are in commercially standardized packages of 5.6 mm and 9 mm diameter. They are stabilized in extended cavity diode laser configuration in home made mounting systems. The compact diode laser systems are user friendly for spectroscopy experiments because of their simplicity, size and cost [157,158]. Detailed descriptions of grating stabilized diode lasers can be found elsewhere [159,160].

A commercially available QFBLD-1550-20 distributed feedback diode laser (from QPhotonics, VA, USA) produced light at wavelength  $\lambda_{IR3}$  with a maximum output power of 17 mW. The frequency of this laser is stabilized with a grating within the semiconductor chip [160]. The light is coupled into a single mode fiber attached to the diode chip. The frequency can be changed by altering the laser's temperature or its operating current. The laser is tunable over a wide frequency range without any mode hops. A commercially available mount LM14S2 (from Thorlabs. Inc., NJ, USA) interfaces the laser in a 14 pin butterfly package to the temperature and the current controller.

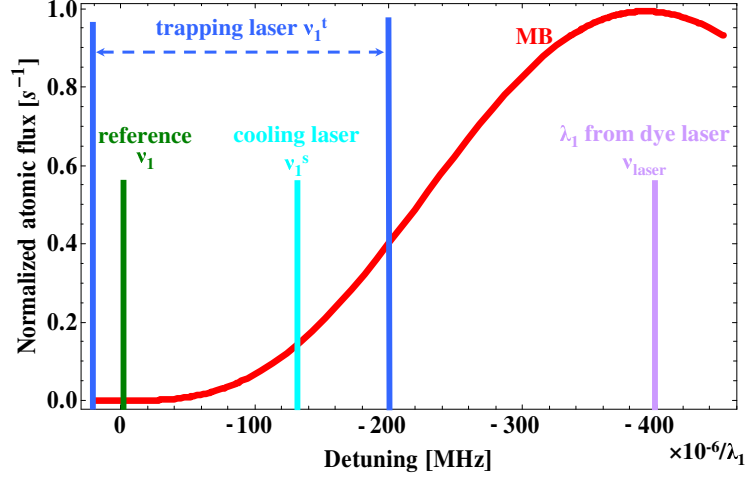


**Fig. 4.3:** Relative position of the laser frequencies for the three individual laser beams at wavelength  $\lambda_1$ . The Doppler shift of barium atoms with a Maxwell-Boltzmann (MB) velocity distribution at 820 K temperature is shown to indicate the scale of the frequency intervals.

### 4.2.1 Multiple Frequency Generation

Multiple close lying laser frequencies are needed near the wavelengths  $\lambda_1$ ,  $\lambda_{\text{IR}2}$  and  $\lambda_{\text{IR}3}$  to achieve both efficient cooling and trapping. For the two infrared wavelengths  $\lambda_{\text{IR}2}$  and  $\lambda_{\text{IR}3}$ , two lasers at each wavelength are used. The frequency offset of these pairs is controlled (see section 4.2.2).

Laser light at the dye laser wavelength  $\lambda_1$  is employed at three slightly different frequencies. Acousto optical modulators (AOMs) can be used to generate these frequencies by modulating the light passing through them (see Figs. 4.2 and 4.3). In these devices (see Table 4.3) an integer multiple,  $m$ , of the modulation frequency,  $\nu_{\text{mod}}$ , is added or subtracted from the laser frequency,  $\nu_{\text{laser}}$ , to achieve the light frequency

$$\nu_{\text{light}} = \nu_{\text{laser}} \pm m \cdot \nu_{\text{mod}}. \quad (4.3)$$

Firstly, about 1 mW light is needed for the stabilization of the dye laser frequency to the resonance frequency,  $\nu_1$ , of the  $6s^2 \ ^1S_0 \rightarrow 6s6p \ ^1P_1$  transition in  $^{138}\text{Ba}$ . Secondly, the slowing of the atomic beam requires up to 30 mW power at a frequency detuning of  $\Delta\nu_1^s$ , which is typically  $-260$  MHz from the atomic transition frequency  $\nu_1$ . Thirdly, optical trapping requires about 30 mW power at a frequency detuning of  $\Delta\nu_1^t$ , which should be around  $\pm 50$  MHz. This light can also serve to probe the velocity distribution of atoms in the ground state  $6s^2 \ ^1S_0$ . For this purpose the frequency detuning  $\Delta\nu_1^t$  can be between  $-260$  MHz

and 50 MHz at a power level of 1 mW.

The reference frequency  $\nu_1$  is generated by using the first ( $m = +1$ ) order of AOM1, which is a model AOM-60 (from IntraAction Corp., IL, USA) and the first ( $m = +1$ ) order of AOM2, which is a model MT-350-AO (from AA-OPTO-ELECTRONIC, Saint Remy Les Chevreuses, France). The light frequency is then

$$\nu_1 = \nu_{\text{laser}} + (\nu_{\text{rf1}} + \nu_{\text{rf2}}), \quad (4.4)$$

where  $\nu_{\text{rf1}}$  and  $\nu_{\text{rf2}}$  are the modulation frequencies to drive the AOMs. AOM1 diffracts about 2% of the dye laser output power and more than 1 mW of light is obtained at the frequency  $\nu_1$ . The operating frequencies are  $\nu_{\text{rf1}} = 60$  MHz and  $\nu_{\text{rf2}}$  varies between 300 MHz and 500 MHz.

The undiffracted beam of AOM1 is split by a combination of a  $\lambda/2$  wave-plate and a polarizing beam splitter cube. This allows to change the splitting ratio by rotating the polarization with the  $\lambda/2$  wave-plate. One beam is used to generate the frequency detuning  $\Delta\nu_1^t$  by double passing AOM3, which is a model TH-200-50 (from BRIMOSE Corp., MD, USA). The frequency detuning of the double pass first ( $m = +1$ ) order beam is

$$\Delta\nu_1^t = 2 \cdot \nu_{\text{rf3}} - (\nu_{\text{rf1}} + \nu_{\text{rf2}}), \quad (4.5)$$

where  $\nu_{\text{rf3}}$  is the operating frequency of AOM3. The double passing has an efficiency of about 30% at a frequency  $\nu_{\text{rf3}} = 200$  MHz. More than 30 mW of light can be generated with the necessary frequency detuning for trapping. For measuring the velocity distribution of atoms in the ground state,  $\nu_{\text{rf3}}$  is tuned between 130 MHz and 280 MHz to cover the low velocity range of the spectrum. The laser light after double passing is power stabilized to better than 1% at around 1 mW over the entire tuning range.

The second beam from the polarizing beam splitter cube is used to generate the frequency detuning  $\Delta\nu_1^s$ , which is the first ( $m = +1$ ) order diffracted beam of AOM4. It is a model TH-200-50 (from BRIMOSE Corp., MD, USA) operating at a radio frequency,  $\nu_{\text{rf4}}$ , which yields

$$\Delta\nu_1^s = \nu_{\text{rf4}} - (\nu_{\text{rf1}} + \nu_{\text{rf2}}). \quad (4.6)$$

This light is used for deceleration of the atomic beam. The frequency  $\nu_{\text{rf4}}$  can be tuned from 160 MHz to 260 MHz while more than 30 mW of light can be obtained.

The AOM's in this setup can also be used for fast switching of the light power in the different laser beams. The switching time for the light was faster than

	AOM1	AOM2	AOM3	AOM4
Part No. Supplier	AOM-60 IntraAction Corp., USA	MT-350-AO, AA-OPTO- ELECTRONIC, France	TH-200-50 BRIMOSE Corp., USA	TH-200-50 BRIMOSE Corp., USA
Modulation frequency [MHz]	60	300 – 500	130 – 280	160 – 260
Purpose	active beam splitter	frequency stabilization  $\nu_1$	trapping laser detuning $\Delta\nu_1^t$	slowing laser detuning $\Delta\nu_1^s$

**Table 4.3:** The relevant frequencies and power ratios can be controlled easily by the modulation frequencies and the power applied to the four AOM's.

1  $\mu$ s. The power, frequency detuning and the time structure of the three laser beams near wavelength  $\lambda_1$  can be controlled independently by this setup.

## 4.2.2 Stabilization of the Lasers

Power stabilization can be implemented for all laser beams behind one of the AOM's. The diffracted power is monitored on a photodiode. An error signal is generated by subtracting a set point voltage from the photodiode signal voltage. This error signal is fed into a phase detector, which acts as a variable attenuator for the rf power which drives the AOM. Only the trapping laser beams are power stabilized rather than the output of the dye laser. The dye laser output has power fluctuations within 3 – 4%. This is reduced to below 1% with stabilization. The power stabilization of the light is essential for probing the velocity distribution in the atomic beam. The output power of the fiber lasers and the diode lasers are stable to better than 0.5% and need no further stabilization.

The distributed feedback diode laser at wavelength  $\lambda_{\text{IR}3}$  drifts far less in its frequency ( $< 10$  MHz/h) than the fiber lasers in a temperature controlled environment. The frequency offset for each pair of lasers at the wavelengths  $\lambda_{\text{IR}2}$  and  $\lambda_{\text{IR}3}$  is stabilized. At wavelength  $\lambda_{\text{IR}2}$  the laser frequency is locked to the frequency of the fiber laser. At wavelength  $\lambda_{\text{IR}3}$  the frequency of the fiber laser is stabilized to the diode laser frequency. For each laser pair about 150-200  $\mu$ W of light is split off. The resulting beams are overlapped on a beam splitter (see Fig.

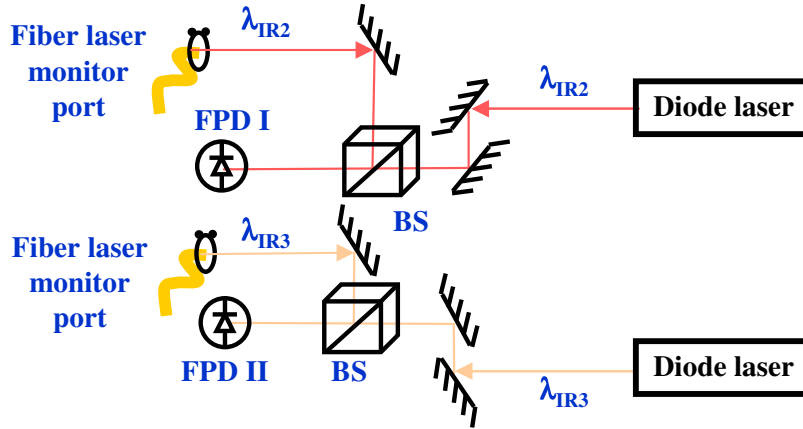


Fig. 4.4: Schematics for generating beat notes at the wavelengths  $\lambda_{\text{IR}2}$  and  $\lambda_{\text{IR}3}$ .

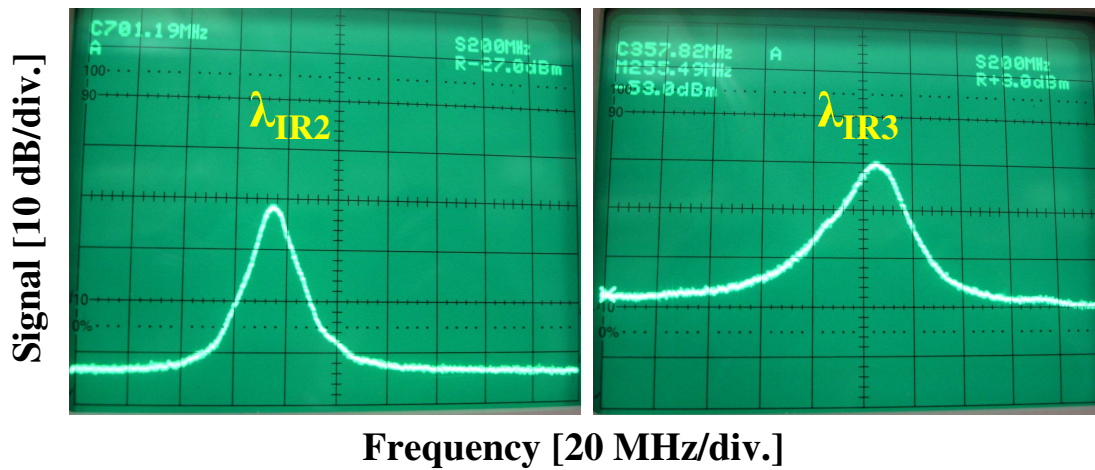


Fig. 4.5: Photographs of the typical beat note signals between two laser beam pairs at the wavelengths  $\lambda_{\text{IR}2}$  and  $\lambda_{\text{IR}3}$ . The estimated width of the beat note spectrum at wavelength  $\lambda_{\text{IR}2}$  is 18(2) MHz and at wavelength  $\lambda_{\text{IR}3}$  it is 24(2) MHz. The signal-to-noise ratio (S/N) is about 30 dB with 1 MHz resolution bandwidth.

	$\lambda_{\text{IR3}}$	$\lambda_{\text{IR2}}$
Signal amplitude	-68 dBm	-27 dBm
PD output across 50 $\Omega$	3.5 mV	8.7 mV
FWHM of typical spectrum	35(5) MHz	20(5) MHz

**Table 4.4:** General characteristics of the beat notes at the wavelengths  $\lambda_{\text{IR3}}$  and  $\lambda_{\text{IR2}}$ .

4.4). The combined beams are focussed onto a fast FGA04 InGaAs photodiode (from Thorlabs Inc., NJ, USA) to detect the beat note signal (see Fig. 4.5). The beat note signal depends on the intensities,  $I_a$  and  $I_b$ , of the two laser beams, the angle,  $\phi$ , between the directions of polarization of both beams, the frequency offset,  $\Delta\nu_{\text{BN}}$ , between the two lasers and the angle,  $\theta$ , between the two beams. The intensity of the two superimposed co-propagating beams at  $\theta = 0^\circ$  is

$$I(t) = (I_a + I_b) + 2\sqrt{I_a I_b} \cdot \cos \phi \cdot \cos (2\pi \Delta\nu_{\text{BN}} t), \quad (4.7)$$

where  $t$  is the time [162]. The photodiode detects the time dependent intensity  $I(t)$ . At parallel polarization of the two laser beams the ac part of the photodiode signal carries information only about the frequency difference  $\Delta\nu_{\text{BN}}$ , i.e., the beat note. The typical parameters of the radio frequency (rf) signal from these diodes are given in Table 4.4. The signals are amplified and split into two parts each. One is fed into a frequency counter which can be read by the data acquisition system. The other part can be exploited for frequency offset locking [161]. For this, the signal  $\Delta\nu_{\text{BN}}$  is feed to a phase locked loop (PLL) circuit on a ADF4007 evaluation board (from Analog Devices Inc., MA, USA). The frequency offset between  $\Delta\nu_{\text{BN}}$  and a reference frequency is converted by the ADF4007 evaluation board into a voltage which is proportional to the frequency deviation. This signal can be used as an error signal as an input to a PID controller. The control voltage is fed to one of the lasers to keep the frequency difference  $\Delta\nu_{\text{BN}}$  constant [163].

### 4.2.3 Optics Layout

The interaction of the atoms with laser beams at the different wavelengths is achieved by spatial overlapping of the individual laser beams (see Fig. 4.6). This is done for several combinations of laser wavelengths. Each pair of infrared laser beams at the wavelengths  $\lambda_{\text{IR2}}$  and  $\lambda_{\text{IR3}}$  is combined with a high efficiency dichroic mirror PRA-1500-90-1037/BBAR-1050-1600 (from CVI Laser Optics, NM, USA)

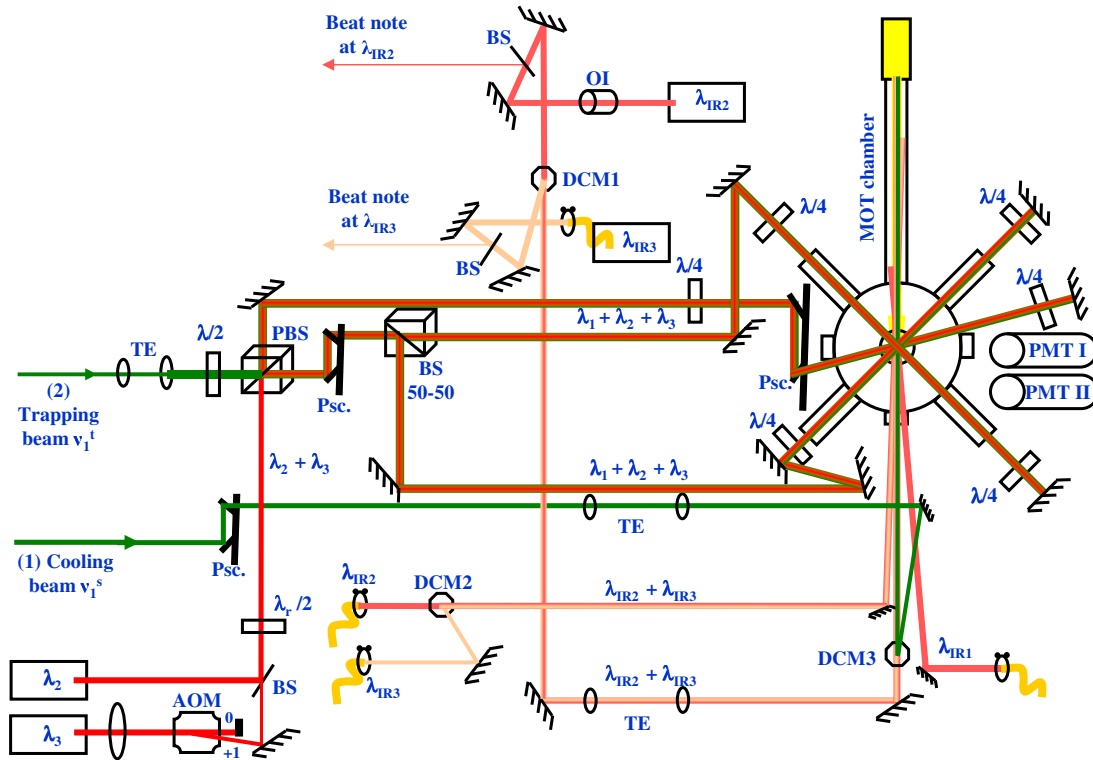


**Fig. 4.6:** Optics arrangement for overlapping nine laser beams of different frequencies. AOM - acousto optic modulator, BS - beam splitter, DCM - dichroic mirror, FPD - fast photodiode,  $\lambda/2$  and  $\lambda_r/2$  - half wave plates,  $\lambda/4$  - quarter wave plate, OI - optical isolator, PBS - polarizing beam splitter, PD - photodiode, Psc. - periscope, PMT - photomultiplier tube, TE - telescope. The drawing is not to scale.

(see Fig. 4.6). These beam splitters are coated such that 75 % of the power at wavelength  $\lambda_{IR3}$  is reflected and 85 % of the power at wavelength  $\lambda_{IR2}$  is transmitted for small incidence angles. The combined laser beams from DCM1 are overlapped with the slowing laser beam at wavelength  $\lambda_1$  on another dichroic mirror PRA-532-98-1037/BBAR-1050-1600 (from CVI laser optics, MN, USA). It reflects 85% at wavelength  $\lambda_1$  and transmits 80% of the power at the wavelengths  $\lambda_{IR2}$  and  $\lambda_{IR3}$ . Two telescopes provide for changing the beam diameters and divergences independently.

The laser beams at wavelength  $\lambda_{IR1}$  and the combined laser beams at the wavelengths  $\lambda_{IR2}$  and  $\lambda_{IR3}$  are brought into the vacuum chamber at a shallow angle with respect to the slowing laser beam. The laser beams at the wavelengths  $\lambda_2$  and  $\lambda_3$  are combined on a beam splitter and are overlapped with the trapping laser beam on a polarizing beam splitter cube. The alignment of all laser beams

relative to each other is crucial for the performance of such experiments, where multiple atomic transitions are involved. The tolerance for overlapping all the laser beams is about 0.5 mm, which is about 1/3 of the trapped cloud diameter.

The vacuum chamber, all lasers and all the optics are mounted on a honeycomb structured optics table (from Newport Corp., CA, USA) with pneumatic damping to isolate the setup from mechanical vibrations. The volume above the table is enclosed by plastic curtains and a continuous laminar air flow from the top cover protects the setup from dust.

### 4.3 Fluorescence Detection

The fluorescence from the atomic beam or from trapped atoms can be detected by two R7205-01 (from Hamamatsu Corp., Shizuoka, Japan) photomultiplier tubes. Narrow band interference filters FB410-10 or FB550-10 (from Thorlabs Inc., NJ, USA) are mounted in front of the photomultipliers to select the fluorescence at the wavelengths  $\lambda_B$  or  $\lambda_1$ . Both photomultipliers have the same field of view.

The imaging system (see Fig. 4.7) consists of a plano-convex lens of focal length  $f = 60$  mm, mounted close to an optical vacuum window (see Fig. 4.1). The lens is at a distance of 135(5) mm from the trap center and collects fluorescence with a solid angle  $\Omega = 4.2 \cdot 10^{-3}$  sr. An aperture is placed at the position of the image plane 155(5) mm downstream of the collection lens. The magnification of the imaging system is 1.20(7). The light transmitted through the aperture is collimated by a lens of focal length  $f = 30$  mm at 30 mm distance from the image  $O'$ . A beam splitter is used to illuminate both photomultipliers simultaneously.

The detection efficiency,  $\epsilon_i$ , at a particular wavelength,  $\lambda_i$  ( $i = 1, B$ ), depends on the solid angle,  $\Omega$ , for the light collection, the splitting fraction  $\epsilon_{BS} = 1 : 2.4$  of the beam splitter in front of the photomultipliers, the transmission,  $\epsilon_f$ , through the interference filters and the quantum efficiency of the photomultiplier cathode,  $\epsilon_i(\lambda_i)$ , at the wavelength  $\lambda_i$

$$\epsilon_i = \Omega \cdot \epsilon_{BS} \cdot \epsilon_f \cdot \epsilon_i(\lambda_i). \quad (4.8)$$

The transmission of both interference filters is  $\epsilon_f = 52(2)$  %. In most of the measurements PMT-I was used with a filter transmitting wavelength  $\lambda_B$ , which gives an efficiency of  $\epsilon_B = 8(1) \cdot 10^{-5}$  and PMT-II with a filter for wavelength  $\lambda_1$  resulting in an efficiency of  $\epsilon_1 = 10(1) \cdot 10^{-5}$ .

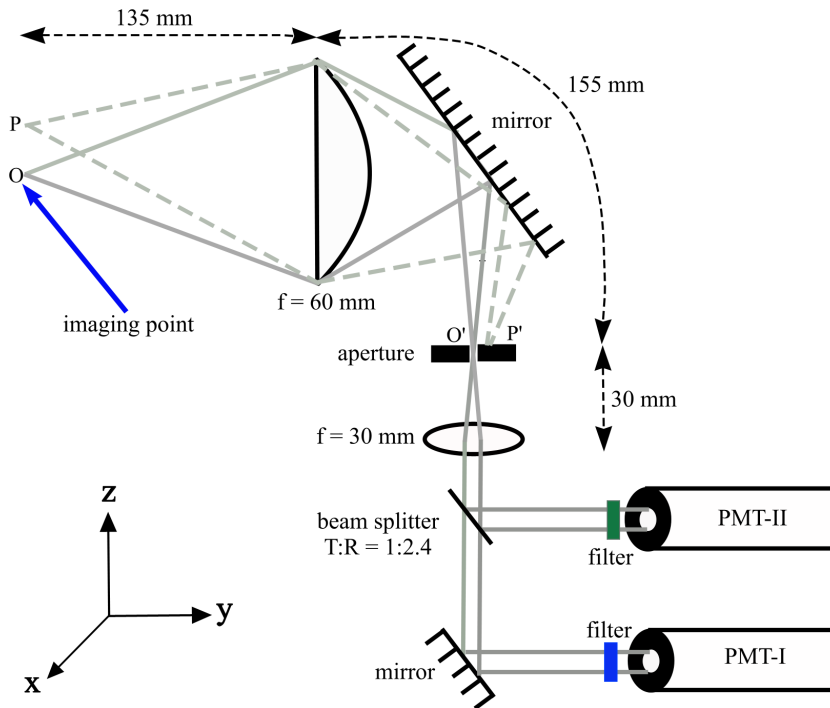


**Fig. 4.7:** Schematics of the optics arrangement for imaging the fluorescence signal onto the photomultiplier photocathodes. The magnification of the imaging system is 1.20(7). The beam splitter transmits about 30% and reflects about 70% of the collected fluorescence light. The imaging volume can be changed by changing the size of the aperture.

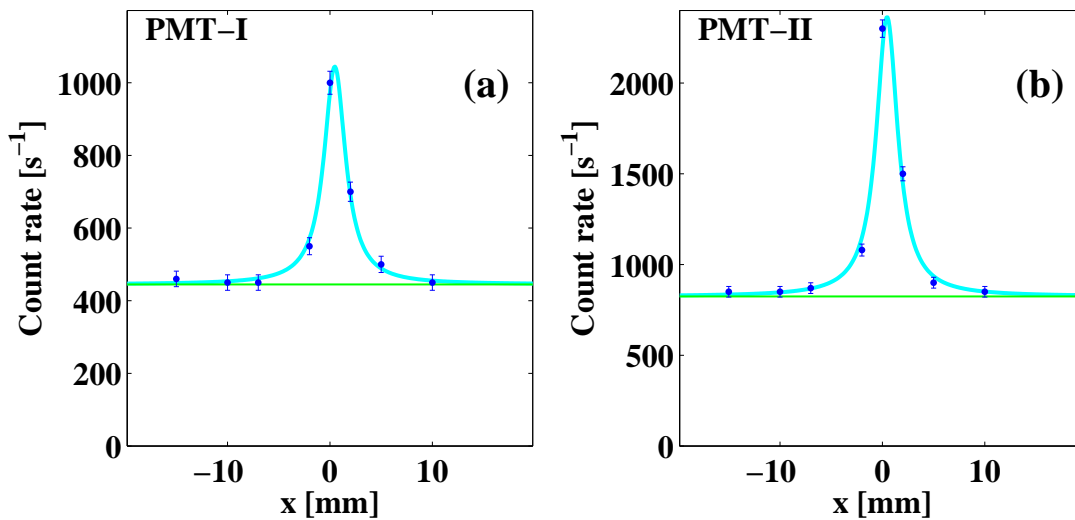


**Fig. 4.8:** Spatial acceptance of fluorescence with an aperture size of 2 mm. The fitted width to the spectra is 2.5(2) mm and the signal ratio in PMT-I and PMT-II is 1 : 2.4(2). The horizontal line corresponds to scattered background photons.

The relative efficiencies and the field of view for the two photomultipliers were verified with the fluorescence signal from the atomic beam. A weak probe beam at wavelength  $\lambda_1$  along the z-axis intersected the atomic beam orthogonally. The position of the probe beam was moved in the x-direction, i.e., along the atomic beam direction of propagation, while the fluorescence at wavelength  $\lambda_1$  was detected on both photomultipliers simultaneously without filters in front of the PMT's. The count rate ratio was 1 : 2.4(2) and the width of the signal was 2.5(2) mm (see Fig. 4.8). Both figures agree well with the design values of the imaging system.

## 4.4 Data Acquisition

The control of the laser frequencies, the readout of the photomultiplier rates and the beat note frequencies is based on GPIB (General Purpose Interface Bus) devices, which are connected via a 488-USB interface (from ICS Electronics, CA, USA) to a personal computer. The scan parameters can be selected and the spectra can be stored for further analysis with a control programme written in C++. The schematics of the control devices and the readout setup are given in Fig. 4.9. Four frequency counters read the beat note frequencies and the count rates from the photomultiplier tubes. All lasers can be set and scanned in their frequencies with 8 analog voltages from a DAC (Digital to Analog Converter) device SR-245 (from Stanford Research Systems Inc., Palo Alto, USA).

## 4.5 Magnetic Field

The quadrupole magnetic field is generated by a pair of coils with identical dimensions separated by a distance (for dimensions see Table 4.5). Both coils carry a current in opposite relative direction (close to anti-Helmholtz configuration). The coils are made from copper wire of 2 mm diameter wound onto aluminium frames. The coils are mounted outside the vacuum chamber along the z-axis and orthogonal to the atomic beam (see Fig. 4.10). The power dissipation at their maximum current of 20 A is about 350 W. The coils are air cooled by a fan unit.

The calculated field gradients produced by the coils along the z-axis and in the radial directions (xy-plane) are  $\alpha_z = 1.85(5) \text{ G cm}^{-1}\text{A}^{-1}$  and  $\alpha_{x,y} = 0.88(2) \text{ G cm}^{-1} \text{ A}^{-1}$  within the trapping volume (see Figs. 4.11 and 4.12). In the MOT, the magnetic field is important only within the trapping volume defined by the

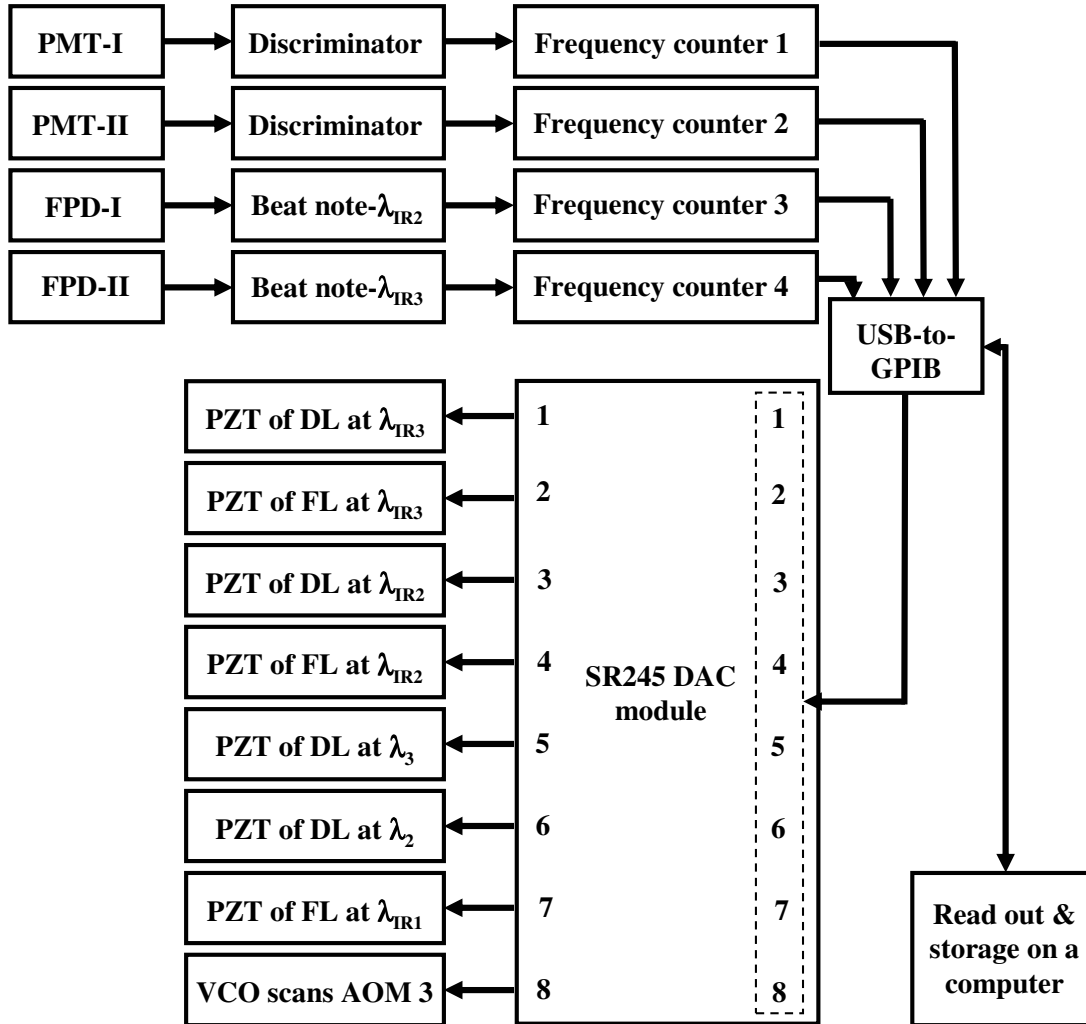


**Fig. 4.9:** Block diagram of the control and data acquisition system. Four frequency counters count the discriminator pulse rates and offset frequencies of the laser pairs at wavelength  $\lambda_{IR2}$  and  $\lambda_{IR3}$  measured via beat notes. The lasers can be scanned with voltage from Digital to Analog Converter channels connected to the laser analog scan inputs. An USB-to-GPIB interface connects the counters and DAC to a personal computer.

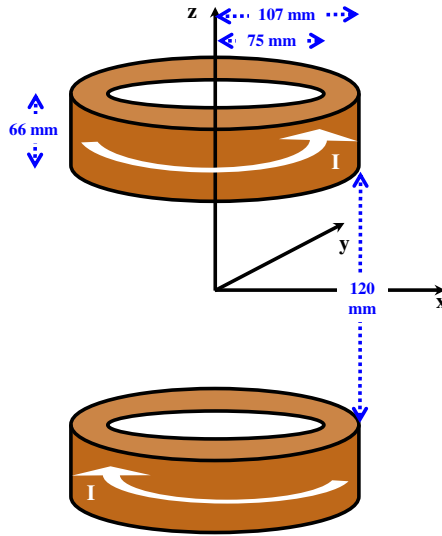


**Fig. 4.10:** Schematics of the coils, which produce a quadrupole magnetic field. The axis of the coils is defined as the z-direction, the atomic beam is propagating along the x-direction. The dimensions of the coils are indicated. The drawing is not to scale.

diameters of the laser beams.

The numerical magnetic field calculation for the coils arranged close to Helmholtz configuration (see Appendix A) was compared with the measured Zeeman splitting of the  $6s^2\ ^1S_0 \rightarrow 6s6p\ ^1P_1$  transition at wavelength  $\lambda_1$ . The ground state  $6s^2\ ^1S_0$  has no Zeeman splitting and the excited state  $6s6p\ ^1P_1$  has three magnetic sub-levels  $m_j = 0, \pm 1$  with the g-factors  $g_j = 1$ . With excitation transverse to the field and along the magnetic field axis the fluorescence was detected radially along the y-direction. This selects only  $\sigma^+$  ( $\Delta m_j = +1$ ) and  $\sigma^-$  ( $\Delta m_j = -1$ ) transitions (see Fig. 4.13 a). At a constant magnetic field B the splitting between the  $\sigma^+$  and the  $\sigma^-$  transitions is

$$\Delta\nu(B) = 2 \cdot \frac{\mu_B B}{h}. \quad (4.9)$$

The splitting,  $\Delta\nu(B)$ , for different values of the magnetic field was measured. A linear function can be fitted to the measurements. An offset of 1.3(7) G arises due to magnetization of the table and environmental stray fields. The calibration constant of the coils is 6.37(6) G/A (see Fig. 4.13 b) which is in good agreement with the calculated value of 6.6(2) G/A. The uncertainty of the calculation arises from the mechanical tolerances of the coils.

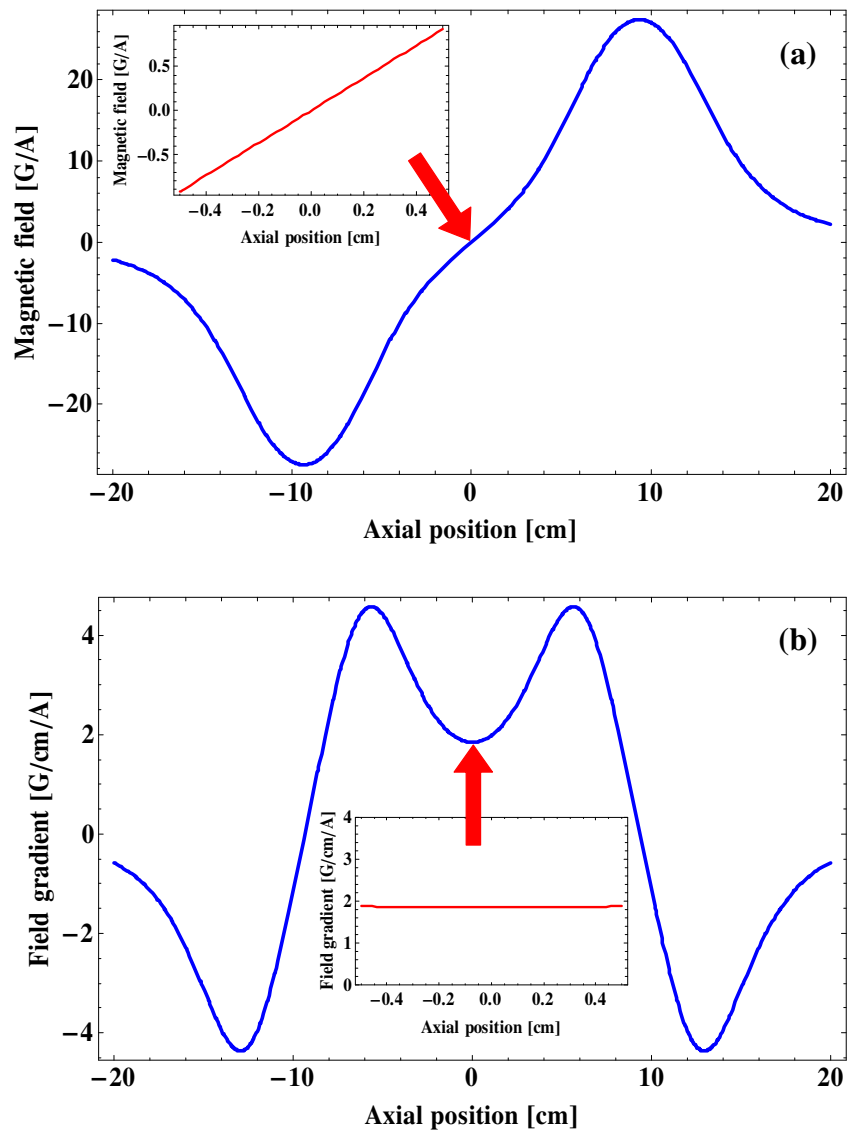


**Fig. 4.11:** (a) Magnetic field and (b) magnetic field gradient per unit current for the MOT coils. The inset is the typical region where trapping occurs.

Inner radius $R_i$	75(1) mm
Outer radius $R_o$	107(2) mm
Axial separation between two close end of the coils $L$	120.0(5) mm
Height of coils $h$	66(1) mm
Number of turns in each coils $N$	215
Diameter of copper wire $\Phi$	2 mm
Resistance of each coil	0.42(2) $\Omega$
Dumped power in total	150 W

**Table 4.5:** Specification of the MOT coils producing a quadrupole magnetic field for the experiments. Both coils are identical in geometry and wired in anti-Helmholtz configuration.

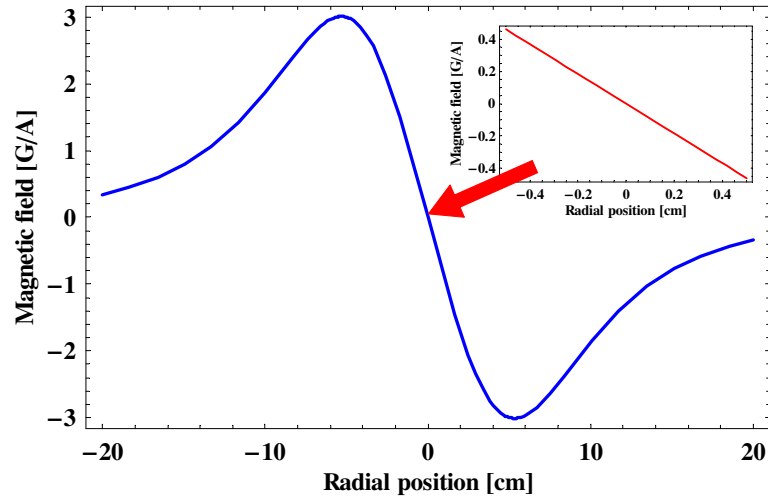


**Fig. 4.12:** Magnetic field produced by the MOT coils along the radial directions, i.e., in the  $xy$ -plane. The inset is the typical region where trapping occurs.

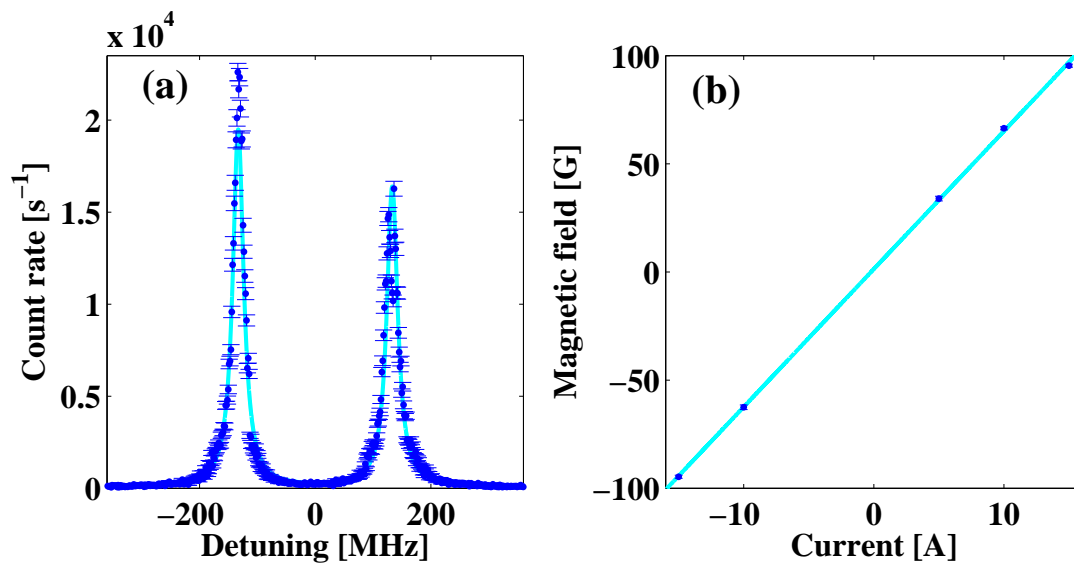


**Fig. 4.13:** Measured (a) Zeeman splitting of the  $6s^2 \ ^1S_0 \rightarrow 6s6p \ ^1P_1$  transition of  $^{138}\text{Ba}$  in a homogenous magnetic field. The different peak heights of the  $\sigma^+$  and the  $\sigma^-$  transitions are due to the spatial acceptance of the PMT. The two resonance appear spatially not symmetric with respect to the detection axis, because of the field offset. The splitting of the lines is  $267(2)$  MHz at a current of 15 A in the coils. (b) Magnetic field according to the Zeeman splitting measurements at various coil currents. The line fitted to the measured data gives a magnetic field calibration of  $B = 6.37(6)$  G/A with an offset  $B_o = 1.3(7)$  G from environmental background.

# Chapter 5

## Laser Cooling of Barium

Light forces arising from the atom-photon interactions are used widely to cool, collect and confine neutral atoms. The known techniques for laser cooling and trapping [164] are described manifold in the literature [165–170]. With the momentum transfer of light the temperature of trapped atoms can be reduced to well below the  $\mu\text{K}$  range. This has been applied for preparing samples for precision measurements of various types including searches for violations of discrete symmetries in weak interactions [171–174] and for synchronizing time to an atomic transition [175–177] as examples.

The bottleneck for laser cooling of barium atoms arises from large leaks in the optical cooling using the  $6s^2\ ^1S_0 \rightarrow 6s6p\ ^1P_1$  transition. The upper state can decay with a relatively large probability to metastable D-states (see Section 3.3.1). Different strategies for the repumping of atoms from these D-states to the cooling transition are possible. One of the possibilities includes repumping of the D-states via the  $6s6p\ ^1P_1$  state of the cooling transition. This method adds further complications due to coherent Raman  $\Lambda$ -transitions [112, 188]. However, it yields a closed 5-level system without additional leak channels.

An alternative possibility is repumping the  $6s5d\ ^3D$ -states via the  $6s5d\ ^3D_1 \rightarrow 5d6p\ ^3D_1^o$  and the  $6s5d\ ^3D_2 \rightarrow 5d6p\ ^3D_1^o$  transitions at the wavelengths  $\lambda_2$  and  $\lambda_3$ . Advantages of this repumping scheme are the strong dipole transitions at the visible wavelengths and the circumvention of the Raman  $\Lambda$ -transitions. The loss to further states from this cooling cycle were determined to  $1.8(2) \cdot 10^{-5}$ . The losses can be as small as  $10^{-6}$  for repumping the  $6s5d\ ^3D_1$  state at wavelength  $\lambda_2$  and the  $6s5d\ ^3D_2$  state at wavelength  $\lambda_{\text{IR}2}$ .

Deceleration of a thermal barium atomic beam was optimized for producing a large flux at velocities below 50 m/s. It depends on intensities and frequency

detunings of all lasers. A large fraction of the decelerated atoms remain in the metastable  $6s5d\ ^3D$ -states. Their velocity distribution was studied with excitation at the wavelengths  $\lambda_2$  and  $\lambda_3$ , which is followed by emission of photons at wavelength  $\lambda_B$ . These measurements yield an estimate of the achieved average deceleration. The decelerated atomic beam can be used to load atoms into a magneto-optical trap.

## 5.1 Decay Branching of the $5d6p\ ^3D_1^o$ State

The  $6s5d\ ^3D_1 \rightarrow 5d6p\ ^3D_1^o$  and the  $6s5d\ ^3D_2 \rightarrow 5d6p\ ^3D_1^o$  transitions are three orders of magnitude stronger than the weak  $6s5d\ ^3D_1 \rightarrow 6s6p\ ^1P_1$  intercombination transition (see Fig. 3.3). They can be driven with low light power from diode lasers. The decay branching of the  $5d6p\ ^3D_1^o$  state is not known accurately. The main decay channels are to the  $6s5d\ ^3D_1$  and the  $6s5d\ ^3D_2$  states (see Chapter 3). The small fraction decaying directly to the ground state  $6s^2\ ^1S_0$  and the fraction decaying to other states  $\zeta$  have been determined. The subsystem of states  $\zeta$  contains the  $5d^2\ ^3F_2$ ,  $5d^2\ ^3P_0$ ,  $5d^2\ ^3P_1$ ,  $5d^2\ ^3P_2$ ,  $5d^2\ ^1D_2$  and  $6s5d\ ^1D_2$  states and the sum of the decay rates is denoted as  $A_\zeta$ . For a quantitative analysis of the branching probabilities the incoming flux,  $F_i$  ( $i = ^3D_1, ^3D_2$ ), of metastable atoms must be the same during all rate measurements. The ratios of the rates are then independent of the absolute flux.

A flux stable metastable atomic beam is produced by optical pumping with a frequency and power stabilized laser beam at wavelength  $\lambda_1$ . The rectangular cross section of the laser beam at wavelength  $\lambda_1$  is  $2 \times 5\text{ mm}^2$  (see Fig. 5.1). The laser beam is orthogonal to the atomic beam. The metastable states are probed by laser beams at the wavelengths  $\lambda_2$ ,  $\lambda_3$  and  $\lambda_{IR1}$  downstream of the production region. Their rectangular cross section is  $5 \times 10\text{ mm}^2$  to cover the full size of the metastable atomic beam. The probe laser beams are parallel to the laser beam at wavelength  $\lambda_1$ . A photomultiplier detects the fluorescence from the probing region at the wavelengths  $\lambda_1$  and  $\lambda_B$ . The 5 mm separation between the two sets of laser beams is sufficient to suppress the fluorescence at wavelength  $\lambda_1$  from the production region.

The maximum laser powers are  $P_{\max}(\lambda_2) = 6.5(3)\text{ mW}$  at wavelength  $\lambda_2$  and  $P_{\max}(\lambda_3) = 17.5(5)\text{ mW}$  at wavelength  $\lambda_3$ . The saturation intensities of the atomic transitions are  $4\text{ mW/cm}^2$  and  $4.2\text{ mW/cm}^2$  respectively. The fluorescence rates become independent of the laser intensity, if the population in the respective

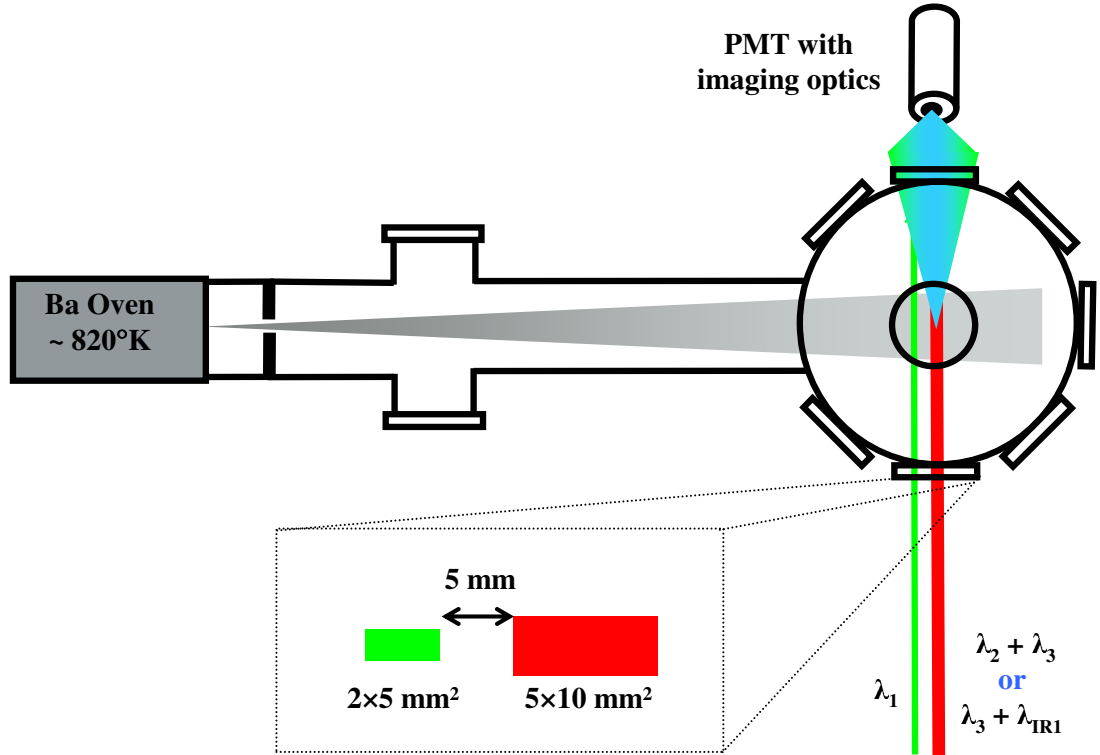


**Fig. 5.1:** A laser beam of cross-section  $2 \times 5 \text{ mm}^2$  at wavelength  $\lambda_1$  produces a metastable atomic beam of known cross section. The atoms pass in a second interaction region 5 mm downstream through a combined set of laser beams at the wavelengths  $\lambda_2$  and  $\lambda_3$  or at wavelength  $\lambda_3$  and  $\lambda_{\text{IR1}}$ . The laser beam cross-section there is  $5 \times 10 \text{ mm}^2$  and larger than the extension of the metastable beam. Fluorescence at wavelength  $\lambda_1$  and  $\lambda_B$  from that region is detected.

metastable state is fully depleted. Then, the fluorescence signals are only proportional to the flux of metastable atoms and independent of other experimental conditions. The solid angle,  $\Omega$ , for the fluorescence detection is identical for all measurements because the same photomultiplier is used.

### 5.1.1 Decay Branching Ratios

From a set of measurements of the signal rates,  $R_i^j$  (see Table 5.1), one can determine the decay branching ratios of the  $6s6p \ ^1P_1$  state to the  $6s5d \ ^3D$ -states and of the  $5d6p \ ^3D_1^o$  state to the ground  $6s^2 \ ^1S_0$  and other states  $\zeta$ . The signal rates  $R_i^j$  are proportional to the fluxes  $F_{3D_1}$  and  $F_{3D_2}$  of the metastable states, the partial decay rates  $A_i$ , and the detection efficiencies of the photomultiplier  $\varepsilon_1$  and  $\varepsilon_B$  at the wavelengths  $\lambda_1$  and  $\lambda_B$ . The subscript of the decay rates,  $A_i$ , refers

Laser wavelength	Detected photons	Rate of the detected signal
$\lambda_2$	$\lambda_B$	$R_2^B$
$\lambda_3$	$\lambda_B$	$R_3^B$
$\lambda_2 + \lambda_3$	$\lambda_B$	$R_{2+3}^B$
$\lambda_3 + \lambda_{IR1}$	$\lambda_B + \lambda_1$	$R_{3+IR1}^{B+1}$

**Table 5.1:** The combination of laser beams in the second interaction region and corresponding fluorescence signal rates at various wavelengths. The subscript  $i$  in the signal rates  $R_i$  refers to the wavelength  $\lambda_i$  of the driving transitions. The superscript of  $R^j$  refers to wavelength  $\lambda_j$  of the detected photons.

to the transition wavelengths  $\lambda_i$  (see Fig. 3.3). The signal rates are

$$R_2^B = F_{3D_1} \cdot \frac{A_B}{(A_3 + A_\zeta + A_B)} \cdot \varepsilon_B, \quad (5.1)$$

$$R_3^B = F_{3D_2} \cdot \frac{A_B}{(A_2 + A_\zeta + A_B)} \cdot \varepsilon_B, \quad (5.2)$$

$$R_{2+3}^B = (F_{3D_2} + F_{3D_1}) \cdot \frac{A_B}{(A_\zeta + A_B)} \cdot \varepsilon_B, \quad (5.3)$$

$$R_{3+IR1}^{B+1} = (1 - B_{IR}) \cdot \left[ F_{3D_1} + F_{3D_2} \cdot \frac{A_2}{A_2 + A_\zeta + A_B} \right] \cdot \varepsilon_1 + R_3^B, \quad (5.4)$$

where  $B_{IR}$  is a small correction due to the branching from the  $6s6p \ ^1P_1$  state to the metastable D-states. To first order one has

$$B_{IR} = \frac{A_{IR2} + A_{IR3}}{(A_1 + A_{IR2} + A_{IR3})}. \quad (5.5)$$

The branching ratios can be extracted from the measured signal rates  $R_i^j$  as they are described in Eqns. 5.1 to 5.4. The ratio of  $R_3^B$  and  $R_2^B$  yields the ratio of the fluxes  $F_{3D_2}$  and  $F_{3D_1}$ , which is identical with the branching ratio between  $A_{IR2}$  and  $A_{IR1}$

$$\frac{F_{3D_2}}{F_{3D_1}} = \frac{A_{IR2}}{A_{IR1}} = \left( \frac{R_3^B}{R_2^B} \right) \cdot \frac{(A_2 + A_\zeta + A_B)}{(A_3 + A_\zeta + A_B)}. \quad (5.6)$$

The ratio of populations,  $N_{3D_2}$  and  $N_{3D_1}$ , in the  $6s5d \ ^3D_2$  and the  $6s5d \ ^3D_1$  states are same as the ratio of fluxes  $F_{3D_2}$  and  $F_{3D_1}$  because the production of metastable atoms are constant.

The ratio of  $R_{2+3}^B$  and  $R_3^B$  yields the sum of the decay rates  $A_B$  to the ground state  $6s^2 \ ^1S_0$  and  $A_\zeta$  to the states  $\zeta$

$$(A_\zeta + A_B) = A_2 \cdot \left[ \frac{R_{2+3}^B}{R_3^B} \cdot \left( 1 + \frac{A_{IR1}}{A_{IR2}} \right)^{-1} - 1 \right]^{-1}. \quad (5.7)$$

Taking the ratio of  $R_{3+IR1}^{B+1}$  and  $R_3^B$  yields the branching of the 5d6p  $^3D_1^\circ$  state to the ground state  $6s^2 \ ^1S_0$

$$A_B = (1 - B_{IR}) \cdot \frac{\varepsilon_1}{\varepsilon_B} \cdot \left[ \frac{R_3^B}{R_{3+IR1}^{B+1}} - 1 \right]^{-1} \left[ A_2 + \frac{A_{IR1}}{A_{IR2}} \cdot (\tau_{3D1^\circ}^{-1} - A_3) \right], \quad (5.8)$$

where  $\tau_{3D1^\circ}$  is the lifetime of the 5d6p  $^3D_1^\circ$  state. In Eqn. 5.8,  $(A_2 + A_\zeta + A_B)$  is replaced with  $(\tau_{3D1^\circ}^{-1} - A_3)$ . The relative detection efficiency,  $\frac{\varepsilon_1}{\varepsilon_B}$ , has been measured for the particular photomultiplier (see Appendix B).

The branching to the states  $\zeta$  can be extracted by subtracting Eqn. 5.8 from Eqn. 5.7. The fact that the decay rates  $A_B$  and  $A_\zeta$  are small compared to  $A_2$  and  $A_3$  is exploited. The decay rates  $A_{IR1}$ ,  $A_{IR2}$  and the lifetime  $\tau_{3D1^\circ}$  were taken as input from published data (see Table 3.4).

## 5.1.2 Measurements

The fluorescence rates  $R_i^j$  were recorded for different laser intensities. As an example, the depletion of the 6s5d  $^3D_1$  state as a function of the intensity  $I_{IR1}$  is displayed in Fig. 5.2. Light at the wavelengths  $\lambda_{IR1}$  and  $\lambda_3$  is used to deplete the 6s5d  $^3D_1$  and 6s5d  $^3D_2$  states. Fluorescence was detected at wavelength  $\lambda_1$ . The laser light at wavelength  $\lambda_3$  was kept on resonance, while the laser light at wavelength  $\lambda_{IR1}$  was scanned in frequency. The measurement was repeated for ten different laser intensities  $I_{IR1}$  at wavelength  $\lambda_{IR1}$ . The signal rate  $R_{IR1+3}^1$  saturates with  $I_{IR1}$ . This specific transition is the weakest one studied in this work.

Typically two laser frequencies were scanned simultaneously to measure the signal rates. By doing this a two dimensional spectrum is obtained, which contains the signal rates at the individual resonances together with the signal rate when both lasers frequencies are on resonance (see Fig. 5.3). The depletion of the metastable states is observed by observing the saturation of the signal rates with laser intensity (see Fig. 5.4). The largest fractional uncertainty arises from  $R_2^B$  because of the small population of the 6s5d  $^3D_1$  state due to the weak branching fraction to this state. The rate  $R_{2+3}^B$  saturates at higher laser beam intensities

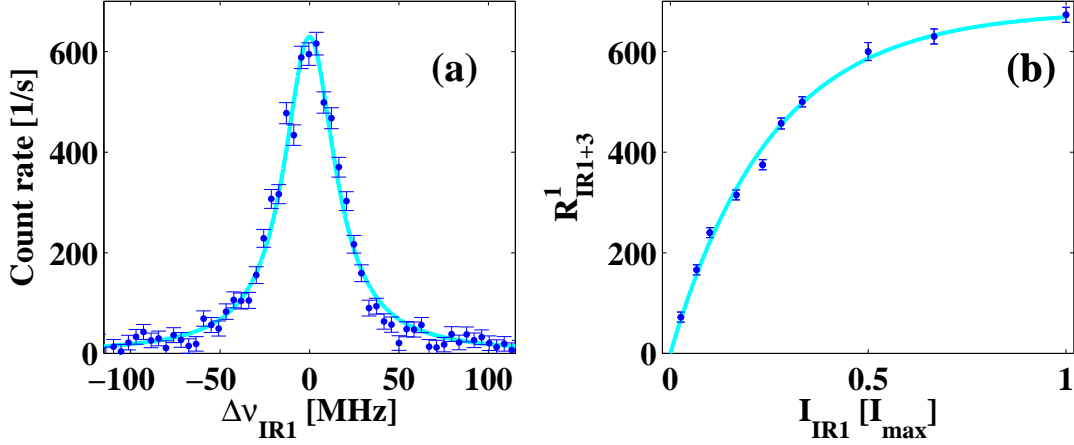


**Fig. 5.2:** (a) Resonance of the  $6s5d\ ^3D_1 \rightarrow 6s6p\ ^1P_1$  transition at wavelength  $\lambda_{IR1}$ . The light power of the laser beams was 80(5) mW. (b) Fluorescence from the  $6s6p\ ^1P_1 \rightarrow 6s^2\ ^1S_0$  transition, i.e., probability of emptying the  $6s5d\ ^3D_1$  state at different powers of the laser beam at wavelength  $\lambda_{IR1}$ . The maximum power in the laser beam was  $P_{\max}(\lambda_{IR1}) = 120(5)$  mW.

Measurement - I	Countrate [ $s^{-1}$ ]
$R_2^B$	$157 \pm 6$
$R_3^B$	$1712 \pm 37$
$R_{2+3}^B$	$28950 \pm 1160$
Measurement - II	Countrate [ $s^{-1}$ ]
$R_3^B$	$228 \pm 10$
$R_{3+IR1}^{B+1}$	$1110 \pm 45$

**Table 5.2:** Signal rates in the branching ratio measurement.

than the laser beam intensities needed to saturate the individual rates  $R_2^B$  and  $R_3^B$  (see Fig. 5.4), because shuffling of atoms between the  $6s5d\ ^3D_1$  and the  $6s5d\ ^3D_2$  states requires on average 25 scattered photons at the wavelengths  $\lambda_2$  and  $\lambda_3$  to deplete both of these states. The signal rates  $R_{IR1}^1$  and  $R_{3+IR1}^{B+1}$  are measured (see Fig. 5.5) by overlapping laser beams at the wavelengths  $\lambda_3$  and  $\lambda_{IR1}$  in the probe region. Both laser frequencies are scanned to produce a two dimensional spectrum. The saturated signal rates are listed in Table 5.2.

The direct decay from the  $5d6p\ ^3D_1^o$  state to the ground state  $6s^2\ ^1S_0$  has a branching ratio of  $A_B \cdot \tau_{3D1^o} = 2.3(2)(1)\%$ , where  $\tau_{3D1^o}$  is the lifetime of the  $5d6p\ ^3D_1^o$  state. The ratio of the populations  $N_{3D_1}$  and  $N_{3D_2}$  in the  $6s5d\ ^3D_1$  and the  $6s5d\ ^3D_2$  states is  $21.1(1.1)(2.5)$ . The first error arises from the uncertainty

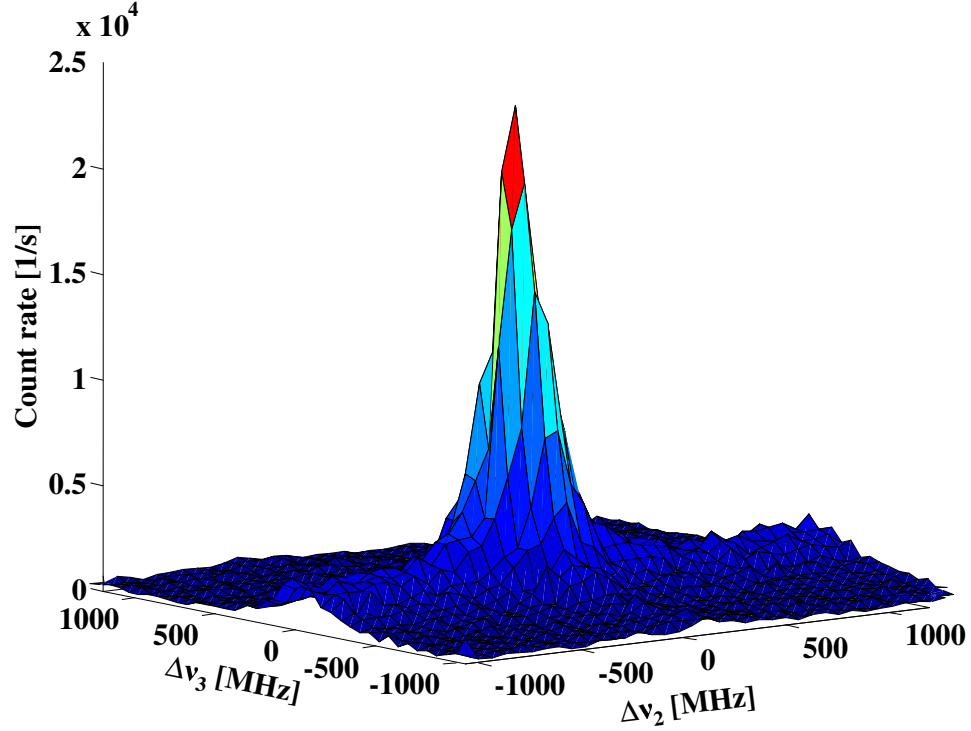


**Fig. 5.3:** Two dimensional plot of the fluorescence rate as a function of the optical frequency detuning  $\Delta\nu_2$  and  $\Delta\nu_3$  from the resonances at the wavelengths  $\lambda_2$  and  $\lambda_3$ . The rate  $R_{2+3}^B$  for both lasers on resonance is much higher than the sum of the individual resonances  $R_2^B$  and  $R_3^B$ .

	Fractional branching (This work)	Fractional branching (Other work)	Equation
$\frac{A_{IR2}}{A_{IR1}}$	21.1(1.1)(2.5)	35(9) [103] 27.7 [91]	5.6
$(A_{\zeta} + A_B) \cdot \tau_{3D1^{\circ}}$	4.3(2)(2) %	4.3(8) % [98]	5.7
$A_B \cdot \tau_{3D1^{\circ}}$	2.3(2)(1) %	2.6(3) % [98]	5.8
$A_{\zeta} \cdot \tau_{3D1^{\circ}}$	2.0(2)(1) %	1.7(7) % [98]	5.7 and 5.8

**Table 5.3:** Decay branching fractions of the  $5d6p\ ^3D_1^{\circ}$  state measured and from the literature. The first error of the values in this work comes from statistics and the second one comes from the uncertainties of  $A_2$  and  $A_3$  in Ref. [98] and  $\tau_{3D1^{\circ}}$  is the lifetime of the  $5d6p\ ^3D_1^{\circ}$  state.

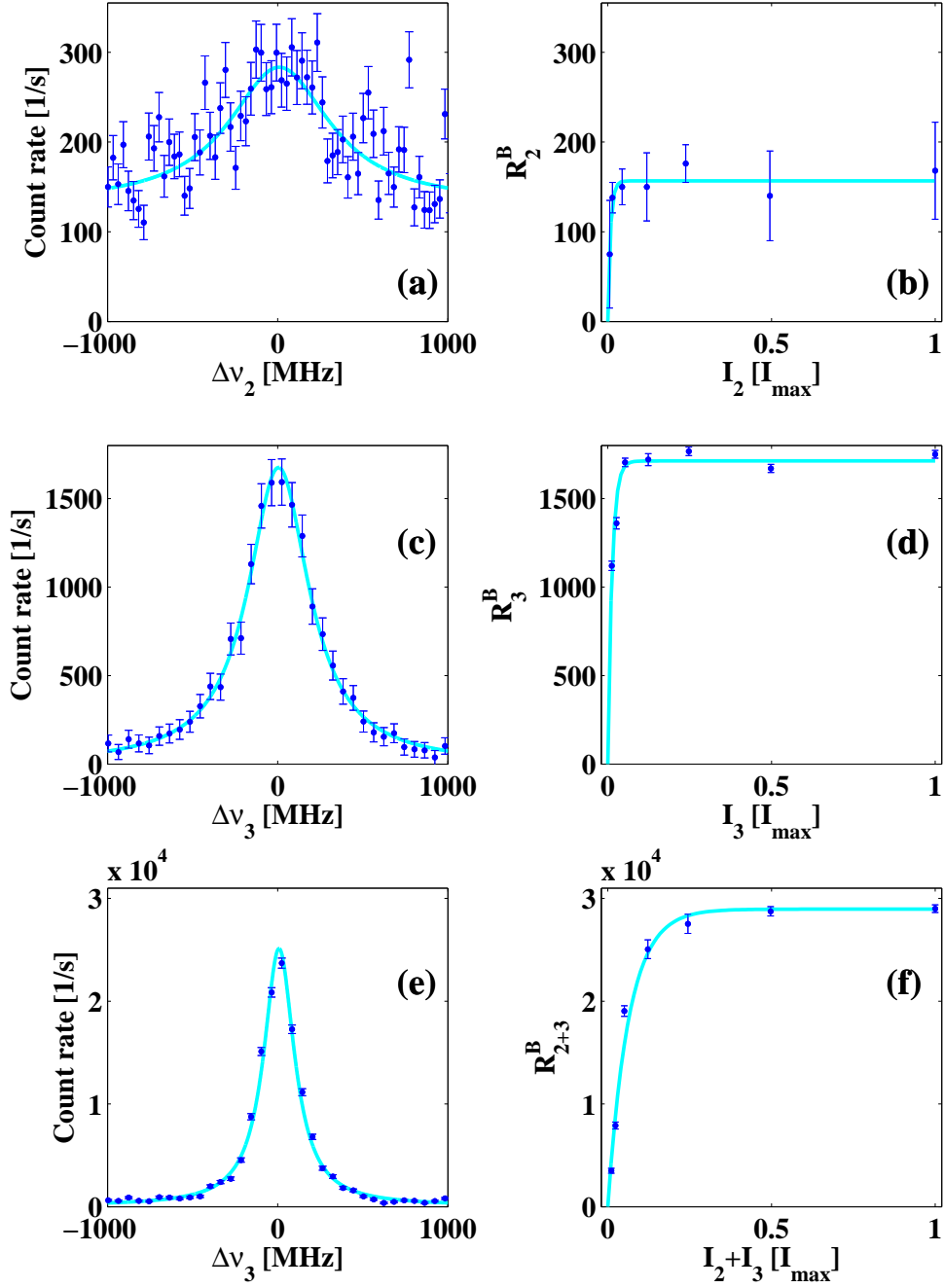


**Fig. 5.4:** Fluorescence spectra of  $5d6p\ ^3D_1^o \rightarrow 6s^2\ ^1S_0$  transition. (a), (c), (e) Signal rates  $R_2^B$ ,  $R_3^B$  and  $R_{2+3}^B$  at different frequency detunings of the lasers at the wavelengths  $\lambda_2$  and  $\lambda_3$ . The spectra were taken at 12% of the maximum intensity  $I_{\max}$  for the lasers at wavelength  $\lambda_2$  and  $\lambda_3$ . (b), (d), (f) The dependence of the population transfer from the  $6s5d\ ^3D_1$  and  $6s5d\ ^3D_2$  states to the  $6s^2\ ^1S_0$  state on the light intensity of the lasers at the wavelengths  $\lambda_2$  and  $\lambda_3$ . The rates saturate exponentially, if the  $6s5d\ ^3D_1$  and  $6s5d\ ^3D_2$  states are empty.

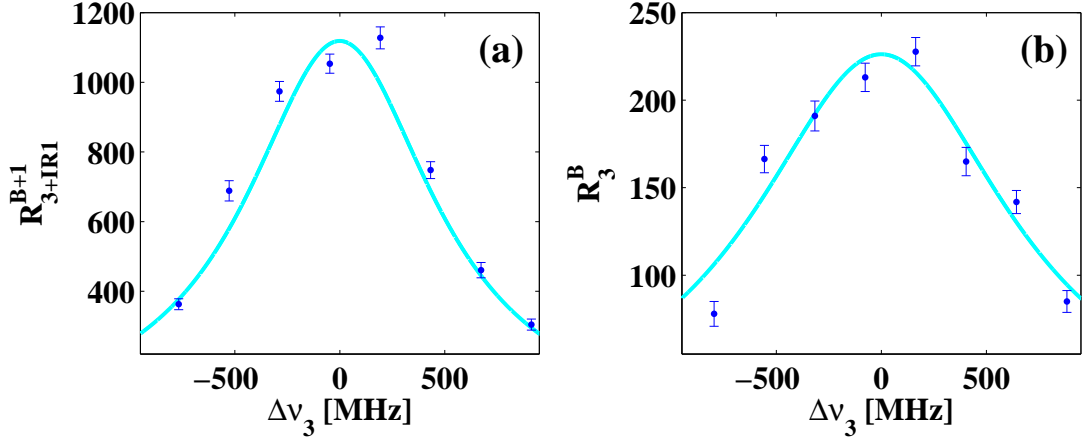


**Fig. 5.5:** (a) Signal rates  $R_{3+IR1}^{B+1}$  as function of the detuning of the laser frequency at wavelength  $\lambda_3$ . (b) Variation of the signal rate  $R_3^B$  at different detuning of the laser frequency at wavelength  $\lambda_3$ .

of the rate measurements and the second error arises from the uncertainties in  $A_2$  and  $A_3$ . The measured ratio of the populations  $N_{3D_1}$  and  $N_{3D_2}$  of 21.1(1.1)(2.5) differs from earlier determinations which yielded 35(9) [103]. The fractional decay to the set of states  $\zeta$  is  $A_\zeta \cdot \tau_{3D1^o} = 2.0(2)(1)\%$ , where the sources for the two uncertainties are the same as above. These results (see Table 5.3) enable a quantitative analysis of laser cooling involving the  $5d6p\ ^3D_1^o$  state.

A laser cooling cycle with lasers at the wavelengths  $\lambda_2$  and  $\lambda_3$  for repumping of the  $6s5d\ ^3D$ -states and a laser at wavelength  $\lambda_{IR3}$  results in a leak rate from the laser cooling cycle of 1 : 55000(6000) assuming that all atoms in the effective states  $\zeta$  are lost. This is about a factor of two better than a cooling cycle with laser light at the wavelengths  $\lambda_1$ ,  $\lambda_{IR2}$  and  $\lambda_{IR3}$ , which serves in this experiment for slowing the atomic beam. A typical scattering rate of  $10^7\ s^{-1}$  from the cooling transition at wavelength  $\lambda_1$  would lead to a loss from the cooling cycle in about 5 ms.

A better repumping scheme for the  $6s5d\ ^3D$ -states can be achieved with laser light at wavelength  $\lambda_2$  for repumping the  $6s5d\ ^3D_1$  state and laser light at wavelength  $\lambda_{IR2}$  for repumping the  $6s5d\ ^3D_2$  state. Here the weak transition at wavelength  $\lambda_{IR1}$  is avoided and most of the  $6s5d\ ^3D_1$  state population is transferred to the  $6s5d\ ^3D_2$  state. The leak rate from the cooling cycle amounts to only 1 : 1200000(200000) because it minimizes the population in the  $5d6p\ ^3D_1^o$  state and the associated losses. This scheme was implemented for trapping.

Theoretical calculations show that the main contribution to  $A_\zeta$  comes from the

decay to the  $5d^2\ ^3F_2$  state for which the lifetime was estimated to be  $190\ \mu\text{s}$  [95]. This  $5d^2\ ^3F_2$  state decays in a cascade to the ground state or other states of the cooling cycle. Properties of the  $5d^2\ ^3F_2$  state could be determined using a trapped sample (see Section 6.3).

## 5.2 Deceleration of the Barium Atomic Beam

Deceleration of an atomic barium beam is achieved by intense counter-propagating laser beams at the wavelengths  $\lambda_1$ ,  $\lambda_{\text{IR}2}$  and  $\lambda_{\text{IR}3}$  (see Fig. 5.6). A red detuned slowing laser beam at wavelength  $\lambda_1$  is combined with two repumping laser beams at the wavelengths  $\lambda_{\text{IR}2}$  and  $\lambda_{\text{IR}3}$ . All the laser beams are focused into the oven orifice by two telescopes. The fixed frequency detuning and finite linewidth of the transition sets a limit on the velocity range for the optical force due to Doppler shifts. The characteristic range for the velocity change is

$$\Delta v_i = \lambda_i \cdot \gamma, \quad (5.9)$$

where  $\lambda_i$  is wavelength of the transition and  $\gamma$  is the decay rate of the upper state in the optical cooling cycle. For the slowing lasers this results in  $\Delta v_1 = 21\ \text{m/s}$ ,  $\Delta v_{\text{IR}2} = 43\ \text{m/s}$  and  $\Delta v_{\text{IR}3} = 57\ \text{m/s}$ .

The velocity distribution is measured via the fluorescence from the  $6s6p\ ^1P_1$  state induced by a probe laser beam at wavelength  $\lambda_1$  (see Fig. 5.7). It intersects with the atomic beam at an angle  $\theta = -45^\circ$  relative to the direction of motion of the atoms. The interaction region is  $0.6\ \text{m}$  downstream of the oven orifice (see Fig. 5.6). The probe laser frequency and the slowing frequency can be controlled independently as well as the power in these beams (see section 4.2). Both these laser beams are frequency and power stabilized. The fluorescence at wavelength  $\lambda_1$  emerging from the interaction region is measured with a photomultiplier.

The velocity of the atoms is determined from their Doppler shift of the  $6s^2\ ^1S_0 \rightarrow 6s6p\ ^1P_1$  transition. The velocity resolution,  $\Delta v_{\text{res}}$ , is given by the characteristic range of velocity change,  $\Delta v_1$ , and the angle  $\theta$ . It is  $v_{\text{res}} = \Delta v_1 \cdot \cos(-\pi/4) = 14.8\ \text{m/s}$ . The increase of the atomic flux at low velocities, i.e., the effectiveness of the slowing process, depends on the frequency detuning and the overlap of all laser beams at the wavelengths  $\lambda_1$ ,  $\lambda_{\text{IR}2}$  and  $\lambda_{\text{IR}3}$ .

The total number of scattered photons,  $N_0(v)$ , from the probe beam depends on the interaction time,  $\Delta t$ , of the laser light with the atoms. The time  $\Delta t$  scales with the inverse of the atomic velocity,  $v$ . The recorded fluorescence spectrum,

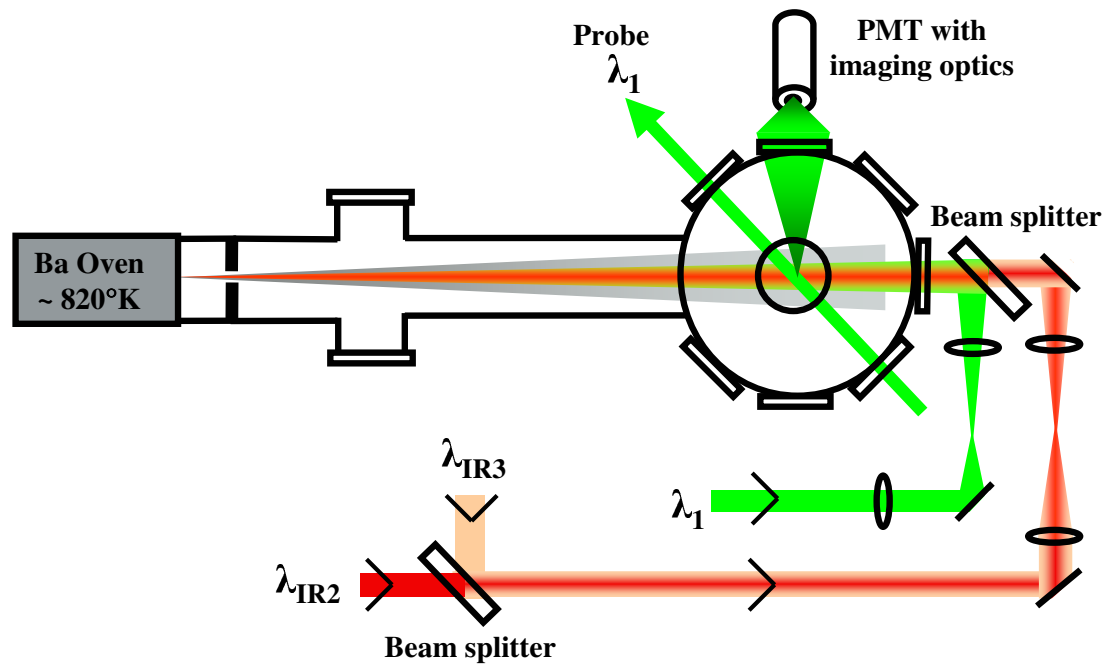


**Fig. 5.6:** Setup for decelerating a barium atomic beam. The overlapped laser beams at the wavelengths  $\lambda_1$ ,  $\lambda_{\text{IR}2}$  and  $\lambda_{\text{IR}3}$  are counter-propagating to the atomic beam. A probe beam crosses the atomic beam at an angle  $\theta = -45^\circ$  to measure the velocity distribution of the atoms. The frequencies of the probe and slowing beams at wavelength  $\lambda_1$  can be changed independently. The fluorescence light from the  $6s6p\ ^1P_1 \rightarrow 6s^2\ ^1S_0$  transition at wavelength  $\lambda_1$  is detected by a photomultiplier tube (PMT).

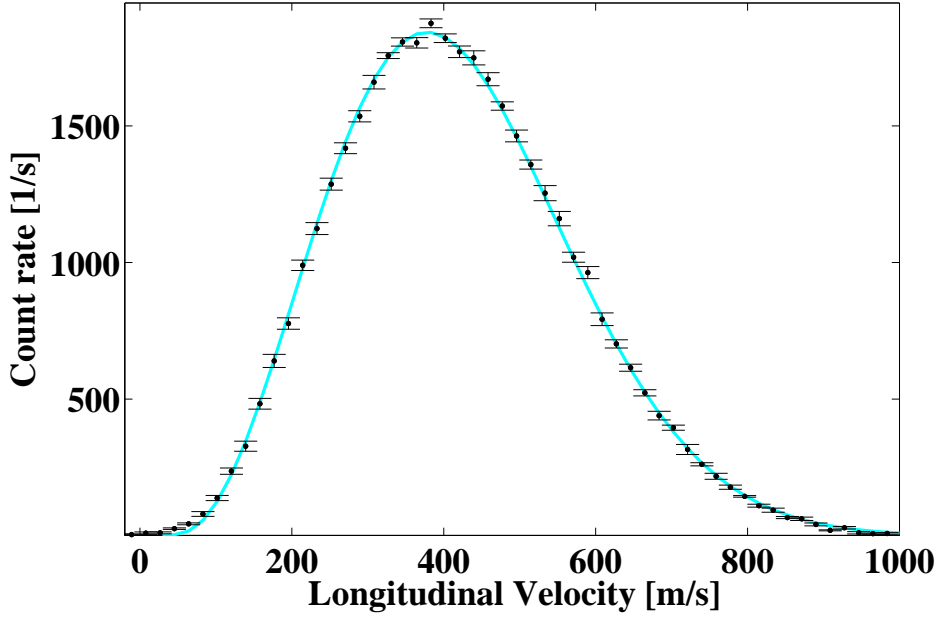


**Fig. 5.7:** Measured velocity distribution of the atomic barium beam from the oven at 820(40) K temperature. A fit yields the mean velocity  $\langle v \rangle = 235(10)$  m/s. The intensity of the probe laser was  $0.35 \cdot I_s$  during this measurement.

$df(v)$ , as a function of the frequency detuning of the probe laser light at wavelength  $\lambda_1$  is different from the velocity distribution,  $\frac{dF_{\text{beam}}}{dv}$ , of atoms in the atomic beam. The fluorescence at a particular velocity is

$$df(v) = \frac{dF_{\text{beam}}}{dv} \cdot N_0(v) \cdot dv, \quad (5.10)$$

where  $N_0(v) = \Delta t \cdot \gamma_1(v)$ ,  $\Delta t = d/v$  is the interaction time with the probe laser beam of diameter  $d$  and  $\gamma_1(v)$  is the velocity dependent scattering rate of the transition at wavelength  $\lambda_1$ . For slow atoms the quantity  $N_0(v)$  is large and leaking to the D-states must be taken into account. This gives

$$N_0(v) = \Delta t \cdot \gamma_1 \left( 1 - \exp\left(-\frac{\Delta t \cdot \gamma_1}{B_c}\right) \right), \quad (5.11)$$

where  $B_c$  represents branching ratio to the D-states (see Table 3.6).

With these corrections a mean velocity of  $\langle v \rangle = 235(10)$  m/s is extracted. This corresponds to a most probable velocity of 400(14) m/s. The measured fraction of atoms in this distribution with velocities smaller than 30 m/s is 0.004(2) %.

### 5.2.1 Cooling Transition

Slowing of a barium atomic beam was already demonstrated in Ref. [112]. This work extracts further details of the slowing process which are relevant to understand the loading into an atom trap. For this, the deceleration is determined as a function of the frequency detuning  $\Delta\nu_1^s$  of the slowing laser light at wavelength  $\lambda_1$  (see Fig. 5.8). During the measurements the powers of the repumping laser beams and the detunings at the wavelengths  $\lambda_{\text{IR}2}$  and  $\lambda_{\text{IR}3}$  were kept constant. The frequency detunings were  $\Delta\nu_{\text{IR}2}^s = -130(12)$  MHz and  $\Delta\nu_{\text{IR}3}^s = -95(10)$  MHz. The dip in the velocity spectra depends on the detuning  $\Delta\nu_1^s$  of the slowing laser frequency. The position of the dip scales linearly with  $\Delta\nu_1^s$  (see Fig. 5.9). If the frequency detuning  $\Delta\nu_1^s$  becomes too small the atoms are stopped before they reach the probe region.

The dependence of the average velocity change,  $\Delta v$ , for different intensities  $I_1^s$  in the slowing laser beam was investigated (see Fig. 5.10). The optimal starting velocity for loading atoms into a MOT can be estimated from this measurement. The maximum in the velocity spectrum shifts towards lower velocities with increasing intensity  $I_1^s$  in the slowing laser beam. This increase of the average velocity change  $\Delta v$  is due to a larger number of scattered photons. The associated optical pumping to the  $6s5d\ ^3D_1$  state leads to an overall decrease of ground state population and thus signal rate. At the highest intensities the cooling force is so large that the slowed atoms are stopped before they reach the probe region. These atoms could not be loaded into a trap and are lost.

Therefore there are two main results extracted from these spectra. First, the position of the peak in the velocity spectra can be obtained as a function of the corresponding power broadened linewidth  $\gamma_1$  (see Fig. 5.12). Second, an integration over the spectra yields the number of slow atoms in the corresponding velocity range (see Fig. 5.11). From these spectra the optimal intensity  $I_{\text{opt}}^s$  of the slowing laser at wavelength  $\lambda_1$  is around  $I_{\text{opt}}^s = 2.0(2) \cdot I_s$ , i.e.,  $28(3)$  mW/cm<sup>2</sup>.

### 5.2.2 Repumping Transitions

The frequency detunings,  $\Delta\nu_{\text{IR}2}^s$  and  $\Delta\nu_{\text{IR}3}^s$ , of the repumping lasers at the wavelengths  $\lambda_{\text{IR}2}$  and  $\lambda_{\text{IR}3}$  are important for slowing an atomic beam efficiently. Since the Doppler shift,  $\omega_D = \vec{k} \cdot \vec{v}$ , is inversely proportional to the wavelength of the transition, the velocity range is larger for the repumping lasers at the wavelengths  $\lambda_{\text{IR}2}$  and  $\lambda_{\text{IR}3}$  than for the slowing laser at wavelength  $\lambda_1$ . The deceleration was measured at different frequency detunings  $\Delta\nu_{\text{IR}2}^s$  and  $\Delta\nu_{\text{IR}3}^s$  with intense repump-

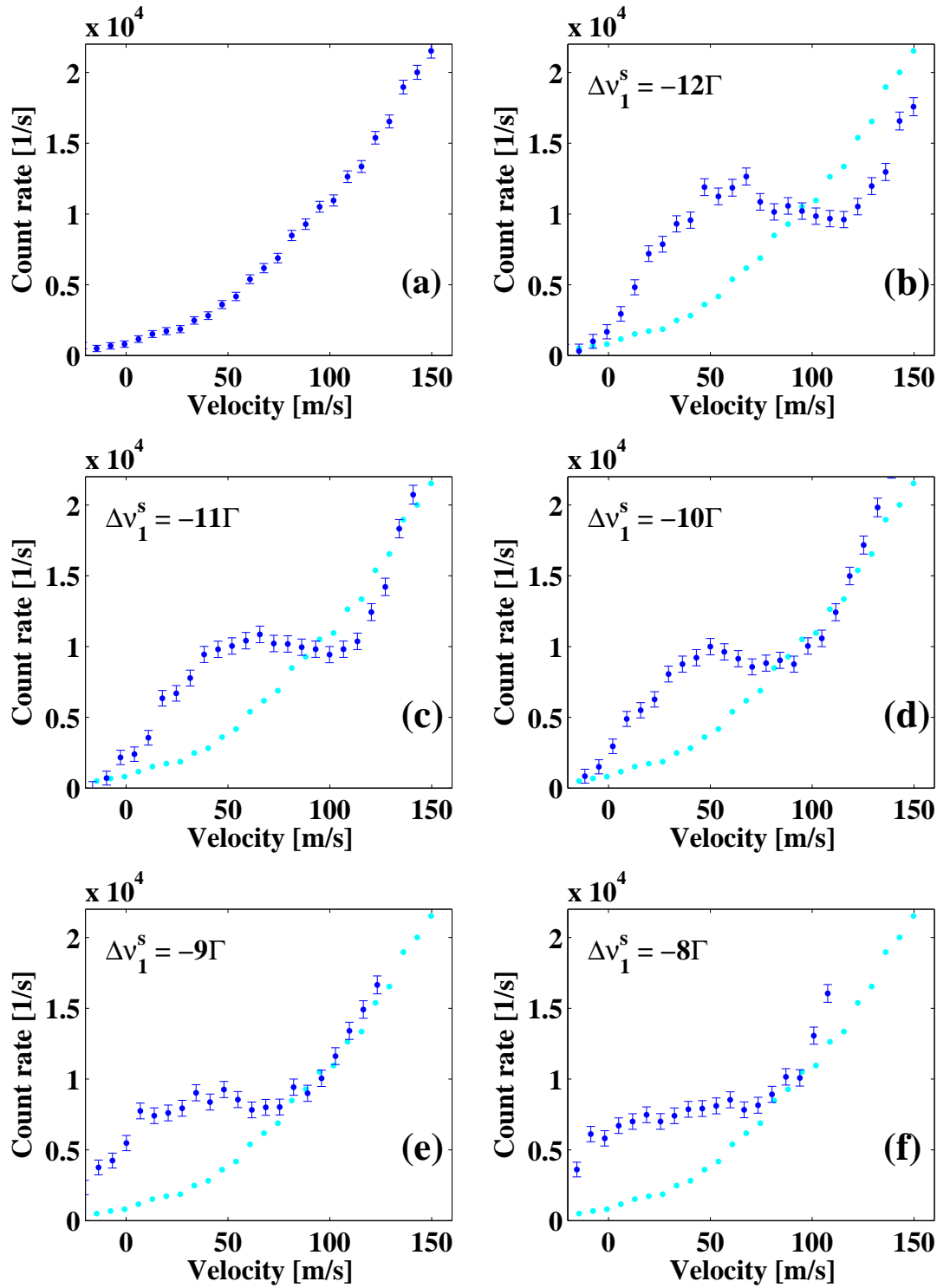


**Fig. 5.8:** (a) velocity distribution in the atomic beam without any deceleration. (b)-(f) Velocity distribution of the decelerated atomic beam for different detunings  $\Delta\nu_1^s$  of the slowing laser frequency at wavelength  $\lambda_1$ . The frequency detuning  $\Delta\nu_1^s$  is given in the unit of natural linewidth  $\Gamma$  of the transition. The original velocity distribution (a) is given in dots for reference.

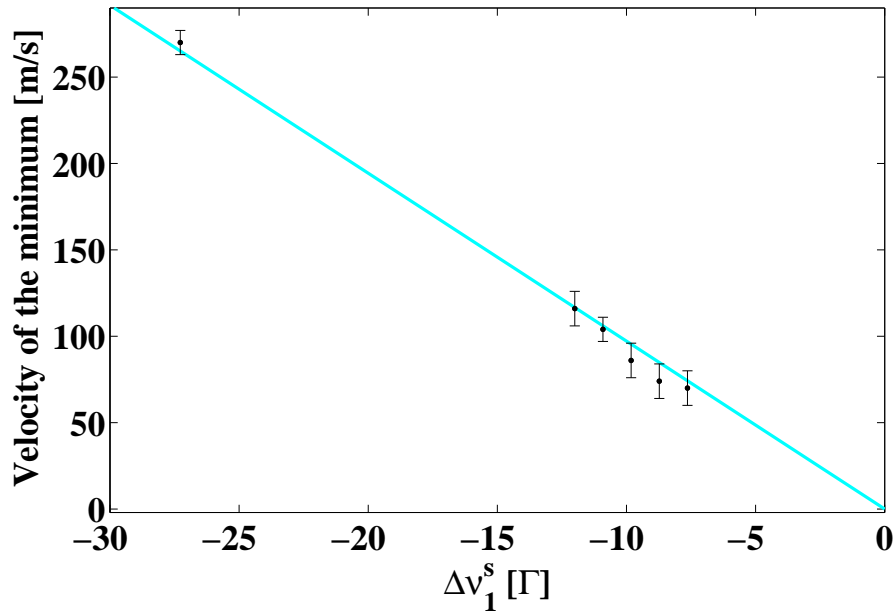


**Fig. 5.9:** Position of the dip in the velocity spectra as a function of the frequency detuning  $\Delta\nu_1^s$  in units of the natural linewidth  $\Gamma$  of the transition. The line shows the expected Doppler shift corresponding to the detuning  $\Delta\nu_1^s$ .

ing laser beams at wavelengths  $\lambda_{\text{IR}2}$  and  $\lambda_{\text{IR}3}$  (see Fig. 5.13). During these measurements the detuning  $\Delta\nu_1^s$  of the slowing laser light corresponded to a velocity of 145 m/s.

The velocity range corresponding to the width of the repumping transitions at wavelength  $\lambda_{\text{IR}2}$  is 53(9) m/s and for the transition at wavelength  $\lambda_{\text{IR}3}$  is 130(15) m/s, which is several times the characteristic velocity range estimated from the natural linewidth of the transition. This is caused by the power broadening due to the highly focussed laser beams and rather long interaction times with the lasers.

Achieving a larger range by increasing the intensity is inefficient. A better solution is frequency broadening. This can be implemented by a second set of lasers at another frequency detuning. It has been implemented in the trapping experiments (see Chapter 6).

### 5.3 Velocity Distribution in the 6s5d <sup>3</sup>D-States

The velocity distribution in the metastable states are part of the dynamics of the many level system. The fluorescence at wavelength  $\lambda_1$  can not be used in this case because of the large scattering rate from the cooling transition. Instead atoms

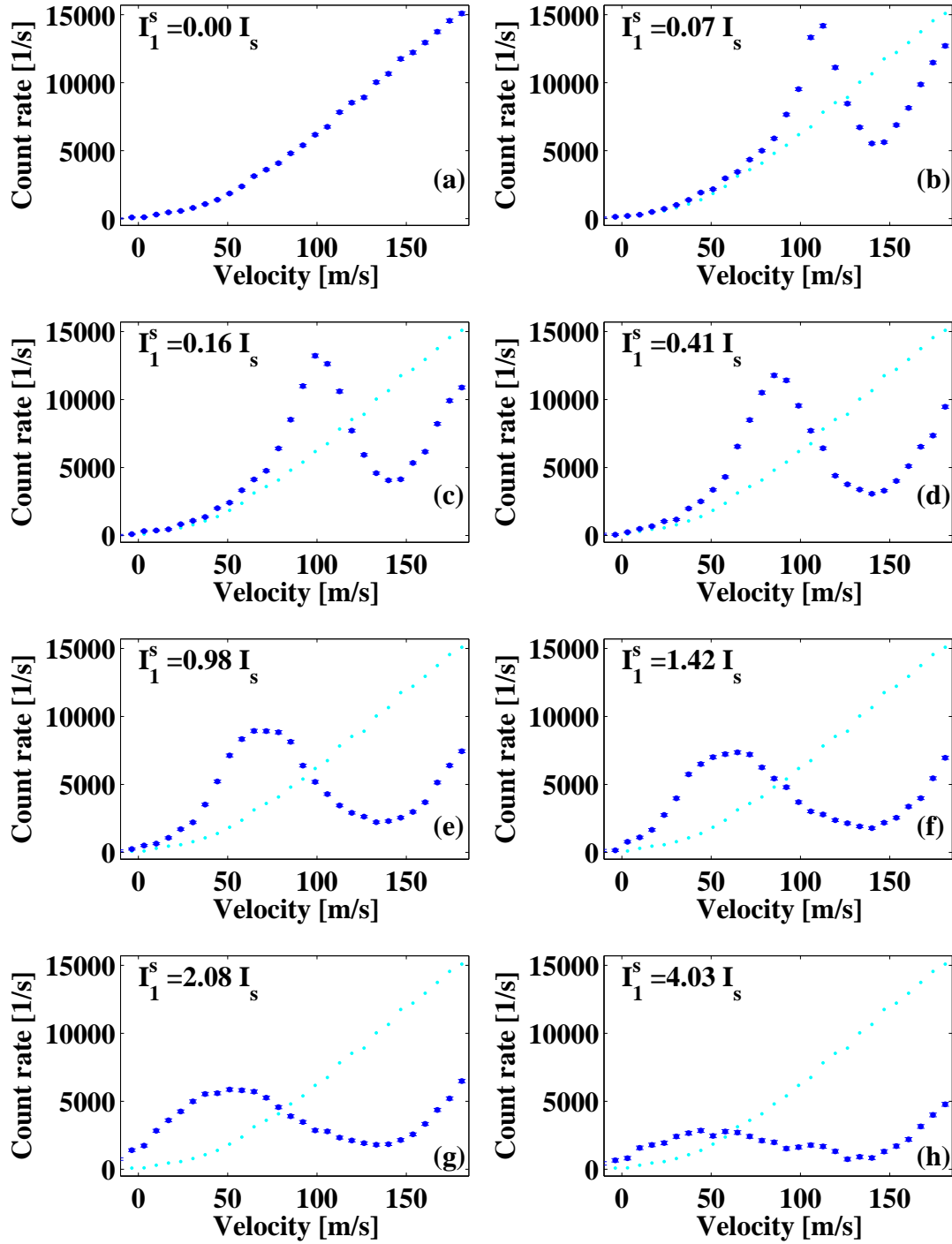
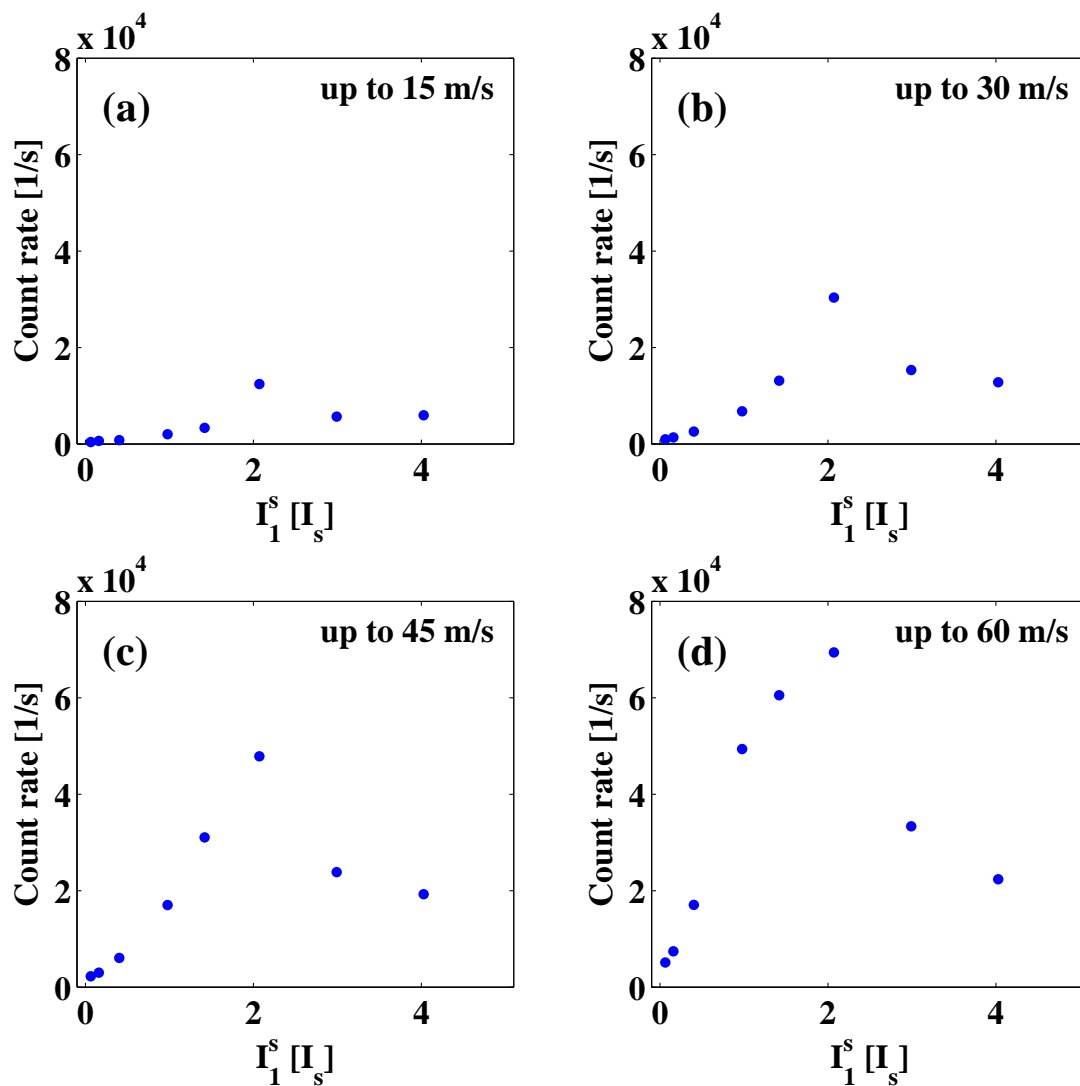
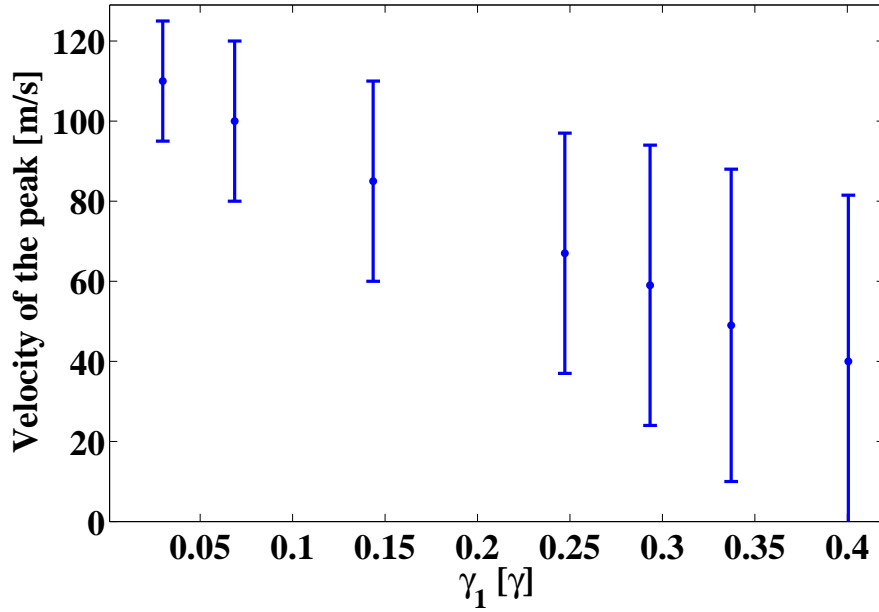


Fig. 5.10: Set of velocity spectra at different intensities  $I_1^s$  of the slowing laser light in units of the saturation intensity  $I_s$  of the cooling transition at wavelength  $\lambda_1$ . The frequency detuning of the slowing laser was  $\Delta\nu_1^s = -260$  MHz. The original velocity distribution (a) is given in dots for reference.



**Fig. 5.11:** Integrated spectra from Fig. 5.10 up to different cutoff velocities. (a) Up to 15 m/s velocity, (b) up to 30 m/s velocity, (c) up to 45 m/s velocity and (d) up to 60 m/s velocity.



**Fig. 5.12:** Position of the peak and the width of the peak in the deceleration spectra (see Fig. 5.10) as a function of the power broadened linewidth. The vertical extent of the symbols corresponds to the width of the cooling peak.

in the metastable states are excited to the higher  $5d6p\ ^3D_1^o$  state (see Fig. 3.3). The weak branching of the  $5d6p\ ^3D_1^o$  state to the ground state  $6s^2\ ^1S_0$  results in fluorescence at wavelength  $\lambda_B$ . The velocity distribution of atoms in the  $6s5d\ ^3D_1$  and the  $6s5d\ ^3D_2$  states can be studied using this emission line.

Probe laser beams at the wavelengths  $\lambda_2$  or  $\lambda_3$  at  $\theta = -45^\circ$  relative to the atomic beam drive the  $6s5d\ ^3D_1 \rightarrow 5d6p\ ^3D_1^o$  and the  $6s5d\ ^3D_2 \rightarrow 5d6p\ ^3D_1^o$  transitions and yield the velocity distribution of atoms in those states. They differ from the ground state velocity distribution. The  $6s5d\ ^3D_1$  state was not repumped for laser cooling of barium and the  $6s5d\ ^3D_1$  state population increase is a direct measure of the number of cooling cycles. The average velocity change in the slowing section of the atomic beam can be estimated from comparison of the velocity dependent population in the  $6s5d\ ^3D_1$  and the  $6s5d\ ^3D_2$  states. The average effective scattering rate  $\gamma_{\text{eff}}$  from the slowing laser beam at wavelength  $\lambda_1$  and the corresponding deceleration  $a_{\text{eff}}$  during the slowing process can be extracted.

The experimental setup for observing the velocity distribution of atoms in the  $6s5d\ ^3D_2$  and the  $6s5d\ ^3D_1$  states is shown in Fig. 5.14. The setup for decelerating the atomic beam was not changed (see Section 5.2). The slowing laser light at wavelength  $\lambda_1$  is set to a frequency detuning of  $\Delta\nu_1^s = -580$  MHz which corresponds to a velocity of 320 m/s. Laser beams at the wavelengths  $\lambda_2$

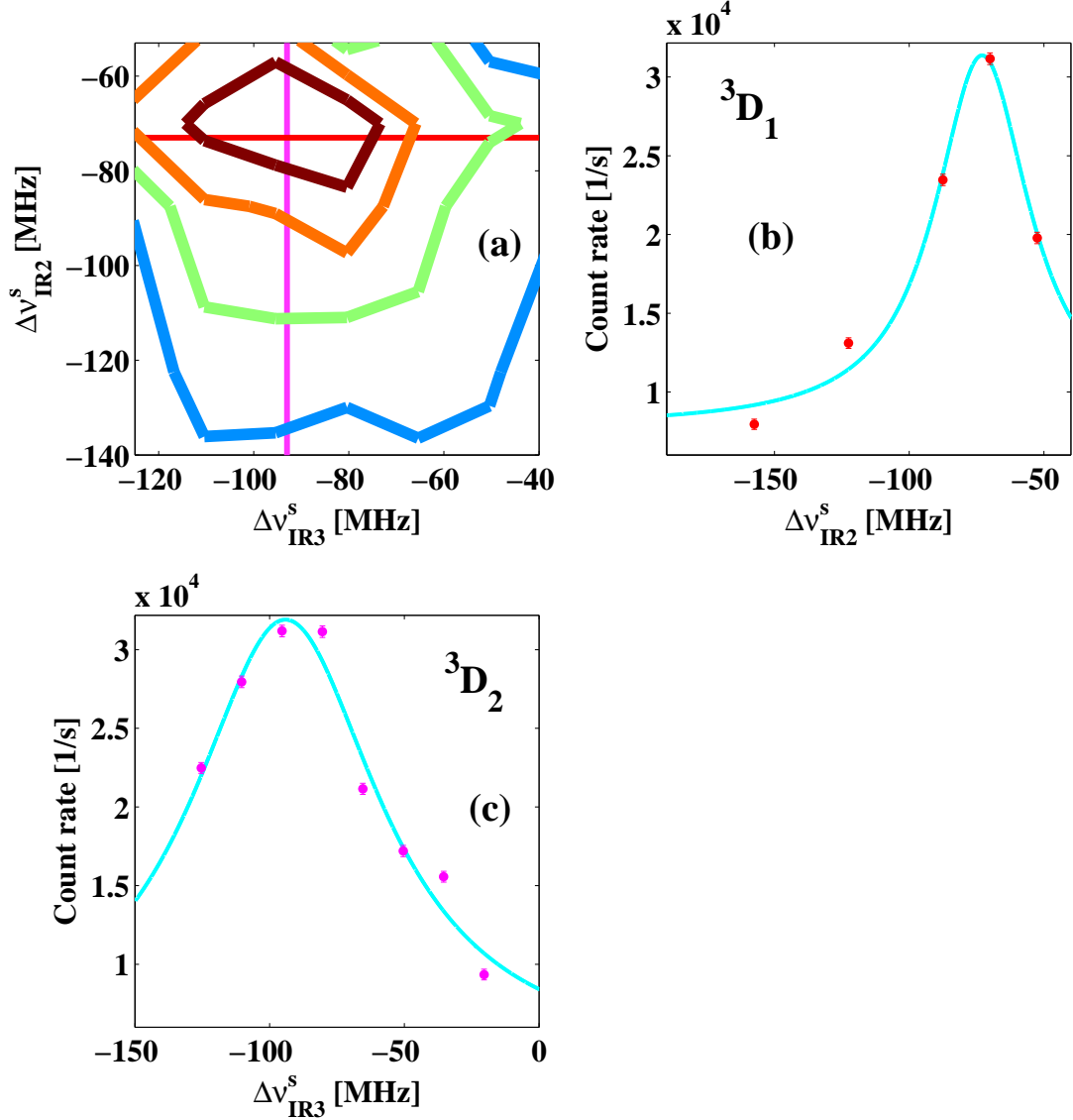


**Fig. 5.13:** (a) Correlation of count rate with the frequency detunings  $\Delta\nu_{\text{IR2}}^s$  and  $\Delta\nu_{\text{IR3}}^s$  of the laser beams at the wavelengths  $\lambda_{\text{IR2}}$  and  $\lambda_{\text{IR3}}$  at 30 m/s velocity. Darker lines correspond to a larger atomic flux. An efficient slowing requires both laser beams. (b) and (c) projections of (a) on the frequency detunings  $\Delta\nu_{\text{IR2}}^s$  and  $\Delta\nu_{\text{IR3}}^s$ . The center frequencies are  $-73(5)$  MHz and  $-93(3)$  MHz with a width of  $60(10)$  MHz and  $-85(10)$  MHz for the lasers at the wavelengths  $\lambda_{\text{IR2}}$  and  $\lambda_{\text{IR3}}$ .

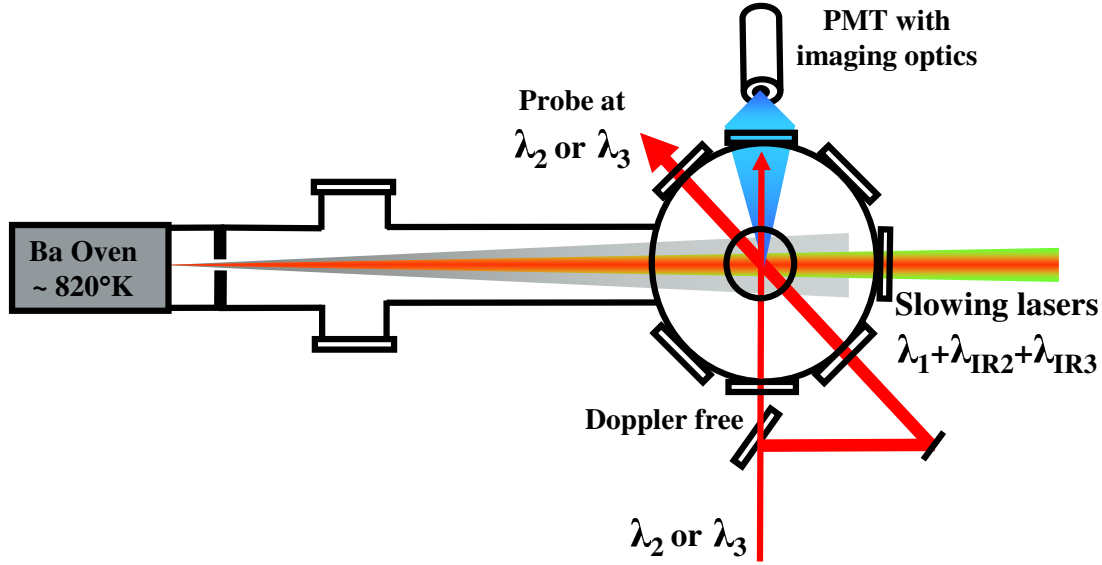


**Fig. 5.14:** Experimental setup for measuring the velocity distribution of barium atoms in the  $6s5d\ ^3D_1$  and the  $6s5d\ ^3D_2$  states. The overlapped laser beams at the wavelengths  $\lambda_1$ ,  $\lambda_{IR2}$  and  $\lambda_{IR3}$  counter propagate the atomic beam for deceleration. Laser beams at the wavelengths  $\lambda_2$  or  $\lambda_3$  are at an angle of  $\theta = -45^\circ$  with the atomic beam to measure the velocity distribution of atoms at the  $6s5d\ ^3D_1$  and the  $6s5d\ ^3D_2$  states. A part of the laser light at the wavelengths  $\lambda_2$  or  $\lambda_3$  is directed perpendicular to the atomic beam and gives the resonance frequency of the respective transitions. Fluorescence is detected at wavelength  $\lambda_B$  with a photomultiplier.

and  $\lambda_3$  are orthogonal to the atomic beam. Part of the same light is aligned to cross the same interaction region with the atomic beam at an angle  $\theta = -45^\circ$ . The laser light power is about 1 mW for each beam. The beam diameters are about 2 mm. Both laser beam frequencies are scanned across the Doppler-free resonance and the velocity sensitive part of the spectrum. A photomultiplier detects the fluorescence at wavelength  $\lambda_B$  from the region where all laser beams are overlapped with the atomic beam. The frequency detuning can be converted to a velocity spectrum from the known Doppler shift. The velocity spectra are recorded with and without repumping of atoms in the  $6s5d\ ^3D_2$  state by a laser light at wavelength  $\lambda_{IR2}$ .

### 5.3.1 Measurements

The effect of repumping atoms in the  $6s5d\ ^3D_2$  state on the deceleration process can be observed by measuring the velocity distribution of atoms in the  $6s5d\ ^3D_1$

and the 6s5d <sup>3</sup>D<sub>2</sub> states. These are identical to the velocity distribution of atoms in the ground state if the repumping laser beams at the wavelengths  $\lambda_{\text{IR}2}$  and  $\lambda_{\text{IR}3}$  are blocked. The velocity distribution of the atoms is modified due to the finite interaction time with the slowing laser beam at wavelength  $\lambda_1$  and their interaction time with the probe laser beams at the wavelengths  $\lambda_2$  and  $\lambda_3$ . The rather long interaction time with the slowing laser beam at wavelength  $\lambda_1$  decreases the probability,  $\rho_s(v)$ , of the atom to be in the ground state

$$\rho_s(v) = \exp\left(-\frac{\gamma_1(\delta\nu) \cdot S}{B_c \cdot v}\right), \quad (5.12)$$

where  $\gamma_1(\delta\nu)$  is the scattering rate at the frequency detuning  $\delta\nu = \Delta\nu_1^s - \nu_D$  in the reference frame of atoms,  $\nu_D = \frac{1}{2\pi} \vec{k} \cdot \vec{v}$  is the Doppler shift is,  $\delta\nu_1^s$  is the frequency detuning of the laser light at wavelength  $\lambda_1$  and  $S$  is the interaction length. The branching ratio to the ground state  $B_c$  is given by Eqn. 3.1. The interaction with the slowing laser beam yields a finite probability,  $P_i^s(v)$ , of the atom to be in the 6s5d <sup>3</sup>D<sub>i</sub> state

$$P_i^s(v) = [1 - \rho_s(v)] \cdot \frac{A_i}{(A_{\text{IR}1} + A_{\text{IR}2} + A_{\text{IR}3})}, \quad (5.13)$$

where  $i = 1, 2$  and the partial decay rates  $A_i$  are defined in Table 3.5. The second modification of the velocity distribution of atoms arises from the velocity dependent interaction time  $\Delta t$  with the probe laser beams at wavelength  $\lambda_i$  of diameter  $d_i$ , i.e.,  $\Delta t = d_i/v$  over which the fluorescence at wavelength  $\lambda_B$  is collected. The modification is

$$P_i^B(v) = \exp\left(-\frac{\gamma_i \cdot d_i}{v}\right) \cdot \frac{A_B}{(A_2 + A_3 + A_B + A_c) - A_i}, \quad (5.14)$$

where  $\gamma_i$  is the scattering rate from the probe laser beams at wavelength  $\lambda_i$ . The velocity spectra,  $F_i(v)$ , of atoms in the 6s5d <sup>3</sup>D<sub>i</sub>-state are

$$F_i(v) = \frac{dF_{\text{beam}}}{dv} \cdot P_i^s(v) \cdot P_i^B(v) dv. \quad (5.15)$$

The velocity distribution of the decelerated atomic beam after introducing the repumping laser beam at wavelength  $\lambda_{\text{IR}2}$  is different for atoms in the 6s5d <sup>3</sup>D<sub>1</sub> and in the 6s5d <sup>3</sup>D<sub>2</sub> states. The velocity distribution in the 6s5d <sup>3</sup>D<sub>i</sub>-state is

$$f_i^{\text{rep}}(v) = \frac{dF_s}{dv} \cdot P_i(v) \cdot P_i^B(v) dv, \quad (5.16)$$

where  $\frac{dF_s}{dv}$  is an unknown velocity distribution of the decelerated atomic beam, which depends on the population of the 6s<sup>2</sup> <sup>1</sup>S<sub>0</sub>, 6s6p <sup>1</sup>P<sub>1</sub>, 6s5d <sup>1</sup>D<sub>2</sub>, 6s5d <sup>3</sup>D<sub>2</sub> and

6s5d  $^3D_1$  states involved in laser cooling.  $P_i(v)$  is the probability of atoms to be in the 6s5d  $^3D_i$ -state after adding the repumping laser light at wavelength  $\lambda_{IR2}$ . The probability  $P_i(v)$  depends on the number of cooling cycles an atom undergoes during deceleration. It is a velocity dependent quantity and dominated by the efficiency of the repumping process.

### 5.3.2 Analysis

The velocity spectra,  $F_1(v)$  and  $F_2(v)$ , of atoms in the 6s5d  $^3D_1$  and the 6s5d  $^3D_2$  states differ only by the probability of decay branching to these states, when they are not repumped (see Fig. 5.15). The signal rates are expected to be proportional to the ratio of the partial decay rates, i.e.,  $\frac{A_{IR2}}{A_{IR1}}$ . A fit to the recorded spectra with a function given in Eqn. 5.15 yields the ratio  $\frac{A_{IR2}}{A_{IR1}} = 17(5)$ , which is in good agreement with the expected value of 21.1(1.1)(2.5) from the branching ratio measurement (see Section 5.1.1).

Repumping laser light at the wavelengths  $\lambda_{IR2}$  and  $\lambda_{IR3}$  in the slowing section increases the population of the 6s5d  $^3D_1$  state, which was not repumped during deceleration. In contrast, the 6s5d  $^3D_2$  state would be depleted completely with perfect repumping. This is reflected qualitatively in the observed spectra (see Fig. 5.15 (b)). The velocity difference in the dip of the velocity distribution in the 6s5d  $^3D_2$  state and the peak in the velocity distribution of the 6s5d  $^3D_1$  state can be used for an estimate of the achieved velocity change as  $\Delta v = 100(20)$  m/s. This velocity change  $\Delta v$  requires a total number,  $n_1 = \Delta v/v_r$ , of scattered photons at wavelength  $\lambda_1$ . The number of repumping cycles needs to be larger than

$$N_{\text{repump}} = \left( \frac{n_1}{B_c} - 1 \right), \quad (5.17)$$

where  $B_c$  is the branching of the 6s6p  $^1P_1$  state decays to the D-states relative to its decay branching to the ground state. The probability,  $P_{3D1}$ , for an atom to be in the 6s5d  $^3D_1$  state is

$$P_{3D1} = 1 - \exp \left( -n_1 \cdot \frac{A_{IR1}}{A_1 + A_{IR1} + A_{IR2} + A_{IR3}} \right). \quad (5.18)$$

The number of scattered photons from the cooling cycles is  $n_1 = 20000(4000)$  and the corresponding probability is  $P_{3D1} \simeq 0.6$ . An estimate for the average effective scattering rate yields

$$\gamma_{\text{eff}} = \frac{n_1}{S/v}, \quad (5.19)$$

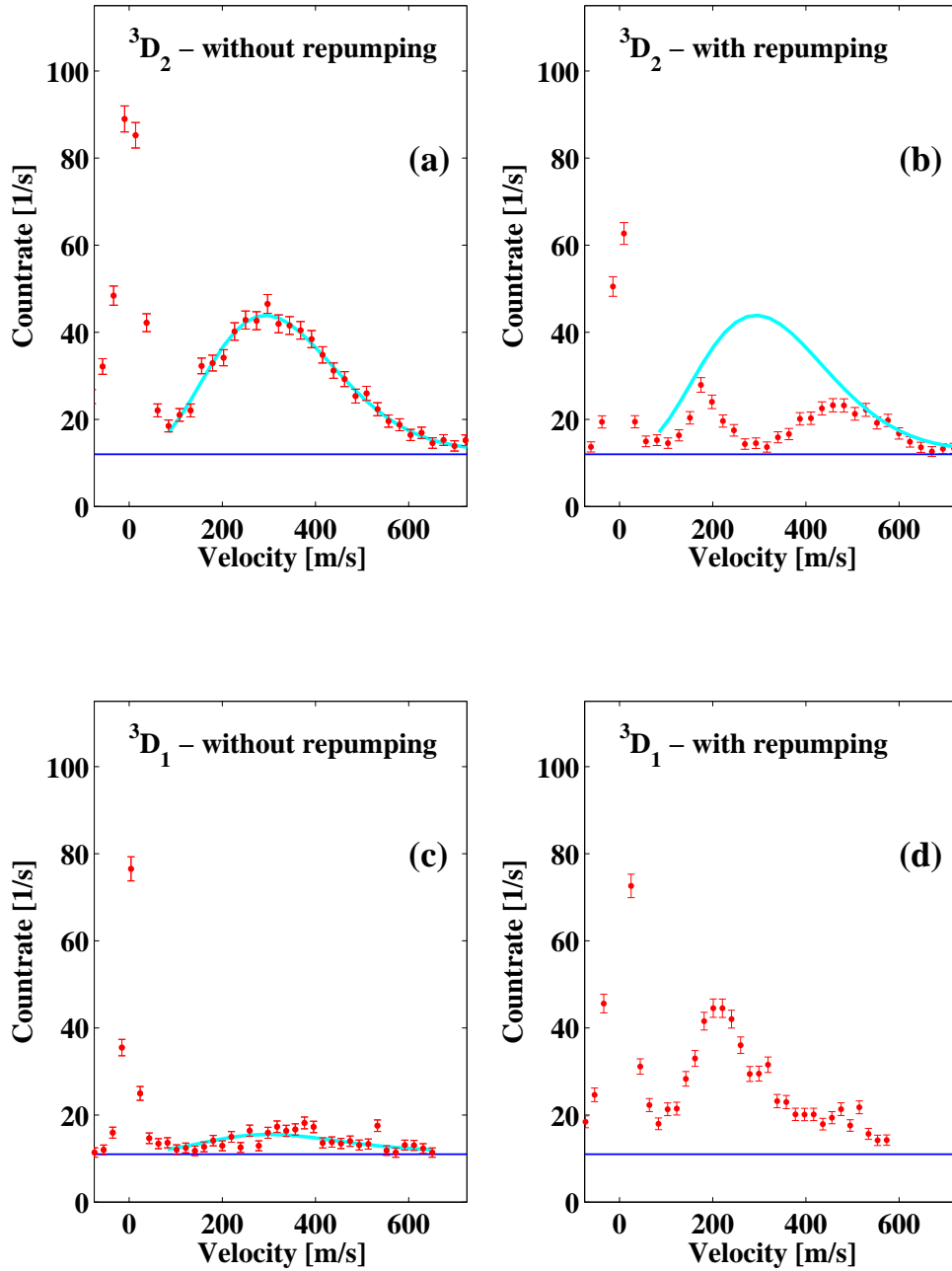


**Fig. 5.15:** Velocity distribution of barium atoms in the 6s5d  $^3D$ -states. Velocity distribution of atoms without (a, c) and with (b, d) repumping of the 6s5d  $^3D_2$  state during deceleration. Repumping from the 6s5d  $^3D_2$  state population results in a decrease of the countrate around 300(20) m/s, which indicates the complete repumping of the state population. The increase of the signal in the 6s5d  $^3D_1$  state velocity distribution is due to the accumulation of atoms in that state, which were not repumped. The line through the data describes theoretical model of the spectrum (see Eqn. 5.15). The background from scattered light is indicated in the spectra by horizontal lines.

where  $S$  is the length of the slowing section. The effective scattering rate is  $\gamma_{\text{eff}} = 1.0(2) \cdot 10^7 \text{ s}^{-1}$  for  $S = 0.6 \text{ m}$  and  $v = 320 \text{ m/s}$ . The average effective deceleration can be determined

$$a_{\text{eff}} = v_r \cdot \gamma_{\text{eff}}, \quad (5.20)$$

where  $v_r = 0.00522 \text{ m/s}$  is the recoil velocity of barium. The average deceleration yields  $a_{\text{eff}} = 52(10) \cdot 10^3 \text{ m/s}^2$  in this experiment. This is about 18.5% of the maximum achievable acceleration,  $a_{\text{max}}$ , for barium (see Appendix C).

The ratio of the velocity distribution in the  $6s5d \ ^3D_1$  and the  $6s5d \ ^3D_2$  states in a decelerated atomic beam is the ratio of the probabilities  $P_i(v)$  of finding atoms in the corresponding D-states (see Eqn. 5.16). In a laser cooling process the population in these states depends on repumping of the atoms. The velocity dependent repumping can be estimated with the ratio of measured velocity distribution of atoms in the  $6s5d \ ^3D_1$  and the  $6s5d \ ^3D_2$  states (see Fig. 5.16). The variation of repumping over the velocity spectra is determined by the choice of the laser frequency detuning and the intensity of the repumping laser light. Efficient repumping transfers the population completely over a certain velocity range and causes a large statistical error over this range.

The conducted measurement gives no access to the velocity distribution after deceleration. To determine the full dynamics of laser cooling of a many level system, the velocity distribution of atoms in each of the states must be measured under identical experimental conditions. The weighted sum of the velocity distributions in all states would give the velocity distribution of the decelerated atomic beam independent of the state.

The slowed atoms in the  $6s5d \ ^3D_1$  state can be regained into the cooling cycle by adding another repumping laser beam at the wavelengths  $\lambda_2$  or  $\lambda_{\text{IR1}}$ . An example is shown in Fig. 5.17, where a repumping laser beam at wavelength  $\lambda_{\text{IR1}}$  was added. The laser beam at wavelength  $\lambda_{\text{IR1}}$  was interacting at a small angle with the atomic beam and partially overlapped with it. The two spectra with and without repumping the  $6s5d \ ^3D_1$  state population differ. A larger fraction of slow atoms is detected, if the  $6s5d \ ^3D_1$  state population is repumped as well (see Fig. 5.17).

The average deceleration  $a_{\text{eff}}$  should be sufficient to stop atoms with velocity up to  $300 \text{ m/s}$  in a slowing section of length  $1 \text{ m}$ . In particular the dynamics of the slowing process of barium can be followed. Tools for monitoring the slowing process are now available, which are essential towards trapping of barium atoms.

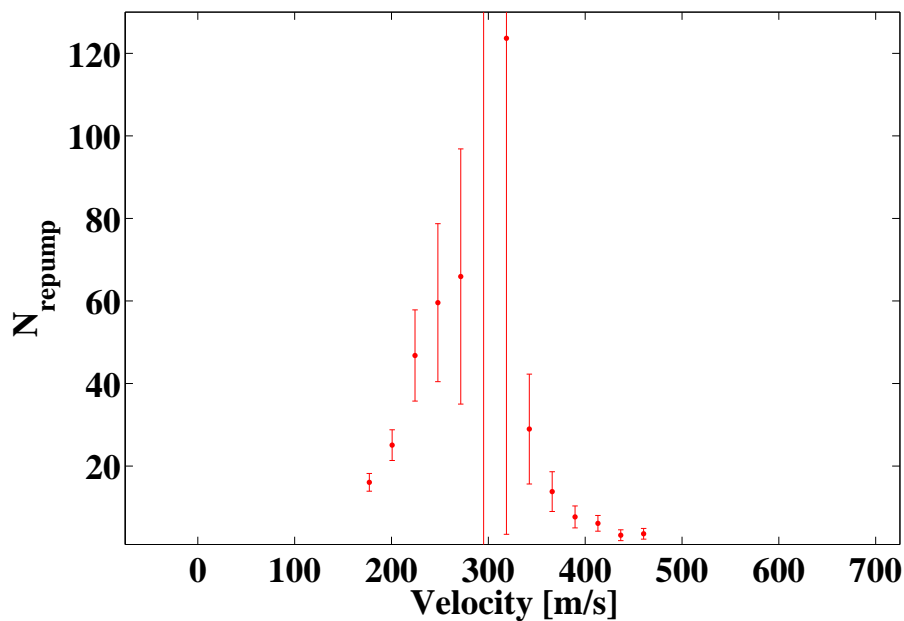


**Fig. 5.16:** Total number of repumping cycles from the 6s5d <sup>1</sup>D<sub>2</sub> and 6s5d <sup>3</sup>D<sub>2</sub> states for different velocity classes during deceleration.

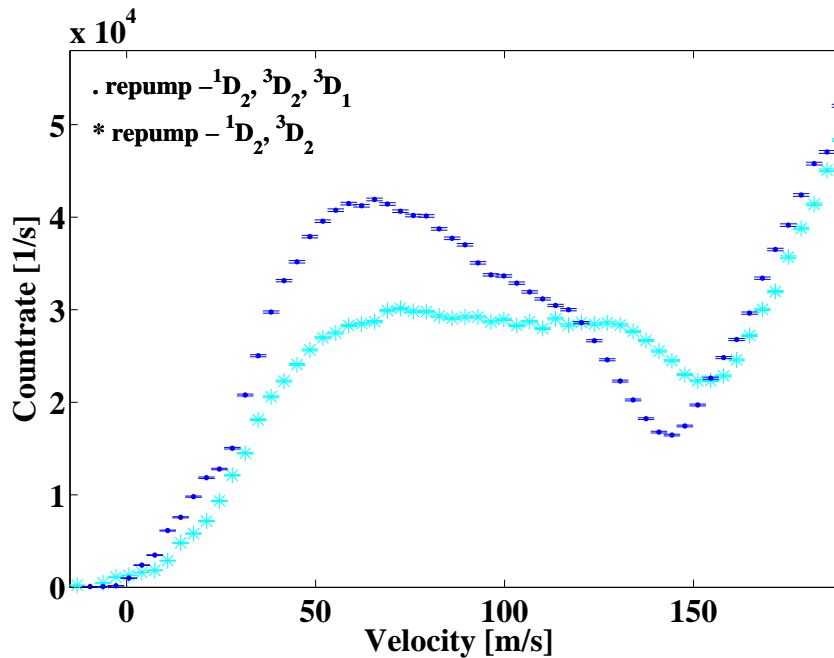


**Fig. 5.17:** Dependence of repumping from the 6s5d <sup>3</sup>D<sub>1</sub> state during the deceleration process. The effect of a repumping laser at wavelength  $\lambda_{\text{IR1}}$  to repump atoms from the 6s5d <sup>3</sup>D<sub>1</sub> state is shown.



# Chapter 6

## Barium in a Magneto Optical Trap

A magneto-optical trap (MOT) has been set up to collect and cool barium atoms. A MOT is robust in terms of small variations of the experimental conditions, e.g., light intensities, detunings of laser frequencies and magnetic field gradients. Furthermore, a large velocity acceptance for capturing atoms into a MOT can be achieved with strong optical scattering forces. Depending on the requirements for a particular experiment, these confined atoms can be further cooled by a second stage cooling or transferred to magnetic traps [178, 179] or to optical dipole traps [180, 181]. Such cold, dense and isotopically clean samples have been utilized in many experiments, e.g., searches for violations of discrete symmetries in weak interactions [171–174] and for synchronizing time to an atomic transition [175–177]. The working principle of a MOT has been described in the literature [165, 166, 169, 170, 182, 183].

In this work magneto-optical trapping is extended to the heavy alkaline-earth element barium (see Fig. 6.1), where cooling can be achieved in a closed five level subsystem ( $6s^2\ ^1S_0$ ,  $6s6p\ ^1P_1$ ,  $6s5d\ ^1D_2$ ,  $6s5d\ ^3D_2$ ,  $6s5d\ ^3D_1$ ) or in a six level system ( $6s^2\ ^1S_0$ ,  $6s6p\ ^1P_1$ ,  $6s5d\ ^1D_2$ ,  $6s5d\ ^3D_2$ ,  $6s5d\ ^3D_1$ ,  $5d6p\ ^3D_1^o$ ) containing a weak leak in the cooling cycle. Eight lasers provide the light to couple all the states. The performance of a MOT employing such a complex subsystem of states is studied to gain insight into the processes which determine trap lifetimes, populations and temperatures of the trapped atoms. The efficiencies for collecting atoms from a thermal beam is analyzed for the combination of slowing of an atomic beam (see Chapter 5) and magneto-optical trapping. Furthermore, trapped barium atoms have been exploited to determine atomic properties of the

$5d^2 \ ^3F_2$  excited state. The developed techniques are applicable for trapping of other leaky systems. In particular they can be applied for efficient trapping of radium.

## 6.1 MOT Setup

This section describes the details of the MOT setup for trapping of barium. A quadrupole magnetic field is produced by a set of two coils in anti-Helmholtz configuration (see Fig. 6.2). The magnetic field strength,  $B(\mathbf{r})$ , vanishes at the position  $\vec{\mathbf{r}} = 0$ . The field strength around the origin can be approximated by

$$B(x, y, z) = \sqrt{\alpha_{x,y}^2 \cdot (x^2 + y^2) + \alpha_z^2 \cdot z^2}, \quad (6.1)$$

where  $\alpha_{x,y}$  and  $\alpha_z$  are the field gradients in the xy-plane and axial z-direction. The field,  $\vec{\mathbf{B}}$ , along the z-axis is either towards the center or away from it depending on the direction of the current,  $I$ , in the coils. If  $\vec{\mathbf{B}}$  points away from the center in the z coordinate, the field in the xy-plane points towards the center. The calculation of the gradients for the set of coils of the experiment is described in Appendix A. The field strength,  $B$ , has been calibrated by measuring the Zeeman splitting of the  $6s^2 \ ^1S_0 \rightarrow 6s6p \ ^1P_1$  transition (see Section 4.5).

The radiative optical force for trapping arises from three pairs of mutually orthogonal, circularly polarized retro-reflected laser beams. The force on an atom in the combined magnetic and light fields is [169]

$$\vec{\mathbf{F}}_{\text{MOT}}(S_0, \delta, \alpha) = -\beta(S_0, \delta) \vec{\mathbf{v}} - \kappa(S_0, \delta, \alpha) \vec{\mathbf{r}}, \quad (6.2)$$

where  $S_0$  is the saturation parameter,  $\delta$  is the frequency detuning and  $\alpha$  is the magnetic field gradient. In the atomic reference frame the frequency detuning,  $\delta$ , includes Doppler shifts and Zeeman shifts. It is

$$\delta = \delta_l - \vec{\mathbf{k}} \cdot \vec{\mathbf{v}} + (m_i g_i - m_j g_j) \mu_B B, \quad (6.3)$$

where  $\delta_l$  is the frequency detuning of light,  $\vec{\mathbf{k}}$  is the wave vector of the cooling transition,  $(m_i g_i - m_j g_j)$  depends on the cooling transition,  $m$  and  $g$  are the magnetic quantum numbers and the Lande g-factors and  $\mu_B$  is the Bohr magneton. For two counter-propagating laser beams

$$\beta = - \frac{8\hbar k^2 \delta S_0}{\gamma [1 + S_0 + (2\delta/\gamma)^2]^2}, \quad (6.4)$$

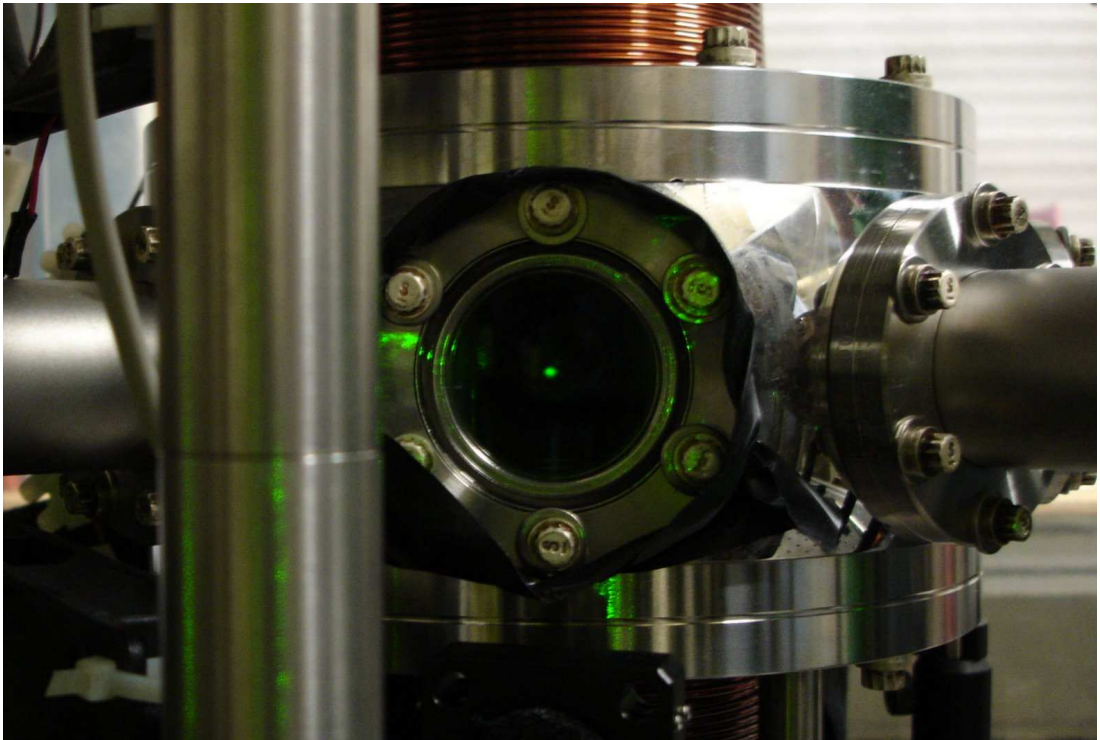


**Fig. 6.1:** Photograph of trapped barium atoms. The bright spot visible through the center of the optical port is the fluorescence at wavelength  $\lambda_1$  from a cloud of trapped barium atoms.

describes a damping force and

$$\kappa = \frac{(m_i g_i - m_j g_j) \mu_B \alpha}{\hbar k} \beta, \quad (6.5)$$

is a spring constant, where  $\hbar$  is Planck's constant. The detuning  $\delta_1$  selects the direction of the force  $\vec{F}_{\text{MOT}}$  relative to the direction of the velocity  $\vec{v}$  of atoms in the absence of a magnetic field. In a magnetic field  $B$  the atoms are slowed to a velocity

$$v_d = - \frac{(m_i g_i - m_j g_j)}{\hbar k} \mu_B \cdot \alpha r, \quad (6.6)$$

which is a drift velocity towards the trap center, where  $|\vec{B}(\vec{r})| = 0$ . A negative detuning of the trapping laser beams is essential for confining the atoms in a trap.

A barium MOT requires at least three repump laser beams which overlap with the crossing of the six trapping laser beams. The setup incorporates laser beams at five additional wavelengths (see Fig. 6.2), which provide for variations of the repumping scheme in the experiment. The relative alignment of the trapping laser beams and all the repumping laser beams is crucial for the performance of the MOT. The center of the trap is at the point where the sum of all forces vanish. Hence, the magnetic field zero point, all six trapping laser beams and the necessary repumping laser beams need to coincide at one point with sufficient overlap. For this, one pair of the trapping beams at wavelength  $\lambda_1$  is orthogonal to the atomic beam and the other two pairs of beams intersect the atomic beam at an angle of  $45^\circ$  in the  $xy$ -plane. The power in each of these beams is up to 10 mW and the beam diameter is 10 mm. The beam diameter is defined by an aperture, which selects the central part of a Gaussian beam with 15 mm diameter ( $1/e^2$  intensity).

Repumping laser beams at the wavelengths  $\lambda_2$  and  $\lambda_3$  are co-propagating with the trapping beams at wavelength  $\lambda_1$ . Three infrared laser beams at the wavelengths  $\lambda_{\text{IR}1}$ ,  $\lambda_{\text{IR}2}$  and  $\lambda_{\text{IR}3}$  are overlapped with the trapping laser beams at the trap center (see Fig. 6.2). They are intersecting the slowing laser beams at a shallow angle (less than  $5^\circ$ ). The trapping region is the volume in which all laser beams overlap around  $\vec{r} = 0$ . The available power of the repumping laser beams are 60 mW at wavelength  $\lambda_{\text{IR}1}$ , 25 mW at wavelength  $\lambda_{\text{IR}2}$  and 5 mW at wavelength  $\lambda_{\text{IR}3}$ . The spatial profiles of all infrared repumping laser beams are measured (see Fig. 6.3) by an optical beam analyzer, which is a model BP109-IR (from Thorlabs Inc., NJ, USA). The radii of the repumping laser beams at the trapping region are determined to 4.25(5) mm ( $\lambda_{\text{IR}1}$ ), 2.75(4) mm ( $\lambda_{\text{IR}2}$ ) and

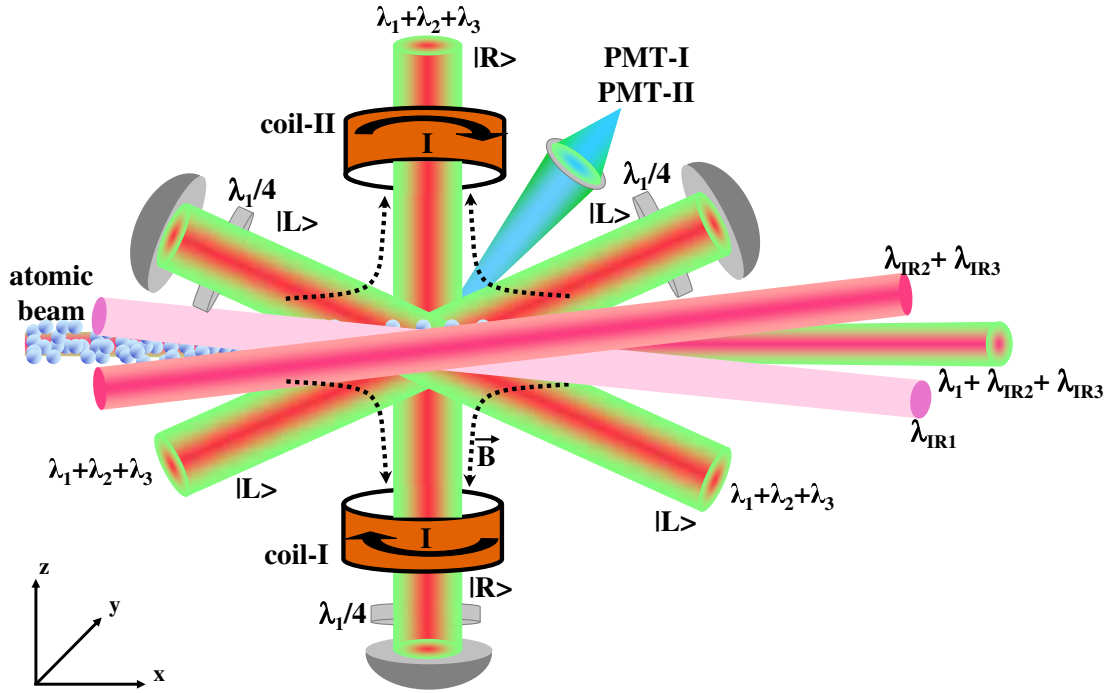


**Fig. 6.2:** Overlap of the laser beams in the trapping region. The current  $I$  in magnetic field coils produces a quadrupole magnetic field  $\vec{B}$  indicated by dotted lines. The laser beams are overlapped with that part in the quadrupole magnetic field where the field strength vanishes. The symbols  $|R\rangle$  and  $|L\rangle$  indicate right and left handed circular polarization of the trapping laser beams. The diameter of the trapping beams at wavelength  $\lambda_1$  are 10 mm. The diameter of the repumping laser beams at the wavelengths  $\lambda_{IR1}$ ,  $\lambda_{IR2}$  and  $\lambda_{IR3}$  are 8.5 mm, 5.5 mm and 5 mm at the position of the trap. The origin of the coordinate system is at the trap center. The figure is not drawn to the scale.

2.50(7) mm ( $\lambda_{\text{IR3}}$ ). The laser beams for the deceleration of the atomic beam at the wavelengths  $\lambda_{\text{IR2}}$  and  $\lambda_{\text{IR3}}$  are pointing against the atomic beam and are focussed in the oven orifice. Both laser beams have a radius of 1.5 mm at the position of the trapping region. The trapping volume has a diameter of about 5 mm. The relative spatial position is depicted in Fig. 6.2. The laser light in all beams can be independently controlled in frequency as well as in power.

The presence of trapped atoms can be detected by observing the fluorescence at the wavelengths  $\lambda_1$  and  $\lambda_B$ . The signal at wavelength  $\lambda_B$  is free from scattered light at any of the laser beam wavelengths used in this work. In that case the noise level is determined by the dark count rate of the photomultiplier tubes. The setup incorporates a pair of photomultiplier tubes PMT-I and PMT-II, which makes the simultaneous detection of fluorescence at both the wavelengths  $\lambda_1$  and  $\lambda_B$  possible.

## 6.2 Characterization of the Barium MOT

The MOT is characterized in terms of the trap population,  $N_{\text{MOT}}$ , and the trap lifetime,  $\tau_{\text{MOT}}$ . The population  $N_{\text{MOT}}$  depends on the intensities,  $I_i$ , of the laser beams and the detunings,  $\Delta\nu_i$ , of the laser frequencies from the resonance frequencies. Further, it depends on the subset of states employed for trapping.

The number of trapped atoms  $N_{\text{MOT}}$  is proportional to the photomultiplier count rate,  $R^1$ , at wavelength  $\lambda_1$ . The scattering rate from the trapping laser beams is  $\gamma_1(I_1^t, \Delta\nu_1^t)$ , where  $\Delta\nu_1^t$  is the detuning and  $I_1^t$  is the intensity of these beams. The count rate is

$$R^1 = \epsilon_1 \cdot \gamma_1(I_1^t, \Delta\nu_1^t) \cdot N_{\text{MOT}} \cdot (1 - \rho_D), \quad (6.7)$$

where  $\epsilon_1$  is the detection efficiency for the fluorescence at wavelength  $\lambda_1$  and  $\rho_D$  is the probability for an atom to be in one of the metastable D-states, where it does not scatter light at wavelength  $\lambda_1$ . The fluorescence at wavelength  $\lambda_B$  can be detected if the  $6s5d \ ^3D_1$  and the  $6s5d \ ^3D_2$  states are repumped with laser light at the wavelengths  $\lambda_2$  or  $\lambda_3$ . While driving the transition at wavelength  $\lambda_i$  ( $i = 2, 3, 2 + 3$ ) the signal rate can be written as

$$R_i^B = \epsilon_B \cdot B_B \cdot N_{\text{MOT}} \cdot \frac{d}{dt} \rho_{3D1^o}, \quad (6.8)$$

where  $\epsilon_B$  is the detection efficiency of the fluorescence at wavelength  $\lambda_B$ ,  $B_B$  is branching of the  $5d6p \ ^3D_1^o$  state to the ground state  $6s^2 \ ^1S_0$  and  $\frac{d}{dt} \rho_{3D1^o}$  is

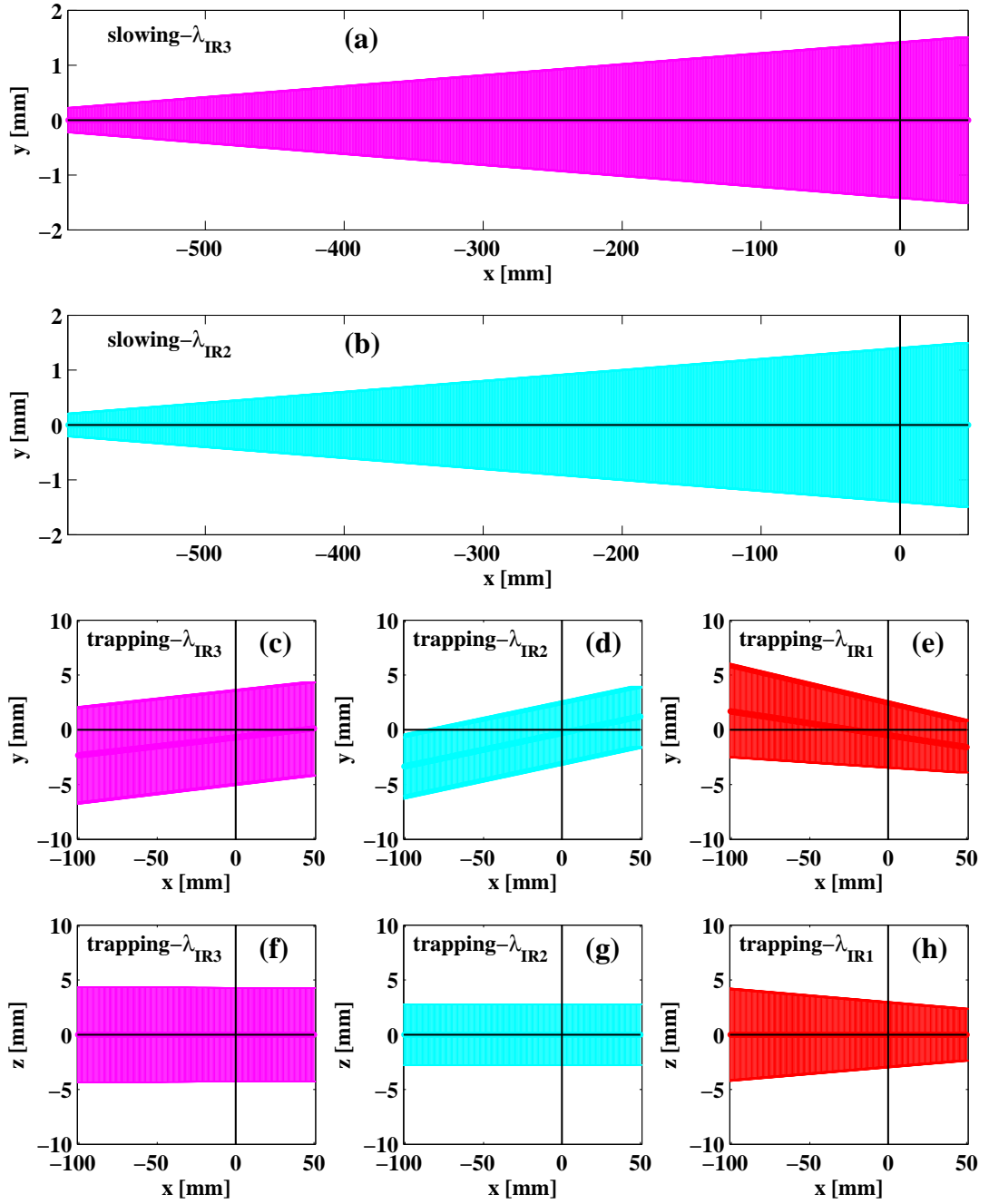


**Fig. 6.3:** Measured spatial variation of the beam diameter for the laser beams at the wavelengths  $\lambda_{\text{IR1}}$ ,  $\lambda_{\text{IR2}}$  and  $\lambda_{\text{IR3}}$ . (a), (b) The laser beams used for slowing the atomic beam are focussed on the oven orifice at  $x = -600$  mm and have a radius of 1.5 mm at  $x = 0$ . (c)-(h) The other laser beams are parallel in the  $x$ - $z$  plane and are introduced at a small angle in the  $x$ - $y$  plane. The origin of the coordinate system is at the trap. The atomic beam is propagating along the positive  $x$ -axis direction.

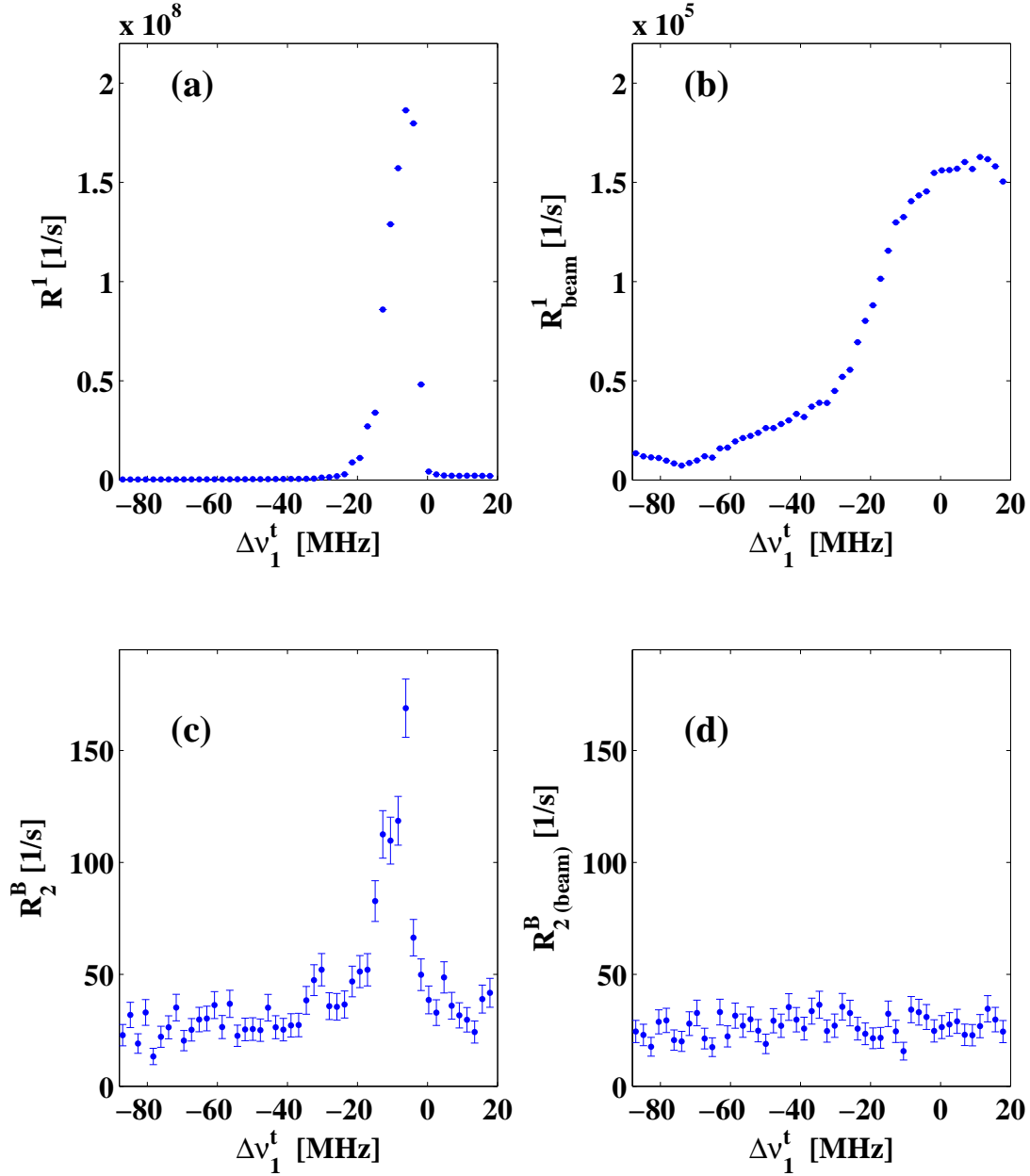


**Fig. 6.4:** Dependence of the MOT fluorescence on the frequency detuning  $\Delta\nu_1^t$  of the trapping laser beams at wavelength  $\lambda_1$ . The total intensity in all six trapping laser beams was  $I_1^t = 3.2 \cdot I_s$  and the magnetic field gradient was  $\alpha_z = 35$  G/cm. The magnetic field gradient was optimized for highest fluorescence from trapped atoms. (a) Fluorescence rate  $R^1$  at wavelength  $\lambda_1$ . The maximum fluorescence is at  $\Delta\nu_1^t = -6.0(5)$  MHz. (b) Rate  $R^1$  in the absence of trapped atoms. (c) Fluorescence at wavelength  $\lambda_B$  from the trapped atoms and (d) corresponding spectrum in the absence of trapped atoms.

the transfer rate to the  $5d6p\ ^3D_1^o$  state. The fluorescence rates  $R_i^B$  are similar to Eqns. 5.1 to 5.3 derived for the measurements with an atomic beam. A difference originates from the presence of coherent Raman  $\Lambda$ -transitions in the case of atom trapping. The Raman transitions facilitate a faster exchange of population between the ground state  $6s^2\ ^1S_0$  and the metastable  $6s5d\ ^3D$ -states than by spontaneous decay alone. In particular the  $6s5d\ ^3D_1$  state is populated only by spontaneous decay, if atoms from that state are repumped only with laser light at wavelength  $\lambda_2$ . The rate from trapped atoms is then

$$R_2^B = \epsilon_B \cdot B_B \cdot N_{\text{MOT}} \cdot \gamma_1(I_1^t, \Delta\nu_1^t) \cdot B_{\text{IR}1}, \quad (6.9)$$

where  $B_{\text{IR}1}$  is the decay branching of the  $6s6p\ ^1P_1$  state to the  $6s5d\ ^3D_1$  state. In this case the ratio of the rates  $R^1$  and  $R_2^B$  at two wavelengths yield an expression for the fraction of atoms in the  $6s5d$  D-states

$$\rho_D = 1 - B_{\text{IR}1} \cdot B_B \cdot \frac{R^1}{R_2^B} \cdot \frac{\epsilon_B}{\epsilon_1}. \quad (6.10)$$

The fluorescence from the trapped atoms at both the wavelengths  $\lambda_1$  and  $\lambda_B$  were detected under these conditions (see Fig. 6.4). All repumping laser beams have been optimized for a maximum trap population. Trapping occurs for a negative detuning  $\Delta\nu_1^t$  of the trapping laser frequency but no trapping occurs for positive detuning. The maximum population  $N_{\text{MOT}}$  is at a detuning of  $\Delta\nu_1^t = -6.0(5)$  MHz for an intensity of all six trapping beams of  $I_1^t = 3.2 \cdot I_s$ . A similar behavior is observed at wavelength  $\lambda_B$ . The position and the shape agree with those of the signal at wavelength  $\lambda_1$  however the absolute rate is smaller. From the count rates  $R^1$  and  $R_2^B$  together with the known detection efficiencies  $\epsilon_1$  and  $\epsilon_B$  (see Section 4.3) and with the branching ratios  $B_{\text{IR}1}$  (see Section 3.2) and  $B_B$  (see Section 5.1) the population in metastable D-states can be estimated as  $\rho_D = 0.5(1)$ . The uncertainty comes mainly from the uncertainties in the measured signal rate  $R_2^B$  and the branching ratios  $B_{\text{IR}1}$ ,  $B_B$ .

The vertical trapping laser beam at wavelength  $\lambda_1$  produces a Zeeman broadened fluorescence from the atomic beam. It can be observed in the absence of trapped atoms as a background count rate  $R_{\text{beam}}^1$  at wavelength  $\lambda_1$  and  $R_2^B$  (beam) at wavelength  $\lambda_B$ . In Fig. 6.4 the peak of the count rate  $R^1$  at wavelength  $\lambda_1$  is 1200 times larger for the trapped atoms compared to the maximum signal produced by the vertical trapping laser beams when atoms are not trapped.

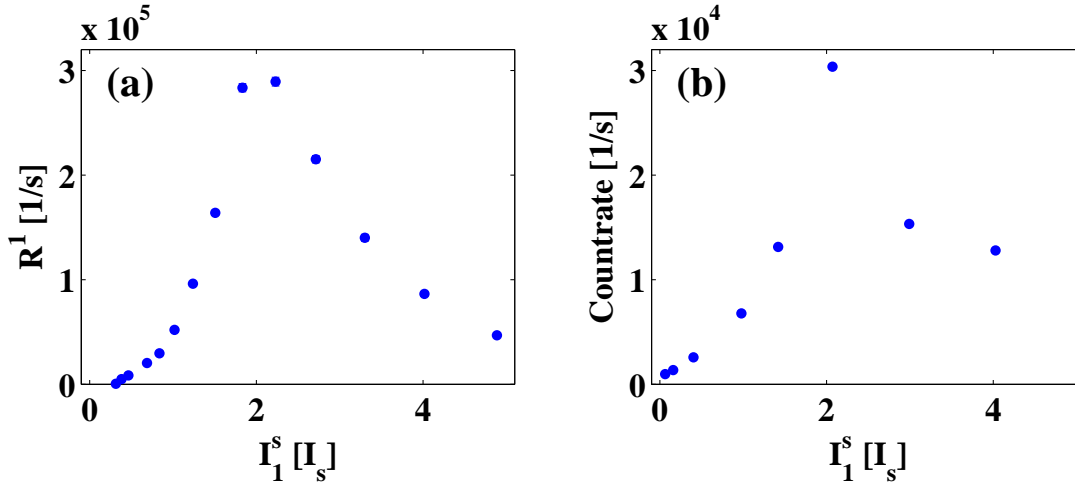


**Fig. 6.5:** (a) The the trap population  $N_{\text{MOT}}$  dependence on the slowing laser intensity  $I_1^s$ . (b) Dependence of the atomic flux below a velocity of 30 m/s in the decelerated atomic beam on  $I_1^s$ . A comparison of both spectra yields a capture velocity  $v_c = 30$  m/s for the barium MOT.

### 6.2.1 Capture Velocity of MOT

The capture velocity,  $v_c$ , of a MOT depends on the frequency detuning  $\Delta\nu_1^t$  and the intensity  $I_1^t$  of the trapping laser beams. It can be estimated for two level systems [169]. A full description for the case of barium would have to include interactions with all laser beams. It still can be studied experimentally. A larger  $v_c$  should lead to a more efficient loading into a MOT from a decelerated atomic beam. For an optimal match of the capturing and the slowing section the capture velocity  $v_c$  should be larger than the velocity of the decelerated atomic beam. The capture velocity  $v_c$  can be obtained from measurements of the trap population, which was determined for different fluxes of atoms at low velocities. The flux of decelerated atoms can be changed by varying the intensity  $I_1^s$  of the slowing laser beam. It has been measured for different intensities  $I_1^s$  in a dedicated set of experiments (see Section 5.2.1). The trap population  $N_{\text{MOT}}$  depends on the slowing laser intensity  $I_1^s$  in a similar way. It increases monotonously up to  $I_1^s = 2 \cdot I_s$  and decreases above that intensity (see Fig. 6.5). The decrease at high intensities  $I_1^s$  is caused by a reduced atomic flux into the trapping region due to stopping of atoms before they reach it. The best match for the intensity dependence of the flux and the trap population  $N_{\text{MOT}}$  is obtained for  $v_{\text{max}} = 30$  m/s.

In order to capture atoms in the MOT they have to be stopped within the trapping volume. Assuming that the deceleration is constant over the stopping

distance and the atoms are stopped within a distance shorter than the diameter  $d$  of the trapping volume the deceleration,  $a_{\text{MOT}}$ , has to be

$$a_{\text{MOT}} > \frac{v_c^2}{2d}. \quad (6.11)$$

This yields  $a_{\text{MOT}} > 5 \cdot 10^4 \text{ m/s}^2$ , which agrees with the estimated deceleration in the slowing section (see Section 5.3). It is about a factor of six lower than the maximum deceleration  $a_{\text{max}}$  for barium, if one would assume a simple two level system. A realistic maximum deceleration is at least smaller by a factor of  $(1 - \rho_D)$  because of the time the atoms spend in the metastable states.

### 6.2.2 Trap Loss

The number of trapped atoms  $N_{\text{MOT}}$  in steady state depends on the loading rate  $L_{\text{MOT}}$  into the trap and on the trap loss rate. The number of atoms in the trap increases with decreasing losses. This is of particular importance for rare radioactive isotopes, e.g., radium. Trap losses are caused by several effects.

1. Collision of trapped atoms with residual gas. The momentum transfer is sufficient to kick atoms out of the trapping volume.
2. Laser induced loss processes like photo-ionization depend on the intensity in the laser beams.
3. Insufficient repumping rate leaves atoms in a state which is not subject to the optical cooling force. Such atoms can fly out of the trap.
4. Collisions among cold atoms and laser assisted collisions can lead to molecule formation.

The first three mechanisms are proportional to the population  $N_{\text{MOT}}$  of the trapped sample, while the loss due to the last process depends on a higher power of  $N_{\text{MOT}}$  [186,187]. The effects can be distinguished by a different time evolution of the free decay of the trap population  $N_{\text{MOT}}$ .

The rate of change of the population,  $\frac{d}{dt}N_{\text{MOT}}$ , depends on the loading rate,  $L_{\text{MOT}}$ , and the loss rate,  $N_{\text{MOT}}/\tau_{\text{MOT}}$ . If these losses are independent of the density of trapped atoms, the rate of change of  $N_{\text{MOT}}$  can be written as

$$\frac{dN_{\text{MOT}}(t)}{dt} = L_{\text{MOT}} - \frac{N_{\text{MOT}}(t)}{\tau_{\text{MOT}}}. \quad (6.12)$$

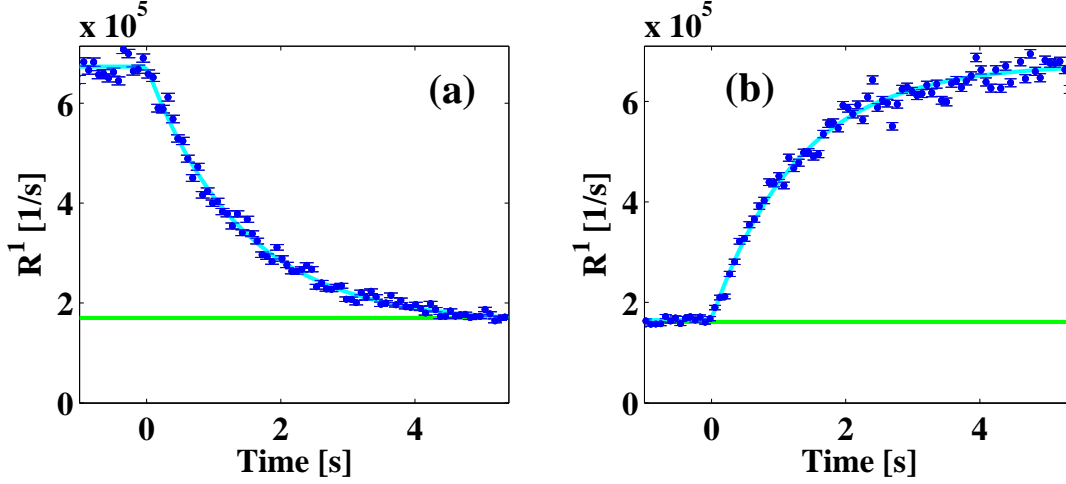


**Fig. 6.6:** (a) Decay and (b) build up of the population  $N_{\text{MOT}}$  for a barium MOT. The fitted decay time of the MOT is  $1.55(5)$  s and the rise time is  $1.45(10)$  s. Intensity of the trapping laser beam was  $I_1^t = 0.6 \cdot I_s$  and the frequency detuning was  $\Delta\nu_1^t = -7(1)$  MHz. The residual gas pressure in the MOT chamber was  $2.3 \cdot 10^{-9}$  mbar. The horizontal straight line indicates the background level without any MOT signal.

For a constant loading rate  $L_{\text{MOT}}$  the population saturates at  $L_{\text{MOT}} \cdot \tau_{\text{MOT}}$ . The population  $N_{\text{MOT}}$  decays exponentially, if the loading rate  $L_{\text{MOT}}$  vanishes at a time  $t = 0$ ,

$$N_{\text{MOT}}(t) = N_{\text{MOT}} \cdot \exp\left(-\frac{t}{\tau_{\text{MOT}}}\right). \quad (6.13)$$

All decay curves measured with trapped barium agree with this exponential model. In this case the total decay rate,  $\tau_{\text{MOT}}^{-1}$ , is the sum of independent partial loss rates

$$\tau_{\text{MOT}}^{-1} = \tau_{\text{vac}}^{-1} + \tau_{\text{ds}}^{-1} + \tau_{\text{cl}}^{-1} + \tau_{\text{pi}}^{-1} \quad (6.14)$$

where  $\tau_{\text{vac}}^{-1}$  is the loss due to collisions with residual gas,  $\tau_{\text{ds}}^{-1}$  is the loss due to escape from the trap in a dark (metastable) state,  $\tau_{\text{cl}}^{-1}$  is the loss from the cooling cycle, and  $\tau_{\text{pi}}^{-1}$  are photo-ionization losses.

The decay rate  $\tau_{\text{MOT}}^{-1}$  has been measured from the buildup and the decay times of the MOT population (see Fig. 6.6). The loading rate  $L_{\text{MOT}}$  was changed by switching the slowing laser beam on and off with AOM4 in the setup (see Fig. 4.2). This changes the flux at low velocities in the atomic beam. The response of the fluorescence signal rate  $R^1$  was fitted with a single exponential function (see Eqn. 6.13). Both the buildup and the decay curves agree with that function. This indicates that losses which are nonlinear in the density of the trapped sample

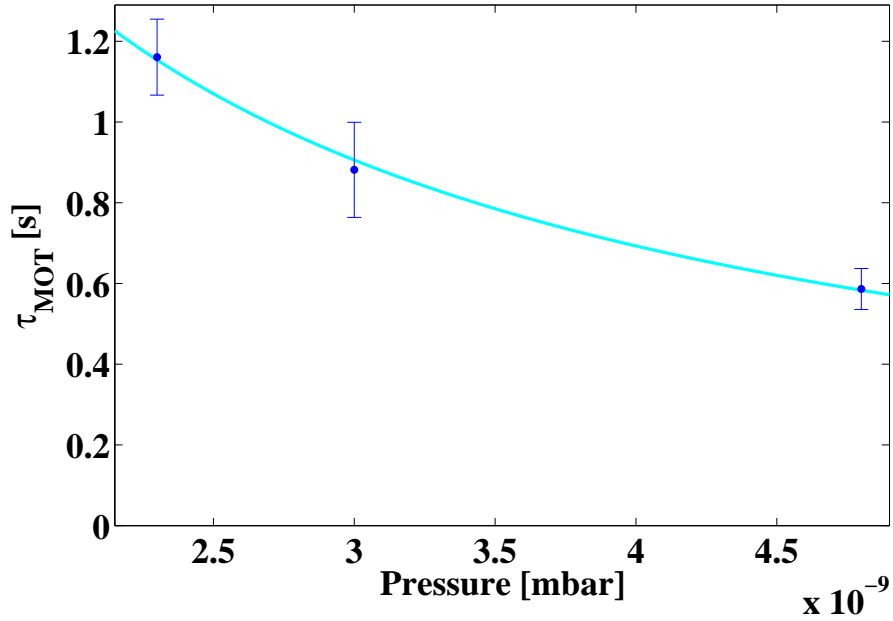


**Fig. 6.7:** The trap lifetime  $\tau_{\text{MOT}}$  as a function of the residual gas pressure  $P$ . The intensity in the trapping laser beams was  $I_1^t = 1.2 \cdot I_s$  and the detuning was  $\Delta\nu_1^t = -8$  MHz. The lifetime decreases for increasing pressure. The line through the data assumes a linear dependence of the trap losses due to the residual gas density.

are negligible [184]. The dependence of the lifetime  $\tau_{\text{MOT}}$  on the experimental conditions, e.g., vacuum condition, intensity  $I_1^t$  of the trapping laser beam and repumping from the metastable states have been explored.

### Vacuum Pressure

The residual gas density in the vacuum chamber is proportional to the vacuum pressure. Thus, the collision rate of trapped atoms with residual gas molecules decreases in higher vacuum. The trap losses due to this (see Fig. 6.7) will be proportional to the pressure  $P$  and a rate constant  $\beta_P$

$$\tau_{\text{MOT}} = \left[ \frac{1}{\tau_0} + \beta_P \cdot P \right]^{-1}, \quad (6.15)$$

where  $\tau_0$  is the lifetime for  $P = 0$ . Fitting the measured lifetimes  $\tau_{\text{MOT}}$  at different pressure  $P$  gives a lifetime  $\tau_0 = 5_{-3}^{+20}$  s and a rate constant  $\beta_P = 0.33(7) \cdot 10^9$  mbar<sup>-1</sup>s<sup>-1</sup>. The pressure dependent loss rate  $\beta_P \cdot P$  can be converted into a collision cross-section

$$\sigma = \frac{\beta_P P}{n v_m}, \quad (6.16)$$

where  $n$  is the density and  $v_m$  is the average velocity of the molecules present in the residual gas. The estimated cross-section is in the range of  $1.0(3) \cdot 10^{-13} \text{ cm}^2$  as expected for such a collisional atomic process. A more accurate determination is not attempted from such measurements because the composition of the residual gas is not well known.

### Intensity Dependent Losses

A correlation of the lifetime  $\tau_{\text{MOT}}$  with the intensity  $I_1^t$  in the trapping laser beams has been observed (see Fig. 6.8). All other experimental conditions were kept constant. The lifetime  $\tau_{\text{MOT}}$  changes nonlinearly with the trapping laser intensity  $I_1^t$ . The intensity dependence of the lifetime  $\tau_{\text{MOT}}$  is parameterized with two components. The intensity independent part, which yields a lifetime of  $\tau_0$  at the intensity  $I_1^t = 0$  in the trapping laser beams. The intensity dependent part is modelled by a rate constant,  $\beta_I$ , and the  $\alpha^{\text{th}}$  power of the intensity  $I_1^t$  to determine the order in photon number for the underlying process. The lifetime can be written as

$$\tau_{\text{MOT}} = \left[ \frac{1}{\tau_0} + \beta_I \cdot (I_1^t)^\alpha \right]^{-1}. \quad (6.17)$$

The exponent  $\alpha$  of the trapping laser intensity  $I_1^t$ , the loss rate  $\beta_I$  and the lifetime  $\tau_0$  are determined from a fit of the function given in Eqn. 6.17 to the data. The fit yields  $\tau_0^{-1} = 1.2(2) \text{ s}^{-1}$  and  $\beta_I = 0.20(3) \text{ s}^{-1} I_s^{-3}$ , where  $I_s$  is the saturation intensity of the transition at wavelength  $\lambda_1$ . The reduced  $\chi^2$  of the fit is 0.9. The exponent  $\alpha = 3.0(1)$  suggests a third order process for the intensity dependent loss from the trap. This could be due to three photon photo-ionization of ground state  $6s^2 \ ^1S_0$  atoms. The ionization potential of ground state  $6s^2 \ ^1S_0$  barium atoms is 5.21 eV and the energy of a photon at wavelength  $\lambda_1$  is 2.23 eV. Thus, ionization of ground state  $6s^2 \ ^1S_0$  barium atoms requires at least the energy of three photons at wavelength  $\lambda_1$ . Trapping times of several seconds can therefore only be achieved at low intensities in the trapping laser beams.

### Repumping efficiency

The lifetime  $\tau_{\text{MOT}}$  is also affected by the parameters determining the repumping process. These parameters are intensities and detunings for the repumping lasers as well as the spatial overlap of the laser beams in the trapping region. The best quantitative measurements influence of the repumping process on the lifetime  $\tau_{\text{MOT}}$  is achieved by changing the intensities in the repumping laser beams (see

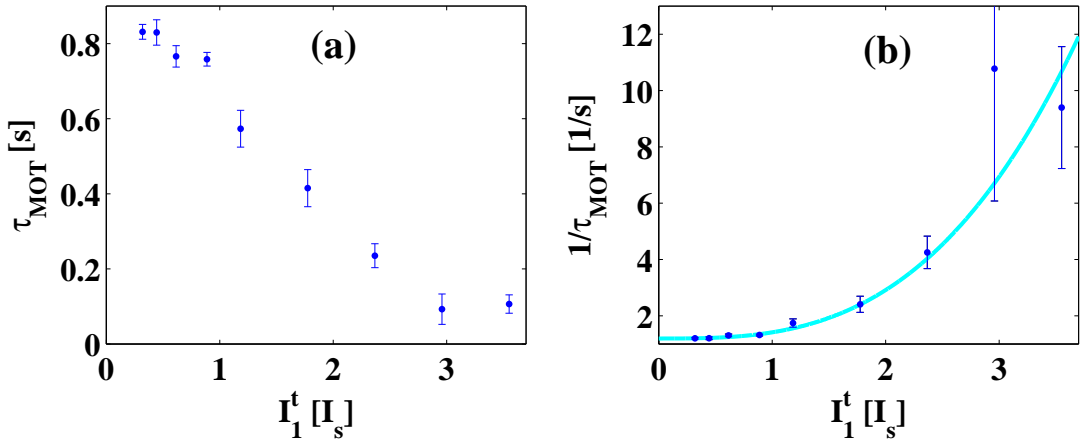


**Fig. 6.8:** (a) Dependence of the MOT lifetime  $\tau_{\text{MOT}}$  on the intensities  $I_1^t$  of the trapping laser beams. (b) The loss rate  $\tau_{\text{MOT}}^{-1}$  as a function of intensity of the trapping laser beams. The line through the data is a fit, which characterizes the intensity dependent trap loss. The trapping laser beams were detuned by  $\Delta\nu_1^t = -9$  MHz. The maximum signal rate  $R^1$  was recorded at the intensity  $I_1^t = 0.9 \cdot I_s$  for that detuning. The magnetic field gradient was 35 G/cm and the residual gas pressure was kept constant at  $5 \cdot 10^{-9}$  mbar during the course of measurements. Intensities  $I_1^t$  are given in units of the saturation intensity  $I_s$ .

Fig. 6.9). A simple functional form for the intensity dependence of the losses can not be given and a qualitative description is given here. Efficient repumping is a prerequisite for a long lifetime  $\tau_{\text{MOT}}$  of the trap. The losses are due to atoms in the metastable states. With decreasing the repumping rate the dwell time of atoms in these states increases. During these times the atoms do not feel the cooling force because they are in a dark state. They could fly out of the trapping volume. Measurements were performed for conditions at which other loss rates are small, i.e., at low intensities  $I_1^t$  in the trapping laser beams and at high intensities in the trapping laser beams, where intensity dependent losses are dominant.

The sensitivity of the lifetime  $\tau_{\text{MOT}}$  is different for the two different repumping transitions (see Fig. 6.10). The intensities at the wavelength  $\lambda_{\text{IR}2}$  and  $\lambda_{\text{IR}3}$  were reduced independently by neutral density filters. The strong dependence of the lifetime  $\tau_{\text{MOT}}$  on the intensity shows that the repumping rate has not reached saturation at the intensities available in the experiment.

The loss rates for each of the repumping transitions to first order are independent of each other. The losses for the two transitions add up when the intensities in both lasers are reduced simultaneously. This supports the assumption that

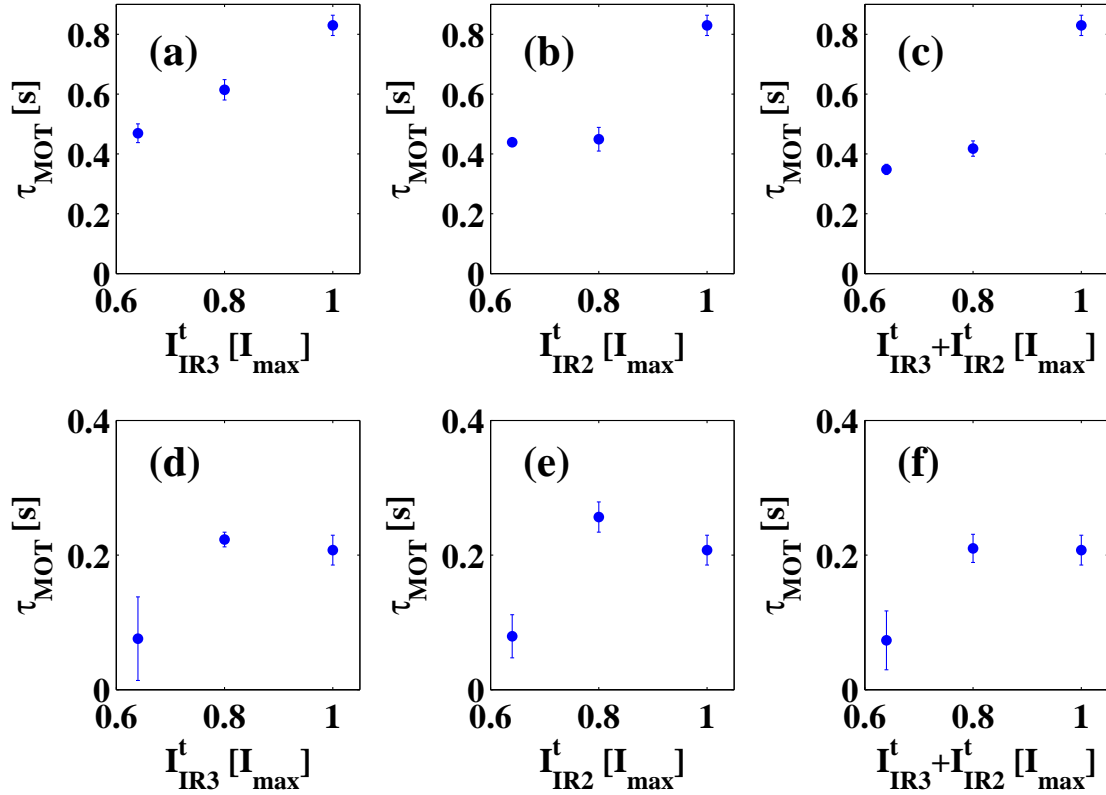


**Fig. 6.9:** The MOT lifetime  $\tau_{\text{MOT}}$  as a function of the intensities in the repumping laser beams at the wavelengths  $\lambda_{\text{IR2}}$  and  $\lambda_{\text{IR3}}$ . (a) and (d) the intensity of the laser beam at wavelength  $\lambda_{\text{IR3}}$ , (b) and (e) the intensity of the laser beam at wavelength  $\lambda_{\text{IR2}}$ , (c) and (f) the total intensity of the laser beams at the wavelengths  $\lambda_{\text{IR3}}$  and  $\lambda_{\text{IR2}}$  were varied. The set of spectra (a), (b) and (c) were taken at an intensity of  $I_1^t = 0.54 \cdot I_s$  in the trapping laser beams (d), (e) and (f) were taken at an intensity of  $I_1^t = 2.4 \cdot I_s$ .

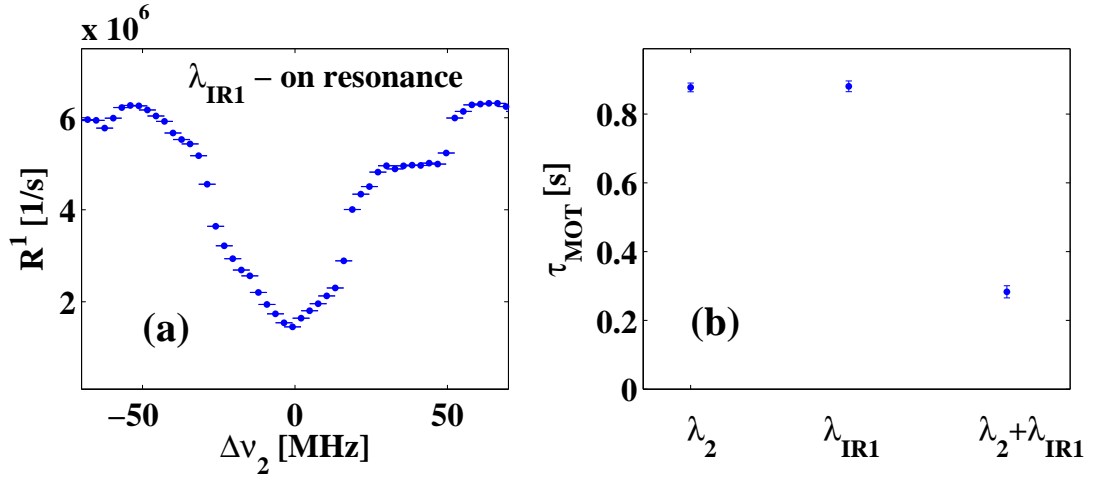


**Fig. 6.10:** Repumping the  $6s5d \ ^3D_1$  state at the wavelengths  $\lambda_{\text{IR1}}$  and  $\lambda_2$ . (a) The fluorescence  $R^1$  from trapped atoms depends on the relative frequency detunings  $\Delta\nu_2$  and  $\Delta\nu_{\text{IR1}}$  of the lasers at the wavelengths  $\lambda_2$  and  $\lambda_{\text{IR1}}$ . (b) Dependence of the MOT lifetime  $\tau_{\text{MOT}}$  on the repumping of the  $6s5d \ ^3D_1$  state. Repumping can be executed individually at the wavelengths  $\lambda_{\text{IR1}}$  or  $\lambda_2$ . In both cases the lifetime  $\tau_{\text{MOT}}$  is the same within their uncertainties. The lifetime  $\tau_{\text{MOT}}$  and the trap population  $N_{\text{MOT}}$  decrease by about a factor of four, if both the repumping lasers are on resonance.

the losses are associated with the escape of atoms from the trapping region while they are in one of the dark states.

### Laser Cooling Scheme

The trap losses are in general not the same for the different cooling schemes investigated in this work. In particular the six level subsystem has a finite leak from the cooling cycle, while the repumping scheme might lead to smaller losses due to escape from the trap in one of the metastable states. The two cooling schemes which differ only by the path to repump the  $6s5d \ ^3D_1$  state. The lifetime  $\tau_{\text{MOT}}$  has been measured for both cases and for both the repumping transitions active at the same time (see Fig. 6.10). The lifetime  $\tau_{\text{MOT}}$  and the trap population was the same for both of the laser cooling schemes. The losses due to the dwell time in the  $6s5d \ ^3D_1$  state can be expected to be minor, since it is associated with the weakest branching from the cooling transition.

An increase of the lifetime  $\tau_{\text{MOT}}$  and the population  $N_{\text{MOT}}$  might be expected if both repumping transitions are driven in parallel. In contrast a shortening of the

lifetime  $\tau_{\text{MOT}}$  and a decrease in population  $N_{\text{MOT}}$  by a factor of four is observed in both cases (see Fig. 6.10). The cooling laser at wavelength  $\lambda_1$  and the repumping laser at wavelength  $\lambda_{\text{IR1}}$  drive the two photon coherent Raman transition in the  $\Lambda$ -system of the  $6s^2\ ^1S_0$ ,  $6s6p\ ^1P_1$  and  $6s5d\ ^3D_1$  states. This yields a larger population in the  $6s5d\ ^3D_1$  state than expected from an incoherent process. The laser at wavelength  $\lambda_2$  probes the population transfer to the  $6s5d\ ^3D_1$  state and destroys the coherence of the Raman  $\Lambda$ -transition. This three photon pumping to the  $5d6p\ ^3D_1^o$  state, increases losses from the cooling cycle (see Section 5.1).

An insight of the trap loss dynamics could be obtained from solutions to the Optical Bloch equations together with the dynamics of the trapped atoms. Such an approach which should include all transitions and states would reveal a rich spectrum of multiphoton transitions.

### 6.2.3 Frequency Detunings of Repump Lasers

The frequency detunings of the repump lasers are critical parameters for the performance of the MOT. Since the trapped atoms are nearly at rest, the repump light frequencies for most efficient trapping are expected to be at the resonance frequencies of the corresponding transitions. In case of inefficient repumping due to low intensities of the laser beams or for large frequency detunings the trapped atoms remain longer in one of the metastable states. During this period in a dark state they leave the trap resulting in trapping losses.

The dependence of the population  $N_{\text{MOT}}$  on frequency detunings of the repumping lasers is shown in Fig. 6.11. A sample of trapped atoms was prepared, then one of the repumping lasers frequency was changed at a time. The fluorescence at wavelength  $\lambda_1$  from the trapped atoms was detected (see Fig. 6.11). The full width at half maximum (FWHM) in frequency of signal rate  $R_1$  for the four repump lasers is different. They are 65(6) MHz at wavelength  $\lambda_{\text{IR3}}$  ( $I_{\text{IR3}}^t = 25(1)$  mW/cm<sup>2</sup>), 25(3) MHz at wavelength  $\lambda_{\text{IR2}}$  ( $I_{\text{IR2}}^t = 105(5)$  mW/cm<sup>2</sup>), 53(5) MHz at wavelength  $\lambda_{\text{IR1}}$  ( $I_{\text{IR1}} = 105(5)$  mW/cm<sup>2</sup>) and 330(15) MHz at wavelength  $\lambda_2$  ( $I_2 = 3.0(3)$  mW/cm<sup>2</sup>). The large width at wavelength  $\lambda_2$  can be attributed to the strong optical dipole transition, which requires lower intensities for repumping. For the other three transitions the width is smaller. The substructure in the spectra could arise from coherent Raman transitions. Such resonances appear, if the frequency detunings from a common excited state are the same for a set of transitions. The coherence phenomena of the laser cooling transitions in barium have been studied extensively elsewhere [112, 188].

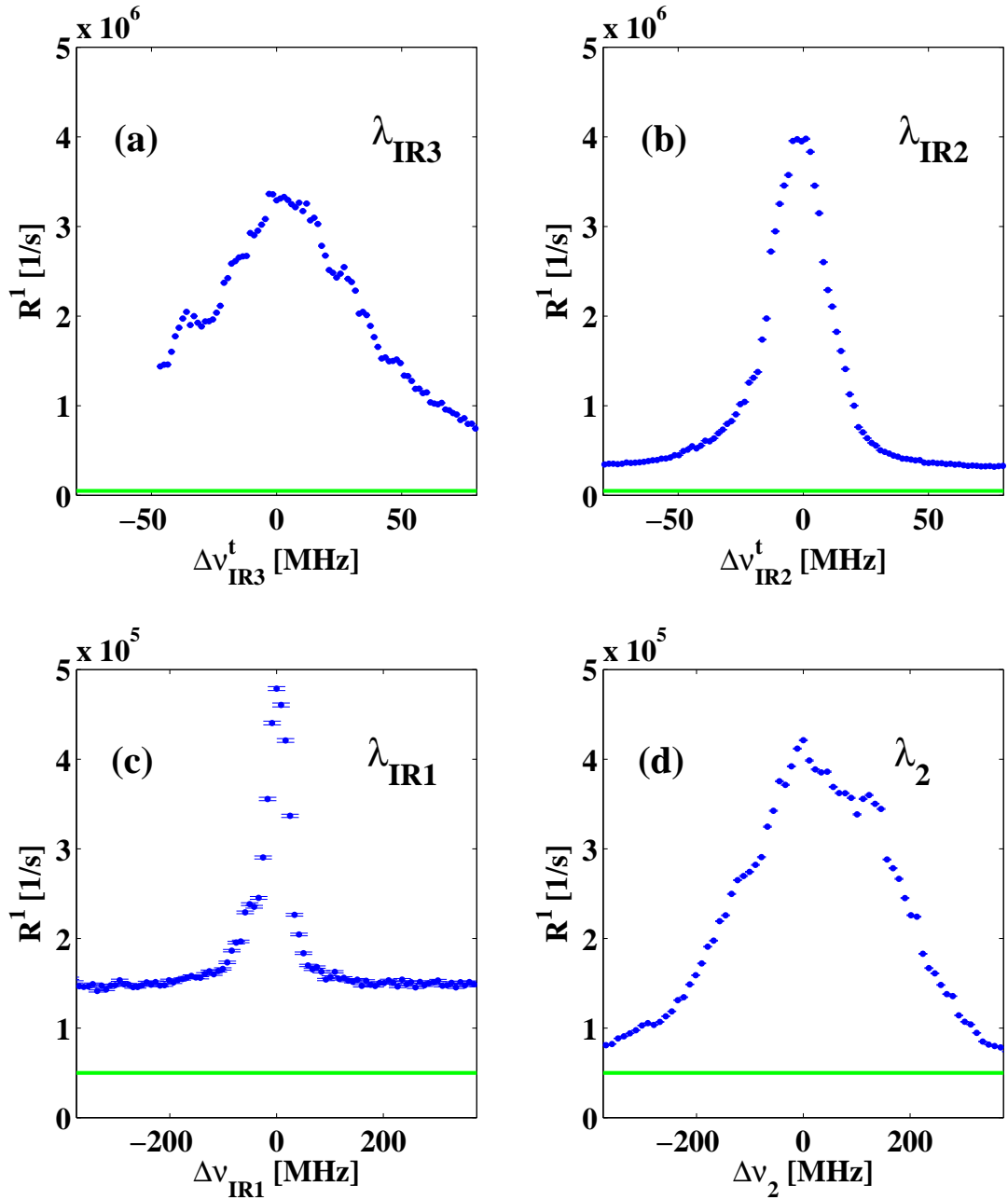


**Fig. 6.11:** Dependence of the fluorescence rate  $R^1$  on the detuning of a single repump laser. (a) Repumping the  $6s5d \ ^1D_2$  state at wavelength  $\lambda_{IR3}$ . The width (FWHM) of the spectrum is 65(6) MHz. (b) Repumping the  $6s5d \ ^3D_2$  state at wavelength  $\lambda_{IR2}$ . The width (FWHM) of the spectrum is 25(3) MHz. Repumping the  $6s5d \ ^3D_1$  state (c) at wavelength  $\lambda_{IR1}$  or (d) at wavelength  $\lambda_{IR1}$ . The widths (FWHM) are 53(5) MHz or 330(15) MHz respectively. The substructures in the spectra have been observed in a reproducible way in many of such scans. They could arise from coherent Raman transitions in the multiple  $\Lambda$  configuration.

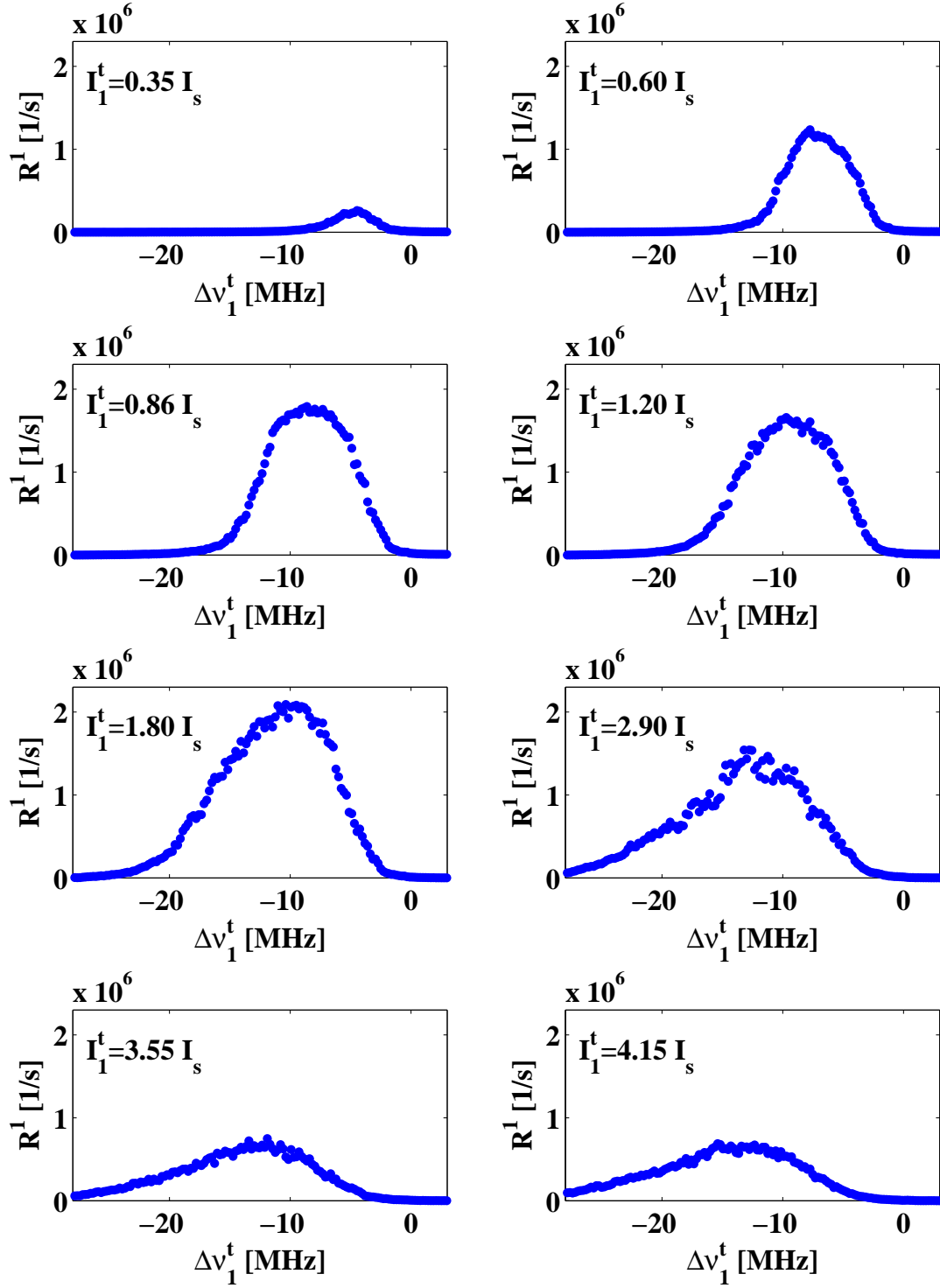


**Fig. 6.12:** Fluorescence at wavelength  $\lambda_1$  recorded from the trapped atoms as a function of frequency detuning  $\Delta\nu_1^t$  for different intensities  $I_1^t$ . The intensity  $I_1^t$  is given in units of the saturation intensity  $I_s$ . The magnetic field gradients, the intensities and the frequency detunings of all other laser beams were kept constant during the measurement.

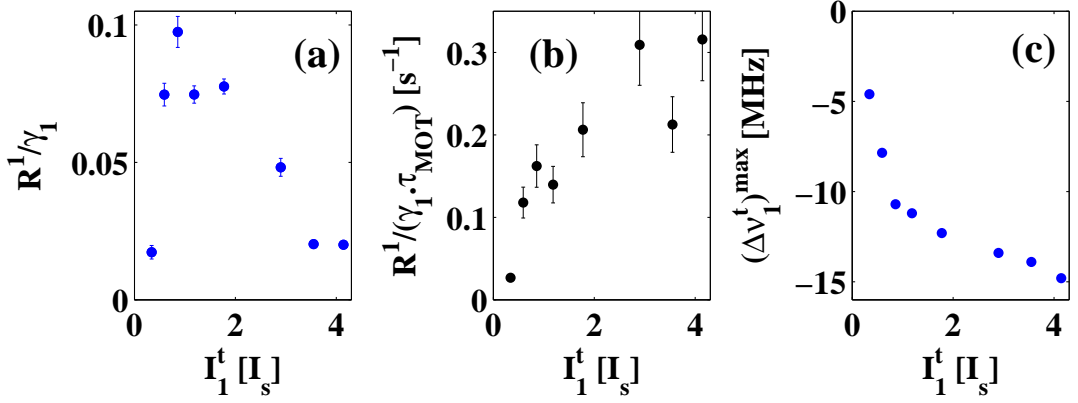


**Fig. 6.13:** Intensity dependence of (a) the number of trapped atoms, (b) the trap loading rate and (c) the frequency detuning  $(\Delta\nu_1^t)^{\text{max}}$  at the maximum number of trapped atoms. The trap population decreases with increasing intensity due to the short trap lifetime  $\tau_{\text{MOT}}$ .

#### 6.2.4 Trapping Laser Intensity

The radiative forces on the atoms increase towards higher intensities  $I_1^t$  in the trapping laser beams. It is expected that this leads to an increase of the capture velocity  $v_c$ . This would increase the loading rate  $L_{\text{MOT}}$  and the trapping efficiency. A measurement of the trap population  $N_{\text{MOT}}$  as a function of the trapping laser beam intensity  $I_1^t$  and the frequency detuning  $\Delta\nu_1^t$  can yield information on the trap loading process (see Fig. 6.12).

Increasing of the intensity  $I_1^t$  has several effects. In addition to the increase of the trap losses (see Section 6.2.2) the frequency detuning of the trapping laser beams at which the trapping population reaches its maximum shifts to larger red detunings,  $\Delta\nu_1^t(N_{\text{MOT}}^{\text{max}})$ , (see Fig. 6.13). The range of detunings for which atoms are trapped increases in a similar way. For the intensities of  $I_1^t$  up to  $4.2 \cdot I_s$  available in the experiments the optimum frequency detuning  $\Delta\nu_1^t$  is always less than the natural linewidth of the cooling transition. The number of trapped atoms  $N_{\text{MOT}}$  increases fast at low intensities and reaches a maximum around  $I_1^t = I_s$ . At higher intensities the population decreases again because of the trapping laser intensity  $I_1^t$  induced losses (see Fig. 6.13).

The loading rate  $L_{\text{MOT}}$  can be determined from the trap population  $N_{\text{MOT}}$  and the lifetime  $\tau_{\text{MOT}}$  (see Eqn. 6.23). The intensity dependence of  $\tau_{\text{MOT}}$  is taken explicitly into account (see Eqn. 6.17). The loading rate  $L_{\text{MOT}}$  increases monotonically over the range of intensities in the experiment (see Fig. 6.13 c). At the saturation intensity the loading rate is of the order of magnitude of

$L_{\text{MOT}} = 10^5 \text{ s}^{-1}$ . A more accurate number would require a significant calibration procedure.

### 6.2.5 Temperature of the Trapped Cloud

The temperature of the trapped atoms in a MOT is related to the characteristic velocity  $\tilde{v}$  (see Eqn. 4.2) of the atoms. The velocity  $\tilde{v}$  can be measured by release-and-recapture (R&R) methods [187, 189, 190] and time-of-flight (TOF) methods [187, 190, 191]. The trapped cloud is assumed to be described by a thermal gas in 3 dimensions

$$dN_{\text{gas}}(v) = N_0 \exp\left(-\frac{v^2}{2\tilde{v}^2}\right) dv, \quad (6.18)$$

where  $\tilde{v}$  is the characteristic velocity. The temperature  $T$  is then given by

$$T = \frac{m}{k_B} \cdot \tilde{v}^2, \quad (6.19)$$

where  $m$  is the mass of atoms and  $k_B$  is Boltzmann's constant. The atom velocity can be measured by releasing trapped atoms by turning off the trapping lasers and observe the time evolution of the expansion of the cloud.

#### Release-and-recapture Method

In this method the trapped atoms are released and the fraction remaining in the trapping volume is determined after a time  $t_{\text{off}}$ . Atoms are loaded into the MOT. At the time  $t = 0$  the trapping laser beams and the slowing laser beam at wavelength  $\lambda_1$  are switched off. In the dark the atomic cloud starts to expand. The densities are low and the velocity distribution is therefore not changed due to collisions. The distance,  $r(t)$ , of an atom from the trap center increases with time  $t$  as

$$r(t) = v \cdot t, \quad (6.20)$$

where  $v$  is the velocity of the atom. The spatial distribution of the cloud of atoms is found by substituting the velocity  $v$  with the radius  $r(t)$  in Eqn. 6.18

$$dN_{\text{gas}}(r) = \sqrt{\frac{2}{\pi}} \cdot \frac{r(t)^2}{t^3 \tilde{v}^3} \cdot \exp\left(-\frac{r(t)^2}{2 t^2 \cdot \tilde{v}^2}\right) dr. \quad (6.21)$$

The radius of the initial velocity distribution of atoms is assumed to be much smaller than the trap dimensions. The fraction,  $f(r_0, t_{\text{off}})$ , of atoms remaining

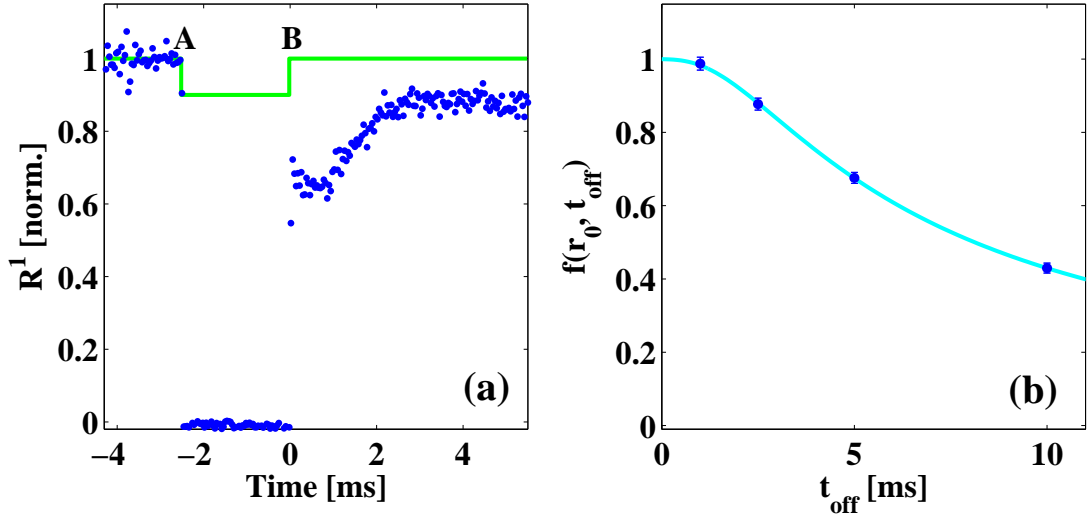


**Fig. 6.14:** Measurements of the MOT temperature. (a) The trapping laser beams were turned off in the period A-B for a time  $t_{\text{off}} = 2.5$  ms. After  $t = 0$  the increase of the signal is due to the recapture of atoms, which went out of the imaging region but still within the trapping volume. (b) Variation of the recapture fraction for different off periods  $t_{\text{off}}$  of the trapping laser beams. The solid line is a fit to the measured data points.

within a volume of radius  $r_0$  can be obtained<sup>1</sup> by integrating Eqn. 6.21

$$f(r_0, t_{\text{off}}) = \int_0^{r_0} \frac{dN_{\text{gas}}(r)}{dr} d^3r = \text{erf}\left(\frac{r_0^2}{\sqrt{2} t_{\text{off}} \tilde{v}}\right) - \sqrt{\frac{2}{\pi}} \cdot \frac{r_0}{t_{\text{off}} \tilde{v}} \cdot \exp\left(-\frac{r_0^2}{2t_{\text{off}}^2 \tilde{v}^2}\right). \quad (6.22)$$

The trapping and slowing laser beams are turned on again at the time  $\Delta t = t_{\text{off}}$ . Atoms which remain in the trapping volume are recaptured and drift back to the trap center. The time scale for transporting atoms is given by the drift velocities (see Eqn. 6.6) in the magnetic field of the MOT.

The trapping and slowing laser light at wavelength  $\lambda_1$  is switched off by AOM3 for the trapping laser beams and AOM2 for the slowing laser beam (see Fig. 4.2). The fluorescence at wavelength  $\lambda_1$  from the field of view of 2.5(2) mm is recorded as a function of time (see Fig. 6.14). Immediately after turning the trapping laser beams on the fluorescence of the atoms which remain in the field of view of the detection system is detected. The fluorescence increases within the next few ms due to the recapture of atoms which have not yet left the effective trapping volume. The temperature can be inferred from the fraction  $f(r_0, t_{\text{off}})$  of recaptured

<sup>1</sup>Since a clearcut definition of the radius,  $r_0$ , is not possible, the parameters obtained with this experimental method have an additional systematic uncertainty.

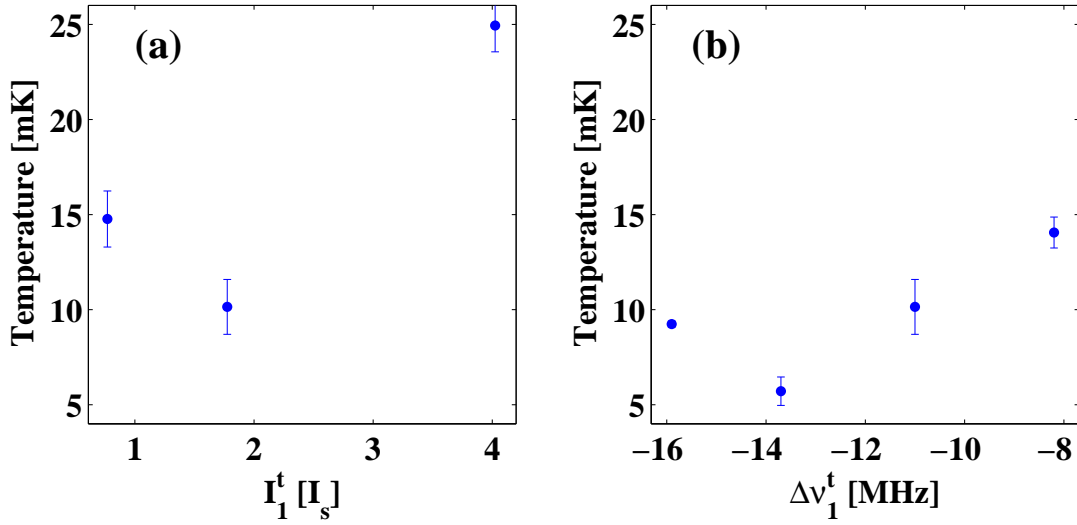


**Fig. 6.15:** (a) Variation of the trapped cloud temperature with the intensity  $I_1^t$  in the trapping lasers. Detuning of the trapping laser beams was constant  $\Delta\nu_1^t = -11$  MHz. (b) Variation of the temperature of the trapped cloud with the detuning  $\Delta\nu_1^t$  of the trapping lasers. The intensity in the trapping laser was  $I_1^t = 1.8 \cdot I_s$ .

atoms for different dark periods  $t_{\text{off}}$  (see Fig. 6.14)..

Note that the repumping laser beams are continuously on. Atoms in the metastable states can be transferred back to the ground state  $6s^2 \ ^1S_0$  during the time  $t_{\text{off}}$ . The fraction of atoms in the ground state  $6s^2 \ ^1S_0$  increases. The effect of this is seen in the first ms after turning on the trapping light at time  $t = t_{\text{off}}$ . The fluorescence rate is larger than expected for a recapture measurement, because the fraction of atoms in metastable states is negligible. The excess in the rate  $R^1$  is on the order a factor of two or about 50% of the atoms in the metastable states in the steady state of the multilevel laser cooling scheme. This is in agreement with the determination of this factor  $\rho_D$  in Section 6.2. A steady state is reached within about 500  $\mu\text{s}$ .

The MOT temperature varies with the intensity  $I_1^t$  and the frequency detuning  $\Delta\nu_1^t$  of the trapping laser light (see Fig. 6.15). All the measurements were performed at constant intensities for all the repumping laser beams, a magnetic field gradient of  $\alpha_z = 35$  G/A and a residual gas pressure of  $5 \cdot 10^{-9}$  mbar. The minimum achieved temperature of the trapped barium cloud was 5.7(8) mK at a frequency detuning of  $\Delta\nu_1^t = -13.5$  MHz and an intensity  $I_1^t = 1.8 \cdot I_s$  of the trapping laser beams.

The temperature of the atoms determined for the barium MOT is larger than the Doppler limit for the temperature  $T_D = 0.44$  mK. The derivation of the Doppler limit is based on an ideal two-level system for laser cooling [192–195], which is not the case for barium. Furthermore, temperatures of trapped atoms higher than the predicted Doppler limits have been observed for other isotopes with nuclear spin  $I = 0$ , e.g., calcium [196, 197] and strontium [198]. The ground state  $6s^2 \ ^1S_0$  of the cooling transition is nondegenerate and no sub-Doppler cooling forces are present. Thus, cooling relies on the simple optical molasses forces (see Eqn. 6.2), but intensity gradients in the counter-propagating trapping laser beams result in spatially dependent optical molasses forces which constitute an extra heating mechanism [199]. The intensity gradients in the laser beam can arise from dust particles on the optical surfaces.

### 6.2.6 Loading Efficiency of the MOT

The efficiency,  $\varepsilon_{\text{MOT}}$ , to transfer atoms from a thermal source into a MOT is affected by the deceleration of the atomic beam, the capture velocity  $v_c$  of the MOT and the losses from the trap. It can be analyzed for the experimental conditions of the barium MOT. Possibilities for increasing the efficiencies at each individual step are discussed in the respective sections.

The efficiency  $\varepsilon_{\text{MOT}}$  of the trap can be written as the loading rate  $L_{\text{MOT}}$  into the trap relative to the flux  $F_b$  in the thermal atomic beam. In steady state the population  $N_{\text{MOT}}$  and the trap lifetime  $\tau_{\text{MOT}}$  give the loading rate

$$L_{\text{MOT}} = \frac{N_{\text{MOT}}}{\tau_{\text{MOT}}}. \quad (6.23)$$

The trapping efficiency can be defined as

$$\varepsilon_{\text{MOT}} = \frac{N_{\text{MOT}}}{F_b \cdot \tau_{\text{MOT}}}. \quad (6.24)$$

The population  $N_{\text{MOT}}$  at a particular frequency detuning  $\Delta\nu_1^t$  and intensity  $I_1^t$  in the trapping laser beams can be extracted from the signal rate  $R^1$  (see Eqn. 6.7). If no atoms are in the trap, the incoming atomic flux,  $F_b$ , is determined from the fluorescence rate,  $R_{\text{beam}}^1$ , due to trapping laser beams which are orthogonal to the atomic beam. This can be achieved by detuning  $\Delta\nu_1^t$  of the trapping lasers light frequency or no deceleration of the atomic beam. This fluorescence rate from the beam is

$$R_{\text{beam}}^1 = \epsilon_1 \cdot \gamma_b(I_b) \cdot F_b \cdot \Delta t, \quad (6.25)$$

where  $\epsilon_1$  is the detection efficiency for the fluorescence at wavelength  $\lambda_1$ ,  $\gamma_b(I_b)$  is the scattering rate on resonance from the trapping laser beams at an intensity  $I_b$  and  $\Delta t$  is the interaction time of atoms in the atomic beam with the trapping laser beam. It is

$$\Delta t = \frac{d}{\langle v \rangle}, \quad (6.26)$$

where  $d$  is diameter of the region from where the fluorescence is collected and  $\langle v \rangle$  is average velocity of atoms in the atomic beam. The efficiency is then

$$\epsilon_{\text{MOT}} = \frac{R^1}{R_{\text{beam}}^1} \cdot \frac{\gamma_1(I_1^t, \Delta\nu_1^t)}{\gamma_b(I_b)} \cdot \frac{\Delta t}{\tau_{\text{MOT}}}. \quad (6.27)$$

The rates  $R^1$ ,  $R_{\text{beam}}^1$  and lifetime  $\tau_{\text{MOT}}$  are taken from measurements. The scattering rates  $\gamma_1$  and  $\gamma_b$  are estimated from the measured light intensities. The average interaction time of atoms with the orthogonal MOT beam is  $\Delta t = 10^{-5}$  s. The condition of trapping atoms as shown in Fig. 6.4 were  $I_1^t = 3.2 \cdot I_s$  and  $\Delta\nu_1^t = 6.0(5)$  MHz. The lifetime of the trap was  $\tau_{\text{MOT}} = 0.15(5)$  s. Neglecting that the scattering rate is reduced due to large populations in the metastable states, the ratio of the two scattering rates is  $\gamma_1(I_1^t, \Delta\nu_1^t) : \gamma_b I_b = 20(2) : 1$ . The efficiency of the MOT yields  $\epsilon_{\text{MOT}} = 0.40(15) \cdot 10^{-2}$ , where the largest contribution to the uncertainty arises from  $\tau_{\text{MOT}}$ . There is a limitation only due to the available optical power in the repumping laser beams.

### 6.3 Lifetime of the $5d^2 \ ^3F_2$ State

Cold atoms can be used to determine atomic properties of long lived excited states. The properties can be compared to atomic structure calculations, which are performed with increasing accuracy [95]. A measurement of lifetimes of states tests the quality of the theoretical calculations.

The  $5d^2 \ ^3F_2$  state is part of the decay chain of the  $5d6p \ ^3D_1^o$  state, which is populated in one of the employed laser cooling schemes. Lifetime of the  $5d^2 \ ^3F_2$  state was recently calculated to  $190 \ \mu\text{s}$  [95]. The small branching of the  $5d6p \ ^3D_1^o$  state to the state  $\zeta$  was determined by measurements in an atomic beam (see Section 5.1). The main content of the state  $\zeta$  is the  $5d^2 \ ^3F_2$  state (see Fig. 6.16). The contributions from  $6s5d \ ^1D_2$ ,  $5d^2 \ ^3P_0$ ,  $5d^2 \ ^3P_1$  and  $5d^2 \ ^3P_2$  states are expected to be minor and cannot be resolved in this experiment. A large fraction from these states cascades back to the cooling cycle. The lifetime and the branching fraction limits the benefit from this transition for slowing fast atoms. The thermal velocity of trapped atoms was determined to be below 1 m/s. Thus,

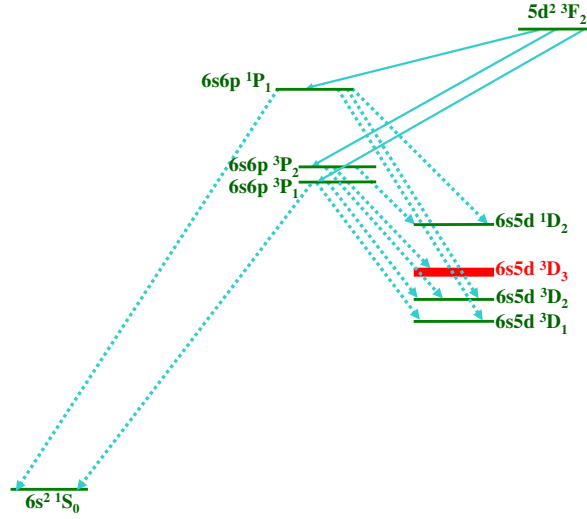
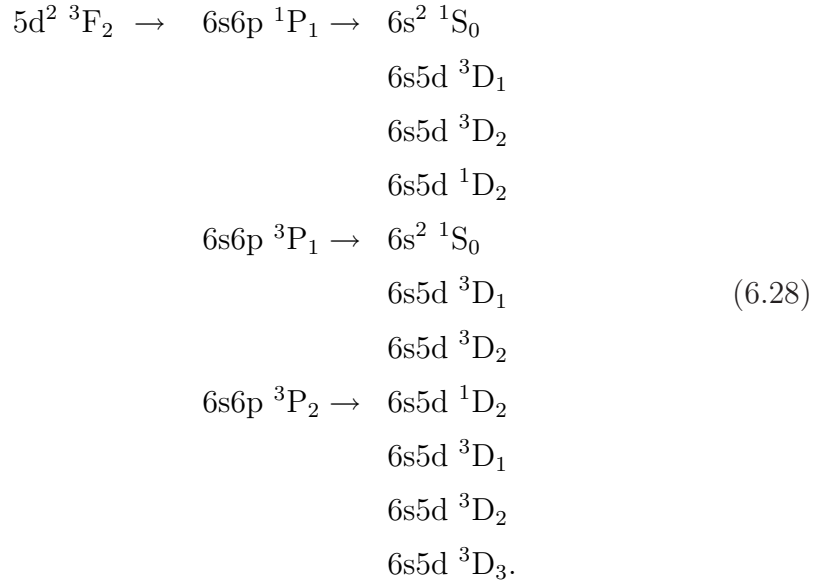


**Fig. 6.16:** Decay branching of the  $5d^2 \ ^3F_2$  state is indicated by solid lines. Cascading of atoms from the  $6s6p \ ^1P_1$ ,  $6s6p \ ^3P_1$  and  $6s6p \ ^3P_2$  states are indicated with dotted lines. Branching to the  $6s5d \ ^3D_3$  state (thick line) is the only loss from the cooling cycle.

they would travel by a distance of 0.2 mm within the lifetime of the  $5d^2 \ ^3F_2$  state and remain in the trapping region for many lifetimes.

The different channels for direct transition and cascading back into the cooling cycle or loss from the trap of the  $5d^2 \ ^3F_2$  population are



Only the branching into the long lived  $6s5d \ ^3D_3$  state is a loss from the cooling cycle. The characteristic decay time is dominated by the lifetime of the  $5d^2 \ ^3F_2$  state, since the lifetimes of the intermediate  $6s6p \ ^3P_1$  and the  $6s6p \ ^3P_2$  states are

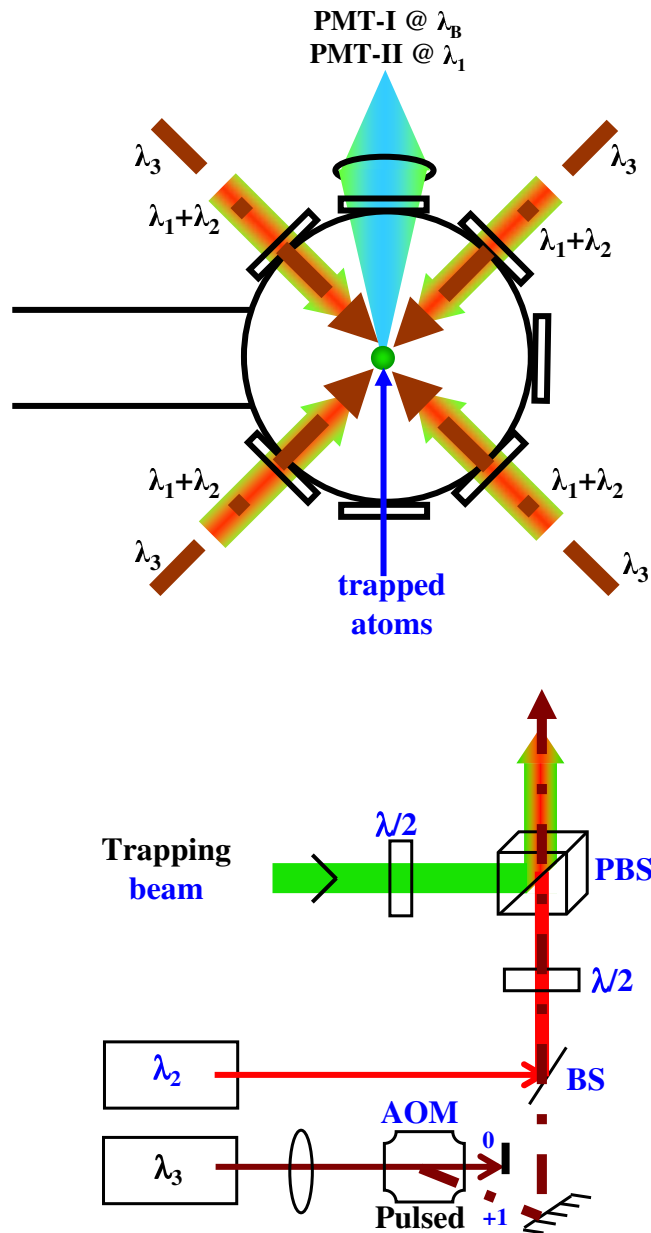


**Fig. 6.17:** Lifetime measurement of the  $5d^2 \ ^3F_2$  state. A laser pulse of around 1 ms duration at wavelength  $\lambda_3$  is generated by an acousto-optical modulator (AOM). The pulse optically pumps a large fraction of the trapped atoms to the long lived  $5d^2 \ ^3F_2$  state. This reduces the population in the cooling cycle and the fluorescence at wavelength  $\lambda_1$  from the MOT decreases. After the laser pulse the cooling cycle population increases with the characteristic time constant for the decay of the  $5d^2 \ ^3F_2$ .

Branching of $5d^2 \ ^3F_2$ state	Fraction [115]	Fraction [95]	Resultant of branching
$6s6p \ ^1P_1$	19%	2%	cooling cycle
$6s6p \ ^3P_1$	42%	89%	cooling cycle
$6s6p \ ^3P_2$	39%	9%	cooling cycle and loss
Branching of $6s6p \ ^3P_2$ state			
$6s5d \ ^1D_2$	$\ll 1\%$	$\ll 1\%$	cooling cycle
$6s5d \ ^3D_1$	2%	3%	cooling cycle
$6s5d \ ^3D_2$	17%	23%	cooling cycle
$6s5d \ ^3D_3$	81%	74%	trap loss
Branching of $5d^2 \ ^3F_2$ state			
Decay to $6s5d \ ^3D_3$ state	$\sim 31.6\%$	$\sim 6.7\%$	loss from the $5d^2 \ ^3F_2$ state

**Table 6.1:** Fractional branching for the decay cascade of the  $5d^2 \ ^3F_2$  state. Only the decay channel via the  $6s6p \ ^3P_2$  state to  $6s5d \ ^3D_3$  state results in losses from the cooling cycle. The last row summarizes the fractional loss from the cooling cycle. The values are taken from calculations which do not give uncertainties and are therefore of limited value.

on the order of  $1 \mu s$ . The branching fractions for these cascades can be found in literature (see Tables 3.4 and 3.5). The calculated losses to the  $6s5d \ ^3D_3$  state amount to 31.6% or 6.7% depending on the published value used (see Table 6.1).

The trapped sample of barium is prepared with laser cooling in the six-level subsystem. In steady state this produces a small fraction of atoms in the  $5d^2 \ ^3F_2$  state due to the repumping at wavelength  $\lambda_2$  (see Fig. 6.16). A larger population in the  $5d^2 \ ^3F_2$  state can be produced by optical pumping at the wavelengths  $\lambda_2$  and  $\lambda_3$ . The laser beam at wavelength  $\lambda_3$  passes through an acousto-optical modulator (AOM). The first order diffracted beam is overlapped with the repump laser beam at wavelength  $\lambda_2$  on a beam combiner (see Fig. 6.17). The laser light at wavelength  $\lambda_3$  can be switched on and off by the AOM in less than  $1 \mu s$  by switching the rf power to the AOM. A set of photomultiplier tubes detects fluorescence at the wavelengths  $\lambda_A$  and  $\lambda_B$  simultaneously from the trapped atoms.

The effective population of the  $5d6p \ ^3D_1^o$  state can be seen by fluorescence

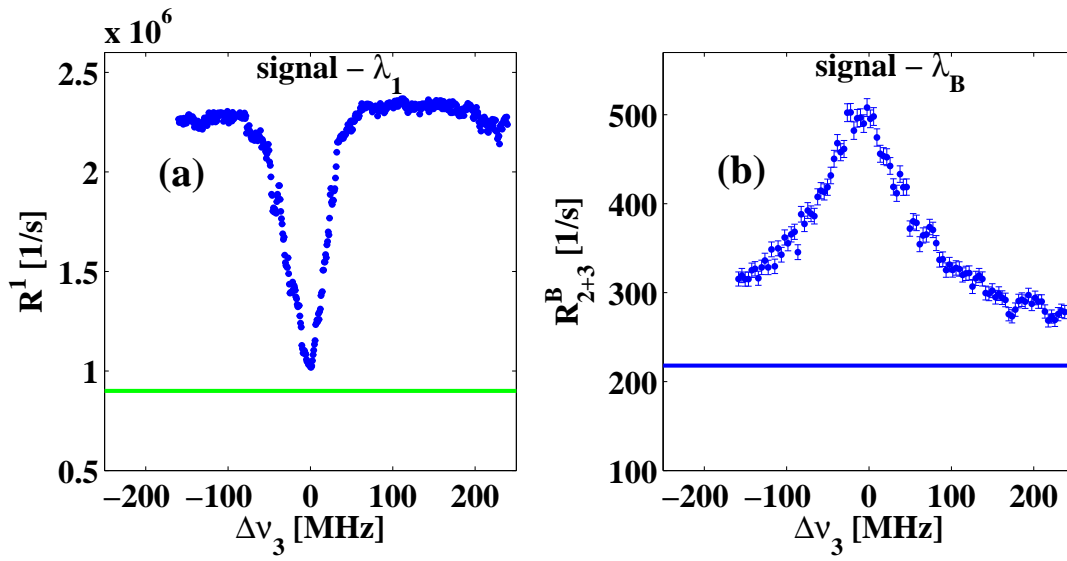


**Fig. 6.18:** The fluorescence from the trapped atoms depends on the detuning at wavelength  $\lambda_3$ . The MOT is prepared with the six-level cooling subsystem. (a) The fluorescence at wavelength  $\lambda_1$  decreases, if the laser at wavelength  $\lambda_3$  is on resonance. The increased losses shorten the trap lifetime and the steady state distribution. (b) The fluorescence at wavelength  $\lambda_B$  increases at the resonance, because of the strong optical pumping to the  $5d6p\ ^3D_1^o$  state. The horizontal line indicates the detected background photon levels.

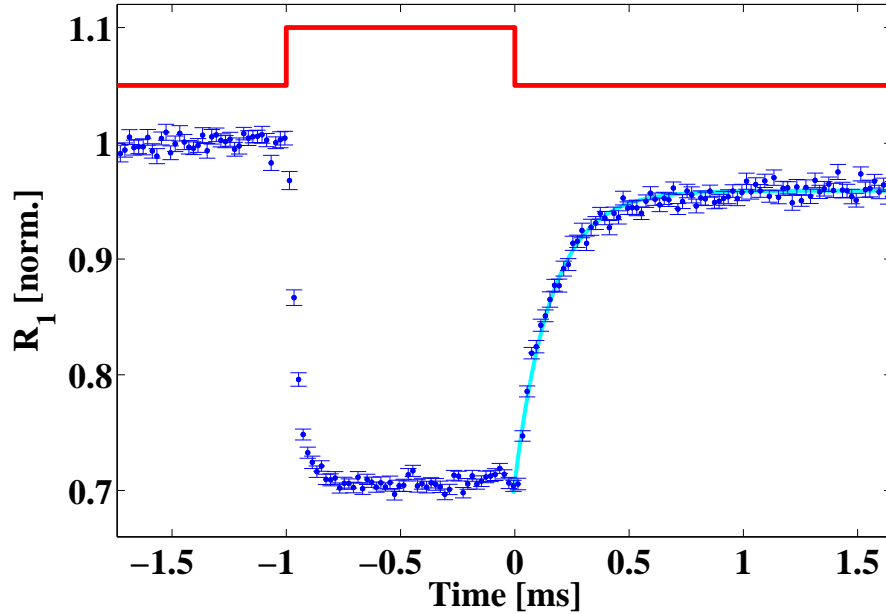


**Fig. 6.19:** Fluorescence from the trapped atoms detected at wavelength  $\lambda_1$  for pulsed excitation of the  $6s5d \ ^3D_2 \rightarrow 5d6p \ ^3D_1^o$  transition at wavelength  $\lambda_3$ . The solid line above the spectra indicates the on-off sequence of the laser pulse. The higher level is on and the lower level indicates the off. The MOT is loaded for several seconds. The laser at wavelength  $\lambda_1$  is at  $t = -1$  ms pulsed for a duration of 1 ms. The fluorescence from the MOT decreases and reaches a level of about 70%. After the end of the laser pulse the fluorescence increases to a lower level than before the pulse. The increase is fitted assuming an exponential decay of the of the  $5d^2 \ ^3F_2$  state. Here, the decay time is  $\tau_{3F_2} = 160(10) \ \mu\text{s}$  and the loss of atoms is  $L = 4.2(2)\%$ . The signals are normalized to the fluorescence level before the laser pulse.

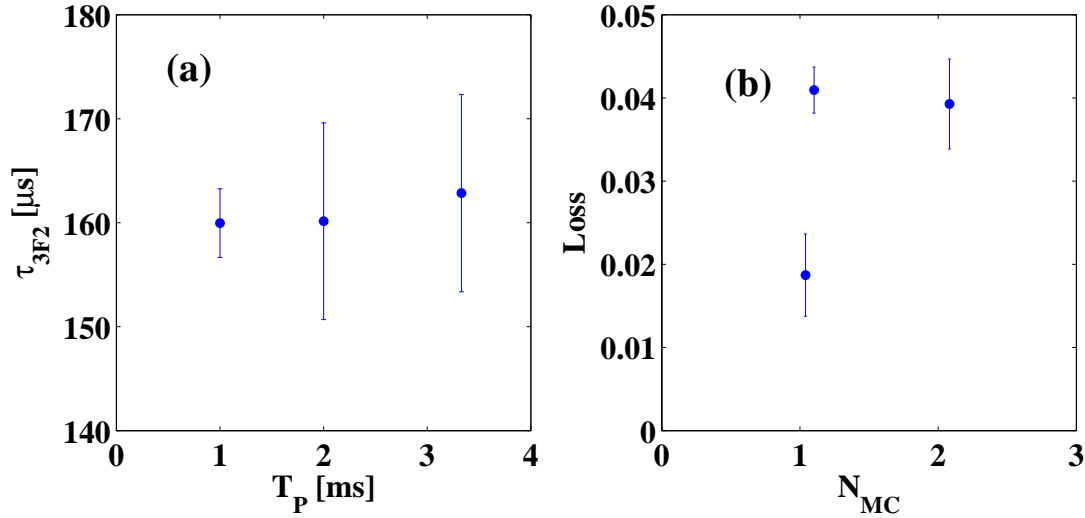


**Fig. 6.20:** (a) Lifetime  $\tau_{3F2}$  of the  $5d^2 \ ^3F_2$  state for different pulse length  $T_P$  of the excitation pulse of the laser at wavelength  $\lambda_3$ . (b) Loss  $\ell$  of atoms from the cooling cycle for different number of excitations  $N_{MC}$ .

from the trapped atoms at wavelength  $\lambda_B$ . The fluorescence depends on the frequency at wavelength  $\lambda_3$  (see Fig. 6.18). On resonance the fluorescence at wavelength  $\lambda_1$  decreases strongly, while the fluorescence at wavelength  $\lambda_B$  increases. The behavior can be understood qualitatively. The trap population is decreased due to the increased losses in the extended cooling cycle. A quantitative analysis would require the measurement of the populations in all states of the cooling cycle, which are not accessible from the measurements.

The lifetime of the  $5d^2 \ ^3F_2$  state can be measured with a pulsed excitation scheme. Atoms are loaded into the MOT for a period of several seconds when the laser beam at wavelength  $\lambda_3$  is switched off (see Fig. 6.6). The fluorescence of the MOT is detected at wavelength  $\lambda_1$ . At  $t = 0$  the laser beam at wavelength  $\lambda_3$  is switched on. The laser pulse of length  $T_p$  optically pumps the population of the  $6s5d \ ^3D_1$  and the  $6s5d \ ^3D_2$  states to the  $5d6p \ ^3D_1^o$  state. About half of the atoms decay directly to the ground state  $6s^2 \ ^1S_0$  and a major fraction from the other half populates the long lived  $5d^2 \ ^3F_2$  state (see Section 5.1). The atoms in the  $5d^2 \ ^3F_2$  state are removed from the cooling cycle and the fluorescence at wavelength  $\lambda_1$  from the MOT decreases (see Fig. 6.19). After the laser pulse the decay from the  $5d^2 \ ^3F_2$  state increases the population in the cooling cycle. The fluorescence increases with this characteristic decay time. The fluorescence saturates at a lower level than before the laser pulse. This missing fraction is the loss  $L$  of atoms during the excitation period  $T_p$ . The measurement cycle is

repeated for different pulse lengths. The contribution from the loading from the atomic beam can be estimated to be on the order of the ratio of the length of the measurement cycle to the trap lifetime  $\tau_{\text{MOT}}$ . The contribution to the population after about 3 ms is on the order of  $10^{-3}$ .

The part of the spectrum after  $t=0$  is described by an exponential decay and a loss fraction

$$s(t) = 1 - P_{3F_2} \exp(-t/\tau_C) - L, \quad (6.29)$$

where  $P_{3F_2}$  is the fraction of atoms in the  $5d^2 \ ^3F_2$  state,  $\tau_C$  is the characteristic decay constant for the cascade into the cooling cycle and  $L$  is the loss of atoms. The decay time  $\tau_C$  is the lifetime  $\tau_{3F_2}$  of the  $5d^2 \ ^3F_2$  state, since all other decay rates in the cascade are much faster than the lifetime  $\tau_{3F_2}$ . The lifetime was determined as  $\tau_{3F_2} = 160(10) \ \mu\text{s}$  (see Fig. 6.20), which is in good agreement with a recent calculation [95].

The depletion of the MOT fluorescence due to the laser pulse is a measure of the steady state population in the  $5d^2 \ ^3F_2$  state. The average number  $N_{\text{MC}}$  of excitations to the  $5d^2 \ ^3F_2$  state during the laser pulse at wavelength  $\lambda_3$  is

$$N_{\text{MC}} = \frac{\int_0^{T_P} s(t) dt}{\tau}, \quad (6.30)$$

where  $s(t)$  is the normalized signal (see Eqn. 6.29) and  $\tau$  is the average time required for cycling once through the  $5d^2 \ ^3F_2$  state. The cycling time  $\tau$  is the sum of the lifetime  $\tau_{3F_2}$  and the time required for pumping it into that state. The latter time can be estimated to be between 30 – 100  $\mu\text{s}$  since about 1100 photons scattered from the cooling transition at wavelength  $\lambda_1$  are sufficient to transfer ground state  $6s^2 \ ^1S_0$  atoms to the  $6s5d \ ^3D_1$  or the  $6s5d \ ^3D_2$  state. In the laser cooling process in a six level system the loss  $\ell$  from the cooling cycle for cycling once through the  $5d^2 \ ^3F_2$  state is

$$\ell = \frac{L}{N_{\text{MC}}}. \quad (6.31)$$

The loss  $\ell = 2.5(8)\%$  is determined from measurements at different pulse length  $T_P$ . The losses from the  $5d^2 \ ^3F_2$  state are larger by the ratio of  $(A_B + A_C)/A_C$ . Taking the values from Table 5.3 the cascading fraction from the  $5d^2 \ ^3F_2$  state to the  $6s5d \ ^3D_3$  state is 5.4(1.7)%, which is in agreement with the a recent theoretical calculation [95].

Trapped barium atoms could be used to study lifetimes and decay branching ratios also for other states with the same method. This would require to add power control to the light power for all lasers. The results of such measurements would be reliable input to test atomic structure calculations in the future.

## Summary and Conclusion

Efficient laser cooling and trapping of barium requires an extended cooling cycle of five or six states rather than two. Trapping of barium has been achieved with this complex cooling scheme using up to seven lasers simultaneously. The strong forces from the  $6s^2 \ ^1S_0 \rightarrow 6s6p \ ^1P_1$  transition facilitate an efficient trapping of barium atoms. The maximal force is reduced by about a factor of two compared to laser cooling in a simple two level system due to the large accumulation of population in the metastable D-states. The probability to capture an atom from a thermal atomic beam into the MOT is determined by the deceleration of the atoms in the beam and the capture velocity for the MOT. The achieved efficiency was 0.40(15)%. The loading rate  $L_{\text{MOT}}$  increases with a higher light intensity of the trapping laser beams at wavelength  $\lambda_1$ . Further improvements should be possible by transverse cooling of the atomic beam and white light cooling with frequency broadened lasers.

Trap lifetimes  $\tau_{\text{MOT}}$  of up to 1.5 s have been observed. The losses, which determine the lifetime  $\tau_{\text{MOT}}$  have been investigated. The main losses could be identified as escape of atoms from the trap while they are in one of the metastable states and losses which depend on the intensity of the trapping laser beams. The first losses can be reduced with a higher light power in the repumping laser beams which can be implemented for a dedicated experiment. The latter losses could be reduced with lower light intensities in the central part of the trapping laser beams only. The higher intensity away from the center could still facilitate large loading rates  $L_{\text{MOT}}$ . The lowest observed temperature of the trapped atoms was 5.7(8) mK. It is limited by intensity gradients in the trapping laser beams. This effect should be lower for isotopes with nuclear spin. In this case sub-Doppler cooling forces should be present and lower temperatures should be reachable. The decay of the excited  $5d^2 \ ^3F_2$  state could be investigated with the trapped atoms. The observed properties agree well with theoretical calculations. The techniques developed within this thesis demonstrate that the number of elements that can be optically cooled and trapped could be extended significantly.

# Chapter 7

## Outlook

The TRI $\mu$ P programme at KVI is focussed on fundamental interactions and symmetries. Searches for electric dipole moments (EDM's) provide important low energy possibility to study the CP and T symmetries in nature. This work contribute particularly to a structured approach towards a search for an EDM in radium isotopes. An indispensable step is the realization of an efficient laser cooling and trapping scheme for this heavy alkaline-earth atoms. Trapping of isotopes minimizes systematic uncertainties of EDM searches and an efficient collection of rare isotopes decreases the statistical uncertainties. The technical possibilities for trapping of radium have been investigated with the chemical homologue barium. It exhibits the same principal challenge as radium as far as optical cooling and trapping are concerned. Barium could be collected in a magneto-optical trap (MOT) for the first time in this work. In particular laser cooling was investigated with a many level atomic scheme and a multi laser system. Furthermore, several decay rates and lifetimes of excited states could be measured for barium as input for the verification of indispensable atomic structure calculations. The design of an efficient collection trap for radium isotope can now be based on the strong  $7s^2 \ ^1S_0 \rightarrow 7s7p \ ^1P_1$  transition for laser cooling. With the knowledge of the results from barium, a qualitative and quantitative analysis of the requirements for efficient laser cooling of radium becomes possible.

Laser cooling of barium and radium is challenging, due to leakage from the best suited strong  $ns^2 \ ^1S_0 \rightarrow nsnp \ ^1P_1$  ( $n=6, 7$ ) cooling cycle. As a remedy a closed subsystems of atomic levels was identified for barium, which includes several transitions driven at the same time by appropriate laser light. A closed system exists which includes the five states  $6s^2 \ ^1S_0$ ,  $6s6p \ ^1P_1$ ,  $6s5d \ ^1D_2$ ,  $6s5d \ ^3D_2$  and  $6s5d \ ^3D_1$ . A sixth state  $5d6p \ ^3D_1^o$  may be added for repumping the  $6s5d \ ^3D$

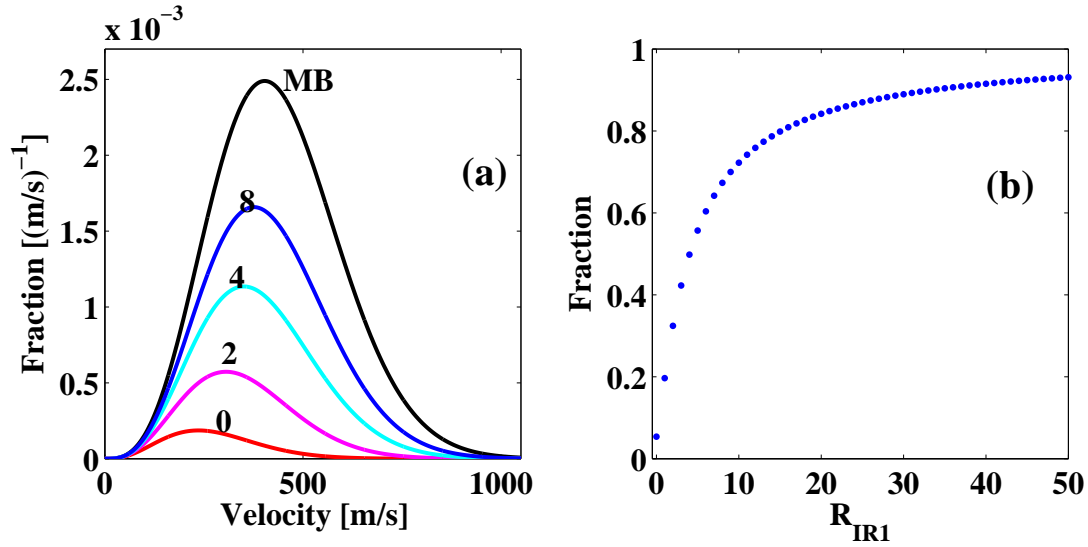


**Fig. 7.1:** In the case of barium: (a) velocity distribution  $f(v)$  of the decelerated atomic beam at different repumping  $R_{IR1}$  compared with a distribution in the Maxwell Boltzmann distribution. The numbers represent number of repumpings  $R_{IR1}$  from the  $6s5d\ ^3D_1$  state. (b) The total number of atoms into the cooling cycle can be regained with the repumping atoms from the  $6s5d\ ^3D_1$  state.

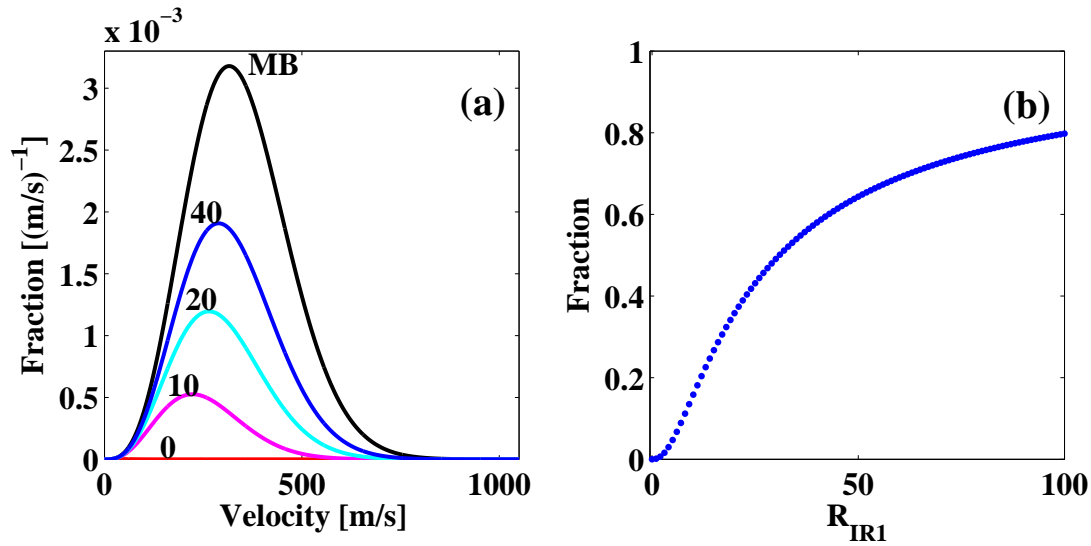


**Fig. 7.2:** In the case of radium: (a) velocity distribution  $f(v)$  of the decelerated atomic beam at different repumping  $R_{IR1}$  and the Maxwell Boltzmann distribution.  $R_{IR1}$  is the number of repumping from the  $7s6d\ ^3D_1$  state. (b) The gain of atoms into the cooling cycle with the repumping atoms from the  $7s6d\ ^3D_1$  state. Higher branching to the  $7s6d\ ^3D_1$  state forces to repump that state for an efficient slowing of the radium atomic beam.

states. The successful cooling scheme requires simultaneous control of several lasers, e.g., a dye laser, three fiber lasers and four diode lasers at the same time.

In order to apply the developed cooling techniques also to radium in the future the requirements for repumping needs to be analyzed. The probability,  $\rho_S(v)$ , of atoms in the ground state  $ns^2\ ^1S_0$  increases with repumping of the  $ns(n-1)d\ ^3D_1$  state, where the principle quantum number  $n = 6$  for barium and  $n = 7$  for radium. If an atom scatters  $n_1$  photons from the cooling transition this probability will be

$$\rho_S(v) = \exp\left(-\frac{n_1}{B_{IR1} \cdot R_{IR1}}\right), \quad (7.1)$$

where  $B_{IR1}$  is the branching to the  $^3D_1$  state relative to the total decay of the  $^1P_1$  state and  $R_{IR1}$  is the number of repump cycles from the  $^3D_1$  state during the deceleration. It is assumed that the  $^1D_2$  and the  $^3D_2$  states are repumped completely. The product of  $\rho_S(v)$  with the velocity distribution in the atomic beam  $\frac{dF_{\text{beam}}(v)}{dv}$  (see Eqn. 4.1) gives distribution of atoms in the decelerated atomic beam in their ground state  $ns^2\ ^1S_0$ , i.e.,

$$f(v) = \frac{dF_{\text{beam}}(v)}{dv} \cdot \rho_S(v) \cdot dv. \quad (7.2)$$

The integral over the decelerated velocity distribution  $f(v)$ , gives the total number of atoms into the cooling cycle. A quantitative estimate of the gain in slow atoms with repumping of the  $ns(n-1)d\ ^3D_1$  state is obtained for both barium and radium, which are shown in Figs. 7.1 and 7.2. As a main conclusion it has been noted that for an efficient deceleration of a radium atomic beam repumping of the  $7s6d\ ^3D_1$  state is necessary.

The maximum velocity,  $v_m$ , of atoms which can be stopped over a distance,  $S$ , at a deceleration,  $a_{\text{eff}} = v_r \cdot \gamma_{\text{eff}}$ , is

$$v_m = \sqrt{2 v_r \gamma_{\text{eff}} S}, \quad (7.3)$$

where  $v_r$  is the recoil velocity of atoms and  $\gamma_{\text{eff}}$  is average effective scattering rate from the cooling transition. In a slowing section of length  $S = 1$  m barium atoms of up to about  $v_m(\text{Ba}) = 320$  m/s can be stopped with our achieved scattering rate  $\gamma_{\text{eff}} = 10^7\ \text{s}^{-1}$  from the cooling transition. For radium it is  $v_m(\text{Ra}) = 250$  m/s with the same length and the same scattering rate.

The strong  $7s6d\ ^3D_1 \rightarrow 6d7p\ ^3D_1^o$  and the  $7s6d\ ^3D_2 \rightarrow 6d7p\ ^3D_1^o$  transitions in radium could be even better suited for repumping from the  $7s6d\ ^3D_1$  and the  $7s6d\ ^3D_2$  states than for barium. The energy difference of the  $6d7p\ ^3D_1^o$  to the

$6d^2\ ^3F_2$  state is smaller than for the respective states in barium, while branching to the ground state  $7s^2\ ^1S_0$  increases due to relativistic effects. This improves the ratio of branching to the ground state  $7s^2\ ^1S_0$  and to the other states  $\zeta$ , i.e.,  $A_B/A_\zeta$  compared to barium. The necessary laser wavelengths are in the visible range at 540.1 nm and 548.3 nm and are commercially available. In radium, the relative position of the lower lying states is the cause why atoms come back more frequently into the cooling cycle with the  $7s6d\ ^3D_1 \rightarrow 6d7p\ ^3D_1^o$  and the  $7s6d\ ^3D_2 \rightarrow 6d7p\ ^3D_1^o$  transitions than in barium.

An advantage of radium over barium is the possibility to use the weaker intercombination line  $7s^2\ ^1S_0 \rightarrow 7s7p\ ^3P_1$  for second stage cooling to achieve a lower temperature. This work has shown that laser cooling and trapping of radium will be possible following the techniques and principles established with barium. With the recent progress in the production chain of the isotopes  $^{210}\text{Ra}$  to  $^{215}\text{Ra}$  at the TRI $\mu$ P facility at KVI [37] a sensitive radium EDM experiment appears to be possible.

# Appendix A

## Numerical Calculation: Magnetic Field

The magnetic induction,  $B(\vec{r})$ , produced by a pair of coils such as it was employed in the experiments can be calculated by numerical integration of the Biot-Savart law. The results were compared to the field strengths measured by the Zeeman splitting of the  $6s^2\ ^1S_0 \rightarrow 6s6p\ ^1P_1$  transition in barium (see Section 4.5).

According to the law of Biot-Savart the vector potential,  $\vec{A}(\vec{r})$ , produced by a single current carrying loop is

$$\vec{A}(\vec{r}) = \frac{\mu_0}{4\pi} \int \frac{\vec{J}}{|\vec{r}'|} \cdot d\vec{r}', \quad (\text{A.1})$$

where  $\vec{J}$  is the current density of a current  $I$  flowing through the loop,  $\vec{r}$  is position vector and  $\mu_0$  is free space permeability. The corresponding magnetic induction  $\vec{B}(\vec{r})$  can be obtained by applying Maxwell's equation for the magnetic induction

$$\vec{B}(\vec{r}) = \vec{\nabla} \times \vec{A}(\vec{r}). \quad (\text{A.2})$$

In particular for a single loop of radius  $R$  perpendicular to the  $z$ -axis at a distance  $d$  from the origin of the reference frame, the axial, radial and azimuthal components  $B_z$ ,  $B_\rho$  and  $B_\phi$  of the magnetic induction can be written as [201, 202]

$$B_z = \frac{\mu_0 I}{2\pi} \cdot \frac{1}{[(R + \rho)^2 + (z - d)^2]^{1/2}} \cdot \left[ K(\kappa^2) + \frac{R^2 - \rho^2 - (z - d)^2}{(R - \rho)^2 + (z - d)^2} \cdot E(\kappa^2) \right], \quad (\text{A.3})$$

$$B_\rho = \frac{\mu_0 I}{2\pi \rho} \cdot \frac{(z - d)}{[(R + \rho)^2 + (z - d)^2]^{1/2}} \cdot \left[ -K(\kappa^2) + \frac{R^2 + \rho^2 + (z - d)^2}{(R - \rho)^2 + (z - d)^2} \cdot E(\kappa^2) \right], \quad (\text{A.4})$$

and

$$B_\phi = 0, \quad (\text{A.5})$$

where  $I$  is the current through the loop,  $K(\kappa^2)$  and  $E(\kappa^2)$  are the complete elliptic integrals of first and second kind of the integrant

$$\kappa^2 = \frac{4 R \rho}{[(R + \rho)^2 + (z - d)^2]}. \quad (\text{A.6})$$

The azimuthal field component  $B_\phi$  is zero due to the cylindrical symmetry of the current loop. The axial and radial components are independent of the azimuthal angle  $\phi$ .

Eqns. A.3 and A.4 are integrated over the current density distribution to obtain the magnetic induction. The field calculations were performed for a coil arrangement close to Helmholtz configuration and to anti-Helmholtz configuration. Zeeman splitting spectroscopy for field calibration was done for the coils operated in the first mode, while the later was used for trapping. The gradients can be determined from the calculated field profiles.

## Appendix B

# Calibration Quantum Efficiency of the PMT

The quantum efficiency,  $\varepsilon_i(\lambda_i)$ , is the number of emitted photo-electrons due to a single incident photon at wavelength  $\lambda_i$ . This is a very specific quantity for individual photocathodes, even if they are made from the same material. In particular the chemical properties of the coating on the photocathode and the production conditions have strong influence. The relative quantum efficiencies of a particular PMT at the two different wavelengths  $\lambda_1$  and  $\lambda_B$  are essential input for several experiments in this work (see Section 5.1). For that purpose the relative quantum efficiencies,  $\varepsilon_1/\varepsilon_B$ , of the PMT used in the experiment was measured.

Radiation from the hot tungsten filament in an evacuated commercial light bulb was used as an ideal black body radiator. For such a light bulb there are no other cooling mechanisms for the filament other than radiation. The dissipated

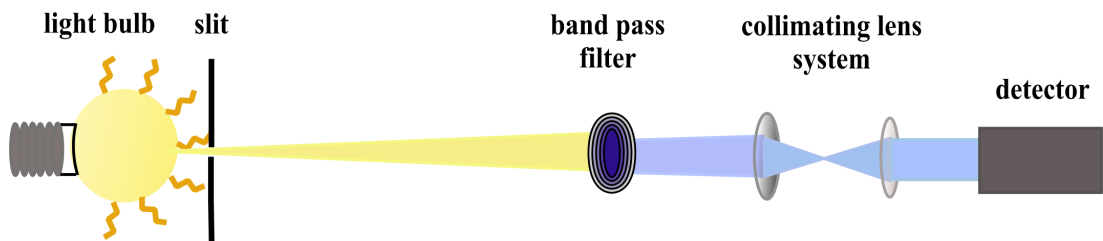


**Fig. B.1:** Setup for measuring the relative quantum efficiency of a photomultiplier. Well defined spectral range are selected by band pass filters from the radiation spectrum of a light bulb. The collimated radiation is detected either with a calibrated photodiode or the PMT, which is being calibrated.

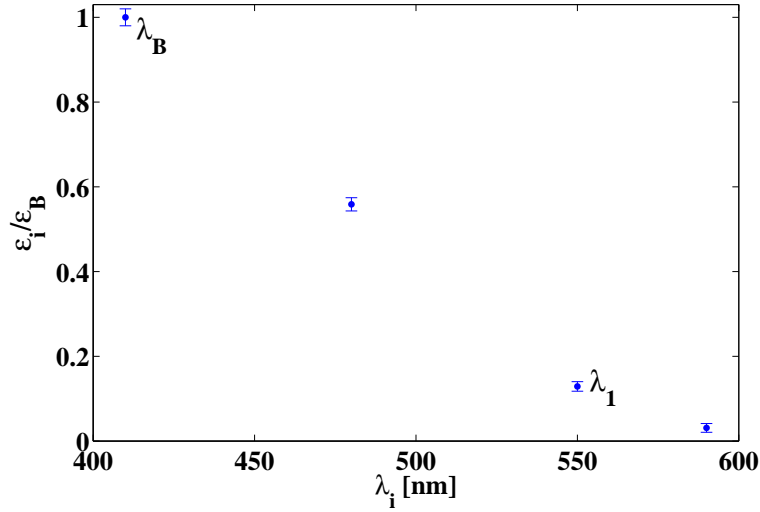


**Fig. B.2:** Relative quantum efficiency of the photomultiplier tube used in the experiments. The wavelengths  $\lambda_B$  and  $\lambda_1$  of the detected fluorescence were selected with interference filters transmitting the wavelength bands  $(410 \pm 10)$  nm and  $(550 \pm 10)$  nm.

electrical power  $W$  in the bulb is the same as the radiated power,  $P$ , which determines the temperature,  $T$ , of the filament

$$P = W = \alpha \cdot \sigma T^4. \quad (\text{B.1})$$

Here  $\sigma$  is the Stefan-Boltzman constant and  $\alpha$  is the ratio between the absolute power radiated by the filament and the measurable electrical power supplied to the bulb. For a light bulb  $\alpha \simeq 1$  in the spectral region 480 nm to 590 nm. The radiated photon flux is the integral of the Planck distribution over the spectral band  $\Delta\lambda$

$$U(\lambda, T) = \int \frac{2h c^2}{\lambda^5} \cdot \left[ \exp\left(\frac{hc}{\lambda k_B T}\right) - 1 \right]^{-1} d\lambda \quad (\text{B.2})$$

where  $h$  is Planck's constant,  $c$  is the speed of light and  $k_B$  is Boltzmann's constant.

A small fraction of the radiation spectrum of a distant light bulb is selected for the measurement. A spectral range  $\lambda \pm \Delta\lambda$  of the spectral distribution is selected by a band pass filter, which has a transmission bandwidth of  $2 \cdot \Delta\lambda = 10$  nm. A pair of lenses collimate the selected light onto the detector. A calibrated photodiode or the PMT detect the radiation spectrum.

The calibration was performed in two stages. First, the optical power transmitted through four different band pass filters,  $F_{410}$ ,  $F_{480}$ ,  $F_{550}$  and  $F_{590}$ , were

measured. The central wavelengths of their respective transmission are 410 nm, 480 nm, 550 nm and 590 nm. A calibrated photodiode, which is a light power meter LaserMate-Q (from Coherent Inc., Palo Alto, USA), is used to measure the optical power  $U(\lambda, T)$ . In a second step the count rate,  $C(\lambda, T)$ , for the PMT R7205-01 (from Hamamatsu Corp., Shizuoka, Japan) was measured for the same optical power  $U(\lambda, T)$ . The measurements were repeated for many different filament temperatures. The characteristic temperature dependence  $U(\lambda, T)$  (see Eqn. B.3) can be used to determine the absolute temperature of the filament. The relative quantum efficiency  $\varepsilon_i/\varepsilon_j$  at the two different wavelengths  $\lambda_i$  and  $\lambda_j$  were obtained by comparing measurements at a fixed temperature  $T_o$ .

$$\frac{\varepsilon_i}{\varepsilon_j} = \frac{C(\lambda_i, T_o)}{U(\lambda_i, T_o)} \cdot \frac{U(\lambda_j, T_o)}{C(\lambda_j, T_o)}. \quad (\text{B.3})$$

The calibrated quantum efficiencies of the PMT are  $\varepsilon(480 \text{ nm}) = 0.55(3)$  (filter  $F_{480}$ ),  $\varepsilon(550 \text{ nm}) = 0.13(2)$  (filter  $F_{5500}$ ) and  $\varepsilon(590 \text{ nm}) = 0.03(2)$  (filter  $F_{590}$ ) relative to the quantum efficiency at wavelength 410 nm (filter  $F_{410}$ ). The filters  $F_{410}$  and  $F_{5500}$  select the fluorescence at the wavelengths  $\lambda_B$  and  $\lambda_1$  used in the experiments with barium. The relative quantum efficiency at the two detected wavelengths  $\lambda_1$  and  $\lambda_B$  is  $\varepsilon_1/\varepsilon_B = 0.13(2)$ .



# Appendix C

## Atom-Photon Interactions

In this appendix the basic equations relevant for laser cooling and trapping are given. For a detailed discussion see the references as given to literature [169, 170, 200]. Deceleration of atoms with laser light arises from the momentum transfer of photons to the atom. The recoil velocity of an atom with mass,  $m$ , due to scattering of a single photon is

$$v_r = \frac{\hbar k}{m}. \quad (\text{C.1})$$

The photon scattering rate of an atom from a single laser beam can be written as

$$\gamma_p = \gamma \cdot \frac{\Omega^2}{\gamma^2 + 2\Omega^2 + 4\delta^2}, \quad (\text{C.2})$$

where  $\gamma = 1/\tau$  is the decay rate of the upper state,  $\delta$  is the frequency detuning of the light from the atomic resonance and  $\Omega$  is the Rabi frequency. The Rabi frequency depends on the light intensity,  $I$ , and the decay rate  $\gamma$ . The saturation parameter at a light intensity  $I$  is

$$S_0 = \frac{I}{I_s} = \frac{2\Omega^2}{\gamma^2}, \quad (\text{C.3})$$

where  $I_s$  is the saturation intensity of the transition. The scattering rate can be written as

$$\gamma_p(S_0, \delta) = \frac{\gamma}{2} \cdot \frac{S_0}{1 + S_0 + (\frac{2\delta}{\gamma})^2}. \quad (\text{C.4})$$

The time averaged optical force on an atom is determined by

$$\vec{F}(S_0, \delta) = \gamma_p(S_0, \delta) \cdot \hbar \vec{k}, \quad (\text{C.5})$$

where  $\vec{k}$  is the wave vector of the transition at wavelength  $\lambda$  and  $\hbar$  is Planck's constant. The optical force  $\vec{F}(S_0, \delta)$  yields a maximum acceleration of

$$a_{\max} = v_r \cdot \frac{\gamma}{2}. \quad (\text{C.6})$$

Characteristic values	Numerical values
Natural linewidth $\Gamma$	18.33 MHz
Saturation intensity $I_s$	14.12 mW/cm <sup>2</sup> , i.e., $S_0 = 1$
Recoil velocity $v_r$	0.0052 m/s
Maximum scattering rate $\frac{\gamma}{2}$	$6 \cdot 10^7 \text{ s}^{-1}$ at $S_0 \gg 1$
Deceleration $a_{\text{max}}$	$310 \cdot 10^3 \text{ m/s}^2$
Doppler velocity $v_D$	0.163 m/s
Doppler temperature $T_D$	0.44 mK

**Table C.1:** Characteristic laser cooling parameters for the barium atom obtained with the simplifying assumption of a two level system formed by the  $6s^2 \ ^1S_0$  and the  $6s6p \ ^1P_1$  states.

The necessary minimal distance  $S$  to decelerate atoms from an initial velocity  $v_0$  is

$$S = \frac{1}{2} \frac{v_0^2}{a_{\text{max}}}. \quad (\text{C.7})$$

The optical force from counter-propagating laser beams can be used to bring atoms to rest. The Doppler cooling theory [192–195] predicts a lowest temperature for atoms in an optical molasses. This temperature is

$$T_D = \frac{\hbar}{k_B} \cdot \frac{\gamma}{2}, \quad (\text{C.8})$$

where  $m$  is the atomic mass. The velocity of atoms corresponding to this temperature is

$$v_D = \sqrt{\frac{\hbar}{m} \cdot \frac{\gamma}{2}}, \quad (\text{C.9})$$

where  $k_B$  is Boltzmann's constant. The minimum velocity  $v_D$  and temperature  $T_D$  given here are for atoms without sublevels in their ground state. The characteristic values for barium under the simplifying assumption of a two level system are given in Table C.1.

# Bibliography

- [1] S. Glashow, Nucl. Phys. **22**, 579 (1961).
- [2] S. Weinberg, Phys. Rev. Lett. **19**, 1264 (1967).
- [3] A. Salam, Elementary Particle Theory: Relativistic Groups and Analyticity, N.Svartholm, Almquist and Wiksell, Stockholm, Nobel symposium 8 (1968).
- [4] G. 't Hooft, and M. Veltman, Nucl. Phys. B **44**, 189 (1972).
- [5] Y. Ashie, (The Super-Kamiokande Collaboration), Phys. Rev. Lett. **93**, 101801 (2004).
- [6] H. P. Nilles, Phys. Rep. **110**, 1 (1984).
- [7] R. N. Mohapatra, and J. C. Pati, Phys. Rev. D **11**, 2558 (1975).
- [8] T. D. Lee, and C. N. Yang, Phys. Rev. **104**, 254 (1956).
- [9] C. S. Wu, E. Ambler, R. W. Hayward, D. D. Hoppes, and R. P. Hudson, Phys. Rev. **105**, 1413 (1957).
- [10] J. H. Christenson, J. W. Cronin, V. L. Fitch, and R. Turlay, Phys. Rev. Lett. **13**, 138 (1964).
- [11] S. Weinberg, Phys. Rev. Lett. **37**, 657 (1976).
- [12] A. D. Sakharov, JETP Lett. **5**, 24 (1967).
- [13] I. B. Kriplovich, and S. K. Lamoreaux, "CP Violation Without Strangeness: Electric Dipole Moments of Particles, Atoms and Molecules", Berlin: Springer, (1997).
- [14] W. Pauli, Nuovo Cimento **6**, 204 (1957).

- [15] V. V. Flambaum, Phys. Rev. A **60**, R2611 (1999).
- [16] J. Engel, J. L. Friar, and A. C. Hayes, Phys. Rev. C **61**, 035502 (2000).
- [17] J. Dobaczewski, and J. Engel, Phys. Rev. Lett. **94**, 232502 (2005).
- [18] V. A. Dzuba, V. V. Flambaum, and J. S. M. Ginges, Phys. Rev. A **61**, 062509 (2000).
- [19] V. A. Dzuba, V. V. Flambaum, J. S. M. Ginges, and M. G. Kozlov, Phys. Rev. A **66**, 012111 (2002).
- [20] C. E. Moore, Atomic Energy levels, **Vol III**, Natl. Stand. Ref. Data Ser., Nat. Bur. Stand. (U.S.), **No. 35** (1971); reprint of Natl. Bur. Stand. (U.S.) Circ. 467 (1958). This references are compilation of the measurements by E. Rasmussen [77, 78] and analysis by H. N. Russel [79].
- [21] M.V. Romalis, W. C. Griffith, J. P. Jacobs, and E. N. Fortson, Phys. Rev. Lett. **86**, 2505 (2001).
- [22] G. P. A Berga, P. Dendooven, O. Dermois, M. N. Harakeh, R. Hoekstra, S. Hoekstra, K. Jungmann, S. Kopecky, V. Kravchuk, R. Morgenstern, A. Rogachevskiy, L. Willmann, and H. W. Wilschut, Nucl. Phys. A **721**, 1107 (2003).
- [23] L. Willmann, G. P. Berg, U. Dammalapati, S. De, P. Dendooven, O. Dermois, K. Jungmann, A. Mol, C. J. G. Onderwater, A. Rogachevskiy, M. Sohani, E. Traykov and H.W. Wilschut; Conference proceeding of COOL05 Workshop, AIP conference proceedings, arXiv : physics/0602022, (2005).
- [24] G. P. A. Berg, O.C. Dermois, U. Dammalapati, P. Dendooven M. N. Harakeh, K. Jungmann, C. J. G. Onderwater, A. Rogachevskiy, M. Sohani, E. Traykov, L. Willmann, and H. W. Wilschut, Nucl. Instrum. Meth. A **560**, 169 (2006).
- [25] M. Sohani, Acta Physica Polonica B **137**, 1001 (2006).
- [26] G. P. Berg, U. Dammalapati, S. De, S. Dean, P. Dendooven, O. Dermois, K. Jungmann, A. Rogachevskiy, M. Sohani, E. Traykov,

- L. Willmann, and H.W. Wilschut, AIP conference proceedings, **831**, (2006).
- [27] G. P. A. Berg, U. Dammalapati, S. De, S. Dean, P. Dendooven, O. Dermois, K. Jungmann, A. Rogachevski, M. Sohani, E. Traykov, L. Willmann, and H. W. Wilschut, AIP conference proceedings **831**, 403 (2006).
- [28] H. W. Wilschut, U. Dammalapati, S. De, P. Dendooven, O. Dermois, K. Jungmann, A. J. Mol, C. J. G. Onderwater, A. Rogachevskiy, M. da Silva, M. Sohani, E. Traykov and L. Willmann, *Hyperfine Interact.* **174**, 97 (2007).
- [29] E. Traykov, A. Rogachevskiy, M. Bosswell, U. Dammalapati, P. Dendooven, O. C. Dermois, K. Jungmann, C. J. G. Onderwater, M. Sohani, L. Willmann, H. W. Wilschut, and A. R. Young, *Nucl. Instrum. Meth. A* **572**, 580 (2007).
- [30] E. Traykov, U. Dammalapati, S. De, O. C. Dermois, L. Huisman, K. Jungmann, W. Kruithof, A. J. Mol, C. J. G. Onderwater, A. Rogachevskiy, M. da Silva e Silva, M. Sohani, O. Versolato, L. Willmann, and H. W. Wilschut; XVth International EMIS, arXiv : 0709.3669, (2007).
- [31] E. Traykov, U. Dammalapati, S. De, O. C. Dermois, L. Huisman, K. Jungmann, W. Kruithof, A. J. Mol, C.J.G. Onderwater, A. Rogachevskiy, M. da Silva e Silva, M. Sohani, O. Versolato, L. Willmann, and H. W. Wilschut; XVth International EMIS 2007, arXiv : 0709.3670, (2007).
- [32] H. W. Wilschut, and K. Jungmann, *Nucl. Phys. News* **17**, 11 (2007).
- [33] E. Traykov, "Production of radioactive beams for atomic trapping", doctoral thesis, University of Groningen, Netherlands (2006).
- [34] A. Rogachevskiy, "Production and trapping of Na isotopes for  $\beta$ -decay studies", doctoral thesis, University of Groningen, Netherlands (2007).

- [35] M. Sohani, "Setup for precise measurements of  $\beta$ -decay in optically trapped radioactive Na", doctoral thesis, University of Groningen, Netherlands (2008).
- [36] A. Rogachevsky, "Production of  $^{213}\text{Ra}$ ", masters thesis, KVI, University of Groningen (2002).
- [37] H. W. Wilschut, private communication (2008).
- [38] E. M. Purcell, and N. F. Ramsey, Phys. Rev. **78**, 807 (1950).
- [39] N. F. Ramsey, Phys. Rev. **109**, 222 (1958).
- [40] L. Landau, Nucl. Phys. **3**, 127 (1958).
- [41] T. G. Vold, F. J. Raab, B. Heckel, and E. N. Fortson, Phys. Rev. Lett. **52**, 2229 (1984).
- [42] T. Chupp, and C. Svensson, "Measurements with Rare Isotopes: The Radon-EDM Experiment", Research proposal E-929, TRIUMF, Canada (2006).
- [43] H. S. Nataraj, B. K. Sahoo, B. P. Das, and D. Mukherjee, accepted in Phys. Rev. Lett., arXiv : 0804.0998, (2008).
- [44] A. Dilip, B. P. Das, W. F. Perger, M. K. Samal, and K. P. Geetha, J. Phys. B: At. Mol. Opt. Phys. **34**, 3089 (2001).
- [45] T. M. R. Byrnes, V. A. Dzuba, V. V. Flambaum, and D. W. Murray, Phys. Rev. A **59**, 3082 (1999).
- [46] V. V. Flambaum, Phys. Rev. A **77**, 024501 (2008).
- [47] D. Cho, K. Sangster, and E. A. Hinds, Phys. Rev. A **44**, 2783 (1991).
- [48] S. A. Murthy, D. Krause, Jr., Z. L. Li, and L. R. Hunter, Phys. Rev. Lett. **63**, 965 (1989).
- [49] L. Willmann, Research proposal, "Precision spectroscopy of radium and the radium ion: investigating fundamental symmetries in nature", KVI, Groningen, Netherlands (2003).

- [50] I. Ahmad, ( $^{225}\text{Ra}$  EDM collaboration), <http://www-mep.phy.anl.gov/atta/research/radiumedm.html>, Argonne National Laboratory, Argonne, USA (2000).
- [51] B. C. Regan, Eugene D. Commins, Christian J. Schmidt, and David DeMille, *Phys. Rev. Lett.* **88**, 071805 (2002).
- [52] R. McNabb, arXiv : Physics/0407008, (2004).
- [53] K. Inami, (Belle collaboration), *Phys. Lett. B* **551**, 16 (2002).
- [54] C. A. Baker, D. D. Doyle, P. Geltenbort, K. Green, M. G. D. van der Grinten, P. G. Harris, P. Iaydjiev, S. N. Ivanov, D. J. R. May, J. M. Pendlebury, J. D. Richardson, D. Shiers, and K. F. Smith, *Phys. Rev. Lett.* **97**, 131801 (2006).
- [55] D. Cho, K. Sangster, and E. A. Hinds, *Phys. Rev. Lett.* **63**, 2559 (1989).
- [56] J. J. Hudson, B. E. Sauer, M. R. Tarbutt, and E. A. Hinds, *Phys. Rev. Lett.* **89**, 023003 (2002).
- [57] D. Kawall, F. Bay, S. Bickman, Y. Jiang, and D. DeMille, *AIP Conf. Proc.* **698**, 192 (2003).
- [58] R. Stutz, and E. Cornell, *Bull. Am. Soc. Phys.* **89**, 76 (2004).
- [59] C. Y. Liu, and S. K. Lamoreaux, *Mod. Phys. Lett. A* **19**, 1235 (2004).
- [60] S. K. Lamoreaux, and S. Eckel, arXiv : physics/0701198v2, (2007).
- [61] L. Pondrom, R. Handler, M. Sheaff, P. T. Cox, J. Dworkin, O. E. Overseth, T. Devlin, L. Schachinger, and K. Heller, *Phys. Rev. D* **23**, 814 (1981).
- [62] F. del Aguila, and M. Sher, *Phys. Lett. B* **252**, 116 (1990).
- [63] R. Escribano, and E. Masso, *Phys. Lett. B* **395**, 369 (1997).
- [64] K. P. Jungmann, arXiv : physics/0501154v2, (2005).
- [65] K. P. Jungmann, *Hyperfine Interact.* **172** 5 (2006).

- [66] C. Chin, V. Leiber, V. Vuletić, A. J. Kerman, and S. Chu, *Phys. Rev. A* **63**, 033401 (2001).
- [67] V. Dzuba, V. Flambaum, and J. Ginges, Annual Report, The University of New South Wales, Sydney, Australia (1999).
- [68] K. Pachucki, private Communication, NIPNET meeting (2002).
- [69] J. Engel, M. Bender, J. Dobaczewski, J. H. de Jesus, and P. Olbratowski, *Phys. Rev. C* **68**, 025501 (2003).
- [70] N. Auerbach, *J. Phys. G: Nucl. Part. Phys.* **35**, 014040 (2008).
- [71] R. A. Seńkov, N. Auerbach, V. V. Flambaum, and V. G. Zelevinsky, arXiv : 0710.3367, (2007).
- [72] P. G. H. Sanders, *Contemporary Physics* **42**, 97 (2001).
- [73] N. Fortson, P. Sandars, and S. Barr, *Physics Today*, **June 2003**, 33 (2003).
- [74] J. P. Jacobs, W. M. Klipstein, S. K. Lamoreaux, B. R. Heckel, and E. N. Fortson, *Phys. Rev. A* **52**, 3521 (1995).
- [75] E. D. Commins, S. B. Ross, D. DeMille, and B. C. Regan, *Phys. Rev. A* **50**, 2960 (1994).
- [76] J. R. Guest, N. D. Scielzo, I. Ahmad, K. Bailey, J. P. Greene, R. J. Holt, Z. T. Lu, T. P. OConnor, and D. H. Potterveld. *Phys. Rev. Lett.* **98**, 093001 (2007).
- [77] E. Rasmussen, *Z. Phys.* **86**, 24 (1933).
- [78] E. Rasmussen, *Z. Phys.* **87**, 607 (1934).
- [79] H. N. Russel, *Phys. Rev.* **46**, 989 (1934).
- [80] F. S. Tomkins, and B. Ercoli, *Appl. Opt.* **6**, 1299 (1967).
- [81] J. A. Armstrong, J. J. Wynne, and F. S. Tomkins, *J. Phys. B: At. Mol. Phys.* **13**, L133 (1980).
- [82] S. A. Ahmad, W. Klempt, R. Neugart, E. W. Otten, K. Wendt, and C. Ekström, *Phys. Lett. B* **133**, 47 (1983).

- [83] S. A. Ahmad, W. Klempt, R. Neugart, E. W. Otten, P. G. Reinhard, G. Ulm, and K. Wendt, Nucl. Phys. A **483**, 244 (1988).
- [84] K. Wendt, S. A. Ahmad, W. Klempt, R. Neugart, E. W. Otten, and H. H. Stroke, Z. Phys. D **4**, 227 (1987).
- [85] E. Arnold, W. Borchers, M. Carre, H. T. Duong, P. Juncar, J. Lerme, S. Liberman, W. Neu, R. Neugart, E. W. Otten, M. Pellarin, J. Pinard, G. Ulm, J. L. Vialle, and K. Wendt, Phys. Rev. Lett. **59**, 771 (1987).
- [86] S. N. Panigrahy, R. W. Dougherty, S. Ahmad, K. C. Mishra, T. P. Das, J. Andriessen, R. Neugart, E. W. Otten, and K. Wendt, Phys. Rev. A **43**, 2215 (1991).
- [87] N. D. Scielzo, J. R. Guest, E. C. Schulte, I. Ahmad, K. Bailey, D. L. Bowers, R. J. Holt, Z. T. Lu, T. P. O' Connor, and D. H. Potterveld, Phys. Rev. A **73**, 010501(R) (2006).
- [88] J. Bruneau, J. Phys. B **17**, 3009 (1984).
- [89] K. D. Sen, and A. Puri, Chem. Phys. Lett. **156**, 505 (1989).
- [90] E. Eliav, U. Kaldor, and Y. Ishikawa, Phys. Rev. A **53**, 3050 (1996).
- [91] V. A. Dzuba, and J. S. M. Ginges, Phys. Rev. A **73**, 032503 (2006).
- [92] V. V. Flambaum, and V. G. Zelevinsky, Phys. Rev. C **68**, 035502 (2003).
- [93] J. Bieroń, P. Indelicato, and P. Jönsson, Eur. Phys. J. Special Topics **144**, 75 (2007).
- [94] J. Bieroń, C. F. Fischer, S. Fritzsche, and K. Pachucki, J. Phys. B: At. Mol. Opt. Phys. **37**, L305 (2004).
- [95] V. A. Dzuba, and V. V. Flambaum, J. Phys. B: At. Mol. Opt. Phys. **40**, 227 (2007).
- [96] D. A. Lewis, J. Kumar, M. A. Finn, and G. W. Greenlees, Phys. Rev. A **35**, 131 (1987).
- [97] L. Jachreiss, and M. C. E. Huber, Phys. Rev. A **31**, 692 (1985).

- [98] S. Niggli, and M. C. E. Huber, Phys. Rev. A **35**, 2908 (1987).
- [99] S. Niggli, and M. C. E. Huber, Phys. Rev. A **39**, 3924 (1989).
- [100] G. Garcia, and J. Campos, J. Quant. Spectrosc. Radiat. Transfer **42**, 567 (1989).
- [101] A. F. Bernhardt, D. E. Duerre, J. R. Simpson, and L. L. Wood, J. Opt. Soc. Am. **66**, 420 (1976).
- [102] G. K. Gerke, and B. A. Bushaw, Phys. Rev. A **37**, 1502 (1988).
- [103] A. Bizzarri, and M. C. E. Huber, Phys. Rev. A **42**, 5422 (1990).
- [104] J. Brust, and A. C. Gallagher, Phys. Rev. A **52**, 2120 (1995).
- [105] D. A. Lewis, J. Kumar, M. A. Finn, and G. W. Greenlees, Phys. Rev. A **35**, 131 (1987).
- [106] S. G. Schmelling, Phys. Rev. A **9**, 1097 (1974).
- [107] M. Gustavsson, G. Olsson, and A. Rosén, Z. Phys. A **290**, 231 (1979).
- [108] R. Aydin, R. Aldenhoven, L. Degener, H. Gebauer, and G. Meisel, Z. Phys. A **273**, 233 (1975).
- [109] A. C. Mueller, F. Buchinger, W. Klempt, E. W. Otten, R. Neugrat, C. Ekstrom, and J. Heinemeier, Nucl. Phys. A **403**, 234 (1983).
- [110] W. A. van Wijngaarden, and J. Li, Can. J. Phys. **73**, 484 (1995).
- [111] P. Grundevik, M. Gustavsson, G. Olsson, and T. Olsson, Z. Phys. A **312**, 1 (1983).
- [112] U. Dammalapati, "Metastable D-state spectroscopy and laser cooling of barium", doctoral thesis, University of Groningen, Netherlands (2006).
- [113] U. Dammalapati, S. De, K. P. Jungmann, and L. Willmann, Submitted in Eur. Phys. J D, arXiv : 0805.2022, (2008).
- [114] P. McCavert, and E. Trefftz, J. Phys. B: At. Mol. Phys. **7**, 1270 (1974).

- [115] P. Hafner, and H. E. Schwarz, *J. Phys. B: Atom. Molec. Phys.* **11** 2975 (1978).
- [116] C. W. B. Jr, R. L. Jaffe, S. R. Langhoff, F. G. Mascarello, and H. Partridge, *J. Phys. B: At. Mol. Phys.* **18**, 2147 (1985).
- [117] C. H. Greene, and M. Aymar, *Phys. Rev. A* **44**, 1773 (1991).
- [118] J. Migdalek, and W. E. Baylis, *Phys. Rev. A* **42**, 6897 (1990).
- [119] A. Lurio, *Phys. Rev.* **136**, A376 (1964).
- [120] W. Neuhauser, M. Hohenstatt, P. Toschek, and H. Dehmelt, *Phys. Rev. Lett.* **41**, 233 (1978).
- [121] W. Neuhauser, M. Hohenstatt, P. Toschek, and H. Dehmelt, *Appl. Phys.* **17**, 123 (1978).
- [122] Z. Lin, K. Shimizu, M. Zhan, F. Shimizu, and H. Takuma, *Jap. J. App. Phys.* **30**, L1324 (1991).
- [123] E. L. Raab, M. Prentiss, A. Cable, S. Chu, and D. E. Pritchard, *Phys. Rev. Lett.* **59**, 2631 (1987).
- [124] R. S. Williamson, and T. Walker, *J. Opt. Soc. Am. B* **12**, 1393 (1995).
- [125] J. A. Behr, A. Gorelov, T. Swanson, O. Häusser, K. P. Jackson, M. Trinczek, U. Giesen, J. M. DAuria, R. Hardy, T. Wilson, P. Choboter, F. Leblond, L. Buchmann, M. Dombisky, C. D. P. Levy, G. Roy, B. A. Brown, and J. Dilling, *Phys. Rev. Lett.* **79**, 375 (1997).
- [126] T. Walker, D. Hoffmann, P. Feng, and R. S. Williamson, *Phys. Lett. A* **163**, 309 (1992).
- [127] G. Gwinner, J. A. Behr, S. B. Cahn, A. Ghosh, L. A. Orozco, G. D. Sprouse, and F. Xu, *Phys. Rev. Lett.* **72**, 3795 (1994).
- [128] D. Sesko, C. G. Fan, and C. E. Wieman, *J. Opt. Soc. Am. B* **5**, 1225 (1988).
- [129] M. D. Dirosa, S. G. Crane, J. J. Kitten, W. A. Taylor, D. J. Vieira, and X. Zhao, *App. Phys. B* **76**, 45 (2003).

- [130] K. Sengstock, U. Sterr, J. H. Muller, V. Reiger, D. Bettermann, and W. Ertmer, *Appl. Phys. B* **59**, 99 (1994).
- [131] A. Aspect, E. Arimondo, R. Kaiser, N. Vansteenkiste, and C. Cohen Tannoudji, *Phys. Rev. Lett.* **61**, 826 (1988).
- [132] F. Shimizu, K. Shimizu, and H. Takuma, *Phys. Rev. A* **39**, 2758 (1989).
- [133] H. Katori, and F. Shimizu, *Japanese. J. App. Phys.* **29**, L2124 (1990).
- [134] C. Y. Chen, Y. M. Li, K. Bailey, T. P. O'Connor, L. Young, and Z.T. Lu, *Science* **286**, 1139 (1999).
- [135] M. Walhout, H. J. L. Megens, A. Witte, and S. L. Rolston, *Phys. Rev. A* **48**, R879 (1993).
- [136] C. C. Bradley, W. R. Anderson, J. J. McClelland, and R. J. Celotta, *Bull. Am. Phys. Soc.* **43**, 1291 (1998).
- [137] A. S. Bell, J. Stuhler, S. Locher, S. Hensler, J. Mlynek, and T. Pfau, *Europhys. Lett.* **45**, 156 (1999).
- [138] G. Uhlenberg, J. Dirscherl, and H. Walther, *Phys. Rev. A* **62**, 063404 (2000).
- [139] K. Honda, Y. Takahashi, T. Kuwamoto, M. Fujimoto, K. Toyoda, K. Ishikawa, and T. Yabuzaki, *Phys. Rev. A* **59**, R934 (1999).
- [140] J. J. McClelland and J. L. Hanssen, *Phys. Rev. Lett.* **96**, 143005 (2006).
- [141] K. A. Brickman, M.S. Chang, M. Acton, A. Chew, D. Matsukevich, P. C. Haljan, V. S. Bagnato, and C. Monroe, *Phys. Rev. A* **76**, 043411 (2007).
- [142] H. Hachisu, K. Miyagishi, S. G. Porsev, A. Derevianko, V. D. Ovsianikov, V. G. Palchikov, M. Takamoto, and H. Katori, *Phys. Rev. Lett.* **100**, 053001 (2008).
- [143] J. E. Simsarian, A. Ghosh, G. Gwinner, L. A. Orozco, G. D. Sprouse, and P. A. Vovtyas, *Phys. Rev. Lett.* **76**, 3522 (1996).

- [144] T. Kurosu, and F. Shimizu, *Jap. J. App. Phys.* **29**, L2127 (1990).
- [145] B. Smeets, R. W. Herfst, L. P. Maguire, E. Te Sligte, P. van der Straten, H. C. W. Beijerinck, and K. A. H. Van Leeuwen, *Appl. Phys. B* **80**, 833 (2005).
- [146] S. J. Rehse, K. M. Bockel, and S. Au Lee, *Phys. Rev. A* **69**, 063404 (2004).
- [147] R. W. McGowan, D. M. Giltner and S. A. Lee, *Opt. Lett.* **20**, 2535 (1995).
- [148] B. Klöter, C. Weber, D. Haubrich, D. Meschede, and H. Metcalf, *Phys. Rev. A* **77**, 033402 (2008).
- [149] J. Prodan, and W. Phillips, *Prog. Quant. Elect.* **8**, 231 (1984).
- [150] W. Ertmer, R. Blatt, J. L. Hall, and M. Zhu, *Phys. Rev. Lett.* **54**, 996 (1985).
- [151] W. Phillips, and H. Metcalf, *Phys. Rev. Lett.* **48**, 596 (1982).
- [152] J. Hoffnagle, *Opt. Lett.* **13**, 102 (1988).
- [153] V. S. Letokhov, V. G. Minogin, and B. D. Pavlik, *Opt. Commun.* **19**, 72 (1976).
- [154] S. Hoekstra, "Atom Trap Trace Analysis of Calcium Isotopes", doctoral thesis, University of Groningen, Netherlands (2005).
- [155] S. Knoop, "Electron Dynamics in Ion-Atom Interactions", doctoral thesis, University of Groningen, Netherlands (2006).
- [156] V. G. Hasan, "MOTRIMS investigations of electron removal from Na by highly charged ions", doctoral thesis, University of Groningen, Netherlands (2008).
- [157] K. MacAdam, A. Steinbach, and C. E. Wieman, *Am. J. Phys.* **60**, 1098 (1987).
- [158] L. Ricci, M. Weidemüller, T. Esslinger, A. Hemmerich, C. Zimmermann, V. Vuletic, W. König, and T. W. Hänsch, *Opt. Comm.* **117**, 541 (1995).

- [159] C. E. Wieman, and L. Hollberg, *Rev. Sci. Instrum.* **62**, 1 (1991).
- [160] L. Hollberg, R. Fox, S. Waltman, and H. Robinson, NIST Technical Note **1504**, May (1998).
- [161] U. Schünemann, H. Engler, R. Grimm, M. Weidemüller, and M. Zielonkowski, *Rev. Sci. Instrum.* **70**, 242 (1999).
- [162] K. Razdan, and D. A. Van Baak, *Am. J. Phys.* **70**, 1061 (2002).
- [163] R. H. L van Wooning, "Laser Frequency Offset Locking", Brede Bachelor of Engineering (BBoE) thesis, KVI and Hanzehogeschool, Groningen, Netherlands (2008).
- [164] A. Migdall, J. Prodan, W. Phillips, T. Bergeman, and H. Metcalf, *Phys. Rev. Lett.* **54**, 2596 (1985).
- [165] W. D. Phillips, *Rev. Mod. Phys.* **70**, 721 (1998).
- [166] W. D. Wineland, and W. M. Itano, *Phys. Rev. A* **20**, 1521 (1979).
- [167] C. C. Bradley, and R. G. Hult, *Expt. Meth. Physical. Sciences* **29B**, 129 (1996).
- [168] A. Ashkin, *Proc. Natl. Acad. Sci.* **94**, 4853 (1997).
- [169] H. J. Metcalf, and P. van der Straten, "Laser cooling and trapping", Springer, New York (1999).
- [170] C. J. Foot, "Atomic Physics", Oxford University Press, Oxford, (2005).
- [171] Z. T Lu, C. J. Bowers, S. J. Freedman, B. K. Fujikawa, J. L. Mortara, S. Q. Shang, K. P. Coulter, and L. Young, *Phys. Rev. Lett.* **72**, 3791 (1994).
- [172] N. D. Scielzo, S. J. Freedman, B. K. Fujikawa, and P. A. Vetter, *Phys. Rev. Lett.* **93**, 102501 (2004).
- [173] J. A. Behr, A. Gorelov, T. Swanson, O. Häusser, K. P. Jackson, M. Trinczek, U. Giesen, J. M. DAuria, R. Hardy, T. Wilson, P. Choboter, F. Leblond, L. Buchmann, M. Dombisky, C. D. P. Levy, G. Roy, B. A. Brown, and J. Dilling, *Phys. Rev. Lett.* **79**, 375 (1997).

- [174] P. A. Vetter, J. R. Abo-Shaeer, S. J. Freedman, and R. Maruyama, Phys. Rev. C **77**, 035502 (2008).
- [175] S. G. Porsev, A. Derevianko, and E. N. Fortson, Phys. Rev. A **69**, 021403(R) (2004).
- [176] Th. Udem, S. A. Diddams, K. R. Vogel, C.W. Oates, E. A. Curtis, W. D. Lee, W. M. Itano, R. E. Drullinger, J. C. Bergquist, and L. Hollberg, Phys. Rev. Lett. **86**, 4996 (2001).
- [177] K. Gibble, and S. Chu, Phys. Rev. Lett. **70**, 1771 (1993).
- [178] H. Friedburg, Naturwissenschaft **38**, 159 (1951).
- [179] H. Friedburg, Zeit. f. Phys. **130**, 439 (1951).
- [180] A. Ashkin, Phys. Rev. Lett. **24**, 156 (1970).
- [181] S. Chu, J. Bjorkholm, A. Ashkin, and A. Cable, Phys. Rev. Lett. **57**, 314 (1986).
- [182] E. Raab, M. Prentiss, A. Cable, S. Chu, and D. Pitchard, Phys. Rev. Lett. **59**, 2631 (1987).
- [183] M. Metcalf, J. Opt. Soc. Am. B **6**, 2206 (1989).
- [184] R. L Cavasso-Filho, A. Scalabrin, D. Pereira, and F. C. Cruz, Phys. Rev. A Rapid Commun. **67**, 21402 (2003).
- [185] E. A. Burt, R. W. Ghrist, C. J. Myatt, M. J. Holland, E. A. Cornell, and C. E. Wieman, Phys. Rev. Lett. **79**, 337 (1997).
- [186] T. C. Killian, D. G. Fried, L. Willmann, D. Landhuis, S. C. Moss, T. J. Greytak, and D. Kleppner, Phys. Rev. Lett. **81**, 3807 (1998).
- [187] S. Chu, L. Hollberg, J. E. Bjorholm, A. Cable, and A. Ashkin, Phys. Rev. Lett. **55**, 48, (1985).
- [188] U. Dammalapati, S. De, K. P. Jungmann, and L. Willmann, submitted in Phys. Rev. A, arXiv : Physics/0708.0332, (2007).
- [189] E. L. Raab, M. Prentiss, A. Cable, S. Chu, and D. E. Pritchard, Phys. Rev. Lett. **59**, 2631 (1987).

- [190] P. D. Lett, R. N. Watts, C. I. Westbrook, W. D. Phillips, P. L. Gould, and H. J. Metcalf, *Phys. Rev. Lett.* **61**, 169 (1988).
- [191] T. M. Brzozowski, M. Mączyńska, M. Zawada, J. Zachorowski, and W. Gawlik, *J. Opt. B: Quantum Semiclass. Opt.* **4**, 62 (2002).
- [192] D. Wineland, and W. Itano, *Phys. Rev. A* **20**, 1521 (1979).
- [193] J. Gordon, and A. Ashkin, *Phys. Rev. A* **21**, 1606 (1980).
- [194] R. Cook, *Phys. Rev. A* **22**, 1078 (1980).
- [195] P. D. Lett, W. D. Phillips, S. L. Rolston, C. E. Tanner, R. N. Watts, and C. I. Westbrook, *J. Opt. Soc. Am. B* **6**, 2084 (1989).
- [196] C. W. Oates, F. Bondu, R. W. Fox, and L. Hollberg, *Eur. Phys. J. D* **7**, 449 (1999).
- [197] A. K. Mollema, "Laser cooling, trapping and spectroscopy of calcium isotopes", doctoral thesis, University of Groningen, Netherlands (2008).
- [198] X. Xu, T. H. Loftus, M. J. Smith, J. L. Hall, A. Gallagher, and J. Ye *Phys. Rev. A* **66**, 011401 (2002).
- [199] T. Chaneliere, J. L. Meunier, R. Kaiser, C. Miniatura, and D. Wilkowski, *J. Opt. Soc. Am. B* **22**, 1819 (2005).
- [200] M. O. Scully, and M. S. Zubairy, "Quantum optics", Cambridge University Press, Cambridge (1997).
- [201] J. D. Jackson, "Classical Electrodynamics", Third Edition, Wiley (1999).
- [202] T. Bergeman, G. Erez, and H. J. Metcalf, *Phys. Rev. A* **35**, 1535 (1987).

# Summary

First laser cooling and trapping of the heavy alkaline-earth element barium has been achieved. The cooling cycle using the strong  $6s^2 \ ^1S_0 \rightarrow 6s6p \ ^1P_1$  transition at wavelength  $\lambda_1 = 553.7$  nm exhibits large leaks to metastable D-states. This makes laser trapping with this transition only impossible. Additional lasers are thus needed to bring the atoms back in to the cooling cycle. In total seven lasers were employed to confine barium atoms in a magneto-optical trap (MOT) (see Fig.C.1).

The properties of the barium MOT were characterized. The efficiency of capturing an atom from a thermal atomic beam into the MOT is 0.4(1)%. Loss rate mechanisms from the trap were studied by observing the decay of the trap population. Typical lifetimes of the MOT cloud are on the order of one second and are limited mainly due to insufficient repumping of D-states. The trapping efficiency and the trap lifetimes may be improved by employing more powerful lasers for repumping. The range of velocities from which barium atoms can be captured into the MOT is about 30 m/s. The velocity capture range could be widened significantly with an intense broadband laser light source in future. Different laser transitions were employed for repumping barium atoms from the  $6s5d \ ^3D_1$  and the  $6s5d \ ^3D_2$  states. They lead to similar trap populations and lifetimes. The temperature of the cold atomic barium cloud was determined to about 5 mK. This is about ten times larger than the Doppler limit known from the theory of laser cooling. Atomic properties of the  $5d^2 \ ^3F_2$  state were studied with trapped atoms, in particular it's lifetime was determined as  $160(10)\mu s$ .

This work has shown a possible scheme to trap atoms with a leaky cooling cycle. Since atoms with such properties are the majority of the elements in the periodic table, the number of optically trapable elements can be significantly enlarged. Of particular high interest is radium, the chemical homologue to barium. The techniques developed here can be used to build an efficient collection MOT for radium using the strong  $7s^2 \ ^1S_0 \rightarrow 7s7p \ ^1P_1$  transition as primary cool-

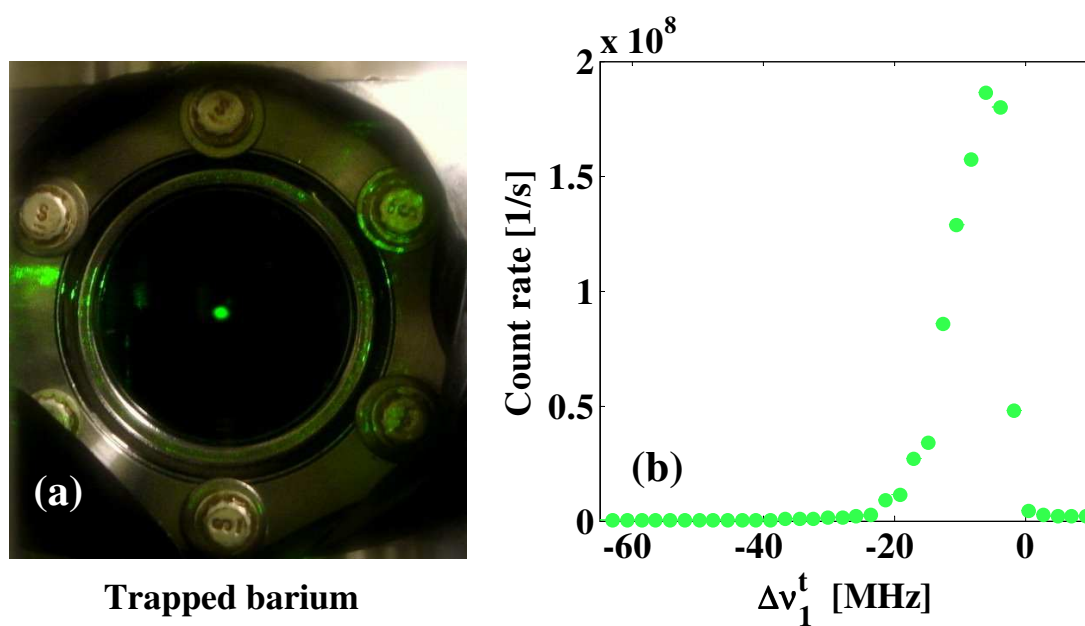


**Fig. C.1:** (a) Photograph of a cold cloud of barium atoms in a magneto-optical trap. The bright spot at the center of the optical port is scattered light at wavelength 553.7 nm of the cooling transition. (b) Dependence of the MOT fluorescence on the frequency detuning  $\Delta\nu_1^t$  of the trapping laser beams at wavelength 553.7 nm.

ing transition. The interest in radium stems from its high sensitivity to possible nuclear and electron permanent electric dipole moments (EDM's). An EDM violates parity as well as time reversal and is therefore of fundamental importance. Searches for such EDM's are among the main research goals of the recently commissioned TRI $\mu$ P facility at KVI.

# Samenvatting

Dit proefschrift beschrijft de eerste succesvolle poging om het zware aardalkali element barium met behulp van laserlicht af te koelen en te vangen. De koelingscyclus die de  $6s^2 \ ^1S_0 \rightarrow 6s6p \ ^1P_1$  overgang met de golflengte  $\lambda_1 = 553.7$  nm gebruikt om de barium atomen af te koelen laat grote lekken zien naar meta stabiele D-toestanden. Atomen die zich in deze toestanden bevinden ontsnappen aan de koelingscyclus. Meer lasers zijn noodzakelijk om de atomen daarin terug te brengen. In totaal werden er zeven lasers ingezet om barium in een magneto optische val (MOT) te vangen (zie Fig. C.2).

De eigenschappen van de barium MOT werden gekarakteriseerd. De efficiëntie om een atoom in te vangen vanuit een thermische atoombundel in de MOT is 0.4(1)%. Typische levensduren van de MOT wolk zijn in de orde van een seconde en worden voornamelijk begrensd door het onvoldoende terugbrengen van de atomen vanuit de D-toestanden. De invangefficiëntie en de vallevensduren zouden verbeterd kunnen worden door sterkere lasers te gebruiken. Het snelheidsinterval waaruit de barium atomen kunnen worden gevangen in de MOT is ongeveer 30 m/s. Atomen uit een bredere interval van snelheden zouden kunnen worden gevangen met een breedbandige lichtbron. Verschillende overgangen zijn gebruikt om de barium atomen die zich in de  $6s5d \ ^3D_1$  en de  $6s5d \ ^3D_2$  toestanden bevonden terug te brengen in de koelingscyclus. Deze leidden tot vergelijkbare MOT-bevolkingen en levensduren. De temperatuur van de koude atomaire barium wolk is ongeveer 5 mK. Dit is ongeveer tien keer groter dan de Doppler limiet wat bekend is van de theorie van laserkoeling. Atoomeigenschappen van de  $5d^2 \ ^3F_2$  toestand zijn bestudeerd met gevangen atomen, in het bijzonder is de levensduur van 160(10) $\mu$ s gevonden.

Dit werk heeft een mogelijk schema laten zien om atomen te vangen die een koelingscyclus met sterke lekken hebben. Aangezien dit zo is voor de meerderheid van de elementen in het periodiek systeem kan het aantal van optisch te vangen elementen aanzienlijk worden uitgebreid met de hier ontworpen meth-

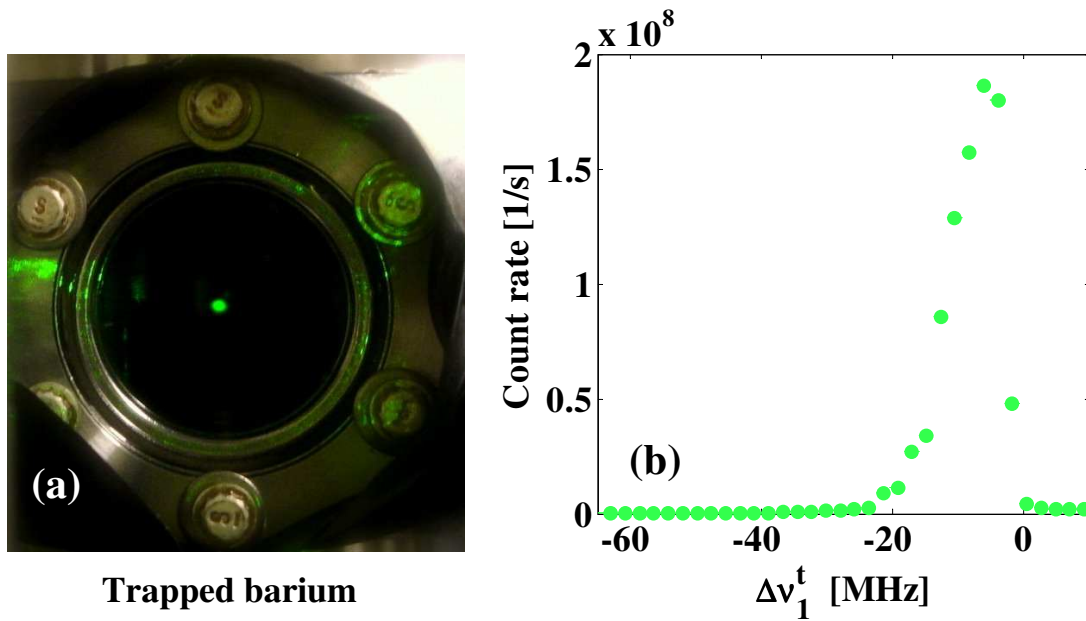


**Fig. C.2:** (a) Een foto van een wolk koude barium atomen in een magneto-optische val. De heldere stip in het midden van de optische toegangspoort is verstrooid licht op een golflengte 553.7 nm van de koelingsovergang. (b) De grafiek laat de afhankelijkheid zien van de MOT fluorescencie op de frequentie verstemming  $\Delta\nu_1^t$  van de laser bundel met de golflengte 553.7 nm.

oden. Van bijzonder groot belang is dat voor het radium atoom, chemisch homolog aan barium. De in dit werk ontwikkelde technieken kunnen worden ingezet om een efficiënte verzamel-MOT te bouwen voor radium door van de sterke  $7s^2 \ ^1S_0 \rightarrow 7s7p \ ^1P_1$  overgang als primaire koelovergang gebruik te maken. De interesse in radium vloeit voort uit de hoge gevoeligheid van dit atoom voor de mogelijke permanente kern- en elektrische dipoolmomenten (EDM'en). Een EDM schendt zowel pariteit als tijdsomkering en is daarom van fundamenteel belang. De zoektocht naar EDM's behoort tot de belangrijkste doelstelling van de recentelijk gereed gekomen TRI $\mu$ P faciliteit op het KVI.

# Acknowledgement

This thesis would not have been written without the knowledgeable support of Dr. Lorenz Willmann and Prof. Dr. Klaus Jungmann. Dr. Umakanth Dammalapati, Thomas Middlemann and Joost van den Berg have also contributed enormously to this work.

My supervisor, Lorenz, showed me how to judge the work by finding discrete steps for achieving a finite goal. He taught me how to build up things like a professional rather than quick fix of things which are useful for long period. I am thankful to him for putting me in the track of research. I express gratitude to my thesis supervisor Klaus for guidance and trenchant critiques on my thesis. I thank Umakanth for teaching me how to use the many pieces of apparatus.

I would like to thank the Stichting voor Fundamenteel Onderzoek der Materie (FOM) for supporting this work under programme 48 (TRI $\mu$ P). I also acknowledge the support of the Ubbo Emmius student fellowship of the University of Groningen.

I am grateful to Prof. Dr. Reinhard Morgenstern (KVI, Groningen, The Netherlands), Prof. Dr. Erling Riis (University of Strathclyde, Glasgow, Scotland, U.K) and Prof. Dr. Peter van der Straten (Universiteit Utrecht, Utrecht, The Netherlands) for spending their time on careful reading of my thesis.

I thank all of my colleagues in the TRI $\mu$ P group namely Prof. Dr. Hans Wilschut, Dr. Gerco Onderwater, Prof. Dr. Ronnie Hoekstra, Prof. Dr. Rob Timmermans, Dr. Otto Dermois, Leo Huisman, Ronald van Wooning, Dr. Bijaya Kumar Sahoo, Dr. Parveen Shidling, Moslem Sohani, Albert Mollema, Valeriu Gabriel Hasan, Marlana da Silva e Silva, Lotje Wansbeek, Wilbert Kruithof, Oscar Versolato, Duurt Johan van der Hoek, Gouri Shankar Giri and Bodhaditya

Santra for their scientific helps in the course of this work. I also thank my former colleagues Gerald Ebberink, Dr. Emil Traykov, Dr. Andrey Rogachevskiy, Aran Mol, Thomas Middlemann, Joost van den Berg, Sander Rikhof and Ulrike Wegener.

I would like to thank all the people working in the electronics, mechanical, electrical, vacuum and IT departments of KVI for their cooperation. I am also grateful to the KVI administration, financial section and personal section, for their help during my stay in Groningen. I would like to give special thank to Hilde Landstra and Hilde van der Meer for taking care of all the paperwork.

I express my gratitude to all my Indian friends in Groningen, who made my life joyful far away from my family. I would like to thank the Groningen Indian Student Association (GISA) for their initiatives in arranging different social occasions. Heartily thanks go to Martha Reijnders for caring me daily in the last few years.

I am thankful to all my teachers starting from my first school days up to my university education. Especially I thank Late Basanta Bhattacharyya, Maya Bhattacharyya, Joydeb Chakraborty, Paresh Nath Roy, Dr. Jiten Nandi, Dr. Promotes Banerjee, and Dr. Prashanta Kumar Dutta, who encouraged me to choose the research life. I am grateful to Prof. Dr. Bhanu Pratap Das for his encouraging words and for helping me in finding out the right routes.

My passion for education came from my two late grandmothers, Molina De and Aloka Das. I like to thank all of my relatives for their help and support. Special thanks go to Samar Prasad Sigha Roy and his family. I thank my fiancée, Tanwee Das, and her family for their support. Finally, I would like to thank my constant source of encouragement, my parents, for their care and support. They made it possible for me to achieve goals in my life. I dedicate this thesis to my parents.

**Subhadeep**